

MODELING AND EXPERIMENTS OF FIRST ORDER MAGNETOCALORIC MATERIAL
PERFORMANCE

By

MICHAEL BENEDICT

A DISSERTATION PRESENTED TO THE GRADUATE SCHOOL
OF THE UNIVERSITY OF FLORIDA IN PARTIAL FULFILLMENT
OF THE REQUIREMENTS FOR THE DEGREE OF
DOCTOR OF PHILOSOPHY

UNIVERSITY OF FLORIDA

2016

© 2016 Michael Benedict

ACKNOWLEDGMENTS

I thank my parents for giving me the opportunities to pursue a life of learning. You have given me the opportunities and love of learning that made this possible.

I would like to acknowledge the help of all my former teachers and especially the help of Dr. Sherif in guiding me through this process. The mentorship of these academics has been essential to my intellectual progress.

I would like to thank David Beers and Venkat Venkatakrisnan who enabled me to pursue this degree. I am fortunate to have had this opportunity and I owe most of this to these two mentors and friends.

I would especially like to thank and acknowledge my wife Jessica whose love and support has made all of this possible. It is not often that one finds such an amazing person with whom such a deep intellectual experience can be shared. You are truly incredible. I am especially lucky to have someone who can share in my love of engineering among everything else.

TABLE OF CONTENTS

	<u>page</u>
ACKNOWLEDGMENTS.....	3
LIST OF TABLES	7
LIST OF FIGURES	8
LIST OF SYMBOLS.....	13
LIST OF ABBREVIATIONS.....	17
ABSTRACT	19
CHAPTER	
1 INTRODUCTION AND OBJECTIVES	20
Motivation.....	20
Objectives	21
2 LITERATURE REVIEW	25
History.....	25
Magnetocaloric Materials.....	28
Modeling of Magnetic Refrigeration.....	29
Magnetocaloric Prototypes.....	41
Gaps in the Current Body of Knowledge.....	52
3 FUNDAMENTALS OF MAGNETIC REFRIGERATION.....	56
Description of MCE.....	56
Thermodynamics of the MCE	57
Models of Specific Heat.....	60
Simplified FOMT Material and Restrictions on MCE	61
Hysteresis	63
Experimental Measurement.....	64
Other MCE Considerations.....	66
Thermodynamics of Cyclical Magnetocaloric Refrigerators.....	67
4 NUMERICAL MODEL OF THE ACTIVE MAGNETIC REGENERATOR.....	75
Idealized Magnetocaloric Refrigerator Operation.....	75
Regenerator Model.....	76
Fundamental Equations.....	77
MCHP Parameters	78

	Boundary Conditions	79
5	EXPERIMENTAL PROTOTYPE	81
	Magnetic System	82
	Hydraulic System.....	84
	Loading and Configurations	86
	Measurement	87
	Accuracy	89
	Physical Design.....	89
	Measurement System.....	92
	Losses	93
	Parameter Space.....	95
6	MAGNETOCALORIC MATERIAL MODEL	107
	Magnetocaloric Material Curves from the Literature.....	107
	General Curve Description.....	108
	Magnetocaloric Material Model Form	109
	Basic Magnetocaloric Material Model Requirements	109
	Magnetocaloric Material Models to be Compared.....	110
	Thermodynamic Data Reconstruction	112
	AMR Model Implementation.....	114
7	EXPERIMENTAL VALIDATION OF AMR MODEL AND MMM.....	124
	Statistical Comparison	124
	Experimental Validation	126
	Operational Parameters.....	127
	MCHP Design Parameters.....	132
	Analysis of Results	139
8	MAGNETOCALORIC PARAMETER SPACE	155
	Heat Pump Parameter Selection	156
	Assumption 1: Ideal MCHP	156
	Assumption 2: Simplified Cycle	157
	Assumption 3: Defined Regenerator Structure and Design Condition	158
	Assumption 4: Average non-MCE Properties	159
	Magnetocaloric Material Selection.....	160
	AMR Model Configuration	161
	Results	164
	Thermodynamic Analysis of Study 1	165
	Study 1 Findings for Hot and Cold Side	168
9	MMM STUDY OF CURRENT MATERIALS PARAMETER SPACE.....	189
	AMR Model Simulation Time Reduction	189

Magnetocaloric Material Selection.....	193
Results	198
Average Impact MMM of Parameters.....	200
An Analysis of the Usefulness of Averaging	203
MMM Parameter Impact on Efficiency.....	205
MMM Parameters and Physical Parameters Interaction	207
Highest 20% of Efficiency	208
Highest 20% of Cooling Capacity.....	209
Highest 20% of Efficiency and cooling capacity.....	210
 10 DISCUSSION AND CONCLUSIONS	 226
MCHP Insights	226
Magnetocaloric Material Model Insights.....	227
Model Validation Insights	228
Modeling Study Design Insights	229
Modeling Study Results Insights	230
Recommendations.....	232
Summary of Contributions.....	233
 APPENDIX	
 A HIGH EFFICIENCY GRAPHS.....	 234
 B HIGH COOLING CAPACITY GRAPHS	 241
 C HIGH COOLING CAPACITY AND EFFICIENCY GRAPHS	 248
 LIST OF REFERENCES	 255
 BIOGRAPHICAL SKETCH.....	 266

LIST OF TABLES

<u>Table</u>	<u>page</u>
2-1 List of models reviewed from the literature created.....	54
6-1 Study parameter levels.....	118
7-1 Test parameters for the HA1 MCHP.....	141
7-2 MMM Parameter values.....	142
7-3 Specification for each of the regenerators tested.....	143
7-4 Parameters for each of the test cases. Magnet rotation refers to the rotation of the outer magnet relative to the stationary inner magnet with 0 degrees being the minimum field.....	143
7-5 Results from tests. Max cooling capacity and cooling capacity span product are both determined from the intersection of the two linear fits and may not correspond to measured points.....	144
8-1 List of parameters that both define a MCHP and its operation.	176
8-2 Full parameter field with parameter eliminations by assumption.	178
8-3 Average parameters used to represent generic currently available FOMT material.	180
8-4 Prediction using a single span point compared to actual measurement.	180
8-5 List of Parameters Study 1.....	181
8-6 Study 2 additional parameters	181
9-1 Values for the speed up parameters from Study 3.....	211
9-2 Values for the MMM parameters to be used in Study 4.	211

LIST OF FIGURES

<u>Figure</u>	<u>page</u>
3-1 A simplified version of total entropy.....	69
3-2 An ideal FOMT displayed as the specific heat of at both zero and high applied field.....	70
3-3 Entropy curves for an ideal FOMT.	70
3-4 Different combinations of combinations of specific heat characteristics.....	71
3-5 The MCE of different simple FOMT materials.....	72
3-6 Illustration of magnetic refrigeration cycle with vapor compression cycle for comparison.....	73
3-7 The magnetocaloric cycle on a portion of the entropy temperature diagram.....	74
4-1 A schematic representation of the node structure and interactions in the AMR model.....	80
4-2 An example profile of normalized volumetric flow for a cycle.	80
5-1 Top view of HA1. Michael Benedict. August 20, 2014. Louisville, Kentucky.	98
5-2 Front view of a twelve segment Halbach array.	98
5-3 The resultant internal flux density for a Halbach array as a function of the number of magnetic segments.....	99
5-4 Field measurements in three dimensions for one of the nested Halbach arrays.....	99
5-5 Hydraulic schematic of HA1.....	100
5-6 A single cycle broken up into steps for HA1.	101
5-7 Hot side heat exchanger constructed for low flow. Michael Benedict. September 20, 2014. Louisville, Kentucky.....	102
5-8 An example of temperature output data from HA1.....	103
5-9 Scaled drawing of the critical flow paths for temperature measurement.	103
5-10 Reverse heat leak measurement with linear trend line for an intercept set to zero.....	103

5-11	Conduction path from regenerator material to ambient.	104
5-12	Fiber temperatures as a function of time.	104
5-13	HA1 flow rate capability as a function of pressure drop in the system.	105
5-14	Parameter space for regenerator designs in HA1.	105
5-15	Maximum operational frequency for the largest possible regenerator in HA1. ...	106
6-1	Characteristic properties of magnetocaloric materials.....	119
6-2	FOMT material raw data compared to the best fit with the simple model.....	120
6-3	FOMT material and the characteristics of these types of curves.	120
6-4	Lorentzian fit of FOMT material data	121
6-5	Hyperbolic secant function show by itself	121
6-6	Percent error to 5,000 point case averaged across all variables.	122
6-7	Average simulation time based on the fidelity of the MMM.....	122
6-8	Individual parameters from the fidelity study showing error as a function of the number of temperature points used for the MMM.	123
7-1	Average coefficient of determination for two FOMT materials represented by the MMMs.	145
7-2	Average coefficient of determination for specific heat	145
7-3	Coefficient of determination compared to the value of the MMM constants.	146
7-4	Results of the hot side sweep test. Span shown as a function of rejection temperature.....	146
7-5	Results of the Baseline test.	147
7-6	Comparison of test to simulated results using both measured data and MMMs.	148
7-7	Relative error at the maximum product of cooling capacity and span. Positive error represents over prediction and negative under prediction.....	149
7-8	Results of AMR modeling study to determine operating conditions for regenerator testing	150

7-9	Lowest temperature from the Baseline test regenerator scaled based on two thirds scaling.	150
7-10	Cooling capacity span curve for the Baseline regenerator test case Test 1.	151
7-11	Baseline Test 1 shown with linear relationships between cooling capacity and span along with the maximum product of cooling capacity and span.	151
7-12	Results from each tests and AMR model predictions.	152
7-13	Test results with individual parameters isolated and related to the maximum cooling capacity span product.	154
7-14	Error between the MMM and test data.	154
8-1	An example of HA1 operating with continuous magnet rotation and the same cycle under ideal operating conditions.	182
8-2	Cumulative distribution of spans at the knee point for experimental results.	182
8-3	Average cooling capacity for all cases compared to displacement. Too much displacement may washout the MCE.	183
8-4	Full temperature data for a single set of MCHP design and operational parameters.	183
8-5	Cooling capacity averaged across the selected cases as a function of the hot side temperature.	184
8-6	Cooling capacity span product averaged across the selected cases as a function of the hot side temperature.	184
8-7	Relative cooling capacity and cooling capacity span product as a function of the hot side temperature.	185
8-8	Average cooling capacity span product and cooling capacity as a function of the cold side temperature.	185
8-9	Average cooling capacity span product and cooling capacity normalized to maximums as a function of the cold side temperature.	186
8-10	Parameters that have a local maximum or low impact on cooling capacity.	186
8-11	Parameters with a large average impact on cooling capacity.	187
8-12	Cooling capacity and pumping power averaged as a function of particle diameter and fluid velocity from Study 2.	187
8-13	Combined results of Study 1 and 2 compared to the results of Study 1.	188

9-1	Flow diagram of additional code implemented to increase simulations speed. .	212
9-2	Results from convergence criteria study.....	212
9-3	Effect on simulation time of C_{min}	213
9-4	Code diagram for program which maintains a constant TR_{cap} for Study 4	214
9-5	Example of a material from Study 4.	214
9-6	Results of the Study 4 runs.....	214
9-7	Physical parameters shown by the percentage of runs at each of the levels of the parameter based on the termination condition of the simulations.	215
9-8	Example of how each of the MMM parameters is normalized.	215
9-9	Comparison of the ΔT MMM parameters on average predicted performance. .	216
9-10	Results from Study 4.	216
9-11	The distribution of completed runs compared to MCHP performance.....	217
9-12	Effect of the amplitude of ΔT on cooling capacity.	217
9-13	Effect of the amplitude of C_p on cooling capacity.	218
9-14	ΔT parameters' influence on cooling capacity.....	218
9-15	C_p parameters' influence on cooling capacity.	219
9-16	Average ϕ as a function of the relative ΔT parameter levels.	219
9-17	Average ϕ as a function of the relative C_p MMM parameter levels.	220
9-18	Material parameters with the largest influence on ϕ	220
9-19	Results from the remaining material parameters.	221
9-20	Comparison of A_{Cp} and the number of stages to high efficiency.....	222
9-21	Interactions from most efficient runs subset.	223
9-22	Highest 20% of cooling capacity results.	224
9-23	High cooling capacity and efficiency results.	225
A-1	$A_{\Delta T}$ with each MCHP parameter.....	234
A-2	$W_{\Delta T}$ with each MCHP parameter.....	235

A-3	$S_{\Delta T}$ with each MCHP parameter.....	236
A-4	A_{Cp} with each MCHP parameter.....	237
A-5	W_{Cp} with each MCHP parameter.....	238
A-6	S_{Cp} with each MCHP parameter.....	239
A-7	O_{Cp} with each MCHP parameter.....	240
B-1	$A_{\Delta T}$ with each MCHP parameter.....	241
B-2	$W_{\Delta T}$ with each MCHP parameter.....	242
B-3	$S_{\Delta T}$ with each MCHP parameter.....	243
B-4	A_{Cp} with each MCHP parameter.....	244
B-5	W_{Cp} with each MCHP parameter.....	245
B-6	S_{Cp} with each MCHP parameter.....	246
B-7	O_{Cp} with each MCHP parameter.....	247
C-1	$A_{\Delta T}$ with each MCHP parameter.....	248
C-2	$W_{\Delta T}$ with each MCHP parameter.....	249
C-3	$S_{\Delta T}$ with each MCHP parameter.....	250
C-4	A_{Cp} with each MCHP parameter.....	251
C-5	W_{Cp} with each MCHP parameter.....	252
C-6	S_{Cp} with each MCHP parameter.....	253
C-7	O_{Cp} with each MCHP parameter.....	254

LIST OF SYMBOLS

β	Relative cooling capacity
δ	Inexact differential
ΔP	Pressure drop
ΔS	isothermal change in entropy due to magnetic field change
ΔT	Adiabatic temperature change due to a changing magnetic field
ΔT_{H2}	Adiabatic magnetization at field change H2
ΔT_{mag}	Adiabatic temperature change on magnetization
Θ_1	Ratio of cooling capacity per cycle to fluid power per cycle
μ_0	Permeability of a vacuum
ρ	Density
σ	Reduced magnetization
Y	Sommerfeld constant
ϕ	Percent of Carnot coefficient of performance
v_{sf}	Superficial fluid velocity
0	Subscript for initial condition (with zero applied magnetic field)
A	Amplitude parameter for the material model
A_{pa}	Frontal area of a particle
A_{pl}	Frontal area of a plate
A_R	Regenerator frontal area
B_{result}	Resulting flux density
B	Base value for the material model
B_j	Brillouin function
B_r	Remnant flux density
c	Cycles

C_1	Specific heat of phase 1
C_2	Specific heat of phase 2
C_d	Debye model of specific heat
C_e	Electronic contribution to specific heat
C_m	Mean field theory contribution to specific heat
C_{min}	Minimum number of cycles
C_{offset}	Offset specific heat
C_P	Specific heat
C_{P0}	Specific heat in zero field
C_{Pf}	Fluid specific heat
C_{PH}	Specific heat in an applied field
d	Exact differential
dCL	Change in cooling load cycle to cycle
dCL_{crit}	Critical change in cooling capacity for convergence
ϵ	Fluid fraction of a regenerator
H	Applied magnetic field
h	Subscript for applied magnetic field
H_f	Final applied magnetic field
k	Thermal conductivity
K_B	Boltzman constant
k_{eff}	Axial dispersion coefficient
L	Latent heat of phase change
L_C	Characteristic length of a particle
L_{node}	Length of a node
L_R	Width of a regenerator

M	Magnetization
m_{do}	Slope in the drop off region of the cooling capacity span curve
M	Mass
m_{pl}	Slope in the plateau region of the cooling capacity span curve
n	Node
N_s	Number of spins per unit mass
N_s	Number of magnetic segments
O	Temperature offset between the maximum amplitude of adiabatic temperature change and specific heat for the material model
Q_{cond}	Heat conducted through bed
P_M	Maximum test cooling capacity
Q	Heat
Q_c	Cooling capacity
Q_c	Accepted heat or cooling capacity
$Q_{C_{cyc}}$	Cooling capacity per cycle
Q_H	Rejected heat
Q_{max}	Maximum cooling capacity
Q_p	Fluid energy for a single flow period
R^2	Coefficient of determination
Re	Reynolds number
r_i	Inner radius
r_o	Outer radius
S	Skew parameter for the material model
S_{ph}	Sphericity
Sp_k	Span at the knee point

T	Temperature
t	Time
T_{amb}	Ambient temperature
T_C	Curie Temperature
TC	Thermocouple
t_{crit}	Maximum allowable simulation time
T_D	Debye temperature
t_{flow}	Time for single flow period
T_{nf}	Node temperature
T_{nf+1}	Adjacent node temperature in right direction
T_{nf-1}	Adjacent node temperature in left direction
T_{nMCM}	Temperature of Magnetocaloric material node
TR_{CAP}	Total refrigeration capacity
T_T	Temperature of transition
U	Internal energy
UA_{MCM-f}	Heat transfer correlation between fluid node and magnetocaloric material node with units of W/K
U_{rad}	Radial heat transfer rate through a regenerator
V_{node}	Volume of a node
W	Work
W	Width parameter for the material model

LIST OF ABBREVIATIONS

AMR	Active magnetic regenerator
Cont	Continuous
COP	Coefficient of performance
DSC	Differential scanning calorimeter
DTU	Danish Technical University
FOMT	First order magnetic transition
Gd	Gadolinium
GWP	Global warming potential
HA1	Halbach array one prototype
ID	Inner diameter
Interp	Interpolated
LVDT	Linear variable differential transformer
MCE	Magnetocaloric effect
MCM	Magnetocaloric material
MCR	Magnetocaloric refrigeration
MCHP	Magnetocaloric heat pump
MFT	Mean field theory
MMM	Magnetocaloric material model
OD	Outer diameter
PDE	Partial differential equation
PDF	Probability density function
Pearson IV	Material model based on the Pearson distribution
Raw	Measured raw material data
SecH	Material model based on the hyperbolic secant function

SOMT	Second order magnetic transition
Sp	Span
SpLo	Split Lorentzian material model
Uvic	University of Victoria
VSM	Vibrating sample magnetometer

Abstract of Dissertation Presented to the Graduate School
of the University of Florida in Partial Fulfillment of the
Requirements for the Degree of Doctor of Philosophy

MODELING AND EXPERIMENTS OF FIRST ORDER MAGNETOCALORIC MATERIAL
PERFORMANCE

By

Michael Benedict

December 2016

Chair: S.A. Sherif
Major: Mechanical Engineering

Magnetocaloric materials offer an attractive new way to effect heat pumping at potentially greater efficiencies than current technology. First-order multi-stage magnetocaloric materials offer high relative cooling capacity with potentially low-cost elements in their production.

The following work presents a new magnetocaloric refrigeration prototype with experimental results along with a series of modeling studies which help to understand the full parameter space of magnetocaloric refrigeration. A unique method of representing the thermodynamic properties of magnetocaloric materials is developed for use in the modeling studies. Validation of this method is carried out through the modeling of experimental results. Both the modeling studies and magnetocaloric refrigerator results offer new insights into the performance of magnetocaloric prototypes. Enabling the treatment of material properties as parameters for modeling investigation offers new possibilities for both materials research and magnetocaloric refrigerator design.

CHAPTER 1 INTRODUCTION AND OBJECTIVES

Motivation

Interest in energy usage has increased at all stages of the energy cycle. Chief among concerns over energy are the environmental impact of greenhouse gases and the limited supply of fossil fuels. Heat pump applications potentially represent more than half of commercial and residential energy usage in the United States (Conti et al., 2014). In addition many traditional refrigerants used in the vapor compression heat pumps that currently dominate the market have a large global-warming potential (GWP). Finding an alternative heat pump technology which can eliminate the use of high GWP refrigerants and lower the power requirements for heat pumps helps to alleviate environmental and energy concerns.

As a material phenomenon the magnetocaloric effect (MCE) has been known for over a century, as a heat pumping technology for low temperature applications it has been in operation for decades. Recently progress in converting this interesting but niche technology into a serious competitor to vapor compression has been progressing rapidly. In theory magnetocaloric refrigeration (MCR) has the potential to achieve higher efficiency than vapor compression (Engelbrecht, 2004) and test devices have been reported which show very high efficiencies in excess of 50% of Carnot (Zimm et al., 1998). Additionally the magnetocaloric refrigerants along with their heat transfer fluids do not represent any GWP. Combining the reduction in Carbon emissions from efficient heat pumping with the elimination of global warming impact from refrigerants MCR can be a very attractive option for future refrigeration and heating.

Objectives

The proposed research attempts to positively influence the three major areas of magnetocaloric research; materials, magnetocaloric refrigeration prototypes, and modeling. To achieve this goal four main objectives and several sub-goals were identified:

- Design and build a unique and highly flexible magnetocaloric refrigeration prototype.
- Test and characterize the magnetocaloric refrigeration prototype with Gadolinium as a baseline material.
- Test the magnetocaloric refrigeration prototype with both of the currently available first order magnetocaloric materials.
- Test each of the magnetocaloric refrigeration parameters universally involved in all magnetocaloric heat pumps.
- Develop new models of first order magnetocaloric materials.
- Down-select from developed models to a single material model.
- Statistically compare the material model to measured data from first order magnetocaloric materials .
- Implement the material model into a numerical model of magnetocaloric refrigeration performance.
- Develop code to incorporate the material model into the magnetocaloric refrigerator model.
- Validate the magnetocaloric refrigerator model against experimental results from the magnetocaloric prototype.
- Validate the material model against experimental results from the magnetocaloric prototype.
- Carry out a modeling study to analyze the impact of material parameters on magnetocaloric refrigerator performance, and to investigate the interactions between magnetocaloric refrigerator and material parameters.
- Develop code necessary to expand the magnetocaloric refrigerator model's capability in order to facilitate a large modeling study.

- Select a parameter space for the modeling study based on analytical and experimental studies
- Analyze the results from the modeling study

Based on these objectives a detailed literature review on the recent publications in magnetocaloric technology was conducted. The review focuses on magnetocaloric prototype designs, results from magnetocaloric prototypes, the use of magnetocaloric materials, numerical modeling of magnetocaloric performance, and modeling of magnetocaloric materials. Special attention was paid to the use of or modeling of first order magnetocaloric materials in multistage regenerators. This chapter gives a good understanding of the currently successful magnetocaloric prototypes as well as the current efforts in implementing magnetocaloric materials.

The fundamental thermodynamics of magnetocaloric materials and magnetocaloric refrigerators are reviewed as part of this work. The material model that was developed must be thermodynamically accurate in order to create useful results. The thermodynamics of the magnetocaloric effect must be understood to develop a realistic model. Other factors which impact the magnetocaloric effect including measurement and hysteresis are considered. Finally the thermodynamics of a cyclical magnetocaloric refrigerator are also considered. The design of the magnetocaloric prototype and the parameter space of the modeling study are heavily influenced by the thermodynamics of the active magnetic regeneration cycle.

The active magnetic regenerator model which was developed outside of this work, but essential to creating results is briefly reviewed where it is necessary for understanding the current work. The form of this model dictates the range of

magnetocaloric refrigerators that can be represented. The fundamental equations give insight into modeling results and the primary impact of certain parameters. The boundary conditions of the active magnetic regenerator model are used to narrow the parameter space of the modeling study. An understanding of the active magnetic regenerator model is also essential to understanding the incorporation of the material model, and the changes made to enhance modeling speed.

The design of the magnetocaloric prototype was focused entirely on the ability to investigate a wide variety of parameters while maintaining measurability. The key subsystems for this prototype are the magnetic and hydraulic systems. Each was designed to maximize reliability and repeatability of measurements. The design of each is described in detail. Measurement systems are also described for the prototype. Finally accuracy is discussed with particular attention on key loss mechanisms which have been measured.

Several material models were then developed. The starting point for these models was measured data from the literature. Basic model requirements were identified. A system for constructing consistent thermodynamic data was identified from the literature and used to compare the viability of the different material models. The implementation of the material model was described.

The material and active magnetic regenerator models were then validated through a series of experiments and statistical comparisons. Based on these results and the basic model requirements a single material model was selected. Each of the magnetocaloric refrigerator parameters was exercised using the two currently available first order magnetocaloric materials. Error between modeling and experimental results

was analyzed and reported. The influence of magnetocaloric refrigerator parameters on performance and modeling error was reported.

A modeling study was designed to investigate both the material and active magnetic regenerator parameters for magnetic refrigeration. Several preliminary modeling studies were carried out. The results of these studies, the literature review, fundamental thermodynamics, and analytical investigation were used to narrow the parameter space. Several pieces of code were developed to enhance the speed and accuracy of the modeling study. The results of the modeling study were analyzed. The impact of different material parameters on magnetocaloric refrigerator performance was reported. The interaction between materials parameters and magnetocaloric refrigerator parameters was also considered. A summary of the key contributions, and results from experimental and modeling studies is finally presented.

CHAPTER 2 LITERATURE REVIEW

History

The magnetocaloric effect's first description is usually credited to Emil Warburg (Pecharsky et al., 2001; Warburg, 1881) who observed that iron could be heated and cooled by applying a magnetic field. Later William Giauque theorized that the magnetocaloric effect could be used as a substitute for the commonly used methods of producing low temperatures (Giauque, 1927). Giauque would go on to win the Nobel Prize in chemistry by using the effect to achieve the lowest temperature recorded at the time in a 1933 experiment. For most of the next four decades MCR and the MCE remained relegated to scientific investigation, or were used as a means to achieve similarly low temperature to those created by Giauque and other early experimenters.

The first major steps toward room temperature refrigeration were taken by Brown in the mid-seventies. In 1976 Brown made several insights that were necessary to make the jump from the low temperature testing of the past, to room temperature cooling of a cyclic nature (Brown, 1976). Brown points out that very low temperature testing on traditional paramagnetic salts is effective because the lattice entropy changes are of similar magnitude to isothermal entropy change. This is not, however, true for magnetic materials near their curie temperatures. In general this research will be focused on magnetocaloric refrigeration near room temperature, and in particular the magnetocaloric heat pump and magnetocaloric materials. The magnetocaloric heat pumps used for refrigeration are generally referred to here as magnetocaloric heat pumps (MCHP). At these temperatures the change in magnetization is on an order of magnitude appropriate for heat pumps, which had been discussed by earlier works. This

was not applicable in the past due to the lack of materials being magnetocalorically active, and having a Curie temperature near room temperature. Brown goes on to describe the magnetocaloric response of Gadolinium (Gd) and to create entropy temperature diagrams which can be used to construct theoretical thermodynamic cycles. Additionally Brown describes a Stirling cycle using Gd as the working material and a constant magnetization to create a regenerative cooling device. This device was constructed and showed good correlation to prediction producing 47 K of span around 300 K becoming the first real example of room temperature refrigeration using the MCE (Franco et al., 2012).

After the work by Brown several other groups expanded on the concepts of MCR with varying MCHP designs and cycles. Through the works Steyert (1978), Barclay (1983), Chen et al. (1992), and others Ericson, Brayton, Stirling, and other cycles were analyzed thermodynamically and in MCHP form. The result of these efforts was proof that room temperature cyclical operation of a MCR device was possible, and that active regenerators were the preferred embodiment for such a device. The cycle generally used in room temperature magnetocaloric applications is the active magnetic regenerator cycle (AMR). The AMR cycle as proposed by J.A. Barclay consists of four steps: magnetize, flow and reject heat, demagnetize, flow and accept heat (Barclay, 1983).

In general, advancements in magnetic refrigeration come in three different, but highly related areas: Modeling, materials, and MCHP designs. These three areas all saw rapid advancement around the late 1990s that helped accelerate research in MCR. First Pecharsky and Gschneidner (1997a) reported the discovery of a “giant

magnetocaloric effect” in $Gd_5(Si_2Ge_2)$ which displayed three unique features necessary for room temperature MCR: First and most simply the effect was present at the necessary temperatures, Secondly the alloy displayed a first order magnetocaloric response greatly increasing the magnetocaloric temperature change (ΔT) along with heat capacity, and third the alloy had hysteresis low enough to cyclically operate as a heat pump. Pecharsky and Gschneidner (1997b) additionally reported the response of the same material family to alloying which could produce a “tunable” first order MCE at different selected temperature. The adiabatic temperature change due to a changing magnetic field (ΔT) is normally less than 5 Kelvin for each Tesla of field change and in first order materials only spans a few degrees. The tunable nature of the MCE means that multiple alloys which are used as “stages” can be produced. These stages are created to have Curie temperatures which cover the entire operational span of a refrigeration device. In this way multistage regenerators of first order materials are created.

In 1998 the successful operation and description in Zimm et al. (1998) of a prototype performing the AMR cycle at room temperature with permanent magnets showed that this cycle could achieve considerable performance. The authors report coefficient of performance (COP) of more than 50% of Carnot measured on their MCHP when the power consumed by their seals was subtracted. This is widely cited as the beginning of modern MCHP creation with an eye toward commercialization.

The rate of reporting and complexity of new time dependent numerical models describing and predicting the operation of MCHPs also started to pick up in this time period. These models are invaluable as a tool for MCHP design.

The aim of this dissertation is to add insight into all of the major areas of MCR research through a focus on the modeling of materials. By introducing an improved model for the behavior of existing and new first order magnetic transition (FOMT) materials it will be possible to better understand the limits of this technology. MCHP design, modeling, and materials research will all benefit as a result.

Materials are the key to magnetocaloric technologies and the availability of a new model which can help to explore new and existing materials will have several benefits. Parameters that describe current materials can be directly manipulated with a sufficiently complete material model allowing for an understanding of how research efforts into the production of these materials will impact their performance in MCHPs. This can help to focus the current and ongoing effort on existing materials families. In a similar fashion the material model will also open up the possibility of exploring the MCE parameter space for new materials. If the existing materials prove to be limited in their potential performance it should be possible to exceed these limitations in the material model and create a guide as to what a successful material would need to look like.

Magnetocaloric Materials

Magnetocaloric material (MCM) is the key to the future of magnetic refrigeration. In general a magnetocaloric material is one that responds to an increase in magnetic field with a change in temperature which is normally positive, but can also be negative (Tishin and Spichkin, 2003; von Ranke et al., 2009). The introduction of first order MCMs by Ames labs in Pecharsky and Gschneidner (1997a) caused a large amount of interest in MCR. Second order magnetic transition (SOMT) MCMs, and in particular Gadolinium have long been the workhorse of magnetic refrigeration. Second order materials have a magnetocaloric effect that is continuous and largely reversible. They

normally operate over a much wider span of temperatures. These MCEs can be modeled directly via the Mean Field Theory, the Debye model, and the Sommerfeld model (Smith et al., 2014) or experimental data is widely available (Dan'kov et al., 1998; Tishin et al., 1999). Because second order materials can be directly described and are less likely to be competitive than first order materials, which is detailed later in the literature review, first order materials will be the focus of this work. Second order materials will be used for base line testing.

Though there is no clear definition for when a material can be considered first order or second order, in general a more first order material will show a more discontinuous MCE. A truly first order material is well described in (Nielsen et al., 2010a) for a theoretical case. There are several materials considered to have a FOMT which have been produced and measured. The two families that currently receive the bulk of the attention are the MnFe family (Tegus et al., 2002; Wada and Tanabe, 2001) and the LaFe family (Barcza et al., 2011; Fujita et al., 2003; Hu et al., 2002). The GdSiGe family has also seen successful testing around room temperature but is under less development. The NiMn or Heusler alloy family of MCM is a topic of ongoing research (Hu et al., 2000; Ingale et al., 2007; von Ranke et al., 2009). This family shows potential for a large MCE, but currently no Heusler alloy has been reported to have been tested cyclically in a prototype.

Modeling of Magnetic Refrigeration

Numerical models are an important tool when a large number of parameters with highly nonlinear relations need to be investigated. AMR models can be broken down into many subcategories, but one of the most basic is the number of dimensions that are taken into account in the model.

Models that do not consider time as a dimension are categorized as steady state. In general steady state models will only be accurate for a certain subset of AMR cycles which does not normally include FOMT material. An example that compared both a steady state and time dependent model used to optimize the same result and compared against an actual prototype can be found in Zhang et al. (2000). Sarlah and Poredos (2010) used a dimensionless model to find heat transfer coefficients and to simulate passive regenerators. This model proved successful for the passive regenerators and later helped to improve higher level numerical models of active regenerators.

Time dependent models make up the bulk of the effort in numerical modeling of AMRs at room temperature. Matsumoto and Hashimoto (1990) presented a numerical model which used gas as the heat transfer fluid for low temperature refrigeration. This model and others like it tend to ignore the thermal mass of the entrained gasses. Gas based heat transfer is prevalent in low temperature applications and especially in cryogenic applications. Because MCR had been used more extensively for cryogenic applications before it's more recent extension to room temperature applications many early models utilized gas as the heat transfer fluid. An accompanying assumption is that pressure drop is negligible for these systems. Degregoria et al (1990) utilized a set of nonlinear partial differential equations (PDE) which couple the material and heat transfer fluid through heat transfer relations. This method forms the basis for a large subset of numerical models. Additionally this model included the effects of axial thermal conduction, thermal dispersion, pressure drop, and viscous generation. These losses were all added at the end of each cycle to the energy balance (Johnson and Zimm, 1996) which represents a simplifying assumption. Many of the more recent models

utilize the same method of solving the coupled PDE, but make improvements in assumptions, losses, and computation schemes. These improvements are reviewed later.

One dimensional models inherently make assumptions that limit their ability to accurately predict the performance of real MCHPs in exchange for modeling speed. Several models have been developed utilizing two dimensions in order to produce more accurate results. Petersen et al. (2008) produced a two dimensional model that is capable of simulating an AMR utilizing parallel plate regenerators. In this model the two dimensional flow equations were solved to directly calculate the pressure drop and heat transfer. Their results showed that a temperature gradient exists in the direction normal to flow. This indicates that the two dimensional model will produce more realistic results. Another effect that can be captured more accurately in a two dimensional model is heat transfer via conduction in the solid mass in the normal direction to flow. Li et al. (2006) developed a one dimensional model and later followed with a two dimensional model in Li et al. (2011) which took into account the variation of temperature in the normal direction to flow due to a heat transfer boundary condition on the surface of the regenerator. When the two models were compared the two dimensional model predicted significant deterioration to MCHP performance in some instances. Liu and Yu (2011) also implemented a two dimensional model considering a heat transfer boundary condition at the regenerator surface along with variable fluid properties. Their results further confirm the influence of two dimensional effects on performance.

Full solving of fluid equations is possible in two dimensions only for two dimensional structures such as plates. Many AMRs utilize three dimensional structures

such as irregular packed beds and spherical packed beds. Since these are a large percentage of experimental MCHPs there have been attempts at three dimensional models that can more accurately predict their performance. Bouchard et al (2009) presented a numerical model which solves the three dimensional Navier Stokes equations for a packed bed. They used the interesting approach of combining spheres with ellipsoids in order to gain the ability to vary packing fraction.

Beyond the dimensions that are taken into account in the numerical model most work has been on refining the additional factors that impact performance to create closer agreement to experimental MCHPs. Generally these refinements fall into a few categories: Heat transfer fluid interaction with MCM, additional forms of heat gain or loss, and magnetic field interaction with MCM.

Though multi-dimensional models utilize additional spatial dimensions to offset the need for heat transfer and fluid flow correlations these higher order models multiply the computational power needed. In addition they make the assumption that the fluid flow can be approximated by a perfect geometry while completely neglecting the irregular portions of a regenerator such as the entrances and walls. For these reasons most models continue to operate in a single spatial dimension while refining the interaction at the fluid solid interface through improved correlations. Adjusting the convective heat transfer correlations is an effective way to increase the accuracy of a one dimensional model. By example this method is displayed in Nielsen et al (2013) for flow maldistribution in parallel plates to increase the accuracy of a one dimensional model by taking three dimensional effects into account. They found that utilizing a single

spatial dimension accurately predicted MCHP performance when additional factors were added to take into account uneven flow of heat transfer fluids.

Initially many models considered only the heat exchange between fluid and solid and at the boundary conditions that represent the ends of regenerator. However in a real MCHP the energy equation would include heat transfer from all directions. In the axial direction, though transport is nearly always taken into account, diffusion is sometimes ignored. With the establishment of a temperature gradient heat will be conducted through both the solid and fluid from the hot to the cold side. It has been shown in Aprea et al. (2012) that considering the cases of no axial conduction, fluid only axial conduction, solid only axial conduction, and axial conduction through both the solid and fluid can lead to considerable differences in predicted performance. In the same manner heat can be conducted across the normal direction to the fluid flow. Adding a heat flux at the regenerator boundary requires a two dimensional model as in Li et al. (2011) and Liu and Yu (2011), but using an approximation many one dimensional models now create so called “1.5D” models by adding an additional term to the energy equation to account for heat leak through the regenerator wall.

The magnetic field of a MCHP is not likely to be perfectly homogeneous in the space or time dimensions. Additionally internal magnetic effects within the regenerator can influence the resultant field that the MCM responds to. Bjørk (2010) is an in-depth look at magnetic design for AMRs. Bjørk also reported a three dimensional understanding of the non-uniformity of magnetic fields. Demagnetization is an effect caused by the geometry and shape of the magnetic material in a regenerator which can lower the functional field applied to the material in a regenerator (Christensen et al.,

2011; Peksoy and Rowe, 2005; Romero-Muñiz et al., 2014). It has been shown in certain geometries demagnetization can have a large effect on both the measured and simulated results of magnetic refrigeration (K. Engelbrecht et al., 2013). These effects can be implemented in a number of ways, but in one dimensional models an averaging scheme must be utilized in the non-exercised dimensions. Such an averaging scheme based off of detailed magnetic analysis can have significant impacts and has been shown to correspond well with real performance (Christensen et al., 2011).

One important aspect of any model is what material will be considered and how the MCE will be implemented. This consideration will be a main focus of the current work. In general MCMs are considered to have constant properties for density and thermal conductivity. The specific heat, adiabatic temperature change, and entropy change are all functions of both temperature and field. Additionally for data to yield meaningful results the MCE must be implemented in a thermodynamically consistent way. Different models rely on different implementations of the MCE which can have large impacts on results.

As mentioned in the introduction this work will focus on materials with a first order magnetic phase transition. However, as part of the work it is necessary to characterize an experimental MCHP as well as a numerical model. For characterization purposes Gadolinium, a material with a SOMT will be used since the MCE is well known and relatively easy to model. In general most models use some combination of Mean Field Theory as exemplified in Morrish (2001) and experimental data to model the MCE of Gd. A good description and rigorous definition of FOMT and SOMT can be found in Smith et al. (2012).

A list of models is created in Nielsen et al. (2011) which contains information on the type of model and many of the parameters investigated. This model list was used as the starting point in an investigation into magnetocaloric models. Information about the MCM used in models including the materials that were modeled, the implementation of the MCE in the model, and the method of modeling multistage regenerators has been collected. It should be noted that many of the models in Nielsen et al. (2011) were presented as conference papers and as such some were left out of this review. In all 31 unique models were found. It is noted that there are many more publications detailing modeling results, but most of these are based off of previous models. Within the list there are a few instances of alterations to previous models which were counted as new because they either modified the original model to include new materials, or used a different material implementation technique. It is the purpose of this work to introduce a new method for analyzing the promising FOMT materials. For any real application with a span greater than a few Kelvin a regenerator of FOMT MCMs must be made from multiple stages with different operating temperatures. For these reasons staging of material and implementation of FOMT MCMs in previous models are given particular consideration. Table 2-1 includes the basic information about the models researched including the implementation of the MCM. The columns include the reference where the model was first found (Reference), the date of the model description (Date), the materials modeled (Material), whether first order materials were modeled (FOMT Material), whether the model had been validated against physical performance (Validated), the method of fitting data if first order materials were used (Fit Method), the type of measured data used if first order materials were used (Data Used), whether or

not multi-stage regenerators were modeled (Multi-Stage), and the method of creating stages (Staging Method). Abbreviations include interpolated data (interp), continuous data (cont), individual different Curie Temperatures (T_{CS}), Specific heat (C_P), Specific heat in zero field (C_{P0}), Specific heat in an applied field (C_{PH}), and isothermal change in entropy due to magnetic field change ΔS .

Of the 31 models found in literature only six dealt at all with FOMT MCMs. The remaining 25 dealt exclusively with SOMT MCMs. Interestingly only nine of the 25 models that focused on SOMT materials looked at SOMT materials other than elemental Gd and of these nine only two: Aprea et al. (2013) and Aprea et al. (2015) looked at a non Gd based material.

Five of the models reviewed included staged regenerators, though only four were of FOMT materials. In actual staged regenerators there are discrete stages of materials with different MCE properties. Since the gradient of temperature in a magnetocaloric regenerator must be continuous and the staging of MCM is discontinuous there must be sections of the regenerator that are not operating at their actual T_c (Smith et al., 2012). Staged regenerators are not, however, always modeled as discrete locations having different MCEs. Neglecting the actual staging of materials will lead to errors for the reasons described, but can improve speed or convergence. There are some examples of modeling that utilize this trade off.

Rowe (2012) used an “idealized MCE” in his model. The magnetocaloric adiabatic temperature change as a function of temperature is assumed to be linear in the idealized MCE. It is also assumed that the specific heat for the idealized material is constant. Rowe notes that this would in fact be thermodynamically impossible, but this

simplifying assumption allows for analytical solutions of his model. The findings from this idealized material show that there are only three factors that impact performance; two of these three factors are the ΔT , and ΔS . Though the idealized material cannot truly be considered first or second order, based on the findings the performance of an idealized material with MCE similar to first order materials should have better performance. These results also point to the importance of exploring the MCE as an input parameter.

Hsieh et al. (2014) compared a pure Gd regenerator to a Gd-Tb regenerator with two and three stages. In both cases the MCE is obtained using the Mean field and the de Gennes model. Staging of the Gd-Tb regenerator was achieved by adjusting the level of Tb which in turn changes the T_C of the material to create discrete stages. All of the materials studied in this case are SOMT materials. The results showed that a two stage regenerator can provide a cooling capacity three times greater than a single stage. They also concluded that a three stage regenerator can outperform the two stage regenerator in span as well as capacity.

Another simplifying assumption is a continuously graded regenerator. In this assumption the material has a MCE that varies continuously from the hot sink temperature to the cold sink temperature. This would represent the ideal physical case, but similar to the simplifying case of a constant MCE is impossible to realize. Brey et al. (2014) compared a continuously graded regenerator to a discretely staged regenerator. To create both they simply shift the temperature of raw data for MCE to create new stages. This paper also compared FOMT material to SOMT. They find that the number of stages positively impacts the performance of both and FOMT and SOMT material,

though FOMT material is more heavily affected by the number of stages. Performance of FOMT materials was also modeled with a scalable hysteresis. It was found that non-hysteretic FOMT material consistently outperforms SOMT material, but that at higher levels of hysteresis the performance of the FOMT material can be surpassed by SOMT material in some cases.

Engelbrecht's 2004 Master's thesis and subsequent PhD thesis (Engelbrecht, 2008, 2004) are the basis for a good portion of the models found. In Engelbrecht (2004) multiple stage beds of Gd-Er were modeled. The stages had a continuously varied T_C along the length of the bed, and the different T_C s were created by shifting the temperature of a single set of experimentally measured MCE. The results showed that multi-stage beds have significantly improved performance over single stage beds even for a SOMT material. Another part of the study examined a layered bed of FOMT material and found improved performance over the layered bed of SOMT materials. It should be noted that other factors were changed in addition to the material including regenerator geometry and MCM structure (from packed spheres to plates).

Another example of improved performance through multiple stages was reported in Aprea et al. (2013). Here SOMT materials were layered by using mean field theory along with the de Gennes model. The T_C was changed for the stages as different binary compounds of Gd with Tb, Er, and Dy were considered. The results showed that performance is heavily influenced by the number of stages. COP was predicted to more than double by going from a single stage of pure Gd to an eight stage bed.

The implementation of FOMT material is handled in different ways by different models. To create first order material in Engelbrecht (2004) the MCE of the second

order material Gd-Er was scaled to resemble data for LaFeSiH. This method was used because of the lack of available data at the time. A curve fitting procedure was considered, but showed poor agreement to the data. It was noted that this would be a preferable option if the proper method could be found. A cubic spline method was used with a table of raw data instead. As previously mentioned the model results showed that the first order material outperformed the second order material.

Two FOMT materials, $\text{Gd}_5\text{Si}_2\text{Ge}_2$ and $\text{MnAs}_{1-x}\text{Sb}_x$, and two different implementations were presented in Aprea et al. (2013) which is an extension of the model introduced in Aprea and Maiorino (2010). Experimental data for the MCE of $\text{Gd}_5\text{Si}_2\text{Ge}_2$ was fit using a Gaussian curve. In order to create stages the curve fit parameter which controls location, which for these curves is the location of maximum MCE, was changed. This technique was used to provide a smoother set of data than was available from experimental measurements. It was noted by the authors that smoothed data proves advantageous for modeling efforts. $\text{MnAs}_{1-x}\text{Sb}_x$ was modeled by the Bean Rodbell model as described by Balli et al. (2007). This method is based off of the mean field theory and phenomenological observations of experimental data. Though this model is based off first principles of the MCM it provided a noticeably poorer fit to the experimental data. The resulting specific heat was oscillatory which is not representative of real materials. In some cases the specific heat can violate thermodynamics when modeled with Bean Rodbell in this way. An example of this is a specific heat with a negative value shown in the paper. Both of the FOMT materials were shown in this paper to outperform Gd. GdSiGe showed universally better

performance than both MnAsSb and all of the SOMT materials also modeled. MnAsSb was shown to be surpassed in efficiency by a multilayer bed of Gd-Tb.

The method of obtaining MCE data was discussed in K Engelbrecht et al. (2013). Specific heat was measured directly at both low field and high field when the material is heated from cold to hot and hot to cold. This data was used to reconstruct the ΔT and compared to directly measured cyclical ΔT data. It was found that the on heating specific heat at zero field and on cooling specific heat in field best matched the measured ΔT . It was proposed that his method of data collection accounts for hysteresis in the model. The material was then modeled using the directly measured data and a look up interpolation scheme.

Another method of evaluating hysteresis in FOMT materials was presented in Brey et al. (2014). A hysteretic heating term was applied to the energy equation of the material. The first order material data was taken from experimentally measured magnetization data. The method of implementing data was a look up table with interpolation. This modeling effort found that the first order materials outperform second order materials, but that large amounts of hysteresis can in some cases cause the second order materials perform better.

Four first order materials (GdSiGe, LaFeMnSiH, MnFePAs, LaFeCoSi) and two second order materials (PrSrMnO, Gd) were modeled in Aprea et al. (2015). All of the materials are curve fit to provide a mathematic function for the MCE. The curve fitting was completed using a commercial curve fitting program which results in complex mathematic functions with no common form. The resulting fits seem to be unstable outside of the small range of measured data, meaning that simulation of a multistage

regenerator would be impossible for a non-steady state condition. This type of instability is common when data is over fit and the resulting model is extrapolated outside of the original data range. The results of simulation showed that first order materials and in particular GdSiGe have the best performance.

Magnetocaloric Prototypes

For the purposes of this proposed work a functional AMR prototype has been designed and constructed in order to confirm the results of modeling. The literature has been surveyed to gain an understanding of existing AMRs. The review has been focused on MCHPs that have been used to confirm models, or have the capability to control a large number of variables as this is the goal of the current work.

A broad understanding of MCR prototypes that have been reported can be gained from the review of Yu et al. (2010) which detailed AMR prototypes before 2010. Many of these prototypes were physically described and a table was developed which summarizes the MCHPs. The variables recorded in the table include: Date of announcement, type of cycle, type of MCHP, maximum frequency, maximum cooling capacity, maximum temperature span, maximum field strength, regenerator material, regenerator construction, and heat transfer fluid. There are 41 MCHPs in the list. A few things of interest immediately stand out: The MCHPs in this list almost exclusively utilized Gd with only five MCHPs having reported non Gd based materials. Nearly half of the MCHPs only reported span or cooling capacity, but not both. In order to fully assess the performance of a MCHP a minimum of both the cooling capacity at zero-span and span at zero cooling capacity are needed. It is preferable to have additional results at intermediate spans and cooling capacities as any real MCHP must simultaneously deliver cooling capacity while producing some useful temperature span.

In addition to performance general MCHP configuration was noted. MCHPs can be classified by many characteristics and a useful system has been proposed to fully define any MCHP Scarpa et al. (2012). For the purposes of reference it is sufficient to classify MCHPs by magnetic design and the implementation of magnetic field. MCHPs fall broadly into two magnetic categories: permanent magnets and electromagnets. There are also three types of magnetic implementations: Rotating field with respect to MCM, Linear field movement with respect to MCM, and switching field where the MCM is stationary and the field is turned off and on. From Yu et al. (2010) it can be seen that much early work utilized electromagnets. Around 2005 permanent magnets became the predominant means of creating fields with only one electromagnetic prototype present in the list after 2005. The implementation is mixed evenly between rotational and reciprocating MCHPs with only a few examples of switching fields.

In addition to the MCHPs reported by Yu et al. (2010) the literature was reviewed from 2010 to the present to include more recent prototypes. A broad range of operating conditions as well as regenerator implementations is necessary to verify numerical models. Any MCHPs used for modeling purposes, reporting a variety of operational parameters, implementing multistage or first order materials, or having exceptional results have been examined here in more depth.

Since model validation is important to this work the previously detailed numerical modeling review is used as the starting point to investigate literature where modeling and experimental results are compared. Of the models listed seven were validated against experimental AMRs either in the original paper or in subsequent papers

referencing the original paper. The following summaries detail the model and MCHP used for verification along with the type of parameters exercised and results compared.

Dikeos et al. (2006) utilized experimental results from the MCHP detailed in Rowe and Barclay (2002) which will be detailed later. The test device was used to validate the numerical predictions of a Gd sphere bed. These validated results were then used to make predictions against a low temperature material DyAl₂ which is proposed for cryogenic operation. The model was validated for predictions of no load span as a function rejection temperature.

Allab et al. (2005) was validated against the MCHP detailed in Clot et al. (2003). The MCHP used Gd MCM in the form of sheets. The numerical model was used to predict a no load transient span which was validated by experimental results with a difference between model and experiment of about 20% for a 4 K span. Experimental results were also compared to the numerical model for no load span as a function of flow rate, but these results showed up to 100% deviation.

Kawanami et al. (2006) describes both an experimental MCHP and a numerical model. Though there were many numerical results reported none are validated by the operation of the MCHP.

Petersen et al. (2008) and Nielsen et al. (2009) both validated their models using the MCHP detailed in Bahl et al. (2008) which is described in more detail later. The validation included experiments for no load span as a function of fluid displacement, no load span as a function of cycle timing, and no load span a function of low field. The numerical model from Nielsen et al. (2009) showed generally better correlation,

however the predictions from this model were often as high as 50 to 100 percent over the experimental results.

Kim and Jeong (2011) detailed both a numerical model and an experimental AMR based on a Halbach array permanent magnet. The experimental MCHP had a unique system of temperature measurement that used a set of thermocouples (TCs) embedded inside the regenerator along its length. Using these TCs the model was validated in predictions of no load temperature span along the length of the regenerator. The model showed good agreement to the experiment. The temperature spans were also modeled and measured as a function of the cycle to show the temperature distribution at all four stages of the AMR cycle.

The model created by Engelbrecht as part of his Master's thesis (Engelbrecht, 2004) and later expanded in his PhD (Engelbrecht, 2008) was validated in both the MCHPs described in Jacobs et al. (2014) and Bahl et al. (2014). In Jacobs et al. (2014) an MCR was described which was built by Astronautics Corporation of America based on an earlier design from the same company (Zimm et al., 2006) both of which are detailed later. The numerical model was used to predict the performance of a six layer AMR regenerator utilizing the FOMT material LaFeSiH. The model showed very good correlation with cooling capacity as a function of span for different flow rates. The model was also used to predict heat rejected as a function of span for different flow rates with good agreement. Utilizing these two results it is possible to calculate the thermodynamic COP for the operating conditions. The implementation method of the MCE was not described, but the heat capacity of the material at zero field is shown. It is known from

the previous investigation into Engelbrecht's models that they are able to use tables of data and typically utilize experimental data fitted with an interpolation scheme.

Comparisons of modeling results from Engelbrecht (2008) to a rotary MCHP at Danish Technical University (DTU) (Bahl et al., 2014), which will be described later, were reported in Lozano et al. (2014) and Lozano et al. (2013). Both used Gd spheres as the MCM and a number of different parameters were investigated including: Temperature span under a cooling load as a function of frequency, no span cooling capacity as a function of frequency, temperature span as a function of rejection temperature at different cooling loads, temperature span at different loads as a function of flow rate, COP as a function of load and hot reservoir temperature, and COP as a function of load and volumetric flow rate.

Chiba et al. (2014) validated their numerical model against an experimental MCHP described in Balli et al. (2012). The only comparison to numerical results is temperature span under zero load as a function of time. The model agreed well with the eventual full span, but the time evolution was not as well correlated.

The design of a MCHP dictates its operation. MCHPs that can vary a large number of parameters are essential for validating numerical models. Additionally MCHPs that can deliver large cooling loads make better subjects for validation since the error associated with MCHP specific losses is smaller relative to the loads being measured. The following are MCHPs from the literature that have been used to verify models and show particular usefulness for this task.

In addition to contributing many of the more well-known and widely used models the DTU also has two very good AMR prototypes. The first, detailed in Bahl et al.

(2008), is of a reciprocating type capable of using either a permanent magnet with 1.05 Tesla field or an electromagnet with 1.4 Tesla field. The MCHP operates at a fairly low frequency of around 0.1 Hz utilizing the standard AMR cycle. The MCHP has been detailed in multiple papers and can vary fluid flow parameters (displacement and velocity) as well as frequency, field strength, and cycle timing (Engelbrecht et al., 2011a; Nielsen et al., 2010b; Petersen et al., 2008a; Pryds et al., 2011). The regenerator section is cylindrical with a fixed size and is made to receive plates. Gd was used in all of the tests with typical plate thicknesses of around 0.9mm. In Engelbrecht et al. (2011a) Gd plates were compared to three stages of $\text{La}(\text{Fe},\text{Co},\text{Si})_{13}$, and a single stage of $\text{La}_{0.67}\text{Ca}_{0.26}\text{Sr}_{0.07}\text{Mn}_{1.05}\text{O}_3$ (LCSM). These experiments were carried out with the previous parameters and an additional parameter of rejection temperature. Controlling rejection temperature is of particular importance for multistage and first order materials that do not have broad ranges of operating temperatures. The results of experiments where no load span is measured as a function of rejection temperature showed a clear spike near the optimum operation point for these materials. The results of Engelbrecht et al. (2011a) also included span as a function of cooling capacity and frequency by making use of a variable cooling load applied by a heater in the cold side of the AMR. An additional degree of flexibility in this MCHP was displayed in Pryds et al. (2011) where a monolithic microchannel regenerator is created from LCSM materials. Though the results did not explore the AMR cycle due to the difficulties in retaining the MCE through the processing of this shape, the MCHP was used to compare the passive regenerator effectiveness of this structure to plates with good correlation.

The second MCHP at DTU is of a rotary configuration with permanent magnets. The design was first introduced in Bahl et al. (2011) with the first results for 2.8 kg of Gd spheres in Engelbrecht et al. (2012). This design has the ability to operate nearly two orders of magnitude faster than the reciprocating DTU design reaching a maximum around 10 Hz. Unlike the reciprocating design the fluid circuit is physically coupled to operation of the magnets. This means that the flow timing cannot be altered though the volumetric flow rate can be controlled by a separate pump. The cold side is connected to heating elements which can vary the refrigeration load. These two control parameters were exercised in Engelbrecht et al. (2012) to produce cooling capacity curves as a function of flow rate and span. Cooling capacity was also experimentally determined as a function of frequency and span. An overall cooling capacity of 400 Watts at 9 K span was reported along with a COP of 1.8. The ability to control rejection temperature as a parameter was introduced in Lozano et al. (2013) where its effect on temperature span at different cooling loads was investigated. Two different sources of Gd spheres were compared in Bahl et al. (2014) and a no span cooling capacity of 1.01 kW was reported.

Astronautics Corporation of America was one of the first commercial companies researching room temperature magnetic refrigeration. They recently reported on a prototype Jacobs et al. (2014) with a maximum no span load of 3 kW which is the largest capacity to date. This MCHP was based off of the earlier designs presented in Zimm et al. (2006). The MCHP utilizes permanent magnets in a rotary design with twelve regenerators arranged circumferentially. Although this is meant to be an industrial design there is still parameter control including rejection temperature, load,

frequency, and flow rate. As noted in the validation section this MCHP is also unique in its reporting of multistage first order materials.

Like DTU the University of Victoria (UVic) has multiple MCHPs that are well suited for the validation of model parameters. Their first MCHP is a reciprocating type utilizing an electromagnet producing a field of two Tesla (Rowe and Barclay, 2002). Although the movement system and flow system are mechanically coupled the MCHP allows for the changing of components (i.e. drive shafts) to adjust the operating frequency and flow rate. The cold section includes heaters to adjust the cooling loads. The results of Rowe and Barclay (2002) included no load spans at different frequencies and MCM masses. The maximum span that was achieved in these experiments is 20 K. Modifications were made to the MCHP to allow for cooling at cryogenic temperatures in Tura et al. (2006). A low temperature gas circulation system controls the ambient temperature of the MCHP which can be maintained below 100 K thereby controlling the rejection temperature. Multiple stages are implemented at room temperature utilizing Gd, Gd_{0.74}Tb_{0.26}, and Gd_{0.85}Er_{0.15} as the MCM. The no load temperature span as a function of rejection temperature was reported and the multi-layer beds showed the best performance with a maximum span of 45 K. The ability to measure work input was added in Arnold et al. (2011) and was used to measure system COP at different operating frequencies, cooling loads, and magnetic field strengths.

The linear MCHP at Uvic has the ability to control many parameters and produce a large field with electromagnets, but is large and parameter control is difficult. For this and other reasons Uvic built a second prototype which they name PM I (permanent magnet one). The stated goals of this prototype included: Compact design, high

frequency operation, ease of access, ease of instrumentation, and modularity (Tura and Rowe, 2011). These design goals are in line with a system capable of confirming models and exploring parameter space. PM I uses a switching field configuration with two stationary regenerators. The field is switched on and off by relative rotation between two concentric Halbach array magnets. The fluid system is mechanically coupled to the magnet rotation, but switching of physical components (i.e. pistons of different diameters) allows for variation of the flow parameters. The first tests were carried out with Gd spheres as the MCM. These tests reported the variation of heat rejection temperature, operating frequency, volumetric flow and velocity, and cooling capacity. The work input is also measured and COP was reported as a function of frequency, cooling capacity, and volumetric flow. The maximum span achieved in this set of tests was 29 K and the maximum cooling capacity reported was 50 W at 10 K span. The regenerator was modified in order to receive plates for the purposes of confirming a two dimensional model in Tura et al. (2012a). The parameters and results reported were the same as for the previous Gd sphere bed. The comparison to the numerical model showed good agreement and the maximum no load span for this case was 12 K. A larger MCHP of generally the same form was described in Arnold et al. (2014) and dubbed PM II. The goal of PM II was stated in Arnold et al. (2014) to increase the volume of the magnetized test section as well as create a more uniform magnetic field wave form. It was noted that PM I using two Halbach arrays created a nearly sinusoidal magnetic field strength between high and low field as a function of cycle. It is desirable to have a squarer waveform where the only two states are high field and zero field. For this purpose three concentric Halbach arrays were used in PM II with two of the arrays

counter rotating while the third remains stationary. The size of the magnetic arrays was also increased to allow for a larger regenerator resulting in a factor 2.5 increase in regenerator volume at the same high field of 1.5 Tesla. The frequency range remained the same between the two devices with the maximum at 4 Hz. The regenerator reported in Arnold et al. (2014) was composed of Gd spheres, and the parameters varied were the same as PM I. The results showed an increase of maximum span to 33 K and a span at 50 W of 15 K.

A MCHP with an adjustable field was presented in Balli et al. (2012). This MCHP uses two permanent magnetic arrays to create a rectangular test section. The height of the field gap is adjustable resulting in a field which can be varied between 1.55 and 1 Tesla for a gap between 22 and 10 mm. The MCHP uses a linear actuator to move regenerators in and out of the magnetic test sections. The regenerators used in Balli et al. (2012) were made from Gd plates and the no load temperature span was reported. The temperature span was made to reverse directions in the middle of a test by reversing the fluid cycle which demonstrated the ability to independently control the fluid operation and to implement this control during cycling. $\text{La}(\text{Fe}, \text{Co})_{13-x}\text{Si}_x$ was used as the MCM in Balli et al. (2012b) and was formed into plates. The plates were made in two stages and fitted into the same regenerator test section. The results showed no load span increases from 14 K for a Gd bed to 16 K for the staged $\text{La}(\text{Fe}, \text{Co})_{13-x}\text{Si}_x$ bed.

A test MCHP with a highly configurable regenerator was reported in Tušek et al. (2013). The architecture is a linear reciprocating MCHP with permanent magnets producing 1.15 Tesla in the test section. Six regenerator structures were tested: Spherical particles, irregular particles, cylindrical particles, plates perpendicular to the

magnet field, and two sets of plates parallel to the magnetic field with different spacing between plates. All regenerators were made from Gd material and fit in the same housing. Testing was carried out varying the volumetric flow rate and operation frequency to find the resultant no load temperature span. The maximum overall frequency tested on this MCHP was 0.33 Hz. A heater was used to apply a load to the cold side of the MCHP and produce cooling capacity span curves at 0.3 Hz. The regenerator with parallel plates and the smallest spacing produced the largest no load temperature span of 20 K. The highest cooling capacity reported was 5 W at 2 K span. In another set of tests focusing on regenerator MCMs five different regenerators were tested in J. Tušek et al. (2014). All of these regenerators consisted of plates oriented parallel to the magnetic field. Four of the regenerators were made of $\text{LaFe}_{13-x-y}\text{Co}_x\text{Si}_y$ material in one, two four and seven layers. The last regenerator was Gd material for reference. Volumetric flow and frequency were again varied to find the no load temperature span. Additionally the cooling load was found as a function of temperature span for each of the regenerators.

Numerical models must be validated against prototypes to understand their abilities and limitations. Many prototypes have been built and provide very good data for validation. In reviewing the existing prototypes it is clear that certain capabilities are necessary for building an effective validation prototype. Most all of the reviewed MCHPs have a minimum of the following: Temperature sensing at the hot and cold side, the ability to apply a measured cooling load, magnetic fields in excess of 1 Tesla, the ability to vary the flow rate in a cycle.

Additional parameter control exists in some of the prototypes and would be necessary for model validation: A wide range of possible operation frequencies, different high magnetic fields, independent fluid and magnetic cycle operation, control of the rejection temperature, flexible regenerator structure for changing of MCM and form factor, pressure drop and flow rate measurement for fluid power, mechanical power input to the magnetic system.

Beyond the parameters and measurement variables that are found to be present in the literature there are some additional MCHP variables which if controlled could help expand the understanding of AMR operation in important ways: Low magnetic field strength, magnetic field as a function of cycle, outgoing and return fluid temperatures at both heat exchangers.

A MCHP that could control and measure all of the parameters listed above would be unique and useful for the investigation of both numerical models and the operation of AMRs in general.

Gaps in the Current Body of Knowledge

It has been shown multiple times in the literature that multi-layered beds have major advantages to single layer beds when it comes to cooling capacity, COP, and temperature span both in experimentation and modeling (Engelbrecht, 2004; Rowe and Tura, 2006; Tušek et al., 2014; Zimm et al., 2006). Every reviewed model that compares staged regenerators to single materials confirms this fact. It is also known that FOMT materials can have a larger magnetocaloric temperature and entropy change than SOMT which has been shown to create superior operation (Aprea et al., 2013, 2012, Pecharsky and Gschneidner, 2005, 1997a). The highest cooling capacity yet reported for an AMR tellingly comes from a MCHP utilizing FOMT (Jacobs et al., 2014). Every

modeling and experimental comparison directly between FOMT MCMs and SOMT MCMs has found some advantage to the FOMT MCMs. Yet the majority of work in the field of MCR is still focused on single layer beds of SOMT. In addition very little work has gone into understanding the MCE of materials. The most common practice when implementing MCM is to use look up tables of experimental data and interpolate. There have been a few attempts at using mathematic functions to represent first order MCM, but for the most part they are unrealistic, or oversimplified. Using a mathematic model can create the opportunity for the exploration of MCM as a parameter of MCHP design. The use of a model also has numerous other benefits including increased accuracy due to consistent data, and lowered computation time (Aprea et al., 2013; Engelbrecht, 2008, 2004).

Beyond the material model there is also a need for validation of FOMT material performance utilizing a prototype has a large number of controllable and measurable parameters. Exploring a large parameter field in a single prototype helps to eliminate noise in the resulting understanding of magnetic refrigeration. In addition multistage test data is also lacking in the literature. Validation of this sort is a necessary step to ensuring that predictions closely match reality.

Table 2-1. List of models reviewed from the literature created.

	Reference	Date	Material	FOMT Material	Validated	Fit Method	Data Used	Multi-Stage	Staging Method
1	(Degregoria et al., 1990)	1990	GdGa-O	no					
2	(Smaïli and Chahine, 1998)	1998	Gd-Dy	no	no			no	
3	(Shir et al., 2004)	2004	Gd	no	no			no	
4	(Engelbrecht, 2004)	2004	Gd, Gd-Er, LaFeSi H	yes	yes	interp	$C_p, \Delta T$	yes	T_{CS}
5	(Siddikov et al., 2005)	2005	Gd	no	no			no	
6	(Allab et al., 2005)	2005	Gd	no	yes			no	
7	(Dikeos et al., 2006)	2006	Gd	no	yes			no	
8	(Li et al., 2006)	2006	Gd	no	no			no	
9	(Kawanami et al., 2006)	2006	Gd	no	yes			no	
10	(Petersen et al., 2008b)	2007	Gd	no	no			no	
11	(Nielsen et al., 2009)	2009	Gd	no	yes			no	
12	(Bouchard et al., 2009)	2009	Gd	no	yes			no	
13	(Sarlah and Poredos, 2010)	2010	Gd	no	no			no	
14	(Aprea et al., 2011)	2010	Gd, Gd-Dy	no	no			no	
15	(Tagliafico et al., 2010)	2010	Gd	no	no			no	
16	(Risser et al., 2010)	2010	Gd	no	yes			no	
17	(Engelbrecht and Bahl, 2010)	2010	Gd, LaFeCo Si	no	Yes	Lorentzian	$\Delta S, \Delta T$	no	
18	(Liu and Yu, 2011)	2011	Gd	no	yes			no	

Table 2-1. Continued

	Reference	Date	Material	FOMT Material	Validated	Fit Method	Data Used	Multi-Stage	Staging Method
19	(Roudaut et al., 2011)	2011	Gd	no	no			no	
20	(Tusek et al., 2011)	2011	Gd	no	yes			no	
21	(Kim and Jeong, 2011)	2011	Gd	no	yes			no	
22	(Risser et al., 2012)	2012	Gd	no	yes			no	
23	(Rowe, 2012)	2012	Idealized FOMT	yes	yes	Cont	NA	yes	Cont
24	(Vuarnoz and Kawanami, 2012)	2012	Gd	no	no			no	
25	(Aprea et al., 2013)	2013	Gd, Gd-R, GdSiGe, MnAsSb	yes	no	Gaussian (GdSiGe)	C _{P0} , C _{PH}	yes	T _{Cs}
26	(Kitanovski et al., 2014)	2013	Gd	no	no			no	
27	(K. Engelbrecht et al., 2013)	2013	MnFeAs	yes	yes	Interp	C _{P0} , ΔT	no	
28	(Hsieh et al., 2014)	2014	Gd, Gd-Tb	no	no			yes	T _{Cs}
29	(Brey et al., 2014)	2014	Gd-Er, LaFeSiH	yes	no	Data	ΔS, C _P	yes	T _{Cs} , Cont
30	(Lionte et al., 2015)	2015	Gd	no	yes			no	
31	(Aprea et al., 2015)	2015	LaFeMnSi, Gd, LaFeCo, MnAs, GdSiGe	yes	yes	multiple	C _P , ΔT	no	

CHAPTER 3 FUNDAMENTALS OF MAGNETIC REFRIGERATION

A background in the thermodynamics of both the magnetocaloric effect and of the cyclical operation of a magnetocaloric heat pump is given here. An understanding of these basic concepts is the beginning step for building a numerical model. The thermodynamic relations also dictate the MCE and therefore help to shape any material model. A failure to follow the laws of thermodynamics would result in unrealistic predictions.

This chapter starts with a background in the important thermodynamic relations and their particular application to magnetocaloric technology. An explanation of the MCE from a thermodynamic background will be given. This explanation helps to inform the implementation of the MCE in a thermodynamically consistent manner. The thermodynamic cycle of a magnetocaloric heat pump is also given. All of the information in these sections is either well established science or the application of this science in a well-known way to magnetocaloric technology.

Description of MCE

In the broadest definition a magnetocaloric material is one that varies its temperature and entropy as a response to a varying magnetic field. This is in fact a phase change phenomenon in which both of the physical phases are solid. The phase change can take place as a second order magnetic transition or as a first order magnetic transition. For a purely SOMT the change in phase is between a ferromagnet and a paramagnet and an increasing external magnetic field causes alignment of the spin moments within the material. A FOMT involves both magnetic ordering and latent heat due to a change in the crystal lattice structure. Both of these transitions represent a

change of order in either the lattice or magnetic systems or both, which also represents a change in the entropy of these systems. The most often reported values of the MCE are the adiabatic change in temperature and the isothermal change of entropy. If the transitions happen adiabatically than ideally this represents an isentropic transition and the total entropy will be balanced between the structural entropy and a change in temperature of the MCM. If the transitions happen isothermally than the entropy changes are only those brought about as a function of the magnetocaloric effect; the ΔS .

Thermodynamics of the MCE

The thermodynamics of the magnetocaloric effect have been covered in detail by many sources, a good example can be found in Tishin and Spichkin (2003). The basic equations can be developed from the fundamental laws of thermodynamics and is often used as an example of an alternate form of work in undergraduate textbooks (Borgnakke and Sonntag, 2013). These relationships are necessary to later implement the MCE in a consistent manner necessitating a brief review. Thermodynamically the MCE can be described in a few steps starting from the first law of thermodynamics, and the reversible definition of entropy for a substance both in derivative form.

$$\delta Q = dU + \delta W \quad (3-1)$$

$$dS \equiv \left(\frac{\delta Q}{T} \right) \quad (3-2)$$

where Q is heat, U is internal energy when potential and kinetic energy are ignored, W is work, T is temperature and S is entropy. Combining these two equations for a reversible substance

$$TdS = dU + \delta W \quad (3-3)$$

The assumption that pressure and volume effects are small and forms of work other than magnetic can be ignored is often made in magnetocalorics. Making this assumption and rearranging Equation (3-3) internal energy is found

$$dU = TdS + \mu_0 H \delta M \quad (3-4)$$

where μ_0 is the permeability of a vacuum H is applied field and M is magnetization. From this equation the Maxwell relation can be drawn

$$\left(\frac{\partial S}{\partial H}\right)_T = \mu_0 \left(\frac{\partial M}{\partial T}\right)_H \quad (3-5)$$

The constant magnetic field specific heat can also be defined

$$C_H = T \left(\frac{\partial S}{\partial T}\right)_H \quad (3-6)$$

Evaluating the total derivative of entropy which is considered as a function of only field and temperature

$$dS = \left(\frac{\partial S}{\partial T}\right) dT = \left(\frac{\partial S}{\partial H}\right) dH \quad (3-7)$$

Then using the above relations the adiabatic change in temperature and the isothermal change in entropy can both be written as an integral between a starting and final field H_0 and H_f respectively

$$\Delta T = \mu_0 \int_{H_0}^{H_f} \frac{T}{C_H} \frac{\partial M}{\partial T} dH \quad (3-8)$$

$$\Delta S = \mu_0 \int_{H_0}^{H_f} \frac{\partial M}{\partial T} dH \quad (3-9)$$

It should be noted that these two descriptions of the MCE are only valid for a SOMT since the specific heat defined in Equation (3-6) would not be valid for a FOMT where

latent heat is involved. Furthermore the specific heat is a function of both field and temperature meaning that these equations cannot be solved explicitly as written.

Total entropy as a function of temperature can be written for a FOMT or SOMT. Rearranging the definition of C_H and taking an integral with respect to temperature the entropy at any field “h” can be found as a function of temperature

$$S_H(T, H = H_h) = \int_0^T \frac{C_H(T, H=H_h)}{T} dT \quad (3-10)$$

Figure 3-1 represents a simplified material’s entropy curve at two different applied fields and can help to illustrate the magnetocaloric effect based on total entropy. In Figure 3-1 S_0 is entropy at an initial field H_0 , S_h is entropy at some higher applied field, and T_0 is the initial temperature. The MCE can be shown between two field levels as either the ΔS or ΔT . ΔT can be described for both SOMT and FOMT materials as the temperature differential at which S_0 and S_h are equal and is a function of T_0 , H_0 , and H_h

$$S_0(T_0, H_0) = S_h(T_0 + \Delta T(T_0, H_0, H_h), H_h) \quad (3-11)$$

ΔS is described as the difference between S_0 , and S_h at a given starting temperature

$$\Delta S(T_0, H_0, H_h) = S_0(T_0, H_0) - S_h(T_0, H_h) \quad (3-12)$$

It should be noted that following this method $\Delta T(T_0, H_0, H_h)$ would be equal to $-\Delta T(T_0 + \Delta T(T_0, H_0, H_h), H_h, H_0)$ which is a consequence of assuming that the transition that is occurring is reversible. SOMT are highly reversible and have very little dependence on the history of the sample while FOMT may display higher hysteresis meaning that C_H and therefor S_H are not just a function of the field and temperature, but also the history

of the sample (Gschneidner, Pecharsky, & Tsokol, 2005). This consideration along with Equations (3-7) to (3-12) play a key role in the modeling of materials.

Models of Specific Heat

Equations (3-7) to (3-12) are all that is needed to create a full thermodynamic explanation of the MCE from entropy which can be determined from heat capacity. One of the most popular ways to model the magnetocaloric properties of second order materials is to sum the contributions of lattice, free electrons, and magnetization to heat capacity. This is most often accomplished using the Debye model, mean field theory (MFT), and the Sommerfeld model respectively (Pecharsky et al., 2001; Rowe, 2012; Tishin and Spichkin, 2003). Each is a simplified model of the systems that they seek to explain.

The Debye model treats atomic vibrations as phonons. Its contribution to specific heat (C_d) can be calculated

$$C_D = \left(\frac{T}{T_D}\right)^3 \int_0^{\frac{T_D}{T}} \frac{x^4 e^x}{(e^x - 1)^2} dx \quad (3-13)$$

where the Debye temperature T_D which is a function of the material is introduced. The MFT in general simplifies a problem of many bodies which interact being acted on by an external field into a problem of many isolated bodies being acted upon by an average field. This contribution to specific heat can be calculated

$$C_m = -\mathbf{H} \frac{\partial M}{\partial T} - \frac{1}{2} \mathbf{N}_{\text{int}} \frac{\partial M^2}{\partial T} \quad (3-14)$$

The MFT model of specific has several constants that must be looked up, and simultaneous equations that must be solved iteratively. The electronic contribution to

specific heat (C_e) is calculated by modeling the free electrons as an ideal electron gas in which electron-electron interactions are neglected

$$C_e = \gamma T C_e \quad (3-15)$$

where γ is the Sommerfeld constant. Summing C_d , C_m and C_e gives the total specific heat. C_d and other material specific values for the constants needed to solve these equations are reported in literature (Tishin and Spichkin, 2003).

Simplified FOMT Material and Restrictions on MCE

A material model whether based on simplified models of atomic behavior or purely phenomenological must create realistic data. There are some limits that are imposed directly as a result of the thermodynamic equations that drive the MCE. A simplified model of a FOMT material helps to illustrate the implications of different thermodynamic properties.

The simplified material will have two different phases with an instantaneous phase transition and associated latent heat between them. The zero field heat capacity C_0 and the high field heat capacity C_H are functions of both temperature and field. In order to define this material in terms of heat capacities all that is needed is the heat capacity of state 1 $C_1(T)$, the heat capacity of state 2 $C_2(T)$, the zero field latent heat L , and the temperature at which the phase change takes place as a function of field $T_T(H)$. Figure 3-2 shows the heat capacity in zero-field and with an applied field for the simplified material model.

The latent heat is discontinuous at the temperature of transition T_T with a value of L . The Latent heat for C_H is fully determined for this material and is therefore not independent. The total entropy of this material can be found by applying Equation (3-10)

to the specific heats. For C_0 all of the parameters are known. In the example material the specific heat of both phases is linear which is similar to the Sommerfeld model given in Equation (3-18) with an offset (C_{offset}) which is used for modeling purposes at high temperatures to simplify the curve. At very low temperatures this would be an oversimplification that violates the laws of thermodynamics, but at high temperatures in a small temperature span these effects are not present. The specific heat and total entropy can be calculated

$$C_p = \gamma T + C_{\text{offset}} \quad (3-16)$$

$$S = \gamma T + C_{\text{offset}}(\ln(T)) \quad (3-17)$$

Since the FOMT is discontinuous the total entropy must be a discontinuous function. The entropy is calculated from Equation (3-20) for the first phase up until T_T where the latent heat is added and entropy is calculated from Equation (3-20) for the second phase. The magnetocaloric effect is constrained between T_T of C_0 and T_T of C_H since this is the only area of change to the specific heat and entropy as a function of an applied field. The change in T_T with field is therefore the only variable that controls the shape of the MCE once the specific heats are known. This also explains why the latent heat of transformation in an applied field is not independent. It must have a value which closes the entropies. The resulting entropy curves around the MCE are shown in Figure 3-3. The slope of the curves is determined by the value of specific heat. The second discontinuity which is caused by the phase transition of the material when exposed to an internal field must have a value that corresponds to the gap in the zero field and high field entropy at this temperature.

The effect of changing C_1 , C_2 , L , or $T_T(H)$ can easily be shown using this simplified material and is presented in Figure 3-4. The MCE of these materials can be analyzed using the method illustrated in Figure 3-1 along with Equations (3-11) and (3-12). The ΔS and ΔT will both be determined from the total entropy and will be impacted by the different specific heats as exemplified in Figure 3-5. Each of the lettered examples in Figure 3-5 has the same specific heat from the lettered examples in Figure 3-4. A similar analysis of a simplified FOMT material was conducted in Pecharsky et al. (2001) which went into less depth about the implications on shape. They compared the simplified model to $Gd_5(Si_2Ge_2)$ a material which displays a very first order transition and showed that even the simplified model could give a good prediction of the MCE especially in terms of shape. Interestingly Pecharsky et al. (2001) makes the simplifying assumption that both phases have the same basic specific heat similar to case (a) in Figure 3-4 and Figure 3-5. Their measured data however shows very clearly that the higher temperature phase has a lower specific heat than the lower temperature phase similar to Figure 3-4 c. When the ΔS was measured the data shows the same decreasing slope Figure 3-5 c further illustrating the usefulness of this simplified model in understanding the behavior of first order materials.

Hysteresis

The MCE thermodynamic equations above are based on an effect that is reversible. In reality no system is fully reversible, and in practice the FOMT generally shows a higher hysteresis than the SOMT (Gschneidner Jr., K. A.; Pecharsky, V. K.; Tsokol, 2005). Hysteresis can diminish the usable effect in a MCM to the extent that it is not useful for more than one cycle in an actual MCHP. The interrelation of the magnetic phases with hysteresis included can clearly display why MCMs with measureable

effects may not produce any performance in cyclical MCHPs (Srivistava and Johnson, 2014). Many papers have been published on the topic of hysteresis including its effect on measurements, methods of modeling hysteresis, and measurement techniques for hysteresis (Brey et al., 2014; K. Engelbrecht et al., 2013; Von Moos et al., 2014). One way to deal with to deal with hysteresis in materials is to use measurement techniques that include the effects of hysteresis. This may include measuring effects in an appropriate direction (Pecharsky et al., 2001). Measurement direction focusing on specific heat measurements is expanded upon in K. Engelbrecht et al. (2013) and Von Moos et al. (2014) for $\text{MnFeP}_{1-x}\text{As}_x$ and $\text{Gd}_5\text{Si}_2\text{Ge}_2$ respectively. It is shown in these two papers that accounting for hysteresis through measurement can accurately simulate MCHPs, and that a lack of attention to hysteretic effects can have large impacts on model predictions.

Experimental Measurement

Experimental measurements are key to understanding the MCE and creating a material model. There are three main methods for measuring the data needed to characterize a MCM. The magnetization can be measured through a vibrating sample magnetometer (VSM) for example ([“Vibrating Sample Magnetometers | Lake Shore Cryotronics, Inc.,” 2016](#)). These measurements can be used in conjunction with Equation (3-5) to obtain ΔS . The ΔT can be directly measured with experimental devices designed for this task. Adiabatic ΔT measurement devices generally have a method of applying a magnetic field, a temperature control system, and a variety of temperature measurement capabilities. An MCM sample is magnetized and demagnetized repeatedly under a changing starting temperature (Dan’kov et al., 1997). The specific heat can also be measured via differential scanning calorimetry (DSC).

DSCs measure the amount of heat required to raise the temperature of a sample in comparison to a reference at controlled temperatures. For MCM a more specialized DSC in field is often used in which an applied field and temperature are controlled. Normal DSC machines are commercially available ([“Differential Scanning Calorimetry \(DSC\) Instruments | PerkinElmer,” n.d.](#)) while DSC in field machines are often custom built for the purpose of MCM measurement (Marcos et al., 2003).

Each of the measurement methods has advantages and disadvantages which must be considered when choosing data for modeling purposes. Adiabatic ΔT is the only method that directly measures the MCE. This method is exclusively carried out on non-commercialized machines which must make temperature measurements in varying magnetic fields. VSM is carried out on highly calibrated commercial equipment, but indirectly leads to ΔS a property which is not normally used for modeling and can be prone to error (Von Moos et al., 2014). DSC without field also uses commercialized equipment and measures heat capacity which is both directly used in modeling and indirectly used in conjunction with either ΔT or ΔS to obtain the remaining MCM properties. Finally DSC in field normally relies on custom equipment, but directly measures the heat capacity data that is normally used in modeling and is the only method that in a single machine can obtain all of the measurements necessary to fully define an MCM and the MCE.

DSC in field can be used to both measure the effects of hysteresis and create experimental data that includes these effects. As discussed in K. Engelbrecht et al. (2013) and Von Moos et al. (2014) utilizing zero field on heating specific heat and high field on cooling specific heat is the most similar to actual MCHP conditions for cooling

applications. In K. Engelbrecht et al. (2013) this method is also compared against adiabatic ΔT measurements and shows very high correlation. For these reasons along with the consideration that DSC in field eliminates errors between machines and directly measures both C_0 and C_H which are needed for numerical modeling in field DSC with confirmation by direct adiabatic ΔT as suggested in K. Engelbrecht et al. (2013) is the preferred method of MCE and MCM data collection. It is noted however that the material model developed in this work can in fact model MCMs using ΔT or ΔS data along with zero field specific heat data.

Other MCE Considerations

The simple FOMT model is restricted to single phase changes and is was only presented with zero field T_{CS} at lower temperatures than those at high field. Other materials exist which display an inverse magnetocaloric effect (Hu et al., 2000). In principle the material model that is presented as part of this work can model inverse magnetocaloric effects. In practice many of these materials have a double effect due to a large decoupling of magnetic and structural phase transitions (Pecharsky and Gschneidner, 2005) which will not be considered.

Nielsen et al. (2010a) highlights another important ramification of the MCE thermodynamics. For a reversible material with a continuous effect it is impossible for the slope of the adiabatic temperature change to be less than negative one

$$\frac{d[\Delta T_{\text{mag}}(T,H)]}{dT} > -1 \quad (3-18)$$

where ΔT_{mag} is the adiabatic temperature change on magnetization as a function of field and temperature. Equation (3-21) can serve to ensure that the material model is not producing thermodynamically inconsistent materials. Nielsen goes on to suggest that a

discontinuous material can in fact break this inequality, but that this would require two discontinuities. Such a material has not been found to exist but is thermodynamically possible. As with inverse materials, materials that display two discontinuities will not be considered.

Thermodynamics of Cyclical Magnetocaloric Refrigerators

The magnetocaloric effect of FOMT materials is constrained by the separation in T_T at zero and high field as was shown with the simplified material model. These separations are normally just a few Kelvin when driven by fields that can be produced by permanent magnets. The solution to provide cooling spans greater than one material can provide has been to use staged material in a regenerative cycle. The specific regenerative cycle most often modeled as the active magnetic regenerative cycle (Barclay, 1983).

The cycle for a single particle consists of four thermodynamic processes combined with two heat transfer processes. Adjacent particles are coupled through the heat transfer processes to form a regenerative structure. The cycle can be described by simple illustration and comparison to a vapor compression cycle as in Figure 3-6. Note that the MCE in this description is for a second order material for visualization purposes.

There are two isofield and two adiabatic processes in the magnetic refrigeration cycle. The arrows represent the magnetic moment for a typical SOMT material undergoing a magnetic phase transition. From step two to three the temperature goes below the starting temperature making refrigeration possible. Normally this type of vapor compression cycle is presented in either a pressure enthalpy diagram. Magnetic refrigeration is normally presented using a temperature entropy diagram for the cycle

described in Figure 3-6. To better illustrate the cycle the temperature entropy diagram from Figure 3-1 is updated according to Figure 3-6 and shown in Figure 3-7. Figure 3-7 operates between two isofield entropy lines. The steps are the same as those from Figure 3-6. This cycle would represent only a single particle and does not include the regenerative aspects of AMR MCHP. The AMR is an idealized cycle which may not include several losses that are present in MCHPs. Like many other heat pumps modeling with the AMR can help to determine the best possible operation of a real world MCHP.

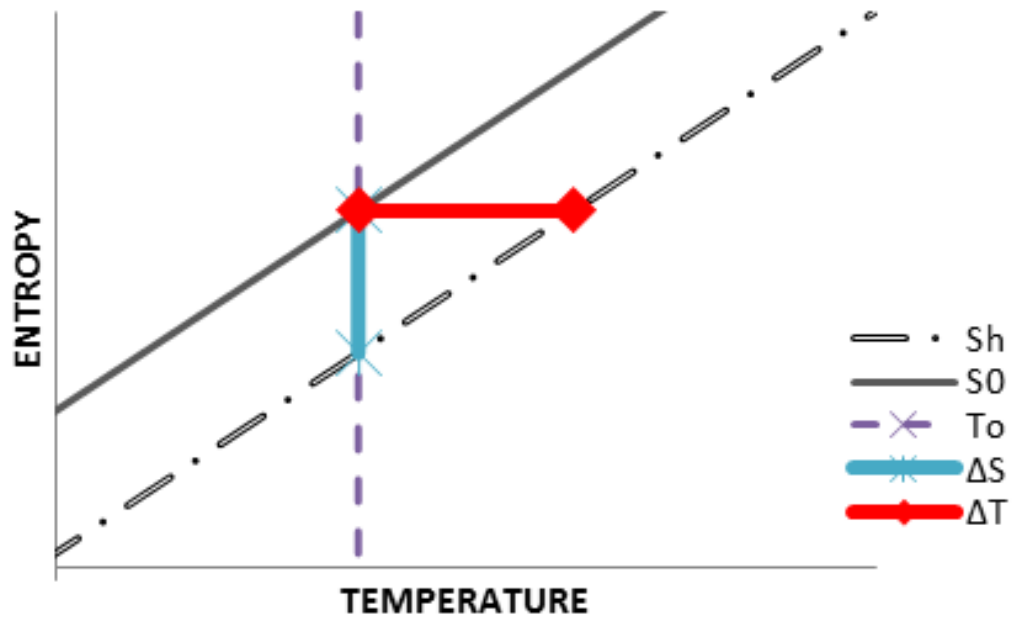


Figure 3-1. A simplified version of total entropy.

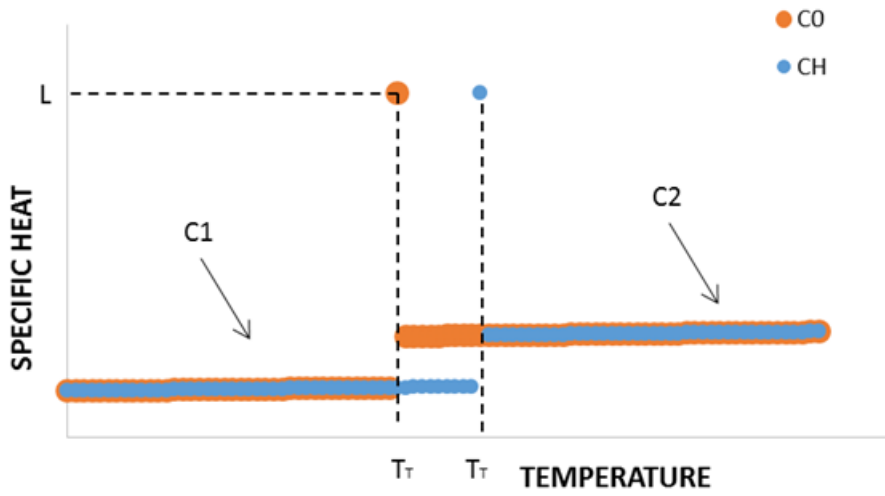


Figure 3-2. An ideal FOMT displayed as the specific heat of at both zero and high applied field.

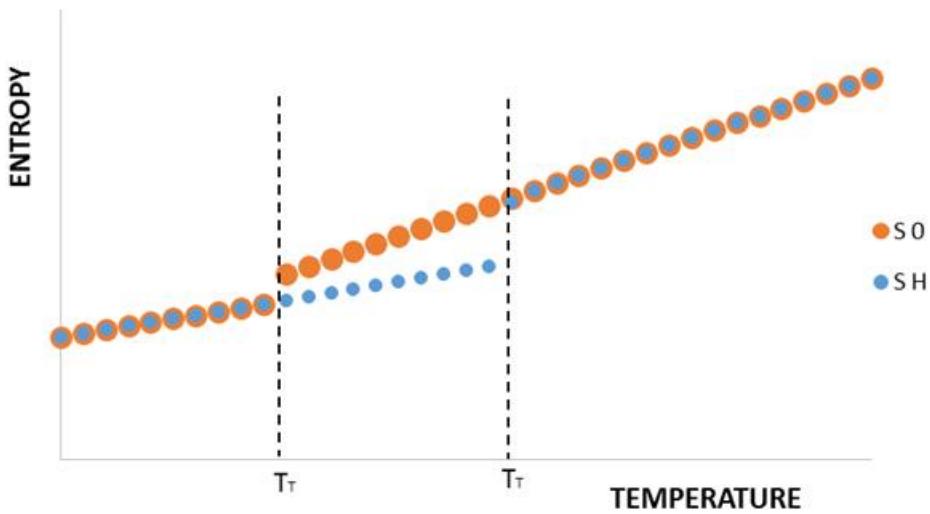
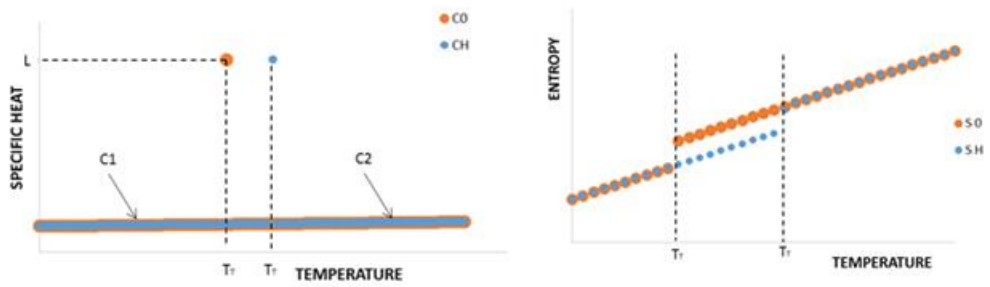
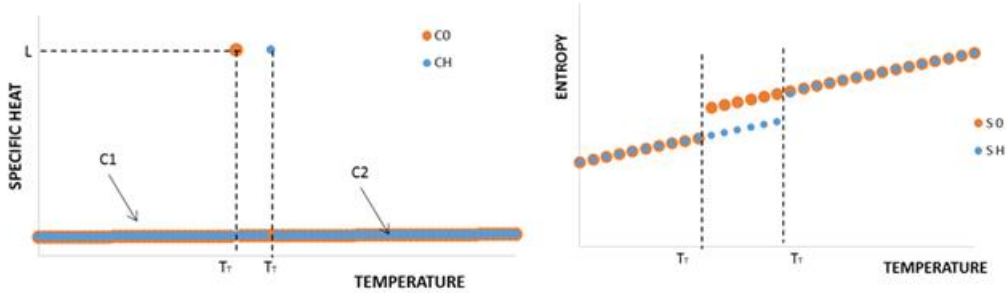


Figure 3-3. Entropy curves for an ideal FOMT.

(a)



(b)



(c)

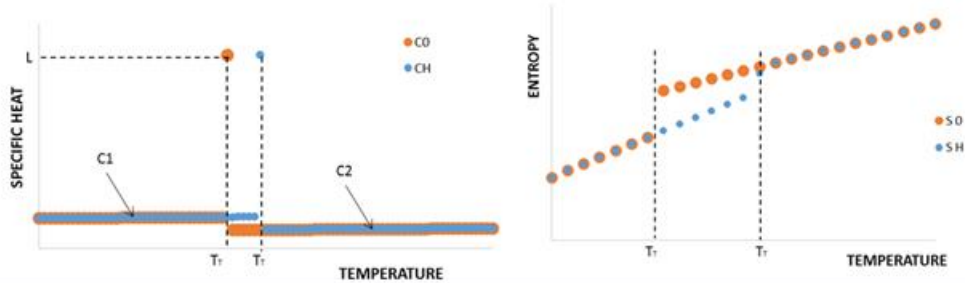


Figure 3-4. Different combinations of combinations of specific heat characteristics. (a) Material with $C_1 = C_2$. (b) Material with $C_1 = C_2$ and a smaller gap between T_1 for high field and zero field. (c) Material with $C_1 < C_2$.

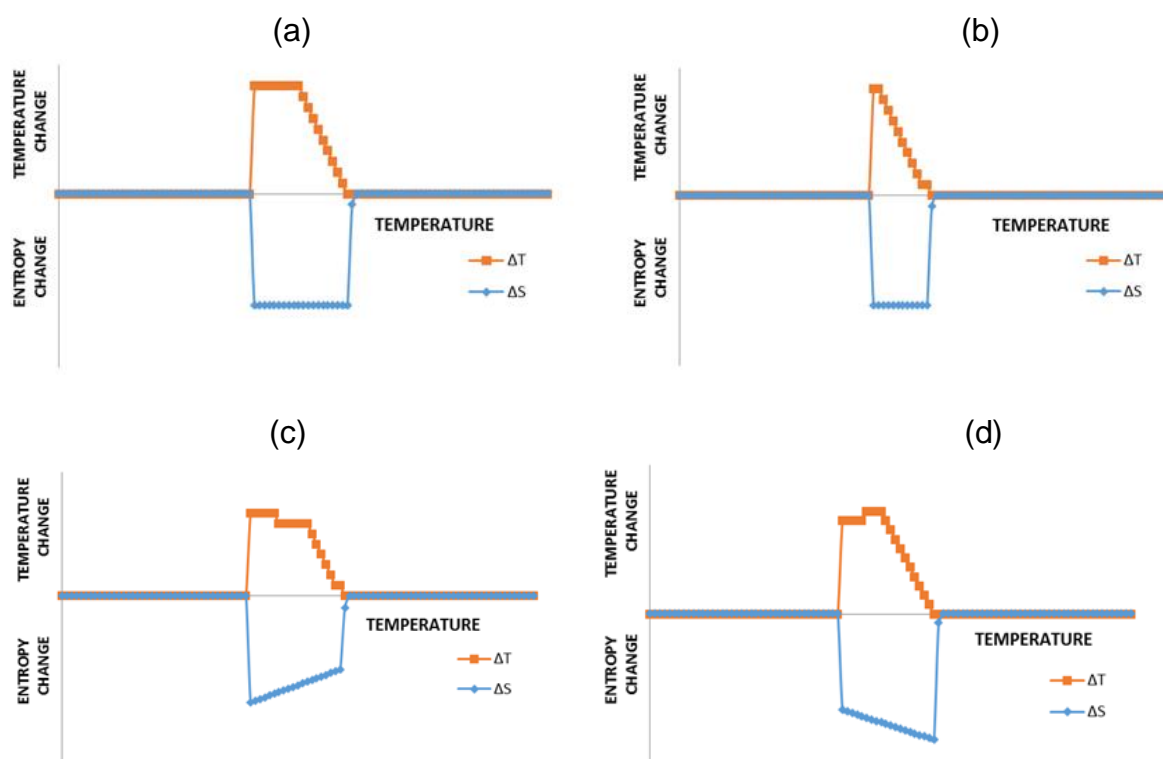


Figure 3-5. The MCE of different simple FOMT materials.

Cycle for magnetocaloric refrigeration and (Vapor compression refrigeration)

A. Starting zero field (low pressure) condition and starting temperature.

1. Magnetic field (pressure) is applied temperature rises.

2. Heat rejected at constant field (pressure)

3. Magnetic field removed demagnetization (expansion). Temperature decreases below starting temperature

4. Heat accepted at constant field (pressure)

Magnetocaloric refrigeration

Vapor compression

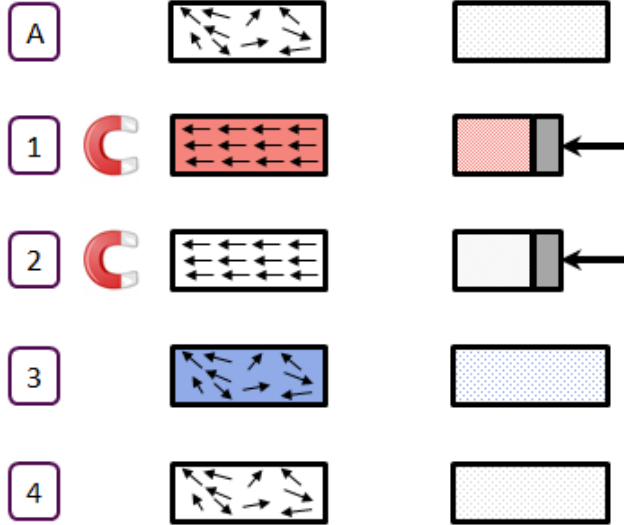


Figure 3-6. Illustration of magnetic refrigeration cycle with vapor compression cycle for comparison.

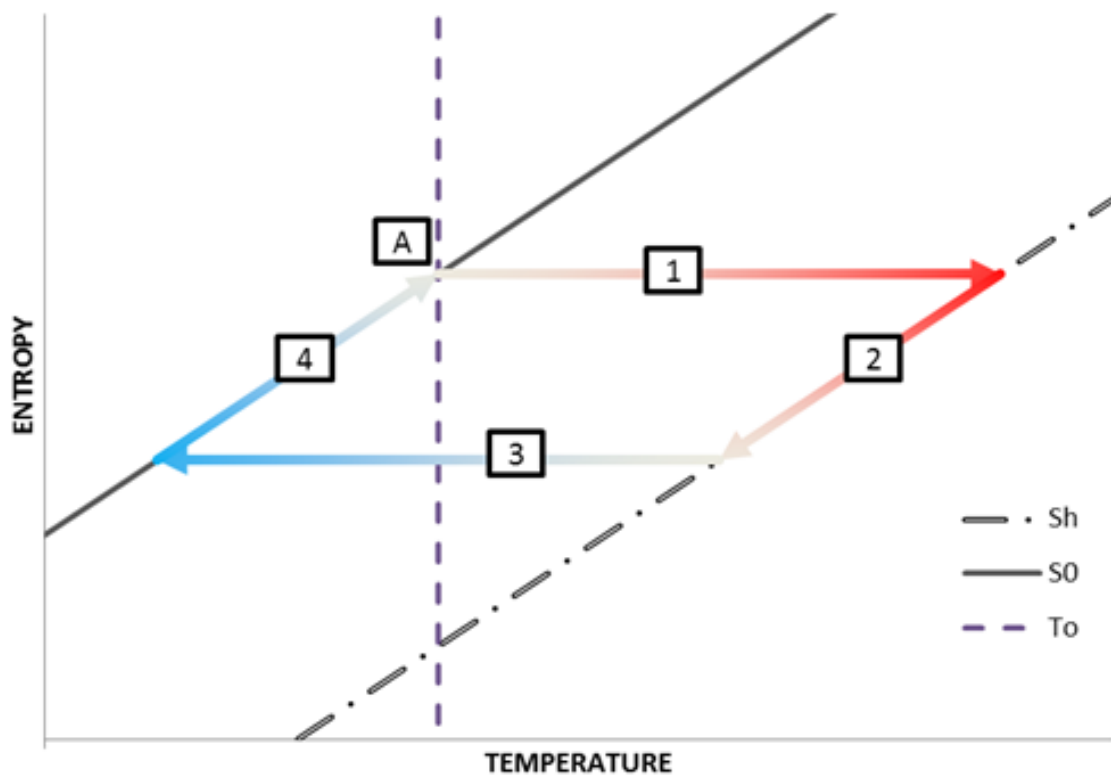


Figure 3-7. The magnetocaloric cycle on a portion of the entropy temperature diagram.

CHAPTER 4 NUMERICAL MODEL OF THE ACTIVE MAGNETIC REGENERATOR

The following chapter gives a basic review of the numerical model used in this work to model the performance of an AMR. This model will be referred to as the AMR model. The AMR model was developed in the open source computer language Python (["Python.com,"](http://Python.com) 2015). As explained later in this work the AMR model was modified to enhance speed, and incorporate the material model, however, the original AMR model was not created as part of this work. Only the fundamentals needed to understand the operation of the AMR model and its impact on the modeling studies, experimental prototype correlation, and material model integration are given. A more detailed explanation of the AMR model can be found in Schroeder and Brehob (2016). Full reference for this chapter is given to Schroeder and Brehob (2016).

Idealized Magnetocaloric Refrigerator Operation

The simplified AMR cycle is used for the basis of all modeling completed as a part of this work. The basic cycle is the same as the one illustrated in Figure 3-6 and Figure 3-7 with a few additional simplifying assumptions. There is no flow during magnetization for the idealized cycle used in these modeling studies. This is a valid assumption for a good proportion of MCHPs, though commercial MCHPs may seek to take greater advantage of available magnetic fields for cost reasons by flowing during changing magnetic fields. It is also assumed that magnetization happens instantaneously. In a real MCHP this assumption cannot be true as there is always some transition time between high and low a field states. During this transition time there must be heat transfer by conduction from the MCM to the heat transfer fluid. The transition time is, however, normally a small fraction of the cycle time. Additionally

accurately modeling a non-instantaneous magnetic field change would require knowledge of the MCE as a function of field. This data is not readily available for most first order materials and the investigation of these properties is an active area of current research. Lastly there was assumed to be no dwell between magnetic field change and flow. This assumption is made only for parameter studies. Assuming no dwell ensures that the MCHP operation is at the highest possible frequency that does not affect flow. When flow is not changed and conduction during dwells is not a large contributor to heat transfer an increase in cycle frequency due to reduced dwell between field change and flow should correspond to a linear increase in cooling capacity (Benedict et al., 2016b). Assuming instantaneous magnetization and zero dwell would therefore be the best case limit for actual MCHPs. These assumptions also greatly increase the speed of modeling.

Regenerator Model

The most basic form of the AMR model takes into account no MCHP design dependent losses. In this version of the AMR model the regenerator is modeled as a series of nodes in the axial direction. Each node has a fluid and MCM element. At the ends of the regenerator there are a hot and cold reservoir. A schematic representation of the interactions and nodes of the AMR model are represented in Figure 4-1. For simplicity only three nodes are represented.

The fluid and MCM nodes are only connected via a single heat transfer term. There is no interaction with the environment when MCHP design specific losses are not considered. As shown in Figure 4-1 the cold and hot reservoirs only interact with the AMR through mass transfer. In the axial direction the MCM is assumed to conduct heat while the fluid nodes have a dispersion term that encompasses axial conduction.

Fundamental Equations

Work is done on the AMR magnetically and hydraulically. Magnetic work derives from the changing of magnetic field to create the MCE while hydraulic work is a result of pumping fluid and is included through viscous heating. The MCE is applied as an instantaneous change in MCM temperature. At each time step a temperature change is calculated for every fluid and MCM node based on the combination of interactions and effects described above

$$\partial T_{\text{fluid node}} = \left(\left(\frac{\partial T}{\partial t} \right)_{\text{mass trans.}} + \left(\frac{\partial T}{\partial t} \right)_{\text{fluid MCM-f heat trans.}} + \left(\frac{\partial T}{\partial t} \right)_{\text{fluid axial disp.}} + \left(\frac{\partial T}{\partial t} \right)_{\text{viscous heating}} \right) \partial t \quad (4-1)$$

$$\partial T_{\text{MCM node}} = \left(\left(\frac{\partial T}{\partial t} \right)_{\text{MCM axial cond.}} + \left(\frac{\partial T}{\partial t} \right)_{\text{MCM MCM-f heat trans.}} \right) \partial t + \partial T_{\text{MCE}} \quad (4-2)$$

The time step between successive iterations is ∂t and temperature change is ∂T . The mass transfer between fluid nodes is calculated from superficial fluid velocity v_{sf}

$$\left(\frac{\partial T}{\partial t} \right)_{\text{mass trans.}} = \frac{v_{sf}}{L_{\text{node}} \varepsilon} (T_{n_f+1} - T_{n_f}) \quad (4-3)$$

where L_{node} is node length, ε is fluid fraction of the packed bed, T_{n_f} is current node temperature, and T_{n_f-1} is adjacent node temperature. When fluid flow direction is changed T_{n_f-1} is replaced with T_{n_f+1} . Heat transfer between the MCM and fluid elements is calculated from a heat transfer correlation $UA_{\text{MCM-f}}$ in units of W/K

$$\left(\frac{\partial T}{\partial t} \right)_{\text{fluid MCM-f heat trans.}} = \frac{UA_{\text{MCM-f}}}{\rho_f V_{\text{node}} c_{p_f} \varepsilon} (T_{n_{\text{MCM}}} - T_{n_f}) \quad (4-4)$$

where ρ_f is fluid density, V_{node} is total node volume, $T_{n_{\text{MCM}}}$ is temperature of the co-located MCM node, and C_{p_f} is fluid heat capacity. An axial dispersion coefficient k_{eff} is used in the axial dispersion calculation

$$\left(\frac{\partial T}{\partial t}\right)_{\text{axial disp.}}^{\text{fluid}} = \frac{k_{\text{eff}}}{L_{\text{node}}^2 \rho_f C_{p_f} \varepsilon} (T_{n_f+1} - 2T_{n_f} + T_{n_f-1}) \quad (4-5)$$

Viscous heating is calculated from the pressure drop across each node length (ΔP)

$$\left(\frac{\partial T}{\partial t}\right)_{\text{heating}}^{\text{viscous}} = \frac{\Delta P_{\text{node}} v_{sf}}{L_{\text{node}} \rho_f C_{p_f} \varepsilon} \quad (4-6)$$

For the MCM axial conduction is calculated between nodes

$$\left(\frac{\partial T}{\partial t}\right)_{\text{axial cond.}}^{\text{MCM}} = \frac{k_{\text{MCM}}}{L_{\text{node}}^2 \rho_{\text{MCM}} C_{p_{\text{MCM}}}} (T_{n_{\text{MCM}+1}} - 2T_{n_{\text{MCM}}} + T_{n_{\text{MCM}-1}}) \quad (4-7)$$

where k_{MCM} is MCM thermal conductivity, ρ_{MCM} is MCM density, and $C_{p_{\text{MCM}}}$ is MCM heat capacity. The MCM to fluid heat exchange from Equation (4-4) is used to determine the corresponding temperature change in MCM

$$\left(\frac{\partial T}{\partial t}\right)_{\text{heat trans.}}^{\text{MCM-f}} = \frac{UA_{\text{MCM-f}}}{\rho_{\text{MCM}} V_{\text{node}} C_{p_{\text{MCM}}} (1-\varepsilon)} (T_{n_f} - T_{n_{\text{MCM}}}) \quad (4-8)$$

The heat transfer calculation from fluid to MCM is based upon a correlation from Wakao et al. (1979), pressure drop is calculated based on an equation based on work from Ergun and Orning (1949), and the axial dispersion is calculated for Stokes flow based on Koch and Brady (1985). More detail on how each of these correlations is specifically applied to this AMR model can be found in Schroeder and Brehob (2016).

MCHP Parameters

There are a number of parameters that arise as a result of MCHP design. Volumetric flow rate as a function of time and magnetic field as a function of time

determine the operation of the AMR cycle. These are both treated as a series of dwell start and stop times, peak start and stop times, and peak magnitudes. An example of a resulting flow profile is shown in Figure 4-2. Any combination of start and stop time for zero flow and maximum flow can be used creating ramped flow profiles. For parameter studies simplified ideal cases will be considered. For fluid flow and magnetization this means square profiles are considered. When actual MCHP performance is being predicted ramped profiles will be used to approximate MCHP operation as closely as possible.

The other important MCHP parameter that is considered in the AMR model is regenerator design. This includes the aspect ratio of the regenerator and total volume. The MCM shape can play a large role in performance as well. For the purposes of this study packed beds are considered in both the MCHP and modeling efforts.

Boundary Conditions

Boundary conditions can heavily impact the operation of a MCHP and the prediction of an AMR model. For this AMR model the hot side is treated as an infinite mass thermal well that fluid flows into and out of. This is equivalent of having a perfect heat exchanger and therefore only a hot side temperature is required for the AMR model. This study will focus on the operation of an AMR in periodic steady state and accordingly the cold side boundary condition is also treated as an infinite thermal well. In this way the cooling capacity resulting from the input parameters can be calculated for different spans and load span curves can be constructed.

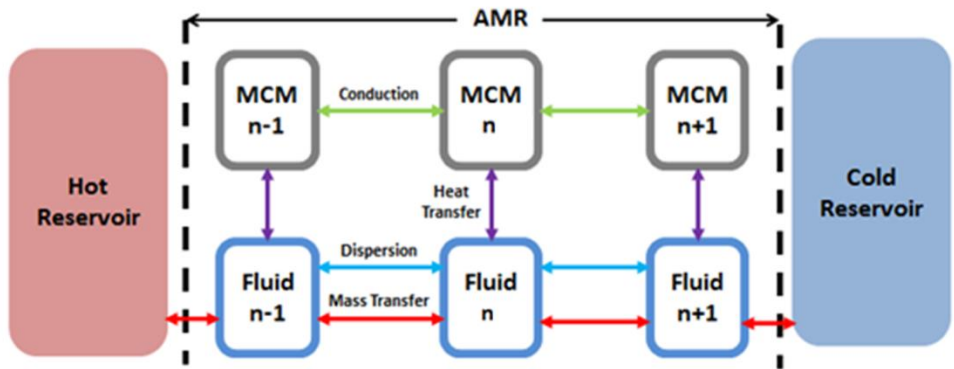


Figure 4-1. A schematic representation of the node structure and interactions in the AMR model.

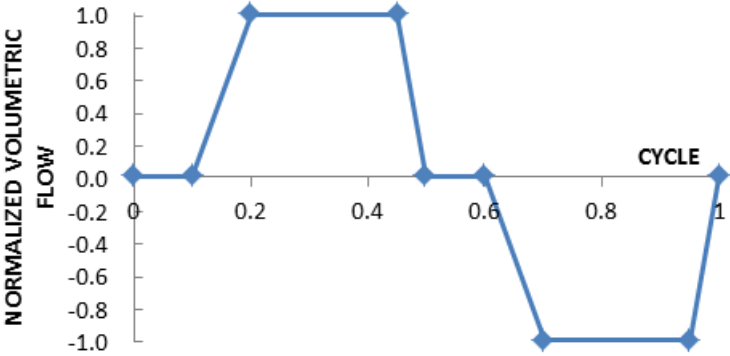


Figure 4-2. An example profile of normalized volumetric flow for a cycle.

CHAPTER 5 EXPERIMENTAL PROTOTYPE

This chapter reviews details of the experimental prototype that was developed. The design theory, measurement and initial testing of the prototype are reported. Much of the original work involved in this chapter was initially reported in Benedict et al. (2016b).

In order to validate the material model as well as the AMR model a magnetocaloric prototype has been developed. The prototype is called Halbach Array Prototype One or “HA1”. Though validation of AMR models with MCHPs has been successful in the past (Bahl et al., 2014; Balli et al., 2012a) most MCHPs used for this purpose were originally developed with commercialization in mind. This means only a small percentage of operational parameters, or a subsection of these parameters’ ranges can be investigated. In contrast the main goal of validating model results means that the HA1 prototype must be flexible, easy to configure, measurable and reliable. These characteristics will allow for a wide range of operational parameters to be confirmed on a single MCHP for the first time, leading to a more accurate AMR model and more accurate predictions.

Magnetocaloric prototypes can be defined in many ways. A useful classification system was proposed by Scarpa et al. (2012). The suggested categories are used to help define the HA1 system. HA1 is a double effect system which means that when one regenerator is magnetized a matching regenerator is demagnetized. The minimum of two regenerators are used in HA1. They are tubular in shape and are concentrically located inside of a set of nested Halbach arrays. The sets of nested Halbach arrays are 180° out of phase magnetically. This means that the two regenerators undergo cycles

180° out of phase from each other thus creating the double effect. The magnetic gap frontal area is circular which is better suited for one dimensional material structures such as particles, spheres, or microchannels. The regenerators have also been tested with plate configurations which lower the utilization of the magnetic field. The MCM can be multiple or single stage. Heat transfer is fluid based with the capability to create oscillating or unidirectional flow on both the hot and cold sides. Magnetic field change is applied by rotating one of the nested Halbach arrays in either a continuous or discontinuous motion. In Figure 5-1, a top frontal view of HA1 is presented. From bottom to top the cold section, magnet arrays, hot sections, and pistons with linear motor are visible. The entire prototype along with chiller, electronics box, and computer fit on a rolling cart approximately one meter tall half a meter wide and one and a half meters long.

Magnetic System

An important consideration for magnetic refrigeration is the production and application of a magnetic field. In order to generate very high fields but maintain a small enough magnet size to keep the overall prototype compact nested Halbach arrays were chosen. This arrangement has been successfully implemented by multiple groups (Arnold et al., 2014; Shir et al., 2004; Tura and Rowe, 2011), and has the advantage of large fields with uniform magnetization.

A Halbach array is a general term for a magnet or set of magnets with a continuously changing magnetic field arrangement. In the case of HA1 the magnets are arranged in the form of a ring. The magnetization direction of the magnet makes exactly two rotations around the circumference of array. This type of Halbach array creates an aligned and uniform field within the annulus of the array. In practice it is hard to make a

single magnet with this sort of magnetic field alignment, and most Halbach arrays of this type are made from arc shaped magnets each with a different orientation which was the method of construction for the magnets of HA1. Figure 5-2 is an example of such a Halbach array.

When two of these arrays with the same internal flux density are located concentrically they can be made to either double the resulting internal flux density when their magnetic fields are aligned, or cancel the internal field when they are opposed. To calculate the internal field of this type of Halbach array an equation involving the inner and outer radius of the magnetic array along with the number of segments was developed by Klaus Halbach (Halbach, 1980)

$$B_{\text{result}} = B_r \left[\frac{\sin(2\pi/N_s)}{2\pi/N_s} \right] \ln \left(\frac{r_o}{r_i} \right) \quad (5-1)$$

The resulting flux density inside of the array is B_{result} while B_r is the remnant magnetic field for each of the segments and N_s is the number of segments. The inner and outer radiuses are r_i and r_o respectively. In this equation end effects present for a finite length array are ignored.

The parameter space of interest for this work has been limited to magnetic refrigeration with permanent magnets. In review of the literature it is found that most MCHPs utilizing permanent magnets have a high field strength limited around 1.5 Tesla which was set as the high field for HA1. Equation (5-1) shows that for an increasing number of segments increasing resultant field can be expected, a fact illustrated by Figure 5-3.

For the arrays of HA1 ten magnetic segments were chosen based upon the diminishing magnet field returns and increased complexity associated with greater

numbers of segments. To ensure that end effects were did not create a non-uniform magnetic field the last 20% on either end of the magnetic arrays is not used. The result is a concentrically located dual Halbach array with a cylindrical test section having a uniform magnetic field measuring 16 cm long and 1.9 cm in diameter. The maximum field is over 1.5 Tesla and the minimum field under 0.1 Tesla for the entire 16 cm length. In order to fully understand the magnetic cycle that the test section experiences as the Halbach arrays are rotated a Hall effect probe was used to create a field map as a function of both depth into the arrays and relative rotation angle. The results are shown in Figure 5-4. This full three dimensional map of the magnetic field coupled with programmable control of the magnet rotation enables the implementation of different magnetic cycles.

Hydraulic System

The heat transfer fluid implementation is an important design consideration for any commercial intent prototype. Viewed independent of the implementation scheme, the actual fluid flow of most prototypes falls into two categories: Fluid which leaves the regenerators at the ends, and fluid which remains in the regenerator toward the middle. The fluid that does not leave the regenerator always oscillates from the hot to cold ends during cyclical operation. Fluid leaving the regenerator needs to exchange heat. The heat exchange portion of the fluid cycle is generally either oscillatory or unidirectional.

The only important control parameter for fluid flow is volumetric flow rate as a function of cycle. Inherent in this parameter are the displacements, velocities, and accelerations that create heat exchange, pressure drop, and forces experienced by the system. A linear actuator moving a double ended piston allows a high degree of accuracy to be achieved in HA1 when implementing volumetric flow rates. The flow that

leaves the regenerator can be made to fully oscillate or circulate in the heat exchangers by means of a check valve system. In the case of full circulation there is nearly no dead volume due to the hydraulic circuit design. The fluid operation is controlled independently from the magnetic field with the ability to change piston displacement, speed, and acceleration within the prototype user interface thus eliminating the need for exchanging parts. A schematic of the fluid system in Figure 5-5 helps to visualize the system in a fully recirculating heat exchange configuration. To create full circulation in the heat exchangers eight check valves are used. There are also two hot side heat exchangers, the temperatures of which are regulated by a single chiller.

The two regenerators undergo cycles exactly 180° out of phase from each other. This arrangement has several advantages. Magnetically because one regenerator is being magnetized when the other is being demagnetized the torque from each of the two double Halbach arrays partially offsets the other. Since one regenerator is always in the demagnetization portion of the cycle the cold side can receive near constant flow. This helps to minimize fluctuations in the cold side temperature. An example of the cycle outlined in Figure 5-6 is shown utilizing the schematic from Figure 5-5 to illustrate the operation of HA1 in the four basic steps of the AMR cycle.

The AMR cycle in Figure 5-6 consists of: (a) Both dual Halbach arrays rotate 180° . The lower array is being magnetized and the regenerator in this array will increase in temperature. The top array is being demagnetized and the regenerator will decrease in temperature. The fluid is stationary during magnet movement. (b) The dual piston is moved upward creating flow from hot to cold side in the top regenerator and cold to hot in the bottom regenerator. The fluid delivers heat to the regenerator in the top array

increasing the MCM temperature and decreasing the fluid temperature. This decrease in fluid temperature enables the refrigeration that is the goal of magnetocaloric refrigeration. (c) The dual arrays are rotated 180° back to their starting positions. The top regenerator is magnetized and the bottom demagnetized. (d) The piston is moved in the opposite direction causing flow in the reverse directions from step (b). Cold fluid now comes from the bottom regenerator while heat is picked up and rejected from the top regenerator.

Loading and Configurations

The heat exchange fluid utilized in HA1 is normally water based, with ethylene glycol for freezing point suppression and a few volume percent of material dependent corrosion inhibitor. Heat exchange is achieved on the hot side via two fluid-fluid heat exchangers connected to a recirculating chiller/heater. The chiller is a Polyscience™ 5260T11A113B capable of 850 Watts at 20°C. The heat transfer for the HA1 prototype is on the order of 100 Watts and the flow rate ranges between 0.01 and 0.1 liters/second. This range of flow is not normally accommodated by off the shelf heat exchangers so two shell in tube heat exchangers were fabricated. The shell has an outer diameter (OD) of 9.5 mm and an inner diameter (ID) of 6.3 mm. The tube has an OD of 4.7 mm and an ID of 3.2 mm. The heat exchanger is arranged in an S shape with a total length of 0.9 m as shown in Figure 5-7. Counter-flow is used in the hot side heat exchanger, with the chiller fluid in the shell side and the heat transfer fluid in the tube side. The large cooling capacity of the chiller relative to the HA1 ensures that the chiller set temperature can be used to set the hot side return temperature to the regenerators. In practice the return temperature normally deviates by less than 1 K from the chiller set temperature.

The cold side is loaded using a resistance heating element in direct contact with the heat transfer fluid. The load can be varied by changing the power delivered to the heating element. Unlike the hot side the temperature for the cold side is a response variable.

Measurement

The entire HA1 prototype is controlled via LabVIEW® software with a user interface designed specifically for HA1. The motors operating the fluid and magnetic system are independently controlled and can be set for displacement, rotation, speed and acceleration. In addition, the motor controlling the Halbach arrays can be set for cyclical operation including pauses or continuous rotation. This is necessary as cyclic operation is limited to an upper frequency of 2 Hz due to acceleration in the magnet system as well as pressure drop in the fluid system. The chiller and cold side loading are also controlled with LabVIEW® and can simulate a range of ambient and loading conditions.

Control inputs are monitored by LabVIEW® as to maintain an active feedback loop and to record their operation. In addition to these inputs, several outputs are also recorded by the LabVIEW® software. TCs monitor temperatures within the system at key points. Up to 15 TCs can be monitored at one time. Constant TC locations include: Hot and cold side inlet and outlet for both regenerators, ambient, and chiller outlet. Pressure is recorded via two digital pressure transducers. These transducers can be moved throughout the system to measure the pressure at any point. They are normally located at each piston since typically 90% of the system pressure drop for particle beds happens in the regenerators. A typical temperature output from a test is shown in Figure

5-8. The system is initially pulled down in temperature for the first 400 seconds and then loads are applied at 750 and 1300 seconds.

During the measurement of span resulting from different applied powers the system is allowed to come to steady state for each of the loading levels. The time to reach steady state depends heavily upon the cooling capacity of the MCHP at the test condition and the thermal mass of the cold side. For this reason the cold side thermal mass is kept as low as possible, however for tests with smaller loads the steady state condition can take an appreciable time as seen in Figure 5-8. Though data from Figure 5-8 is typically used to report the span resulting from an applied load other interesting information can be obtained. During the pull down time (from 0 to 700 seconds in Figure 5-8) the slope of the cold side curve with respect to temperature gives information about the cooling capacity of the prototype at different spans with greater negative slopes representing greater cooling capacities. This information is not typically used for exact measurements for relative tests it can be used very well to compare different test conditions and regenerators.

The pairs of hot or cold thermocouples also give additional information about the test conditions. The HA1 prototype utilizes a positive displacement piston to drive flow meaning that the flow rate at any time is well recorded by the system. Because the inlet and outlet temperatures are known as function of time the heat accepted and rejected can be obtained from the temperature data in Figure 5-8. Indeed it can be seen in the example that span between the inlet and outlet for each of the loading conditions increases as the load increases. The span between the inlet and outlet of the hot side is also near a maximum during the beginning of pulldown lowering to a minimum as the

span reaches its limit reflecting the cooling capacity of the regenerator during the full range of spans.

Accuracy

The usefulness of HA1 is directly impacted by the accuracy of the measurements that it can make. In order to increase the accuracy of these measurements efforts were made both in the physical design of the system and the selection of measurement equipment. Losses will always be present in any physical system and so they are measured or calculated and used to increase AMR modeling accuracy.

Physical Design

The effects of the physical system on accuracy were explicitly considered during the initial design of HA1. The primary measurements of importance are flow rate, temperature, and cooling capacity. The primary loss modes reported in literature are losses due to two dimensional factors in the frontal plane of the regenerator, and heat leaks (Bjork and Bahl, 2013; K Engelbrecht et al., 2013; Nielsen et al., 2013).

Two dimensional considerations can take the form of flow maldistribution, internal regenerator demagnetization, and temperature gradients in the normal directions to flow due to heat leak. For the case of flow maldistribution the errors arise because in an AMR model the flow is assumed to be the same in the dimensions not considered by the AMR model. This however is not the case in the physical system. As with any randomly distributed effect, a larger number of samples leads to a closer approximation of the average. The use of particles in these studies represents the maximum number of flow paths for currently available materials and therefore the closest approximation of the average flow assumption in the AMR model as possible. A good example is the difference in flow paths between plates and particles, the two most commonly used

MCM form, in a square regenerator. The number of flow paths is approximately equal to the number of particles or plates in a single cross section of the regenerator which is approximately equal to the ratio of areas between the regenerator to the particles or plates multiplied by the void fraction. If the particles are of random size, but assumed to have on average a square frontal area than the calculation can be made

$$\text{Number of plates} = (1 - \varepsilon) * A_R / A_{Pl} \quad (5-2)$$

$$\text{Number of particles} = (1 - \varepsilon) * A_R / A_{Pa} \quad (5-3)$$

$$A_{Pl} = L_C * L_R \quad (5-4)$$

$$A_{Pa} = L_C * L_C \quad (5-5)$$

where ε is the void fraction of the regenerator, A_R , A_{pl} , and A_{pa} are the frontal areas of the regenerator, plates, L_R , is the width of the regenerator, and L_C is the characteristic length for the particles and plates. Equation (5-6) can be rewritten with a ratio of the particles length to the ratio of the length of the regenerator

$$A_{Pa} = L_C * \frac{L_C}{L_R} * L_R \quad (5-6)$$

Substituting Equation (5-6) into Equation (5-3) and rewriting in terms of the number of plates

$$\text{Number of particles} = (\text{Number of plates})^2 \frac{1}{(1-\varepsilon)} \quad (5-7)$$

The result in Equation (5-7) is that the number of flow paths for particles is greater than the number of flow paths for plates squared. The same ratio holds true for the length dimension of a regenerator as well meaning that the number of flow paths for particles is generally at least two orders of magnitude larger than that of plates resulting in a much closer approximation to the assumptions made in the AMR model.

There is also a special case of flow maldistribution at the wall of a regenerator. Here the formation of flow paths is different because of the interactions between particles and a wall as opposed to between particles. To minimize this effect the ratio of particle to wall flow paths should be much smaller than particle to particle flow paths; effectively equivalent to the ratio of the perimeter of a regenerator to its frontal area. This is by definition at a minimum when the frontal area of a regenerator is a circle as is the case for HA1. Since radial heat leak with respect to regenerator volume is dependent on the surface area through which unwanted heat is lost or gained the same ratio of perimeter to area should be minimized to mitigate this unwanted effect.

Internal demagnetization takes place when the applied H field of regenerator is locally counteracted by the magnetization within the particles that make up the regenerator. The result is that the applied H field which is easily measured and normally used for AMR modeling may not be, on average, what the particles within the regenerator experience. The effective field is a function of both the bulk regenerator cross sectional area and the individual particle shapes. In a theory proposed by Skomski et al. (2007) the ideal bulk shape is an ellipsoid having a relative demagnetization effective of zero. The demagnetization of a circular cross section is low at 0.33 on a scale of 0 to 1. Bjork and Bahl (2013) showed that randomly packed beds having rectangular cross sections when minimized could at best approach a demagnetization of 0.33 showing that a circular cross section has a very low demagnetization, especially relative to functionally achievable shapes.

Temperature measurement in HA1 is designed to avoid heat transfer into the heat transfer fluid coming from sources other than the regenerator on the outlets. The

return fluid temperature measurements are similarly made so that the heat transfer to or from the fluid between measurement and entry into the regenerator is minimized. Figure 5-9 shows a cross sectional area of the regenerator flow path up to the measurement points with the dimensions of the flow paths, and insulation.

The entire assembly shown in Figure 5-9 is made either of plastics or insulation (closed cell polyethylene) with the exception of the magnets. The use of plastics is made possible by the circular cross section of the regenerator. Alternate prototypes with rectangular cross sections were to not be able to withstand the pressures of the system with plastics as the construction materials. For a typical displacement the fluid contained between the MCM and the measurement location represents $1/20^{\text{th}}$ of the total displaced volume. Additionally the thermal mass of the entire flow path up to the measurement (excluding the insulation) is roughly $1/10^{\text{th}}$ of the fluid displaced on typical cycles. Lastly by using unidirectional flow transient heat leak into the flow path is minimized because temperature pulsations are low when compared to reciprocating flow through the flow path. It should be noted that ideally the measurement thermocouples would be placed directly at the end of the regenerators. It is necessary to introduce space between the thermocouples and the magnets due to the rapidly changing magnetic field. If the thermocouples are placed in a region where the change in magnetic flux is high then a voltage will be induced in the thermocouples which is read as an artificial spike in temperature change. The measurement location shown above has no measurable interference from the magnetic fields.

Measurement System

The thermocouple measurements are taken at a data acquisition unit with a common cold junction. The calibrated accuracy is 0.5 K absolute with a relative

accuracy of 0.11 K. The magnetocaloric system typically operates with a temperature change across the heat exchanger on the order of the ΔT or approximately 5 K at maximum for the fields in HA1. To further ensure their accuracy temperature measurements are taken at a speed of 50 Hz over the course of a minimum of ten cycles with the results averaged.

To ensure that the cyclical parameters are being carried out as programmed there is redundant feedback built into the control system for both the piston stroke and the rotational location of the magnets. For both cases stepper motors with internal feedback are used to control movement. The linear position of the fluid pistons is additionally measured through a mechanically coupled linear variable differential transformer (LVDT) having a relative accuracy of 0.25% and a maximum stroke of 9 cm. The rotational location of the magnets has a relative accuracy of 1 degree with the absolute position set during calibration.

Losses

Several of the residual losses that cannot be eliminated are accounted for in the AMR model. The major losses are heat transfer to the cold side, heat transfer radially into the regenerator, and heat transfer axially through the regenerator. Heat transfer along the regenerator is built into the heat transfer correlation as an axial dispersion term, while the other two losses are added to the AMR model as separate energy equation terms based on analytical and measured data.

The area and thermal mass, insulation, and surface area of the cold side are kept constant independent of all other variables. The heat leak is determined through a reverse heat leak measurement. In this method a known load is applied to the cold side heater. The cold side is left attached to the rest of the system, but without cooling or

flow. The temperature of the cold side is allowed to come to equilibrium at several cooling capacities and the temperature difference from cold side to ambient measured. In this way a value of heat leak in terms of Watts per degree temperature difference between cold side and ambient is reliably and accurately measured. Figure 5-10 shows the results of the reverse heat leak measurement.

The test from Figure 5-10 was stopped after three measurements because the temperatures were approaching the damage limit for several of the plastic components. A zero intercept is set to make the trend line more realistic and the resulting slope of 0.042 [W/K] represents the heat that leaks into the cold side.

Heat can also be transferred between the regenerator and ambient. Because the path for heat from the regenerator to ambient is a series of concentric cylinders an analytical estimation of the heat leak can be made in this case assuming that the outer surface of the outer magnet is at the ambient temperature and that the contents of the regenerator are at a constant temperature. From here a 1-D cylindrical heat conduction calculation can be used to determine the heat transferred per unit length and degree Kelvin. Figure 5-11 shows the concentric conduction paths from the material temperature to ambient.

The air gaps between the regenerator bed and inner magnet as well as the inner magnet to the outer magnet are assumed to be quiescent. The resulting resistive network has a heat transfer coefficient of 1.01 W/mK. To confirm this analytical measurement a test was carried out to determine the heat leak rate radially into a bed. The test setup involved embedding a fiber optic cable into the center of a regenerator. The fiber optic cable utilizes a fiber bragg grating at 1 cm intervals along its length to

reflect a laser which is channeled through the fiber. The reflection of the laser is sensitive to the temperature at the grating and can thus be used to measure temperature. For the radial heat transfer test the entire regenerator was brought to a uniform temperature in order to help eliminate heat transfer axially through the bed. The regenerator was then allowed to come to equilibrium with the ambient temperature while the temperature was monitored. The results of the fiber measurement are shown in Figure 5-12 for a few of the centermost measurement points.

The heat transfer rate can be directly inferred from this data by assuming that the fiber measurement represents 1/16th of the regenerator. The thermal mass of each of the temperature points is then calculated and for each time step (temperatures were taken every tenth of a second) the heat transferred is calculated based on the change in temperature for the thermal mass. The heat transfer coefficient is then found

$$U_{\text{rad}} = A_R \left(V * \rho_f * C_{\text{pf}} + (1 - V) * \rho_{\text{MCM}} * C_{\text{pMCM}} \right) * \frac{(T - T_{t-1})}{(T_{\text{amb}} - T)} \frac{1}{t} \quad (5-8)$$

where A_R is the area of the regenerator, ρ is the density, subscript f is the heat transfer fluid, T is temperature, t is the time step size, T_{amb} is the ambient temperature and T_{t-1} is the temperature of the previous time step. Taking the average across all of the time steps and for each of the length increments the measured heat transfer rate radially 1.28 [W/mK] which is higher than the analytical calculation. This higher measured value is used in AMR modeling studies.

Parameter Space

Based on the design of this system a wide range of parameters can be covered. The parameters which effect the AMR modeling studies of this work are described here.

The fluid flow is controlled by the linear actuator which moves the dual pistons. For a set piston diameter the maximum volumetric flowrate is dictated either by actuator maximum speed or the actuator maximum power, and is therefore a function of the pressure drop of the system. The relationship between maximum possible flow rate and system pressure drop is shown in Figure 5-13. The piston diameter also dictates the maximum total volume displaced because of the limited stroke of the linear actuator. A piston diameter of 1.6 cm is used because this represents the maximum ID of the regenerators. With this diameter piston the HA1 prototype is always able to exchange a maximum of the entire fluid volume in the regenerator beds.

Magnetic actuation is limited by the torque and speed capabilities of the motor which rotates the Halbach arrays. In order for the magnets to be completely started and stopped before fluid flow the motor must be able to overcome the inertial mass of the Halbach arrays. In practice the rotational speed of the magnets is kept below the theoretical maximum to help extend bearing life. A full 180° rotation of the magnets corresponding to a 0 to 1.5 Tesla field change can take place as fast as 0.2 seconds.

The magnetic system also limits the size and shape of regenerators that can be utilized in the HA1 prototype. The maximum dimensions of a regenerator are decided by the ID of the inner magnets and the length of uniform field as in Figure 5-4. The minimum dimensions are set by a requirement that any dimension of each stage be at least 10x the dimension of the particles that constitute it. In this way particles of an average diameter of 1 mm must have a stage length of at least 10 mm and a regenerator diameter of at least 10 mm. This requirement helps to minimize the relative size of the wall effects and also is a safe guard against complete mixing between

particles of different stages when using a staged regenerator. The parameter space for regenerator design is shown in Figure 5-14. The aspect ratio in Figure 5-14 is the regenerator length divided by its diameter. The maximum aspect ratio as a function of particle size is shown by the upper solid black line. The minimum aspect ratio as a function of particle size is shown for different numbers of stages by the lines in the legend. The parameter space for a given number of stages is the area between the solid black line and the minimum line for that number of stages. The parameter space is stopped here at 0.1 mm although it could be extended further down. Currently particle sizes under 0.1 mm are hard to obtain because of safety concerns for powdered metals.

The cycle frequency of the HA1 prototype is impacted by every design and operational parameter. As an example it is interesting to consider the maximum frequency for a regenerator which occupies then entire magnetic volume of HA1. This regenerator would have an aspect ratio of 9.6 and a total volume of 30 cm^3 . From Figure 5-14 this regenerator would be limited to a particle size of 0.4 mm for 30 stages, or 1 for 15 stages. The maximum frequency for such a regenerator is shown in Figure 5-15.

The maximum frequency based on the percentage of fluid in the regenerator that is exchanged assuming a void fraction of 40% is shown for different superficial fluid velocities. It should also be noted that for smaller particle sizes Figure 5-13 would need to be taken into account as the superficial velocity may be limited by the pressure drop in the system. Figure 5-15 is shown for the largest regenerator operating at the maximum magnetic field change; smaller regenerators operating at smaller field change can achieve higher operational frequencies.

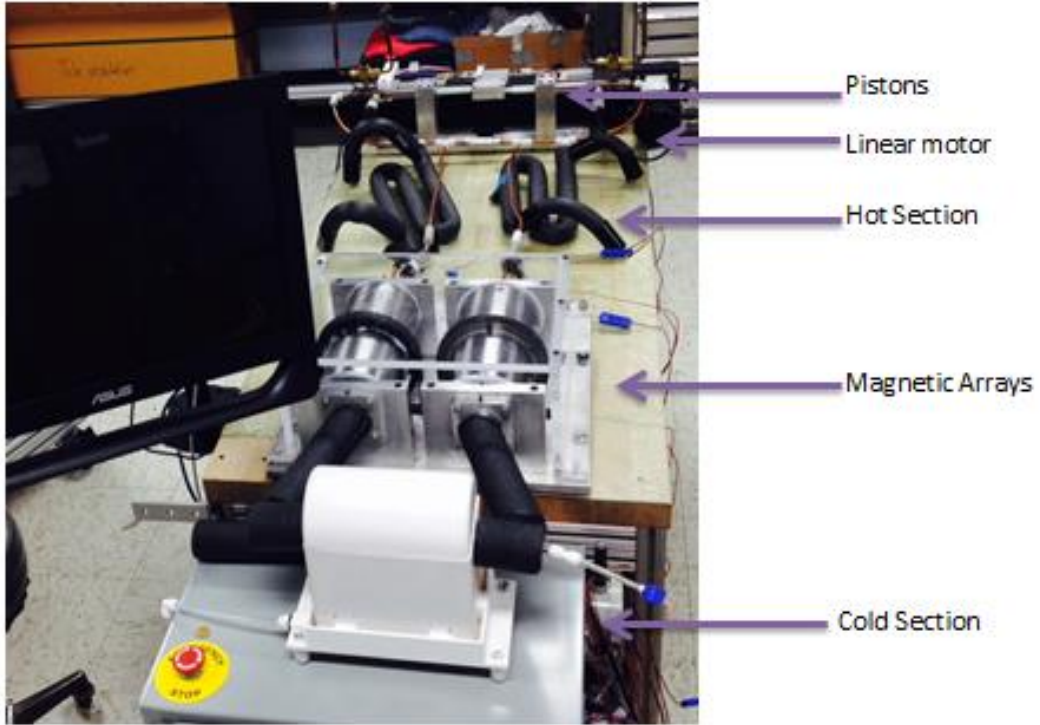


Figure 5-1. Top view of HA1. Michael Benedict. August 20, 2014. Louisville, Kentucky.

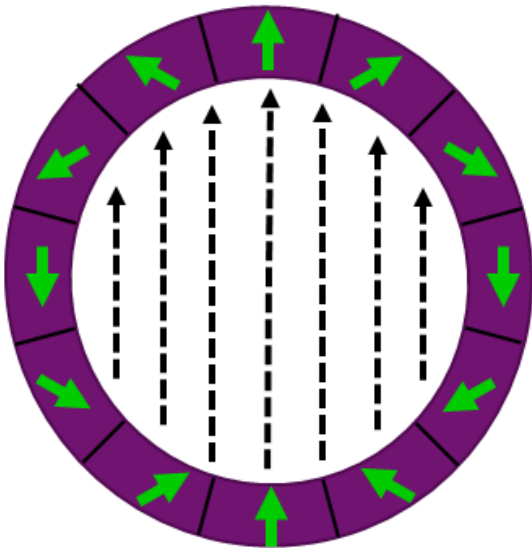


Figure 5-2. Front view of a twelve segment Halbach array.

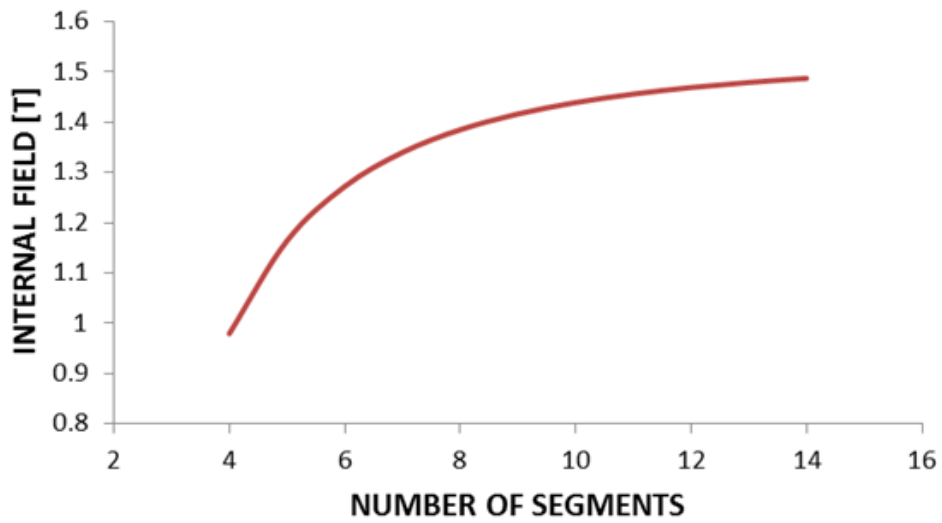


Figure 5-3. The resultant internal flux density for a Halbach array as a function of the number of magnetic segments.

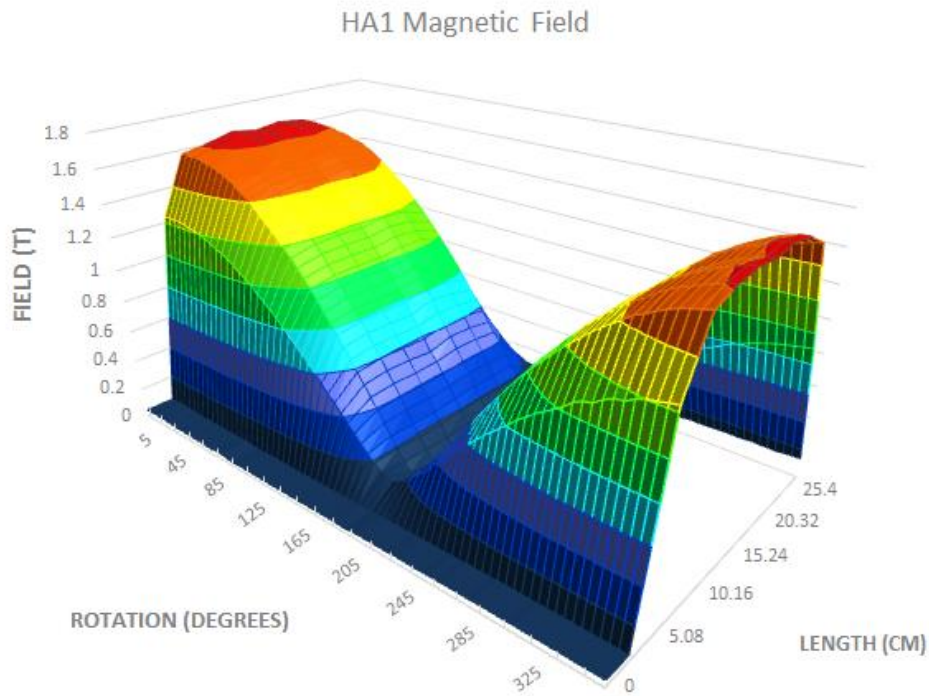


Figure 5-4. Field measurements in three dimensions for one of the nested Halbach arrays.

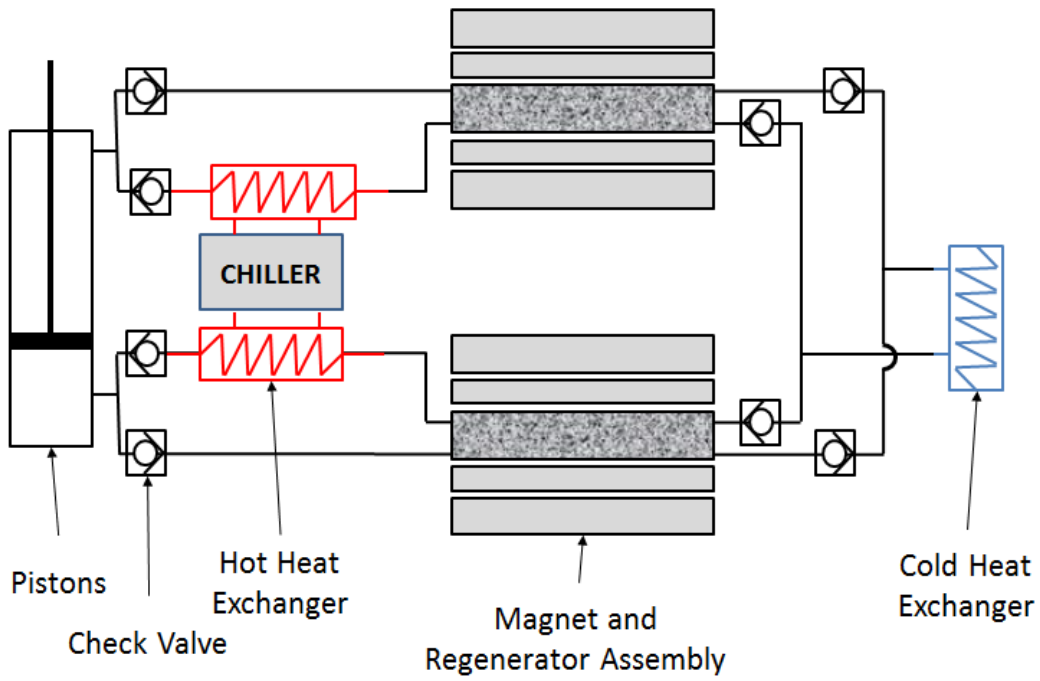


Figure 5-5. Hydraulic schematic of HA1.

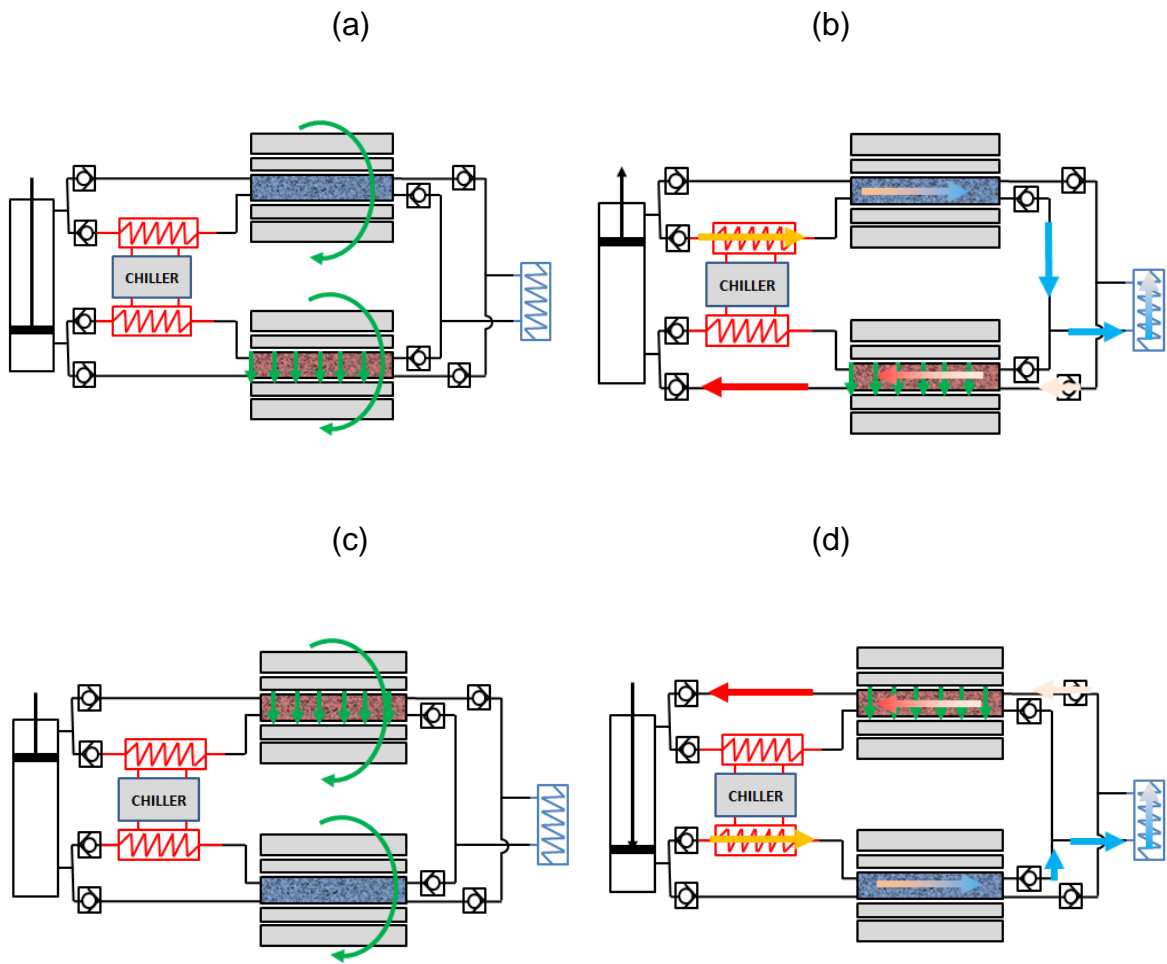


Figure 5-6. A single cycle broken up into steps for HA1.



Figure 5-7. Hot side heat exchanger constructed for low flow. Michael Benedict. September 20, 2014. Louisville, Kentucky.

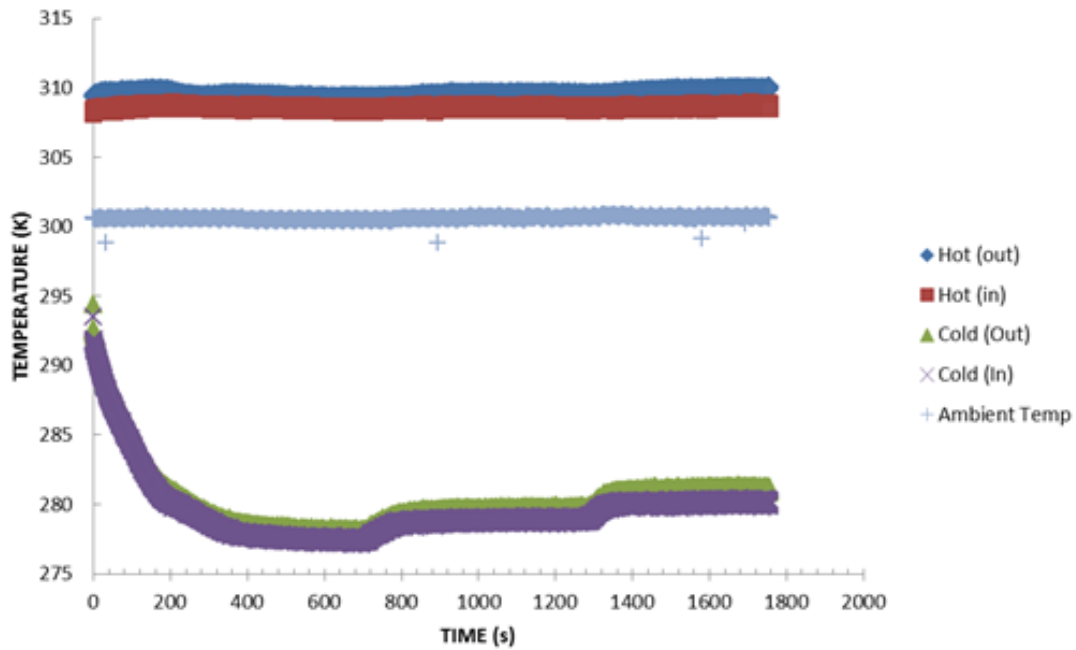


Figure 5-8. An example of temperature output data from HA1.

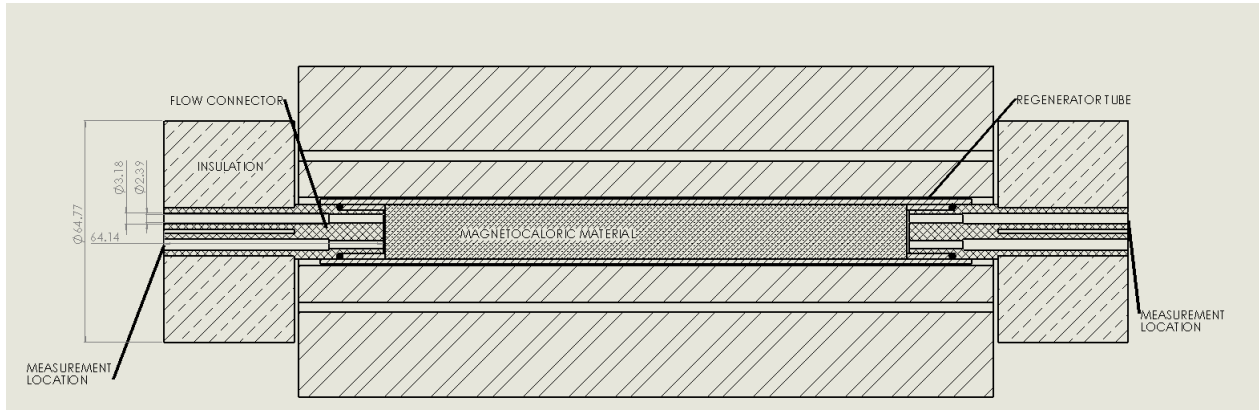


Figure 5-9. Scaled drawing of the critical flow paths for temperature measurement.

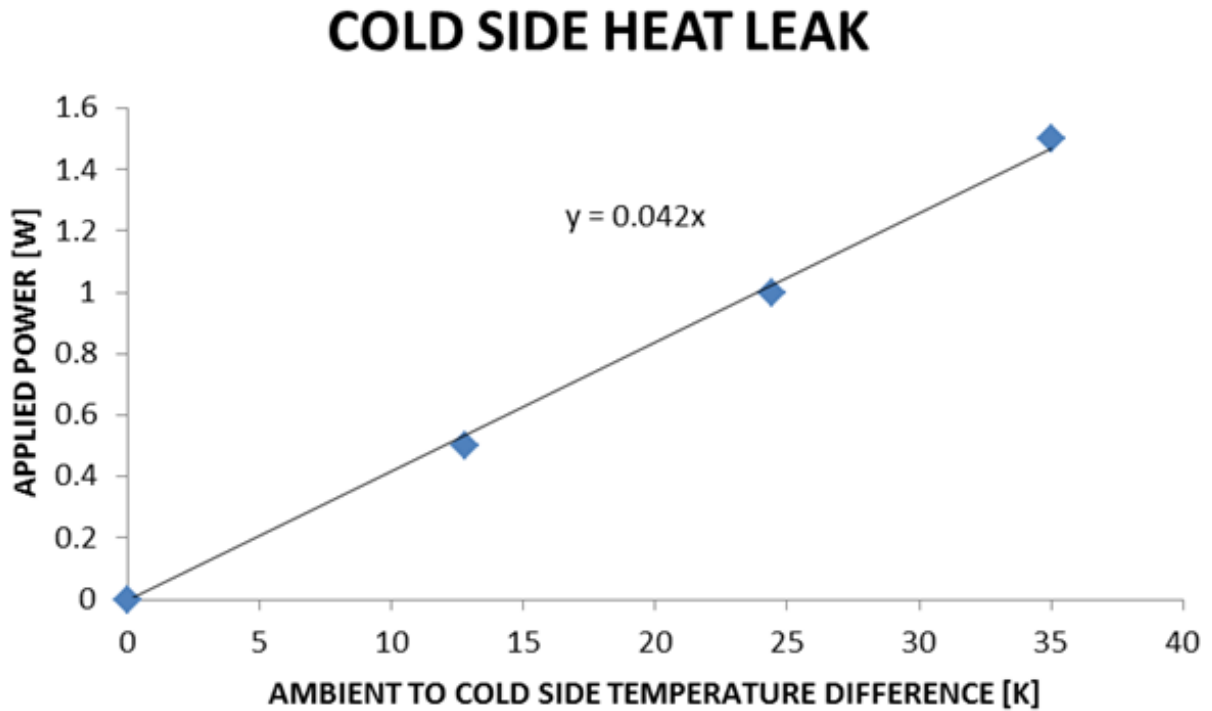


Figure 5-10. Reverse heat leak measurement with linear trend line for an intercept set to zero.

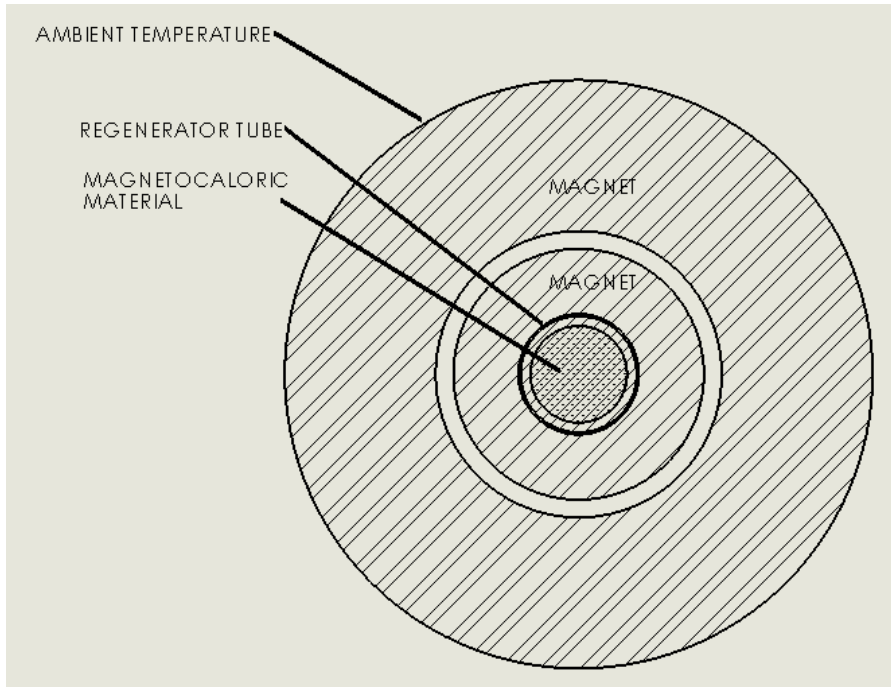


Figure 5-11. Conduction path from regenerator material to ambient.

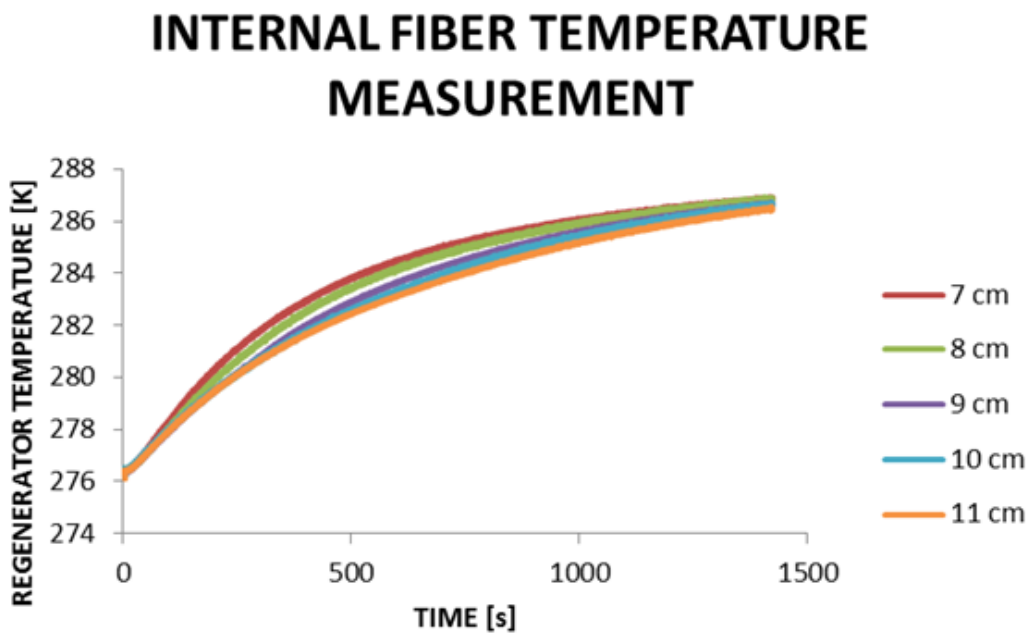


Figure 5-12. Fiber temperatures as a function of time.

Maximum Flow Rate

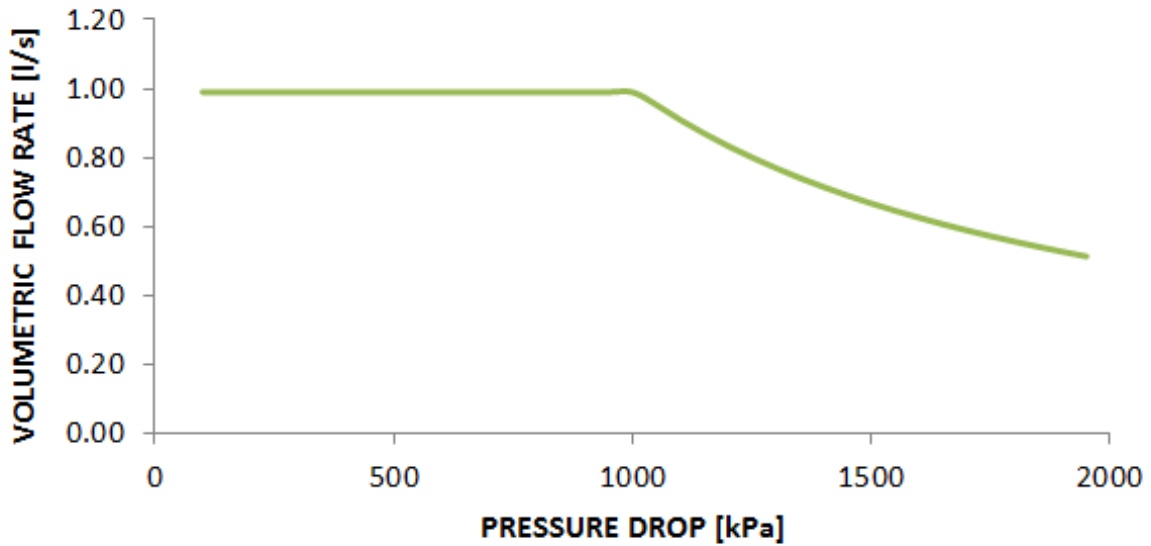


Figure 5-13. HA1 flow rate capability as a function of pressure drop in the system.

REGENERATOR DESIGNS

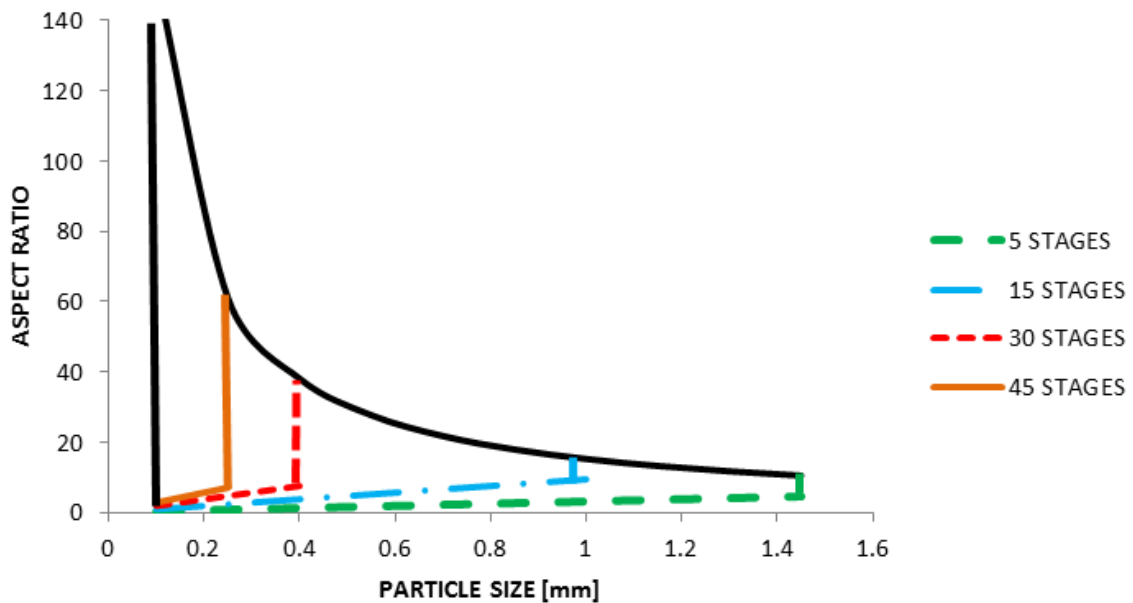


Figure 5-14. Parameter space for regenerator designs in HA1.

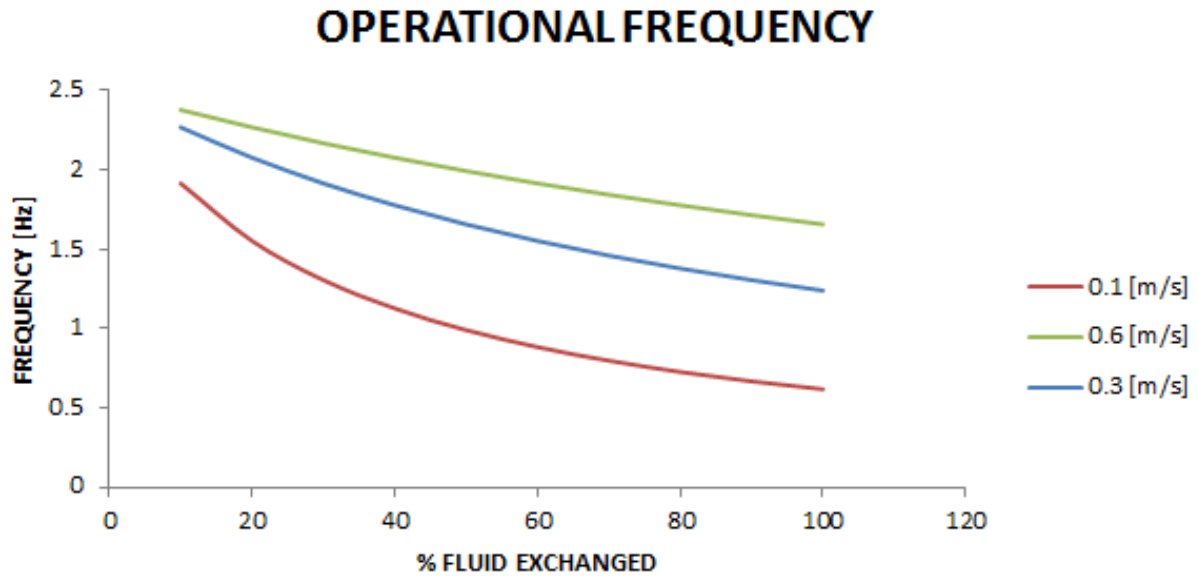


Figure 5-15. Maximum operational frequency for the largest possible regenerator in HA1.

CHAPTER 6 MAGNETOCALORIC MATERIAL MODEL

This chapter reviews details of the magnetocaloric material models (MMM) that were developed. The basic requirements, existing materials and mathematic descriptions of the MMM are reported. Much of the original work involved in this chapter was initially reported in Benedict et al. (2016a).

The main goal of the MMM is to describe the response of first order magnetocaloric materials to changing magnetic fields. Using a model for the magnetocaloric materials enables AMR modeling studies to include the MCM as a parameter instead of an input. It also simplifies the amount of data that is necessary to make accurate predictions. To enable the simplification of data while expanding the scope of AMR modeling studies the materials are described by mathematic models that include parameters representing the physical data. The reduction of error is another potential benefit of an MMM. For this reason the MMM that is developed needs to be thermodynamically consistent. Consistency can be a large source of error in AMR modeling even leading to instabilities.

Magnetocaloric Material Curves from the Literature

Currently there are a handful of FOMT materials that have been reported to have been successfully tested in MCHPs. These are the materials that the MMM must be able to accurately represent. The two families that have a significant MCE near room temperature and are currently being investigated as possible commercial candidates are MnFe and LaFeSi. These are also the materials that have been most extensively tested in prototypes. Reproduced with permission from K. Engelbrecht et al. (2013) and Basso et al. (2015) the specific heat and adiabatic temperature change of MnFeP1-

xAsx and La(Fe-Mn-Si)13-H are shown in Figure 6-1. Though the properties of these first order materials are more concentrated than that of Gd, they are also not as sharp as the properties of a theoretical material as described in Figure 3-2 through Figure 3-5.

General Curve Description

A certain number of coefficients are used to describe a curve shape. With an increasing number of coefficients comes an increasingly complex curve description. The level of complexity that is selected for a given curve is an important consideration. The goal of the current effort was to ensure that the coefficients each describe a property of the MCE curve that is based in some physical phenomenon. Over fitting can lead to curve fits that are not universally useful, and are prone to error when making extrapolated predictions. By way of example the simplified material model introduced earlier which represents a fully first order material needs only five constants to describe all of the thermodynamic properties associated with the MCM as well as the MCE. The simplified material model based on specific heats can be written

$$C_{P0}(T) := \begin{cases} C1 & T < T_{c0} \\ L & T = T_{c0} \\ C2 & T = T_{c0} \end{cases} \quad C_{PH}(T) := \begin{cases} C1 & T < T_{cH} \\ L_H & T = T_{cH} \\ C2 & T = T_{cH} \end{cases} \quad (6-1)$$

In this equation T_{c0} , T_{cH} , L , $C1$ and $C2$ are the constants, and L_H is fully mathematically determined. The constant L is the latent heat for the low field heat capacity, $C1$ and $C2$ are the heat capacities of the low temperature and high temperature states respectively, and T_{c0} and T_{cH} are the low field and high field transition temperatures respectively. Figure 6-2 shows a comparison of an actual material specific heat to the simplified material model. The real material properties are not instantaneous. The latent heat is spread out over a range of temperatures. This spreading of temperatures is, by

definition missing in Equation (6-1). The resulting poor description of a real material is obvious in Figure 6-2.

The simple material model is not useful when describing the measured heat capacity of FOMT MCMs. Typical FOMT materials share a similar curve shape for specific heat and adiabatic temperature change. Figure 6-3 shows the typical characteristics of FOMT materials with the different physical properties assigned a constant. In Figure 6-3 A is amplitude and is related to latent heat, B is base related to the underlying specific heat of the material, W is width and describes the temperature range over which the effect is active, T_C describes the temperature where the maximum effect takes place, and S is skew which describes how the effect is weighted. Though this curve is presented as a specific heat the ΔT as shown in Figure 6-1 or ΔS have similar shapes and can be described by the same parameters.

Magnetocaloric Material Model Form

As a part of the MMM development several MMMs were considered. Of these three were evaluated against actual materials. The best of these three based on several criteria was chosen to complete AMR modeling studies for FOMT materials.

Basic Magnetocaloric Material Model Requirements

There are several characteristics which are desired of the MMMs which help to determine their usefulness. These characteristics are directly related to the goals of increased speed, increased AMR modeling scope, and lower error in modeling. As mentioned previously the MMM should be as simple as possible while accurately describing materials. Simplicity in the MMM helps to increase the speed of AMR modeling, however, the MMM should not be so simple as to introduce error from an inaccurate description of the MCM. The MMM should be parameterized in such a way

that is useful for AMR modeling studies. This means that the constants which are used in the MMM should be related to physical properties of the MCM which can be related back to materials research in a useful way. The MMM also needs to be thermodynamically accurate to reduce the overall error in the AMR model. The thermodynamics of the MCM described in Chapter 3 along with the fundamental laws of thermodynamics cannot be violated.

Magnetocaloric Material Models to be Compared

Three MMMs were developed and compared. The three MMMs are named SechH, Split Lorentzian, and Pearson IV. The formulas are given in the same order:

$$\text{MCE} = \left\{ \frac{\text{sech}\left(\text{asinh}\left(\frac{T-T_c}{W}\right)+S\right)}{W \sqrt{\left(\frac{(T-T_c)^2}{W^2}+1\right)}} + B \right\} \quad (6-2)$$

$$\text{MCE} = \begin{cases} \left\{ \frac{A-B}{\left(\frac{T-T_c}{W}\right)^2+1} + B \right\} & \text{For } T < T_c \\ \left\{ \frac{A-B}{\left(\frac{T-T_c}{WS}\right)^2+1} + B \right\} & \text{For } T \geq T_c \end{cases} \quad (6-3)$$

$$\text{MCE} = A \left\{ 1 + \left(\frac{T-T_c}{W}\right)^2 \right\}^{-S} \exp \left\{ -C \left(\text{atan} \left(\frac{T-T_c}{W} \right) \right) \right\} + B \quad (6-4)$$

The SechH fit is a unique function that was developed solely to be an MMM, the Split Lorentzian is a conditional modification of a normal Lorentzian function, and the Pearson IV (Pearson, 1894) is a statistical distribution. Each of the above functions includes the five constants (A,B,S,W and T_c) which are generally related to resulting curve shape in a manner similar to what is described in Figure 6-3, but not necessarily directly equivalent. Additionally the Pearson IV includes the constant C which is related to the skew.

The Pearson type IV was the first of the three MMMs to be considered. Of the three it is the only fully pre-existing function. This equation is normally used as a probability density function (PDF) in statistics. Though the Pearson IV has the ability to fit data as well as the other two functions it was eliminated for two reasons. Firstly, there is no direct integration for the Pearson IV distribution. The MMM selected to represent the MCE is also intended to represent that specific heat. According to the Maxwell relations the entropy at a constant field can be obtained from the integral of the specific heat divided by temperature with respect to temperature. This means that for the Pearson IV distribution the entropy cannot be directly obtained. Since the entropy is useful for analyzing thermodynamic cycles, and for obtaining ΔT (Pecharsky et al., 2001) this is a disadvantage. Additionally, as previously described, there are five notable physical characteristics for the specific heat and ΔT curves. The Pearson IV distribution contains six constants while providing no additional benefit to data fitting which will be shown later. This additional parameter is unnecessary and makes the relationship to the physical features of the data harder to understand.

The Split Lorentzian fit is based off of the existing Lorentzian or Cauchy distribution. The normal Lorentzian function is symmetric and therefore unable to describe the skew present in magnetocaloric materials. Figure 6-4 shows the results of a Lorentzian fit to actual MCM data. The material in Figure 6-4 is from the MnFe family. The coefficient of determination (R^2) (Ott and Longnecker, 2004) for this fit is 0.85. It will be shown later that the MMMs including skew average 10-15% better. To add the skew necessary for the Lorentzian to describe the MCMs the Split Lorentzian has an additional conditional statement. At temperature equal to T_C the curve gains the

additional skew term S . This S term can have any value greater than zero. Skew less than one represent a material which has a greater width for temperatures below T_C , while S greater than one have a greater width for temperatures above T_C .

The SeCH curve is developed based on trigonometric functions in order to ensure continuity and the ability to directly integrate. This function can be deconstructed from the outer terms to the inner terms to understand better how it was developed. The first function in the numerator is the hyperbolic secant plotted in Figure 6-5. Similar to the Lorentzian function the hyperbolic secant is symmetric. To create skew a second trigonometric function, the inverse hyperbolic sine, is added within the brackets of the hyperbolic secant. This function along with the term S compresses one or the other side of the overall function. Lastly the center term $\left(\frac{T-T_C}{W}\right)$ shifts the center location and increases the width of the overall function. The additional terms in the denominator are normalizing terms that ensure that the function can be directly integrated.

Thermodynamic Data Reconstruction

In order to implement MCMs in the AMR model the MCE must be translated as a function of field and temperature. This can be accomplished several ways as outlined by Equations (3-8) to (3-12). In general two thermodynamic measurements are required to establish the thermodynamic behavior of a material at two different field states.

Although constant temperature entropy change on magnetization change is often reported in the literature it is insufficient without specific heat data and so is a less robust measurement for AMR modeling. The two preferred measurement sets for implementing materials in an AMR model are adiabatic temperature change on

magnetization with zero field specific heat, and zero field specific heat with specific heat at applied field.

Measured data or MMM data is always implemented with only two sets of starting data. A third can be used to check the validity of the reconstruction, but is never used directly for AMR modeling due to inconsistencies that can arise from differences in the measurement techniques used to acquire material data. To implement the thermodynamic properties with specific heat in zero and high field first both sets of data are integrated either directly for MMM data or numerically for measured data. The ΔT can then be found as in Equation (3-8) as the temperature differential between the temperatures at which high field entropy equals low field entropy. On magnetization the ΔT is taken as this differential starting from the low field entropy and on demagnetization ΔT is taken starting from the high field entropy. If ΔT and specific heat are the starting values than entropy at zero field is again found for the integral of specific heat in zero field. Then entropy in field can be found by adding the ΔT to the temperature for the entropy at zero field as in Equation (3-8). With both entropies the ΔT on demagnetization can be found in the same fashion as described for data sets of zero field specific heat and in field specific heat. The in-field specific heat is found from the derivative of the entropy in field.

It is noted that the preferred data set has been shown in the literature to be specific heat at zero and high field K. Engelbrecht et al. (2013). This is due to the ability of these data sets to directly incorporate hysteresis that can otherwise create unrealistic MCE, and because normally this data is created using a single measurement instrument which eliminates the cross instrument error existing in other data sets. In the absence of

specific heat in zero and high field, specific heat in zero field measurements made coming from colder temperatures to hotter temperatures with ΔT measurements should similarly minimize the effects of measurement hysteresis (K. Engelbrecht et al., 2013).

AMR Model Implementation

The coupling of the MMM with the AMR model plays a key role in the overall accuracy, stability and speed of the AMR model. There is normally a tradeoff between accuracy and AMR model speed. This relationship holds true when implementing the MCE for the AMR cycle. As can be seen in Equations (4-1) and (4-2) the MCE needs to be implemented in every time step at every node in the form of specific heat. The adiabatic temperature change is additionally implemented at time steps when the magnetic field change takes place. Both the ΔT and C_p are functions of field and temperature. This means that for a single steady state calculation the MCE may need to be calculated tens or hundreds of thousands of times. To establish the best method for implementing the MCE the MMM has been tested in the AMR model for speed and accuracy.

There are two methods by which the MMM can be implemented in the AMR model. The first is to create a function for the ΔT on magnetization and demagnetization along with the C_p in high and low field. These four quantities are all that the AMR model needs, and the MMM functions created for them can be solved at every point based on temperature and field state. The second method of implementing the MMM is to create four tables one for each of the values mentioned above. The AMR model can then select the appropriate table based on the field state and interpolate to correct temperature to obtain a value.

The method of using lookup tables is used for reasons of speed. In terms of error lookup tables have the ability to be more accurate. There is error associated with both methods. In the direct calculation method because there is no way to directly calculate whichever two functions are not given by the measured data these two functions must be fit to the data obtained by the method described in 5.3.3. Typically R^2 for such calculations is above 98%. The lookup table is essentially the discretized data that the direct functions are derived from. This means that by definition the direct calculations can only be as accurate as the original table of data that they are calculated from. In the limit of an infinitely long lookup table with infinitely small steps in temperature the lookup table would have no errors. In terms of speed the lookup table is clearly faster. This may seem counterintuitive, but in steady state the AMR model only fluctuates between a small range of temperatures at each node. This means that the multiple calculations that are needed can be outpaced by the lookup table without large losses in accuracy.

Using a lookup table means balancing a tradeoff between the fidelity of the table and the speed of the AMR model. Less temperature values means that the interpolations will be prone to more error especially around the peak effects where the gradient is the largest. More temperature values take longer to look up.

To determine the tradeoff in fidelity and error a baseline set of calculations was run. A regenerator was constructed with typical FOMT material properties for the MMM. This regenerator was then tested with varying levels of fidelity in the lookup table. The MCE is implemented with ΔT and C_p driving the thermodynamic properties and the SpLo method to create the data. Parameters were varied in addition to the implementation of the MMM in order to make sure that secondary interactions were

taken into account. The operational parameters of superficial fluid velocity, and flow time and the MCHP parameters of regenerator length, particle size, regenerator area, number of stages, were each set to a high and low level in a full factorial manner. The material span was kept constant with peak ΔT for the hottest stage 30°C above that of the coldest stage which was set to 0°C . The beginning and ending stage Curie temperatures were also kept constant. Other constant parameters include the material conductivity at 5 W/mK , fluid properties (water at 20°C), hot side rejection temperature at 35°C , void fraction at 50% and sphericity of the particles at 0.50. The operational span of the regenerator was varied to create different resulting loads. Table 6-1 shows the levels for each of the varied parameters. Material data is created with the MMM between the temperatures of 60°C and -40°C which should account for all temperatures seen by the regenerator in normal operation for the spans selected. The fidelity of the MMM which is the number of increments at which material data is created is set to five evenly spaced levels between 100 and 1,600 with an additional case having 5,000 increments used as the baseline. The total number of AMR modeling runs was just over 1,000.

With the 5,000 point case taken as the baseline the average error across all of the variables is shown in Figure 6-6. The percent error is calculated by the difference between the baseline case and the current case in the prediction of cooling capacity divided by the baseline case. The maximum percentage error for the predictions is low at just over 0.4%. The error associated with the fidelity of the MMM falls very quickly to nearly zero which is a good indicator that the baseline case of 5,000 points was incremented finely enough.

Figure 6-7 shows average simulation time for each of the levels of fidelity. The simulation time is seen to increase nearly linearly with the increase in fidelity of the MMM. The simulation time from the lowest fidelity to the highest is approximately double while the decrease in error is at best 0.1% on average. The average percentage error and number of temperature points is also shown for each of the parameters from the study in Figure 6-8. The operational span and regenerator length show a clear interaction with the number of temperature points with respect to error. The number of stages and particle size may also have an interaction. This interaction is however only significant below the 500 temperature point level and quickly becomes less important as the number of temperature points increases. From Figure 6-8 it can be seen that above 500 temperature points the average relative error is less than 0.1% for any of the study parameters. Taking into account the linear increase in speed shown by Figure 6-7 the number of temperature points should be set as low as possible keeping error in mind. Because there is an interaction with some of the study parameters the number of temperature points is set at 750 for the remainder of this work. Though this is above the 500 mark which showed the greatest increase in speed relative to decrease in error the extra fidelity will help to ensure that the observed interactions do not lead to unforeseen increases in error for different parameter combinations.

Table 6-1. Study parameter levels.

Length [cm]	Particle Diameter [mm]	Regenerator Area [cm ²]	Superficial Velocity [m/s]	Flow Time [s]	Stages	Span
2	0.2	0.8	0.0254	0.2	31	27
10	1	7	0.127	1	16	22 17

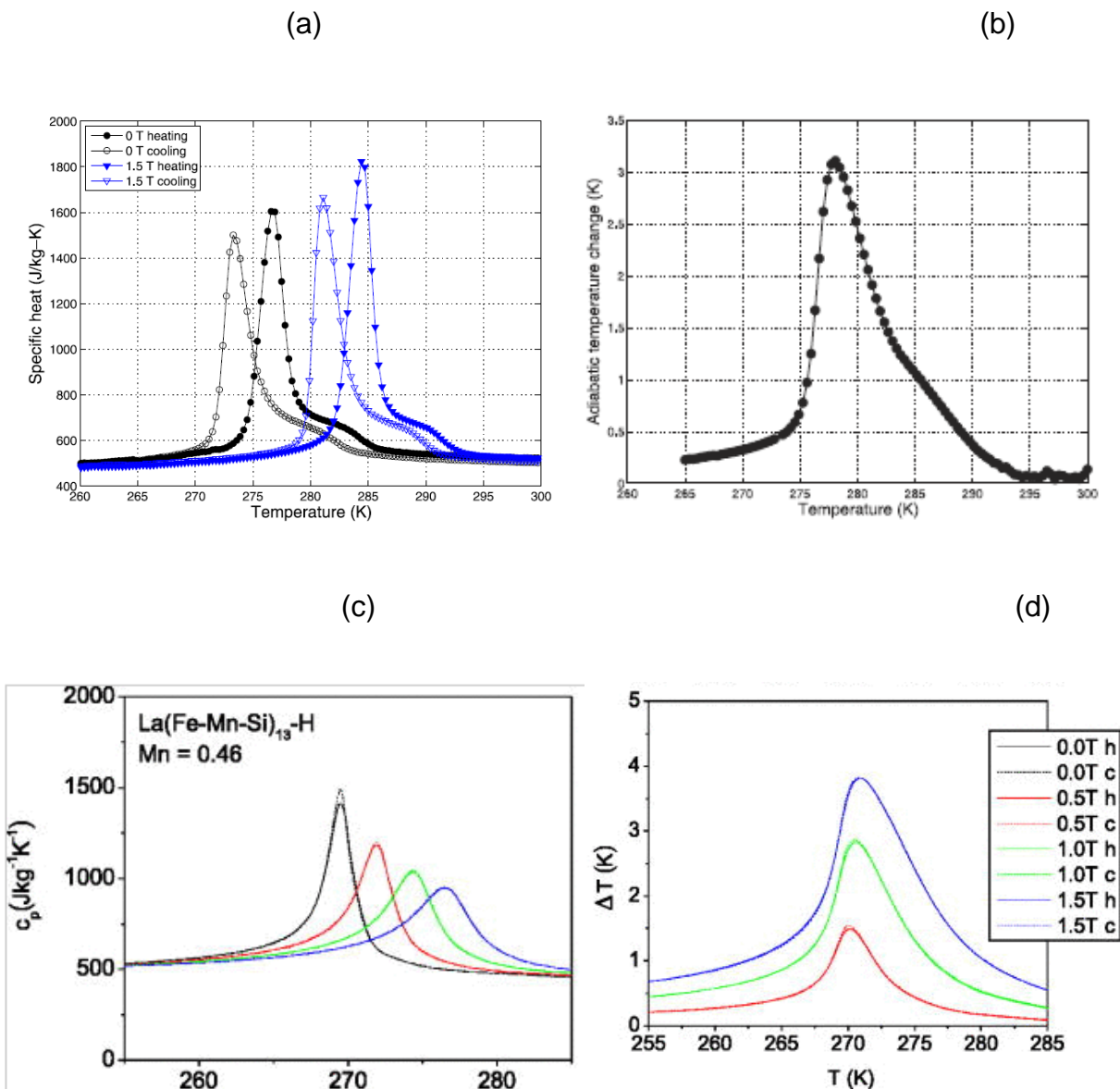


Figure 6-1. Characteristic properties of magnetocaloric materials. (a) Specific heat MnFeP1-xAsx (b) Adiabatic temperature change MnFeP1-xAsx (c) Specific heat La(Fe-Mn-Si)13-H (d) Adiabatic temperature change La(Fe-Mn-Si)13-H.

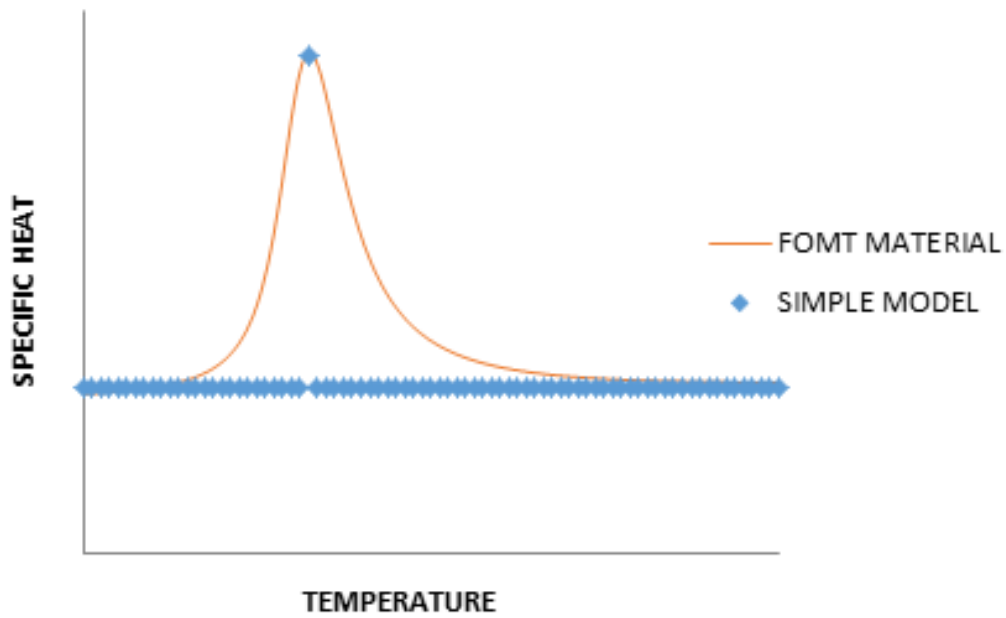


Figure 6-2. FOMT material raw data compared to the best fit with the simple model.

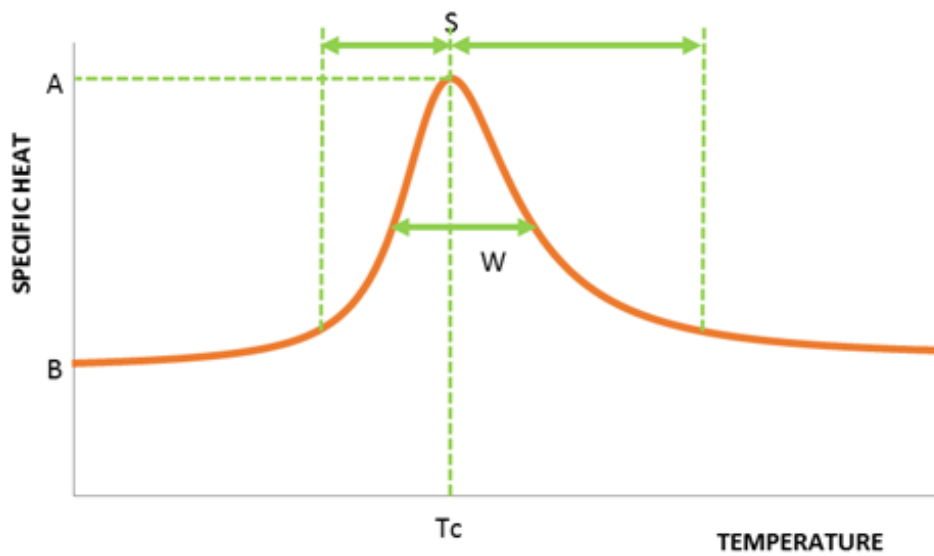


Figure 6-3. FOMT material and the characteristics of these types of curves.

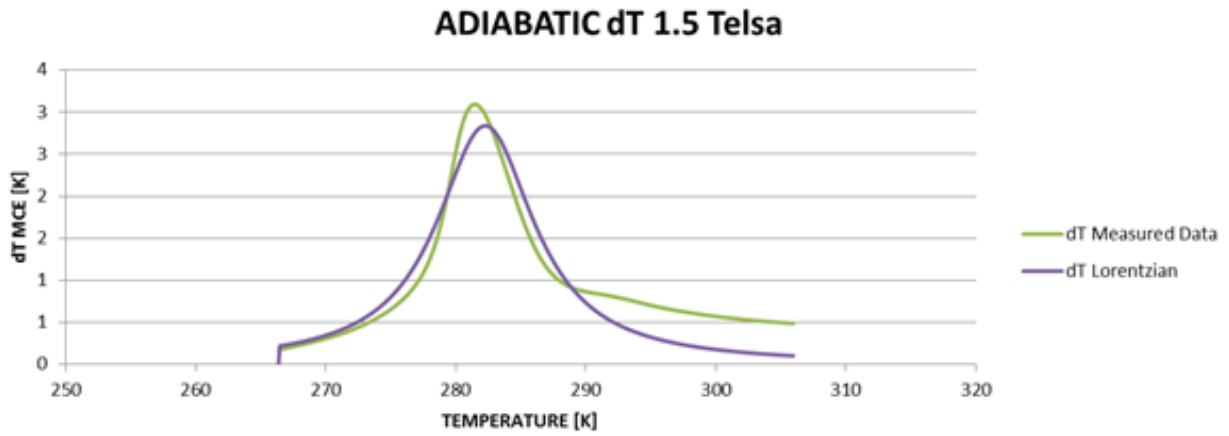


Figure 6-4. Lorentzian fit of FOMT material data

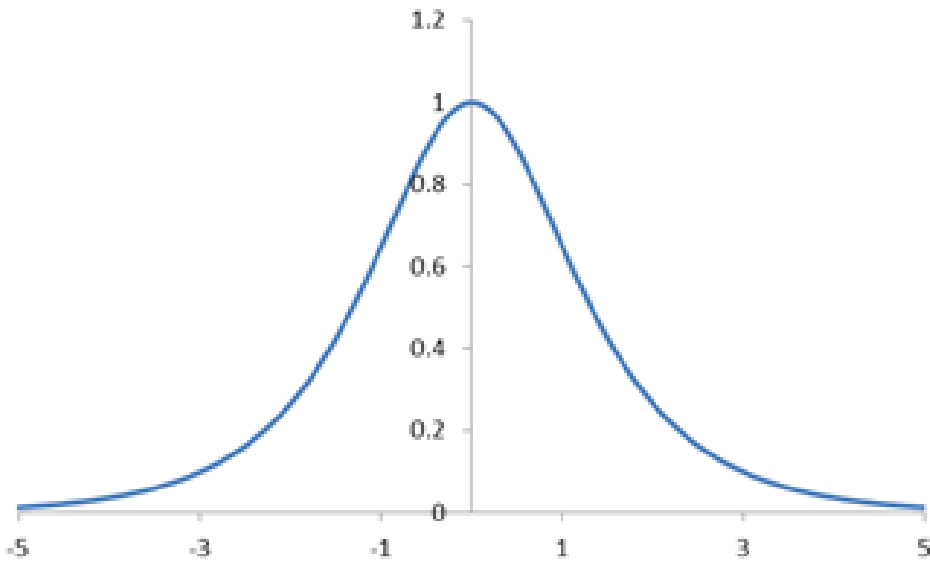


Figure 6-5. Hyperbolic secant function show by itself

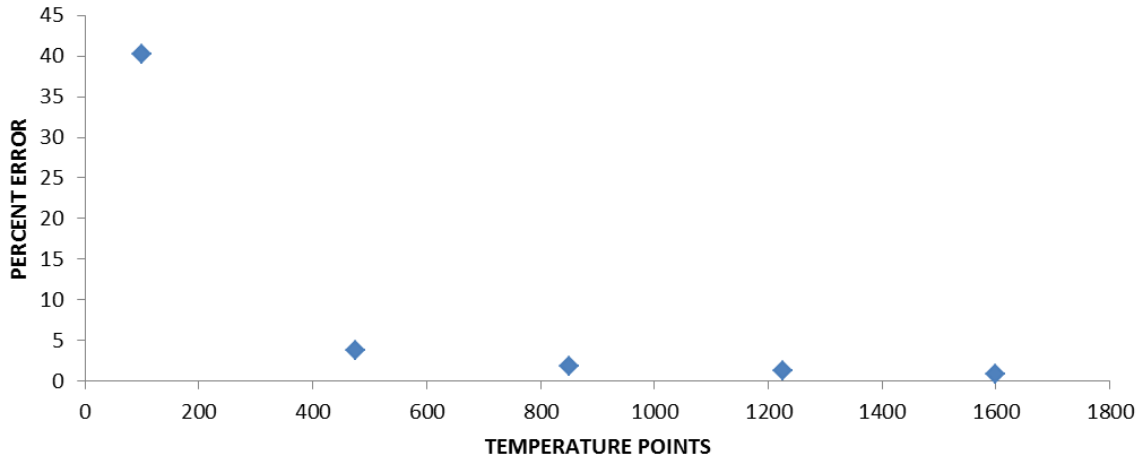


Figure 6-6. Percent error to 5,000 point case averaged across all variables.

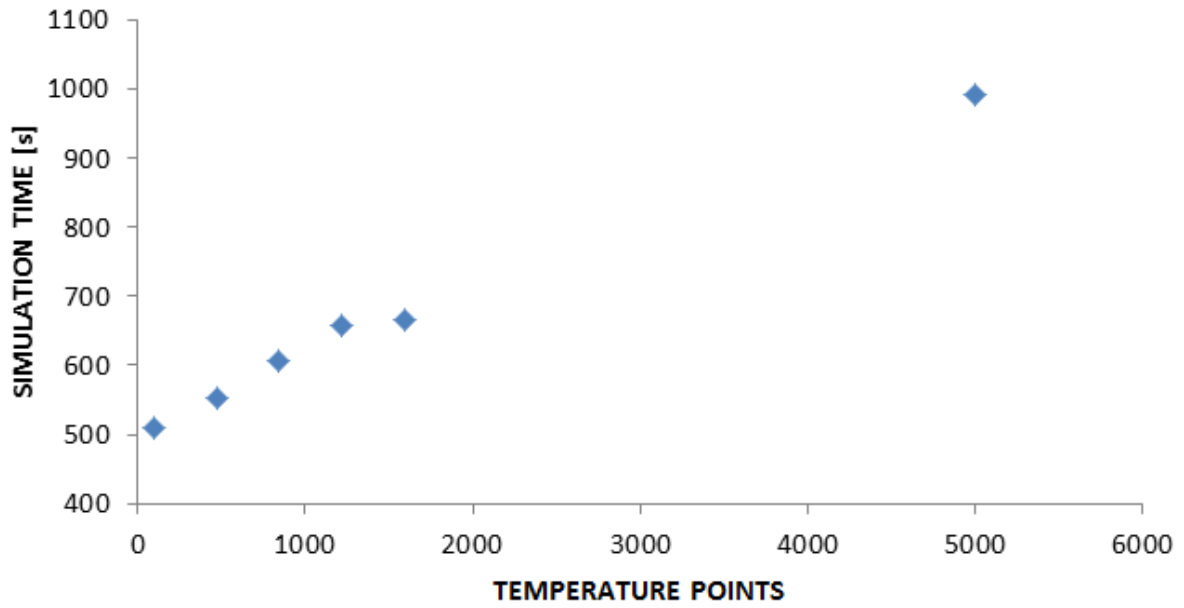


Figure 6-7. Average simulation time based on the fidelity of the MMM.

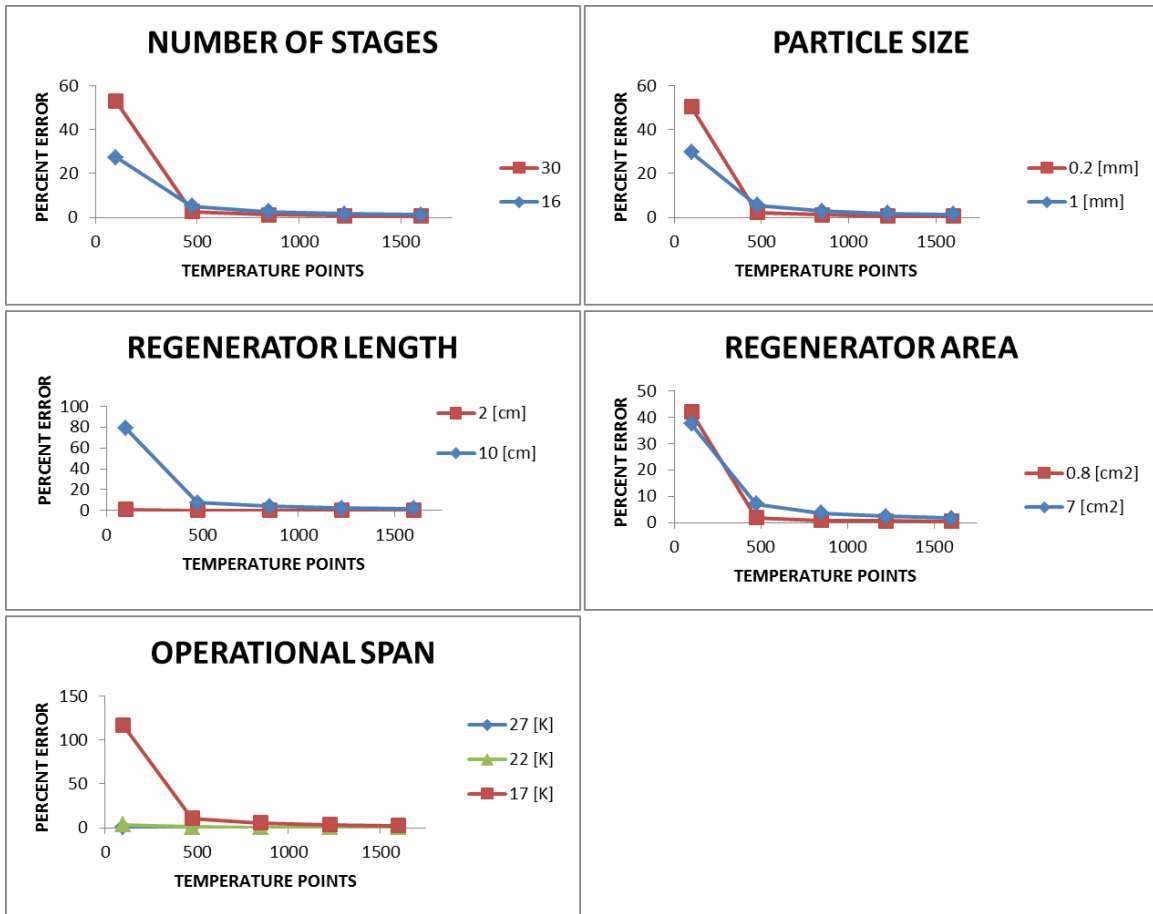


Figure 6-8. Individual parameters from the fidelity study showing error as a function of the number of temperature points used for the MMM.

CHAPTER 7 EXPERIMENTAL VALIDATION OF AMR MODEL AND MMM

This chapter reviews details of two series of experiments and statistical analysis that were used to validate both the AMR model and MMM. Error between AMR model and experiment are reported and a single MMM is selected for the remainder of the work. Much of the original work involved in this chapter was initially reported in Benedict et al. (2016a, 2016c).

The ability of the MMM to represent FOMT materials was confirmed using a number of studies. Statistical methods are used to check the error when the MMM is used to represent measured data in the form of C_p and ΔT . The HA1 prototype is also used to obtain results from cyclical operation of multistage FOMT regenerators. Predictions using measured data for these materials give an indication of the error intrinsic to the AMR model while results using MMM data show the relative error between measured data and MMM data.

Statistical Comparison

Using error minimization the MMM can be fit to measured data. The routine used to model the measured data involves first locating the maximum response. The value of the maximum response as well as the temperature at which it is located give values for A and T_C from Chapter 6. The other constants from Equations (6-2) to (6-4) are found by minimizing the error between the MMM and the measured data. Excel GRG Nonlinear is used to perturbate the values of the constants. To compare the fits the two most widely available FOMT materials mentioned in Chapter 6 were both modeled using the MMMs. The data from over 50 different stages of both the MnFePAs and LaFeSiH were modeled.

Figure 7-1 shows the average R^2 value across the three MMMs. In general the difference in the R^2 values was very small between the MMMs. The average R^2 values for the Split Lorentzian, SecH, and Pearson IV respectively across the measured ΔT data sets were 96.6, 96.1, and 97.6. The fit is similarly high when C_p is modeled using the MMM owing to the similar shape between ΔT and C_p for FOMT materials. Figure 7-2 represents the R^2 values averaged across the three MMMs for the C_p s of the same materials.

Figure 7-1 and Figure 7-2 show that the specific heat is slightly better represented by the MMM than the adiabatic temperature change. In the case of specific heat there seems to be no trend with respect to T_C of the materials and the ability of the MMM to represent the materials. The effect of temperature also seems to be absent from the LaFeSiH material for the ΔT . The MnFePAs seems to show slightly higher agreement between MMM and measured data at elevated T_C values. The slope of the trend is very low, however, indicating that its significance is low.

The other MMM constants do not have an effect on the ability of the MMMs to model FOMT material. Figure 7-3 shows the R^2 as a function of the value of S, W, and A for ΔT of both of the materials, the effect of T_C is shown in Figure 7-1 and there is no B for ΔT . The Split Lorentzian is used for this comparison because the magnitude of S, W, and A are similar allowing them to be shown simultaneously, the trend was similar for the other two MMMs. Figure 7-3 implies that the error between the MMMs and the measured data is mostly random in nature. As with any measurement there is random error or noise inherent to the MCE measurements which no doubt contributes to the random error between the MMM and directly measured data.

The modeling results for the MnFePAs and LaFeSiH do not show a large difference in R^2 values. The average for the MnFePAs was slightly higher at 96.6 while the LaFeSiH average was 96.2. The average R^2 for both materials was well within one standard deviation of the R^2 of the other material meaning that the two FOMT materials are modeled equally well, a fact that can also be discerned from the significant overlap in values from Figure 7-1 and Figure 7-2.

To simplify later studies of the magnetocaloric parameter space a single MMM was selected. The description of what makes a MMM useful from Chapter 6 provides a good guideline for selecting one of the MMMs.

As explained in Chapter 5 the lack of a direct integral and the use of an additional term mean that the Pearson IV was the first to be eliminated. The statistical advantage of this additional term has been shown to be negligible. The Pearson IV may prove to be useful if more complicated FOMT MCE responses are discovered.

The SeCH was specifically designed to be directly integratable. This fit also provides a more complex form of skew than the Split Lorentzian and is a continuous function across the entire temperature range. Only the Split Lorentzian and SeCH are compared going forward as they both have direct integrals of C_P , and none of the MMMs shows a significant advantage statistically to the other when modeling existing FOMT materials.

Experimental Validation

Experimental validation is necessary to determine the ability of the MMM to predict the cyclical performance of a magnetocaloric heat pump. The experimental validation was carried out with the goal of varying the operational and MCHP design parameters in order to evaluate the robustness of the MMMs. The cycle used for the

AMR modeling in this work is kept as an ideal AMR cycle with no MCHP design dependent losses so that the results may be broadly applied to wide variety of designs. With this in mind the experimental cyclical operation is kept as close as possible to the ideal AMR cycle. Practically this means that dwell times are eliminated, magnetization and fluid flow take place completely separately, and there is minimal ramp time for fluid flow. The remaining operational parameters are the superficial velocity of the heat transfer fluid during flow and the amount of fluid exchanged. The time it takes for the material to be magnetized is added as a parameter as this can never actually be instantaneous in a real MCHP. The MCHP parameters include the regenerator and magnetic field design. These two parameter sets are studied using the two FOMT materials from the previous chapter.

Operational Parameters

With set MCHP geometry the operational parameters are the variables that control cyclical performance. Most MCHPs have the ability to vary one or more of the operational parameters; a good example is the overall frequency of a MCHP which is almost always variable. To ensure that the MMM makes accurate predictions over a wide range of these parameters multistage regenerators were constructed using the FOMT material MnFePAs prepared by BASF corporation using the methods described in K. Engelbrecht et al. (2013). The MCHP design parameters which control the regenerator geometry and magnetic field are held constant for this study. Two identical regenerators were used concurrently in the HA1 prototype in order to achieve the maximum possible cooling capacity.

Fourteen BASF alloys were used to create two matching regenerators for the HA1 prototype. The regenerators have an outer diameter of 19 mm and an inner

diameter of 15.9 mm. Each of the regenerators is 152.5 mm long with a material weight of 100 grams evenly distributed between the stages for a total weight of 200 grams. The material was in the form of irregular particles with a mean particle size of 0.5 mm. With the regenerator dimensions set the percent fluid exchanged, regenerator superficial fluid velocity, and magnetization time are varied. A baseline set of test conditions was chosen with each of the run parameters at a value in the middle of the normal testing range. As an assurance that the testing would be well within the normal operating conditions for the material a hot side sweep test was run to establish a hot side temperature that would be low enough to not be a factor in testing. Next a set of cooling capacity span points was run for the baseline. After the baseline was established each of the parameters was independently run at values above and below the baseline to exercise the MMM in a variety of run conditions. A total of 8 separate test sets and more than 30 data points consisting of thousands of measurements were collected. Table 7-1 lists the run conditions for each of the set points along with the cycle time for reference.

The titles from Table 7-1 describe the parameter that was varied; Stroke refers to the piston stroke and effects the percentage of fluid in the regenerator bed that is displaced in each flow period, speed refers to the superficial velocity of the fluid within the regenerator bed, and mag speed is the time that it takes for the magnetic field to transition between high and low field states. Cycle time is given for reference but is fully determined by the other variables.

The initial hot side sweep test was run under zero-load to the cold side. The resulting span indicates at what hot side temperature the regenerator starts to fail. The peak value of ΔT and specific heat are centered around 310.5 K for the hottest stage.

Figure 7-4 shows the span as function of hot side temperature. There is a nearly linear increase in span up until 312 K. At this point the span starts to increase more slowly and eventually peaks at 314.5 K. The heat being rejected for this zero load test is only due to the losses of the MCHP which is very low compared to the eventual values for the test. The hot side for the remaining tests is set below 312 K where the slope started to decrease to ensure that the regenerator will be able to reject heat without being limited by the span of the regenerator. As the load is increased to the cold side this heat is carried through the regenerator and must be rejected on the hot side. With a fixed hot side rejection temperature, and therefore a relatively fixed return temperature, the hot side outlet temperature must rise to compensate. This means that at higher loads and the same rejection temperature the hot side material will effectively work at higher temperatures as can be seen by Figure 7-4.

The remainder of the tests focused on operational parameters. For each test several loads were applied to the cold side of HA1. The resulting span is measured as the difference in temperature of the rejection-side fluid returning to the regenerator to the temperature of fluid returning to the regenerator on the cold side. The cooling capacity span curves for these tests all share a characteristic shape. By way of example Figure 7-5 shows the cooling capacity span curve for the Baseline test. Three points are highlighted for the baseline test that are of use for discussing results. First, point one is the zero-span cooling capacity. At this point the accepting temperature and rejecting temperature are the same and the Magnetocaloric heat pump will produce maximum cooling capacity. Point three is the zero cooling capacity span. Here the MCHP is supporting only loads from losses and the maximum span will be reached. Point two is

referred to here as the “knee”. Between points one and two the cooling capacity is nearly linearly related to the span. This area is referred to here as the “plateau”. Points two and three are connected by a second linear relationship between cooling capacity and span that is steeper than that of the plateau and is referred to here as the “drop off”. These are generalizations that are used to help explain results and do not apply well to second order materials as shown in Benedict et al. (2016).

The results of each measurement were simulated using the AMR model with the BASF material represented by both the SecH and Split Lorentzian MMMs. The parameters for these two MMMs are shown in Table 7-2. As a control the tests were also simulated with the measured BASF data. The results show that the MMMs both are very effective at predicting MCHP performance. Simulations using the measured data are labeled “Raw”, and those using the Split Lorentzian are labeled “SpLo”. Figure 7-6 compares the different tests with the AMR model results. From Figure 7-6 a few general trends are observable. All of the AMR model results over predict the zero-span cooling capacity. The drop off shows better agreement in general than the plateau section of these curves. Within the plateau region the AMR model with MMM data tends to predict lower cooling capacity than the AMR model with measured data. This under-prediction shows better agreement to the experimental results which on average are over-predicted across the entire test range.

The knee of the curve represents the condition where there is a large span with a high cooling capacity. This point is where commercial and other applications are likely to run because they can provide large amounts of cooling capacity at useful spans. The knee can be rigidly mathematically defined as the point where the product of span and

cooling capacity is maximized. For the purposes of comparing AMR model error it is therefore interesting to normalize the error in prediction of cooling capacity at the test condition to the cooling capacity at the knee point. Since only discrete temperature spans and cooling capacities are tested the error has been normalized as the error in cooling capacity predicted divided by test cooling capacity at the highest cooling capacity span product tested. Figure 7-7 compares the average relative errors for the three data types for each of the test conditions. With the exception of the Speed Max and Stroke Max tests the MMMs have a lower magnitude of error than the measured data. In general the two MMMs are very close to each other in terms of error. The average magnitude of error for both the SecH and Split Lorentzian MMMs is about 5%.

One of the most interesting results of this study is the difference in predictions between the MMMs and the measured material data; particularly the fact that the MMMs tend to make better predictions. A related trend in the predictions is that the MMMs make lower predictions in almost all of the tests. A possible explanation for this comes from the rules used to fit the MMMs. While fitting the curves for the ΔT the base value for the curve is set to zero. This forces the functions to trend toward zero for temperatures further from T_C which is not necessarily the case for the measurements. It can be seen in Figure 6-4 that the MCE for the MMM approaches zero much more rapidly than the measured data. For a truly first order material, as in any of the cases from Chapter 3, the magnetocaloric effect is limited to the temperature span between the change in C_P at zero field and some applied field. Outside of this range there is no ΔT . For this reason the MMMs are always set with a zero base for ΔT , and in this set of tests that provided better simulated predictions. This does not create much error in the

statistical measurements because though the MMMs do diverge from the measured data the small relative size of the values in the sections far from T_C where the divergence takes place means that the error is also relatively small for the calculation of the coefficient of determination.

MCHP Design Parameters

The size and shape of the regenerator along with the strength of the magnetic field make up the MCHP design parameters. Though they are categorically separated from the operational parameters they may have as heavy an influence on the performance of the materials in a regenerator as the operational parameters themselves. The use of a MMM was tested at different levels of the MCHP design parameters to ensure that they make accurate predictions over a wide range of values. In this case multiple multistage regenerators were constructed using the FOMT material $\text{La}(\text{Fe}, \text{Mn}, \text{Si})_{13}\text{H}_z$ prepared by Vacuumschmelze GmbH & Co. This FOMT material has good performance and has been shown to be more stable over time than partially hydrogenated materials of the same family (Barcza et al., 2011). The regenerators are of a cylindrical design with the regenerator housing made from Garolite G-10 a composite material of epoxy and fiberglass. The regenerator housing for each of the cases are 1.6 mm thick. Though the focus of this study is the MCHP design parameters a few of the tests also varied the operational parameters to ensure that all of the non-material parameters were examined.

The regenerators were constructed with a constant mass of 80 g. The stages are evenly spaced with a peak adiabatic temperature change for a magnetization from 0 to 1.5 Tesla at 292.6 K for the hottest stage and 283.8 for the coldest. Four regenerators were made in total each varying a single parameter from a baseline case. The

parameters varied in the building of the test regenerators were aspect ratio, particle size, and number of stages. Additionally the magnetic field strength was varied. Table 7-3 contains the exact specification for each of the four regenerators. The high aspect ratio regenerator has an aspect ratio 95% greater than the baseline, the half stage regenerator has an average stage spacing 166% of the baseline, and the small particle size regenerator has particles 44% smaller than the baseline.

The cycle for each of the tests was an AMR cycle with the flow and magnetization fully separate. For all of the tests the magnetization time was kept to 0.2 seconds. There is no dwell between the magnetization and flow. An initial set of numerical simulations was run to determine the operating parameters of displacement per cycle and superficial fluid velocity. Five hundred simulations including all regenerator configurations with the hot rejection temperature at 290 K and the cold acceptance temperature at 283.5 K were run varying only the flow parameters. Figure 7-8 shows the results of this simulation. All of the simulations predicted that higher superficial velocities would lead to greater cooling performance. Displacement showed an optimal value around 7.5cm^3 . Each of the regenerators is run at the predicted optimal displacement of 7.5cm^3 , with a superficial velocity of $.076\text{ ms}^{-1}$ which was the highest value used in the AMR modeling study. The goal of the study was to investigate the magnetic and regenerator subsystem so the magnetic field was also varied as a testing parameter. As shown in Figure 5-4 the magnetic field has for HA1 has been measured as a function of rotation. In order to test at lower applied fields the magnet is rotated only a portion of the way to 180° . The demagnetization and magnetization rotations take place in opposite directions. The smallest possible rotation is always

used. This ensures that the magnetization time is constant on both the magnetization and demagnetization portions of the cycle. This also prevents the regenerator from going through an unneeded magnetization and demagnetization. Table 7-4 summarizes the tests that were carried out.

The operational parameters of Test 1 were selected from the initial study. These parameters are repeated for each of the different beds and for each of the different magnetic field strengths. Additionally the flow parameters are varied at least once for each of the beds. The baseline bed is run at both higher and lower flow velocity along with higher displacement. The half stages bed and high aspect ratio bed are both run at higher fluid velocities which were outside the original AMR modeling range, but should show better performance if the trend from the study is extrapolated. The small particles bed is run with a lower flow rate since very high flow rates with smaller particles can lead to high pressure drops. The chiller which controls the hot side heat exchanger temperature as described in Chapter 5 is set to 291 K for all of the tests.

The parameter varied for Tests 6 and 7 is the high magnetic field. In both cases it has been lowered from the maximum field used for the other tests by changing the rotation of the outer Halbach array. The ΔT data is not available for all field changes so an assumption has to be made in order to create the missing data. It has been shown that a two thirds scaling of the ΔT has a fundamental basis in second order materials and can also be applied to first order materials with accurate results (Smith et al., 2014). The other information set used to construct the material properties is the specific heat at zero field, therefore the scaling of the ΔT is the only adjustment needed to take the

different magnetic field changes into account if the low field for both cases is at zero tesla. To implement the scaling in the measured data a constant multiplier is applied

$$\Delta T_{H2} = \Delta T_{H1} \left(\frac{H_2}{H_1} \right)^{\frac{2}{3}} \quad (7-1)$$

where ΔT_{H2} and ΔT_{H1} are the adiabatic temperature changes due to magnetization for the new field and at the original field respectively. H_2 is the field for which data is not available and H_1 is the field at which the original data was taken. For the Split Lorentzian MMM the need to first multiply the original data by a scaling factor and then refit the MMM parameters can be eliminated by applying the scaling factor directly to the MMM parameter for amplitude which can be shown. Starting from Equation (6-2) which has been shortened to only the temperatures above T_C to simplify the example

$$\Delta T_{H1} = \left\{ \frac{A-B}{\left(\frac{T-T_C}{WS} \right)^2 + 1} \right\} + B \quad (7-2)$$

substituting the modified Equation (7-2) into Equation (7-1):

$$\Delta T_{H2} = \left[\left\{ \frac{A-B}{\left(\frac{T-T_C}{WS} \right)^2 + 1} \right\} + B \right] \left(\frac{H_2}{H_1} \right)^{\frac{2}{3}} \quad (7-3)$$

Since the base for ΔT is always assumed to be zero the B values can be eliminated.

This allows for A to be brought outside the brackets and combined with the two thirds scaling factor

$$\Delta T_{H2} = \frac{A_2}{\left(\frac{T-T_C}{WS} \right)^2 + 1} \quad \text{for } A_2 = A \left(\frac{H_2}{H_1} \right)^{\frac{2}{3}} \quad (7-4)$$

Using this method the original fit constants for the MMM can be retained without the need to modify the measured data and re-fit new parameters. Figure 7-9 shows an

example of a single material ΔT scaled using Equation (7-4) to the magnetic fields used for the study.

Each of the test cases from Table 7-4 were run with a series of applied loads to the cold side. The resulting span is reported as the average temperature of the fluid returning to the regenerator after heat rejection on the hot side, and the average temperature returning the regenerator after heat acceptance on the cold side. Since the HA1 prototype does not have constant flow the temperature measurements are averaged over several cycles of data taken at 50 Hz only during the flow time.

The resulting cooling capacity span curves are very similar to those from the previous study as is expected since both of these material families are very first order in nature. The results of the baseline bed from Test 1 are shown in Figure 7-10. The knee, plateau and drop off can clearly be seen in these results. The linear relationship is further exemplified by fitting linear curves to the two different sections as shown in Figure 7-11. The results from Figure 7-11 can be represented by creating a three part representation for the test results. This representation requires only four inputs: Maximum cooling capacity, plateau slope, knee point span, and slope for the plateau. Equations (7-5) and (7-6) describe the linear simplification of cooling capacity span

$$\text{cooling capacity} = P_M - Sp(m_{pl}) \quad \text{For } Sp < Sp_k \quad (7-5)$$

$$\text{cooling capacity} = P_M - Sp_k(m_{pl}) - Sp(m_{do}) \quad \text{For } Sp > Sp_k \quad (7-6)$$

where P_M is the maximum cooling capacity, Sp is span, Sp_k is the span at the knee, m_{pl} is the slope of the plateau, and m_{do} is the slope for the drop off. This set of equations was written into a Python code which systematically determined the value of the constants by determining initial values of the two slopes from the first two and final two

points of a test set, and taking the maximum cooling capacity as an initial guess of the zero-span maximum cooling capacity. From these initial values final values are determined by iteratively changing the constants and minimizing the square error. This method is useful because for this study there are a large number of points which are hard to directly report the values of. With minimal data loss this method can report for example Test 1 with only four pieces of information. Table 7-5 contains the results of fitting Equations (7-5) and (7-6) to the test results. The max cooling capacity span product is also reported in Table 7-5. It is noted that this is the max cooling capacity span product for the fitted curves and in some cases does not represent actual tested points. The large slope in the drop off area makes it difficult to perform tests precisely at the knee. As will be shown, however, where the knee point is close to a test point the agreement between Equations (7-5) and (7-6) to the test results is very good.

All of the MMMs were shown to have similar ability to represent FOMT materials both statistically and experimentally. As previously described the SecH MMM has coefficients which are not directly related to the values of the MCE which they represent. The SpLo is therefore used for the material modeling in this study and going forward in this work. The SecH may prove to be useful in the future if FOMT materials are found which need a more flexible description of skew.

Each test point was predicted using the AMR model with the MMM data and the measured data for comparison.

Figure 7-12 shows the results of the tests and the AMR model. The average error over all of the test points was 0.69 W for the MMM and 1.9 W for the measured data

with positive error indicating an over prediction of the tests. The average measured cooling capacity for all of the tests was 19 W.

The AMR model results utilizing MMM data again show better agreement than for measured data. The average error is 3.6% of the average test cooling capacity for the AMR model with MMM data and 10% of the average test cooling capacity for the AMR model with measured MCM data. Individual parameters from the study are confirmed to effect the operation of the HA1 prototype. Figure 7-13 shows how magnetic field change, aspect ratio, stage spacing, and particle size impact the test results.

From Table 7-5 Tests 1 and 3 have almost identical maximum cooling capacity span products, but the slope is steeper for the larger particles in both the plateau and drop off. When the results are plotted on the same graph it can be seen that this results in higher cooling capacity for the larger particles in the plateau, but a lower maximum temperature span. Aspect ratio defined as length divided by diameter shows a positive relationship to the maximum cooling capacity span product. This means that within the range of the parameters tested longer lower diameter regenerators show an advantage over shorter larger diameter regenerators. For both stage spacing and aspect ratio tests, higher fluid velocities showed universally improved results which are in accordance with the original predictions of the AMR model. Field change shows a positive and slightly non-linear influence on the maximum cooling capacity span product. For all three cases of field change the minimum field was held constant at the minimum possible field achievable by HA1 which is shown in Figure 5-4 while the maximum field was changed.

Figure 7-12 shows that although the AMR model with the MMM data in general makes good predictions certain parameters were not as accurately modeled as others. The parameters from Figure 7-13 are analyzed in Figure 7-14 in the context of error between AMR model and experimental results. Larger particle size predictions show a larger spread in error while smaller particle predictions consistently over predict performance. Stage spacing tends to show a much lower magnitude of error for the large spacing. Aspect ratio as well has much lower average error at higher aspect ratios. From Figure 7-14 it can be seen that these near zero averages represent very small errors across all of the high aspect ratio and larger stage spacing tests. Field change shows the highest error of all of the parameters. Both of the lower magnetic field cases consistently over predict the results of the tests by an average of 3 Watts. The 1.5 Tesla test case is actually under-predicted by the AMR model. The fit at the knee for the lower field cases is still relatively good with errors of only a few Watts for any of the tests representing 10% or less of the experimental values.

Analysis of Results

Three MMMs for representing FOMT MCMs have been presented. Two of the MMMs were selected to compare statistically to measured data, against AMR modeling results using measured data, and to actual tests carried out on a magnetocaloric prototype with FOMT MCM. The tests varied all of parameters common to magnetocaloric heat pump design and operation. The statistical comparison of the MMMs to measured data showed very high correlations even though it was noted that certain constraints applied to the MMMs force disagreement at temperatures far from T_C . Over the range of tested variables the MMMs were shown to make accurate predictions; normally more accurate than measured data. Error for the MMM based

predictions averaged only a few percent of the test results when compared either to the average cooling capacity or the knee cooling capacity. Certain parameters were seen to show larger error than others, but in these cases the error in prediction was lower with the MMM than the measured data and the error was only on the order of a few Watts for maximum cooling capacity measurements in the tens of Watts. The Split Lorentzian MMM was singled out for future work due to factors explained above, however it was noted that both the SecH and Pearson IV fit have unique advantages that may prove useful in future work. Additionally a simplified method of presenting multistage FOMT MCM results was first presented and then automated. It can be concluded from these studies that the method of using MMMs can accurately predict the performance of FOMT MCMs over a wide range of commonly varied magnetocaloric heat pump parameters.

Table 7-1. Test parameters for the HA1 MCHP.

Test	Rejection Temperature [K]	% Exchanged	Superficial Velocity [m/s]	Magnet Change Time [s]	Cycle Time [s]
HS Sweep	300 to 317	18.3	0.058	0.21	1.37
Baseline	308.7	18.3	0.058	0.21	1.37
Stroke Min	308.7	10.0	0.058	0.21	0.93
Stroke Max	308.7	26.7	0.058	0.21	1.80
Speed Min	308.7	18.3	0.041	0.21	1.79
Speed Max	308.7	18.3	0.076	0.21	1.14
Mag Speed Min	308.7	18.3	0.058	0.29	1.53
Mag Speed Max	308.7	18.3	0.058	0.17	1.29

Table 7-2. MMM Parameter values.

Split Lorentzian										
Stage	ΔT Amp	ΔT T_C	ΔT Skew	ΔT Width	ΔT Base	C_P Amp	C_P T_C	C_P Skew	C_P Width	C_P Base
Stage 1	2.99	310.9	2.06	3.48	0.00	1463	311.0	0.68	3.07	539
Stage 2	3.02	308.1	1.82	3.71	0.00	1212	307.4	0.73	2.71	509
Stage 3	2.94	306.8	1.73	3.08	0.00	1308	306.0	0.74	2.59	553
Stage 4	3.08	303.8	1.79	3.30	0.00	1284	303.1	0.81	2.46	496
Stage 5	3.08	302.1	1.53	4.09	0.00	1263	302.1	0.42	3.87	538
Stage 6	2.95	299.0	1.95	3.29	0.00	1359	299.0	0.65	2.48	461
Stage 7	2.77	297.2	2.05	3.09	0.00	1528	297.1	0.78	2.12	508
Stage 8	2.97	293.6	2.28	2.80	0.00	1543	294.1	0.56	2.74	517
Stage 9	3.49	292.6	2.32	2.91	0.00	1611	292.2	0.85	1.68	493
Stage 10	2.98	289.4	2.04	3.23	0.00	1321	289.0	0.88	2.39	477
Stage 11	2.74	287.3	2.09	3.74	0.00	1287	287.0	0.96	2.27	455
Stage 12	2.67	284.9	2.12	4.30	0.00	1328	285.4	0.65	3.04	458
Stage 13	2.37	283.7	1.76	4.13	0.00	1196	283.9	0.67	3.09	454
Stage 14	2.81	280.9	2.26	2.91	0.00	1612	280.9	0.78	1.95	509
Sec H										
Stage	ΔT Amp	ΔT T_C	ΔT Skew	ΔT Width	ΔT Base	C_P Amp	C_P T_C	C_P Skew	C_P Width	C_P Base
Stage 1	0.051	309.3	-0.98	4.18	0.00	7.61	311.5	0.52	2.40	1.74
Stage 2	0.051	306.7	-0.79	4.44	0.00	5.34	307.8	0.43	2.23	1.66
Stage 3	0.040	305.8	-0.70	3.69	0.00	5.53	306.4	0.42	2.15	1.81
Stage 4	0.046	302.6	-0.75	3.98	0.00	5.80	303.4	0.32	2.18	1.64
Stage 5	0.052	300.9	-0.62	4.68	0.00	6.48	303.0	1.16	1.97	1.79
Stage 6	0.047	297.6	-0.89	3.95	0.00	6.13	299.3	0.56	1.89	1.54
Stage 7	0.043	295.9	-0.94	3.77	0.00	6.44	297.3	0.34	1.82	1.71
Stage 8	0.046	292.2	-1.09	3.41	0.00	7.41	294.5	0.72	1.87	1.76
Stage 9	0.057	291.1	-1.09	3.59	0.00	5.97	292.3	0.22	1.54	1.69
Stage 10	0.050	288.0	-0.93	3.93	0.00	6.54	289.2	0.21	2.22	1.65
Stage 11	0.054	285.5	-0.97	4.54	0.00	6.45	287.1	0.11	2.22	1.59
Stage 12	0.062	282.8	-1.01	5.15	0.00	7.62	285.9	0.59	2.30	1.61
Stage 13	0.047	282.1	-0.80	4.83	0.00	6.71	284.4	0.57	2.37	1.61
Stage 14	0.047	279.5	-1.06	3.57	0.00	6.83	281.1	0.34	1.69	1.81

Table 7-3. Specification for each of the regenerators tested.

Name	Length [cm]	ID [cm]	Stages	Mean particle size [mm]
Baseline	9.75	1.59	10	0.9
High aspect ratio	15.24	1.27	10	0.9
Half stages	9.75	1.59	6	0.9
Small particles	9.75	1.59	10	0.5

Table 7-4. Parameters for each of the test cases. Magnet rotation refers to the rotation of the outer magnet relative to the stationary inner magnet with 0 degrees being the minimum field.

Test name	Regenerator	Displacement [cm ³]	Velocity [cm.s ⁻¹]	Magnet Rotation	Rotation Speed [Hz]	High Field [T]	Cycle Frequency [Hz]
Test1	Baseline	7.54	7.62	180	2.5	1.5	0.69
Test2	Baseline	10.05	5.08	180	2.5	1.5	0.41
Test5	Baseline	7.54	11.43	180	2.5	1.5	0.90
Test6	Baseline	7.54	7.62	90	1.25	1.1	0.69
Test7	Baseline	7.54	7.62	126	1.75	1.4	0.69
Test3	Small particles	7.54	7.62	180	2.5	1.5	0.71
Test4	Small particles	7.54	5.08	180	2.5	1.5	0.53
Test10	Half stages	7.54	7.62	180	2.5	1.5	0.71
Test11	Half stages	7.54	11.43	180	2.5	1.5	0.90
Test12	High aspect ratio	7.54	7.62	180	2.5	1.5	0.71
Test13	High aspect ratio	7.54	11.43	180	2.5	1.5	0.90

Table 7-5. Results from tests. Max cooling capacity and cooling capacity span product are both determined from the intersection of the two linear fits and may not correspond to measured points.

Test name	Regenerator	Max Cooling Capacity [W]	Slope Plateau [W/K]	Span at Knee [K]	Slope Drop Off [W/K]	Cooling capacity span Product [W.K]
Test1	Baseline	36.5	-1.20	7.0	-6.95	196
Test2	Baseline	28.5	-0.77	7.2	-6.47	165
Test5	Baseline	37.1	-0.90	7.6	-11.47	229
Test6	Baseline	18.0	-0.66	8.0	-6.73	102
Test7	Baseline	27.4	-1.12	7.7	-9.64	145
Test3	Small particles	32.1	-0.99	8.1	-6.14	195
Test4	Small particles	24.2	-0.75	7.9	-6.53	145
Test10	Half stages	34.3	-1.03	7.8	-9.25	205
Test11	Half stages	39.2	-1.21	8.7	-14.66	249
Test12	High aspect ratio	37.1	-1.39	7.3	-7.16	204
Test13	High aspect ratio	43.5	-1.24	7.3	-9.24	252

Adiabatic Temperature Change

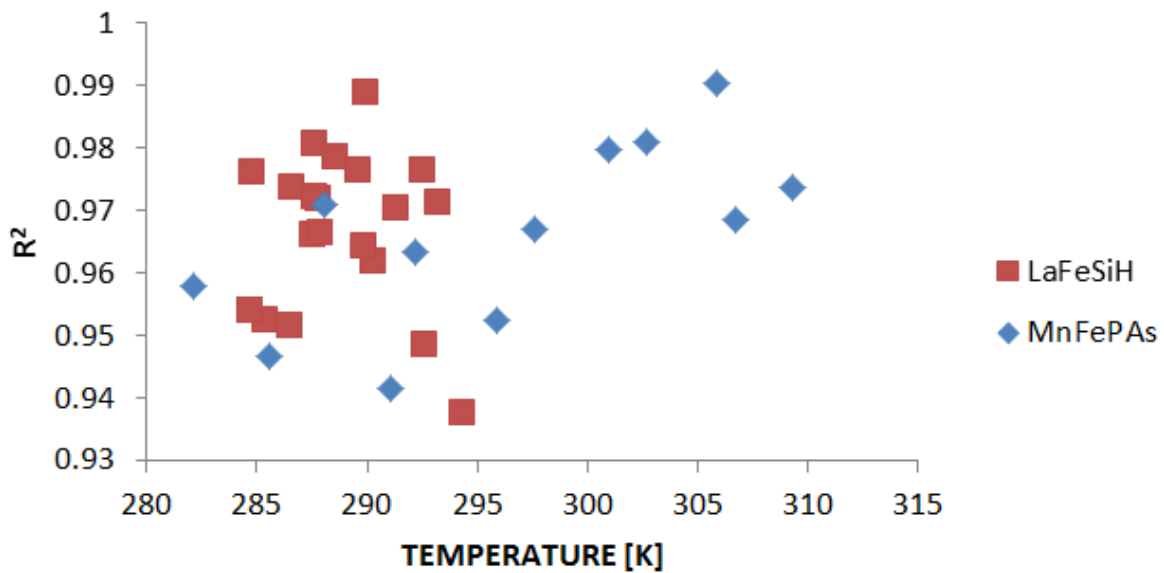


Figure 7-1. Average coefficient of determination for two FOMT materials represented by the MMMs.

Specific Heat Zero Field

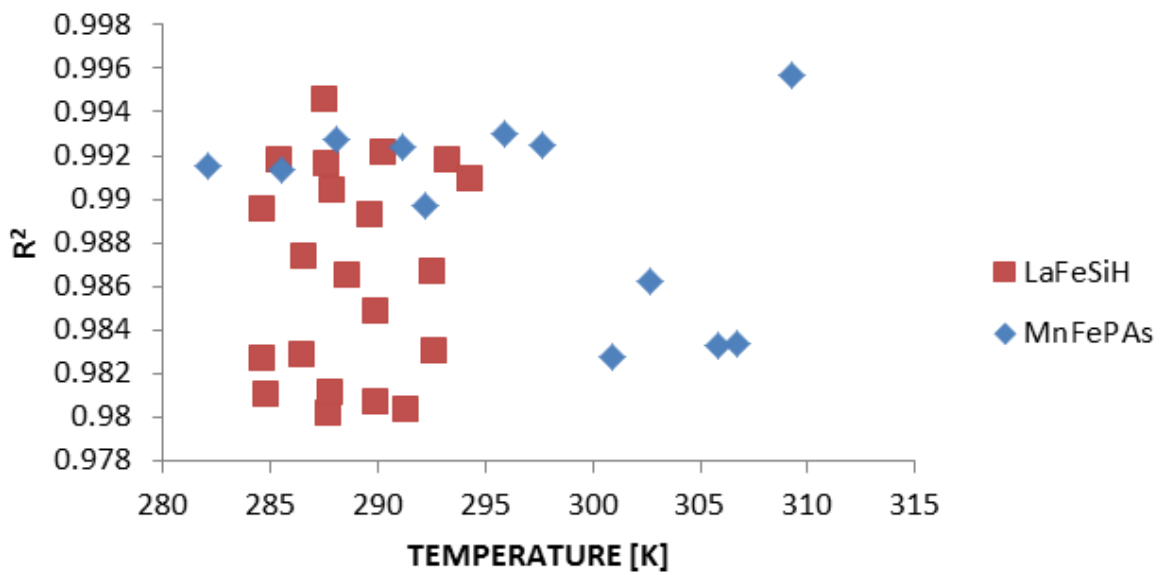


Figure 7-2. Average coefficient of determination for specific heat

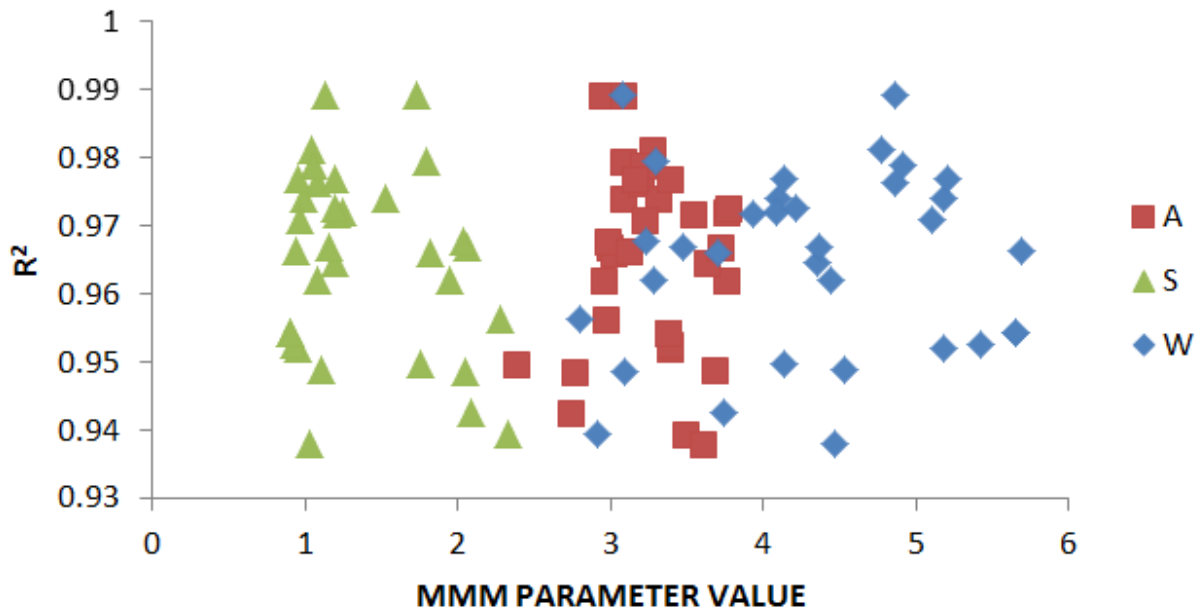


Figure 7-3. Coefficient of determination compared to the value of the MMM constants.

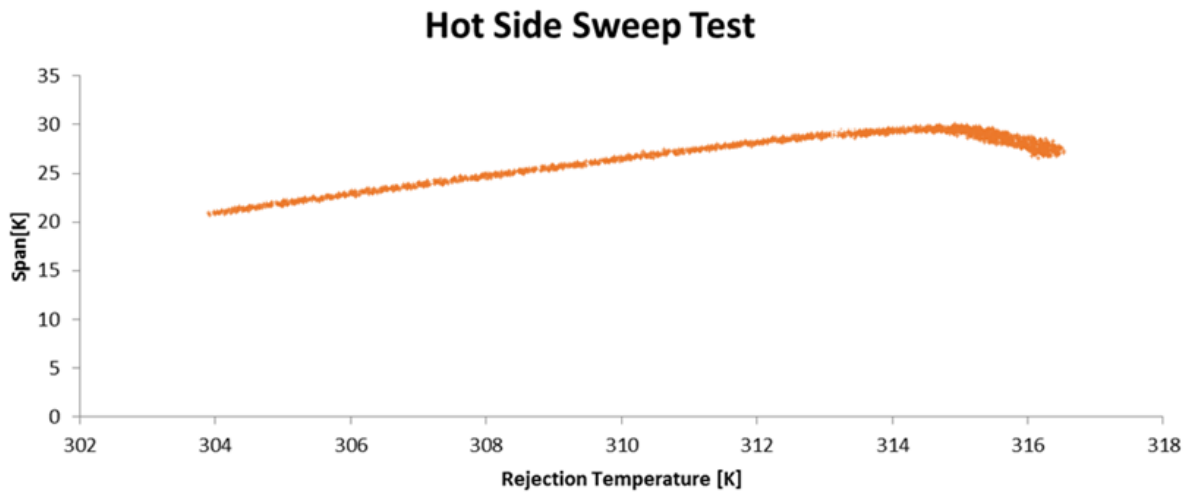


Figure 7-4. Results of the hot side sweep test. Span shown as a function of rejection temperature.

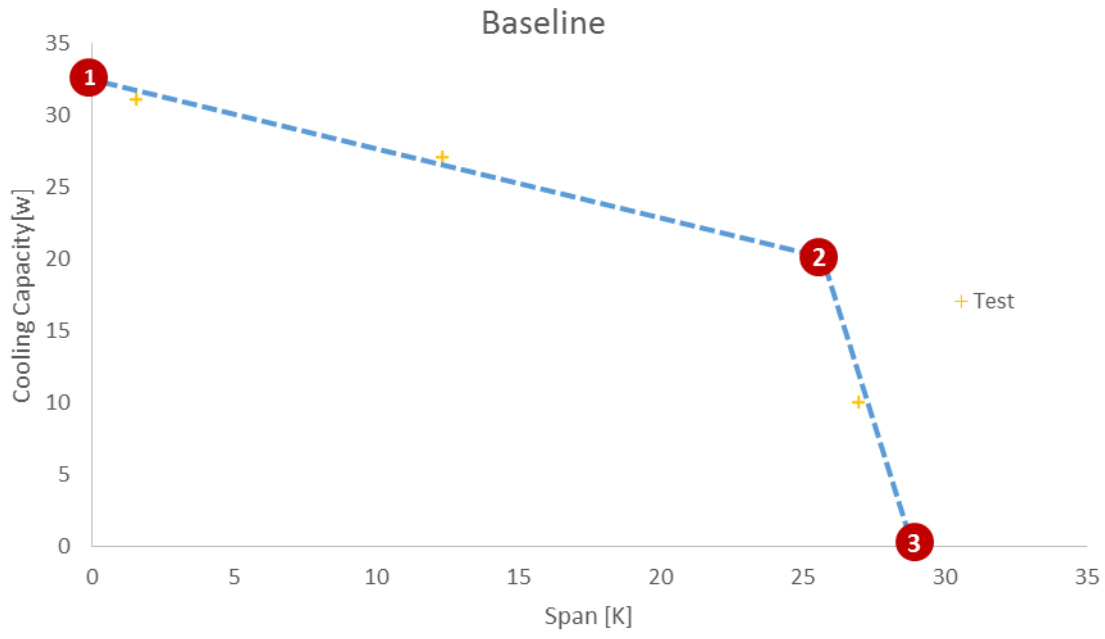


Figure 7-5. Results of the Baseline test.

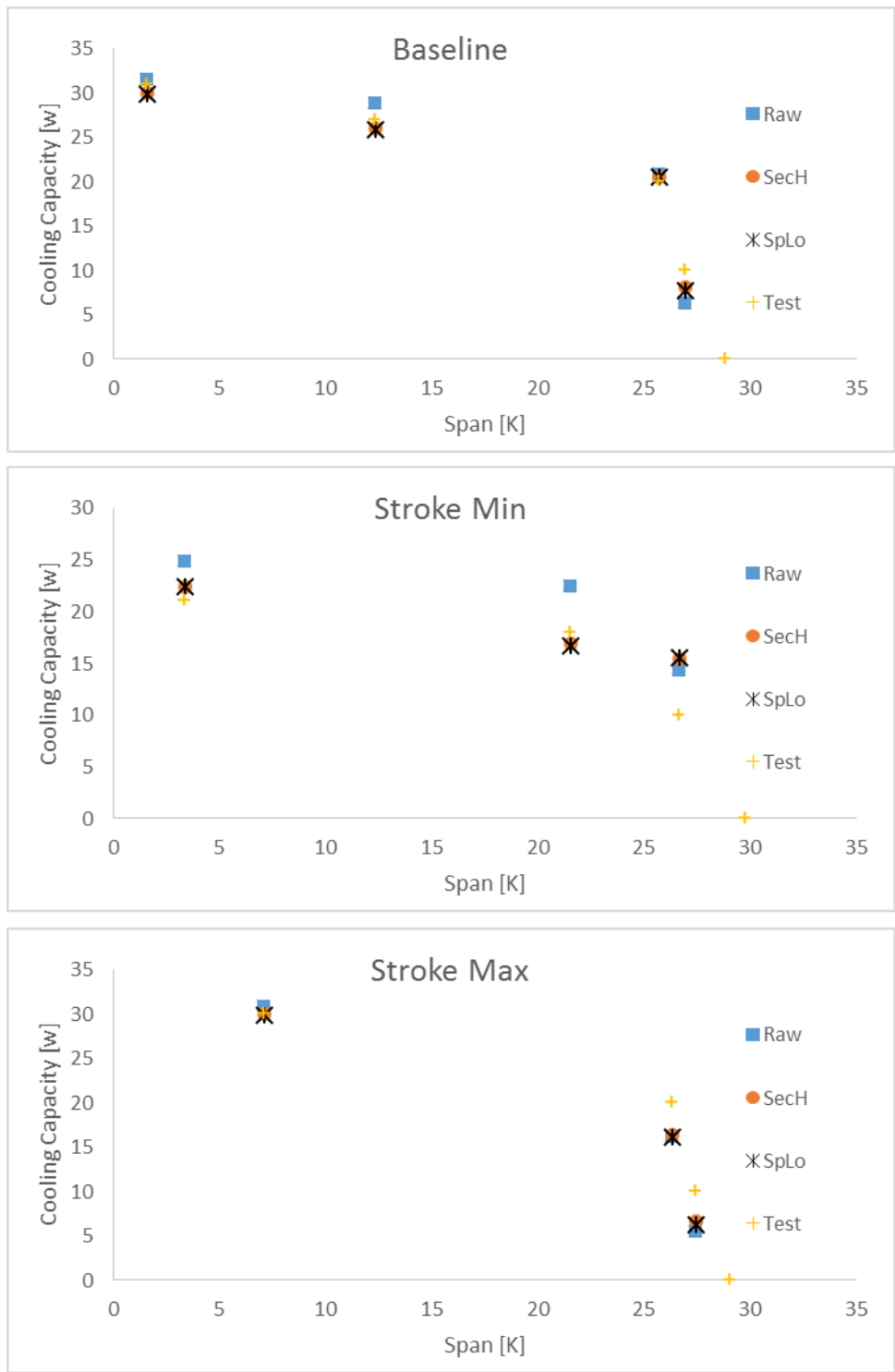


Figure 7-6. Comparison of test to simulated results using both measured data and MMMs.

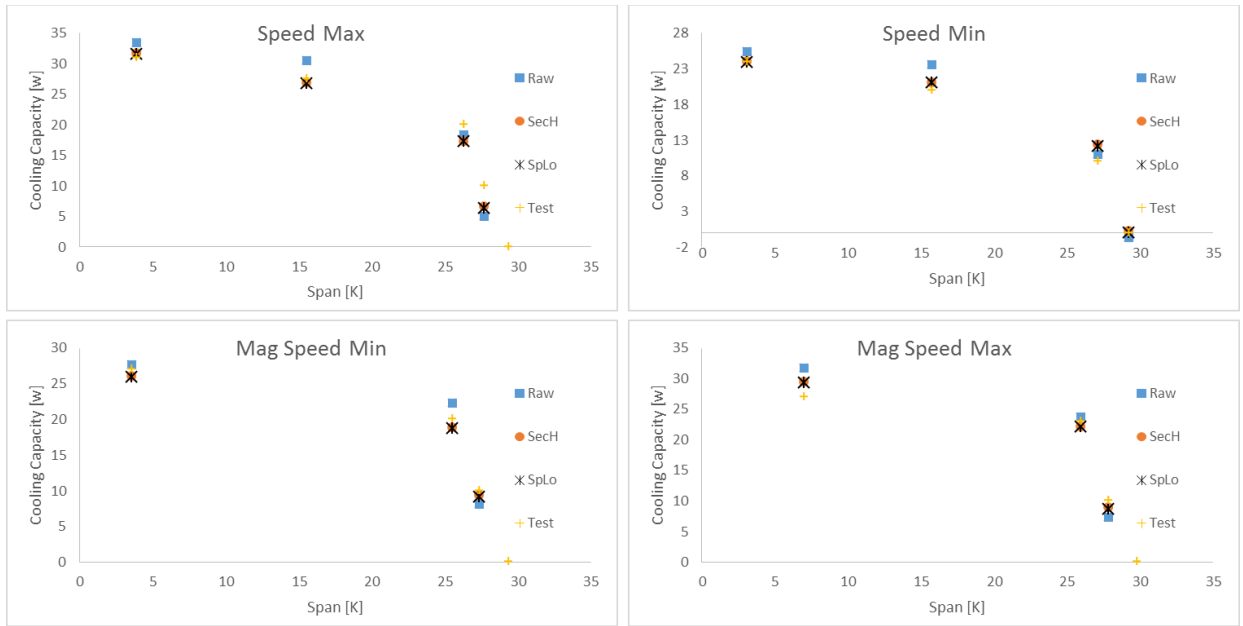


Figure 7-6. Continued

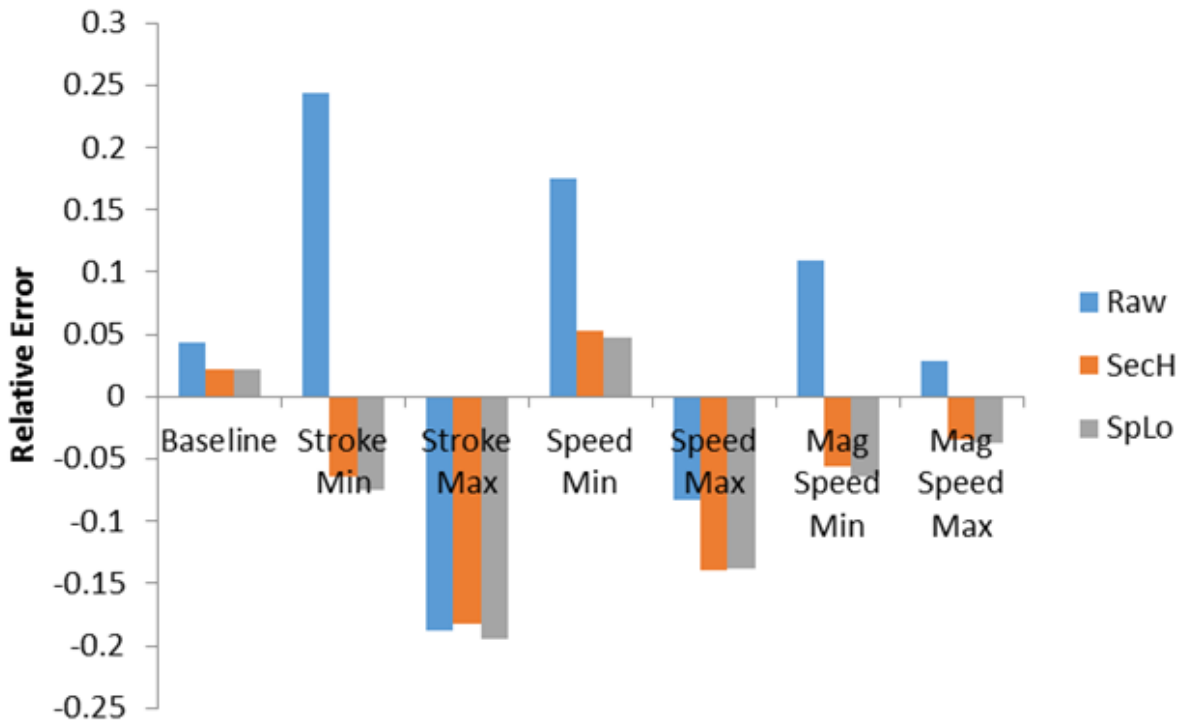


Figure 7-7. Relative error at the maximum product of cooling capacity and span. Positive error represents over prediction and negative under prediction.

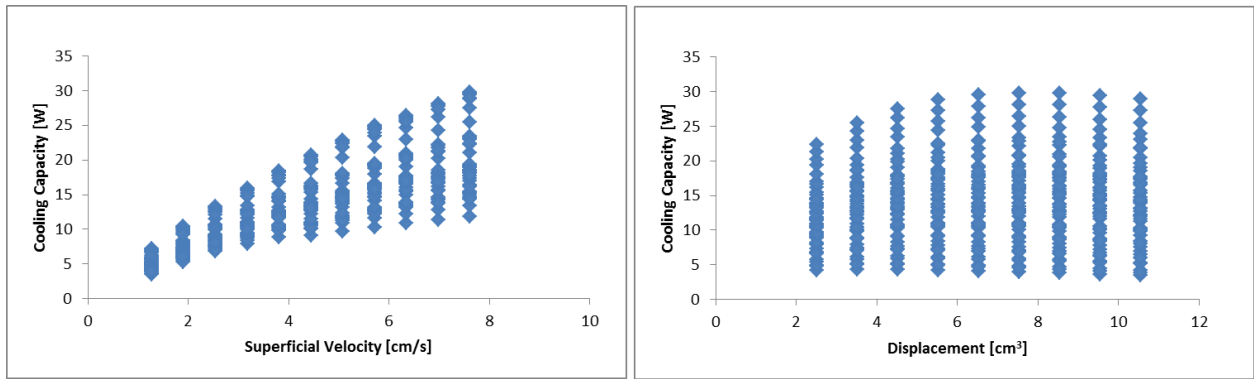


Figure 7-8. Results of AMR modeling study to determine operating conditions for regenerator testing

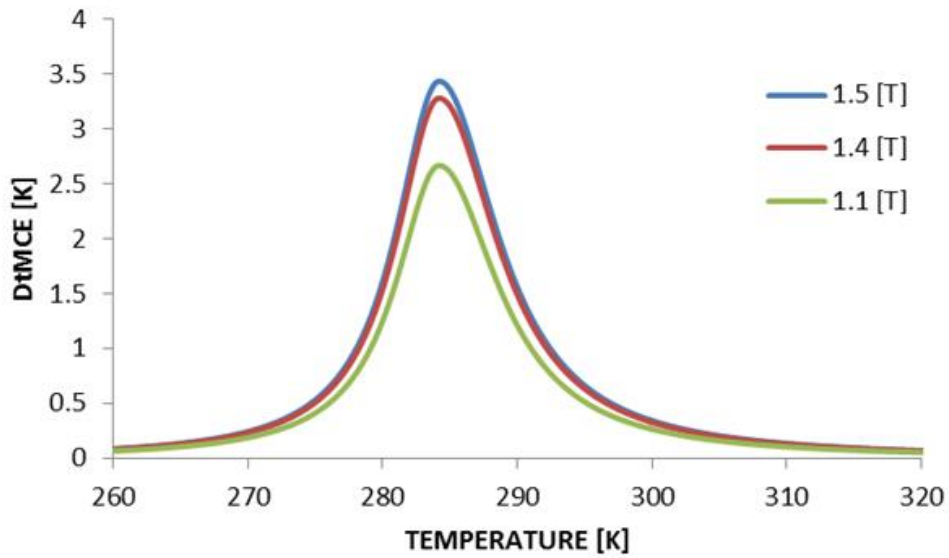


Figure 7-9. Lowest temperature from the Baseline test regenerator scaled based on two thirds scaling.

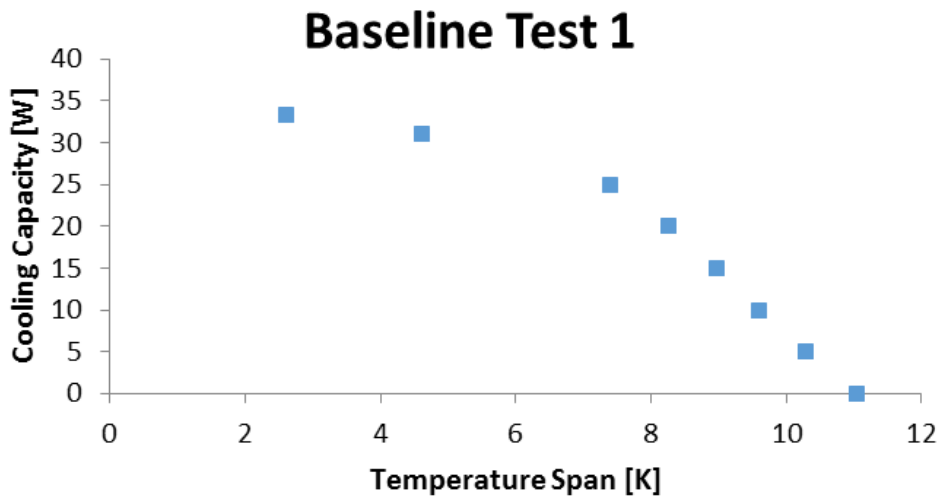


Figure 7-10. Cooling capacity span curve for the Baseline regenerator test case Test 1.

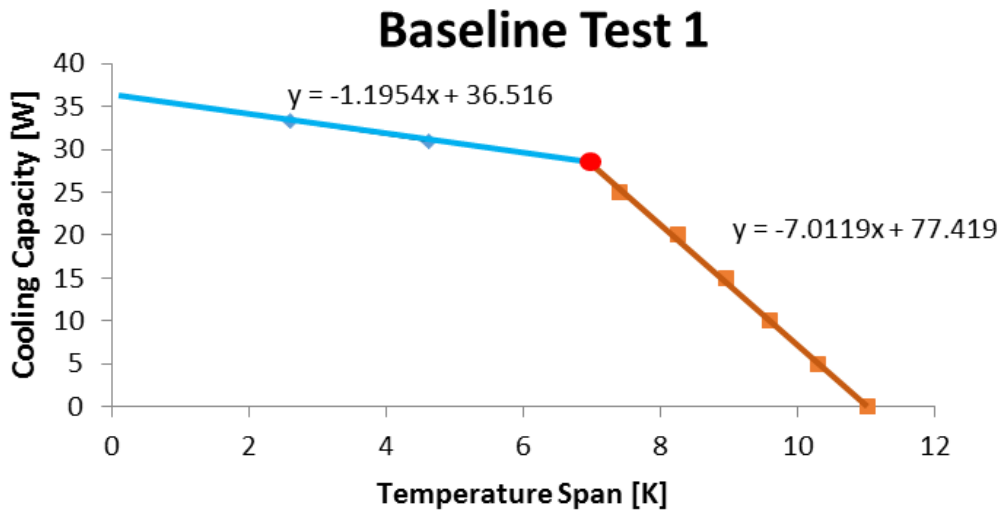


Figure 7-11. Baseline Test 1 shown with linear relationships between cooling capacity and span along with the maximum product of cooling capacity and span.

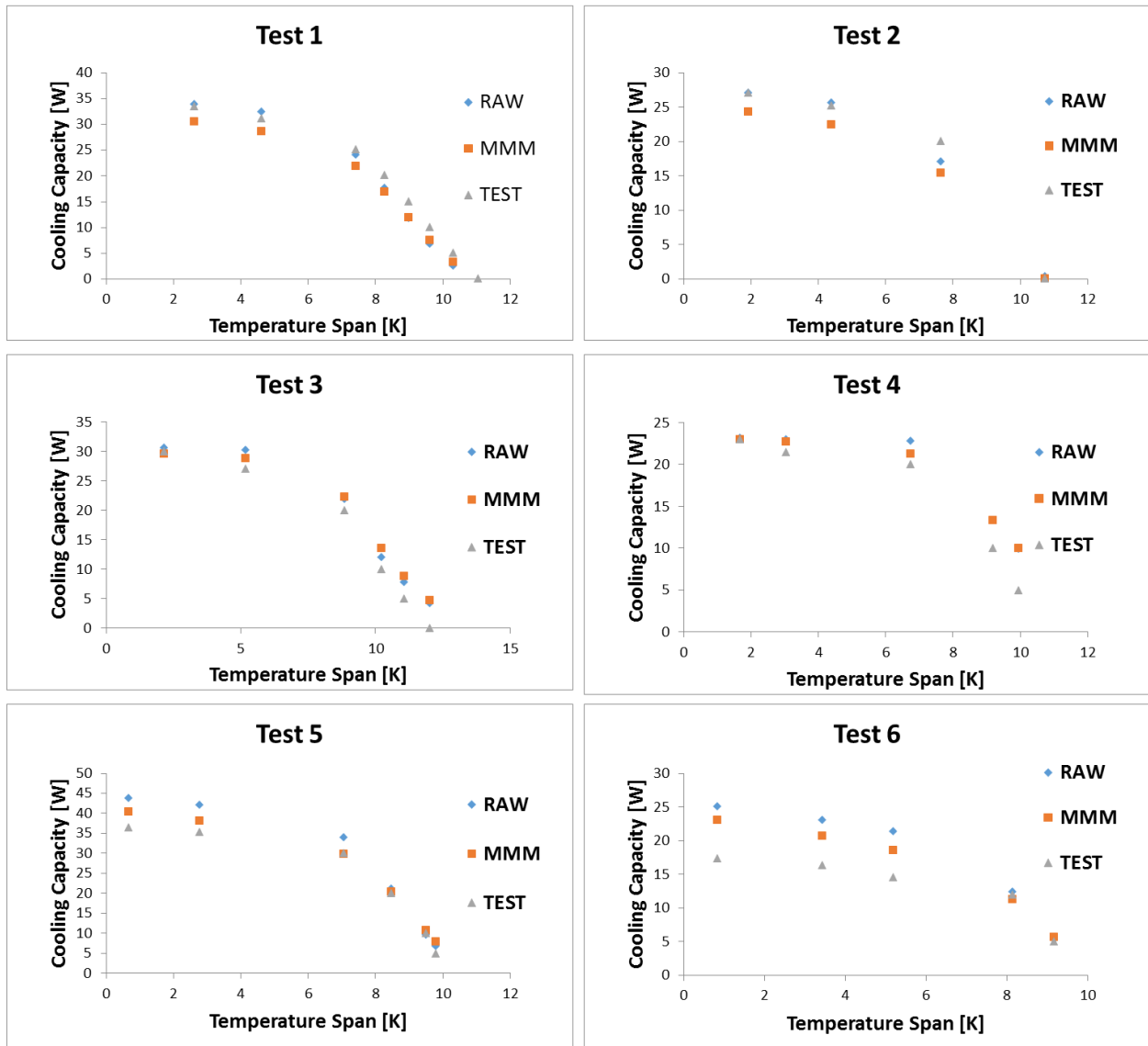


Figure 7-12. Results from each tests and AMR model predictions.

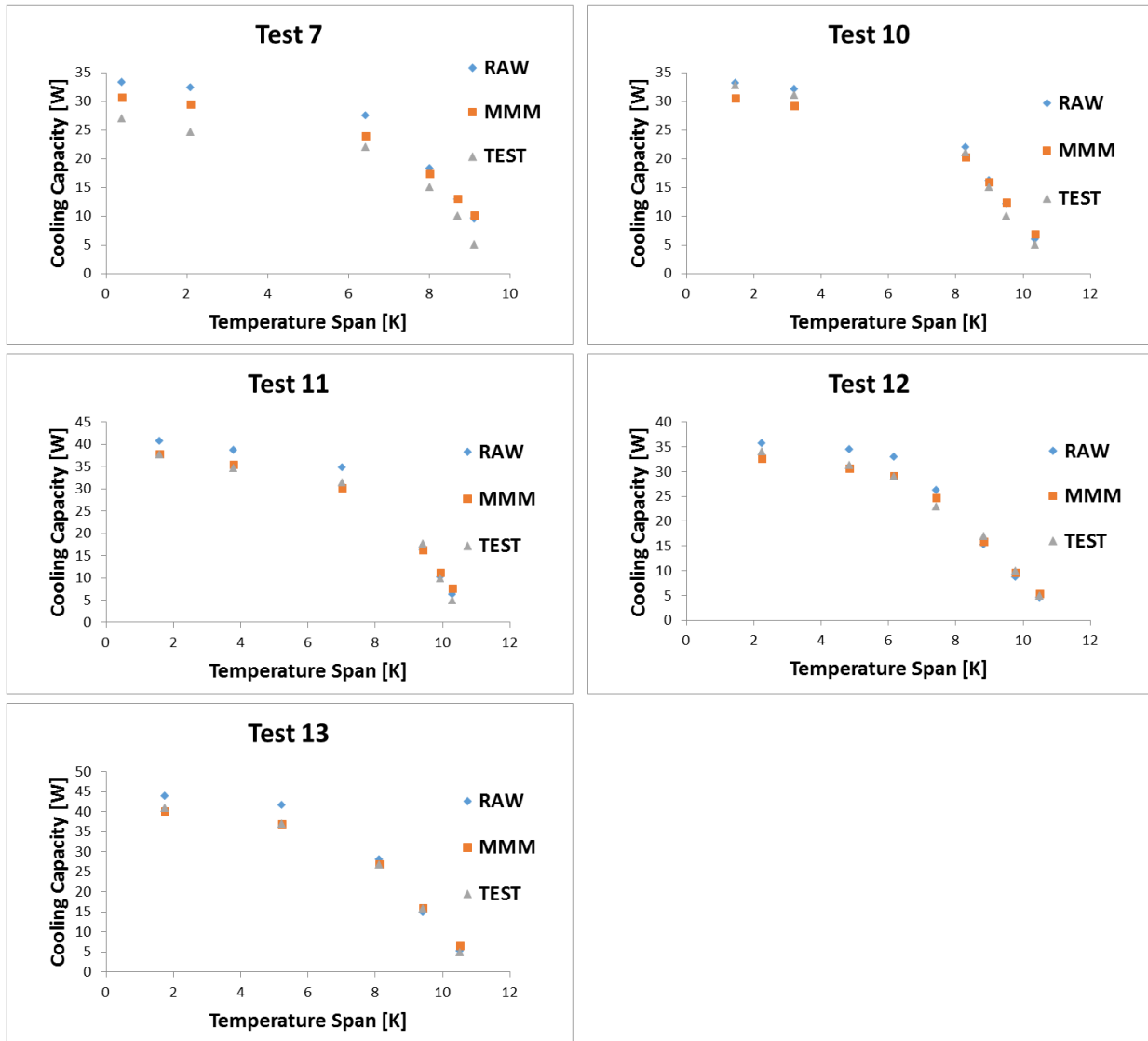


Figure 7-12. Continued

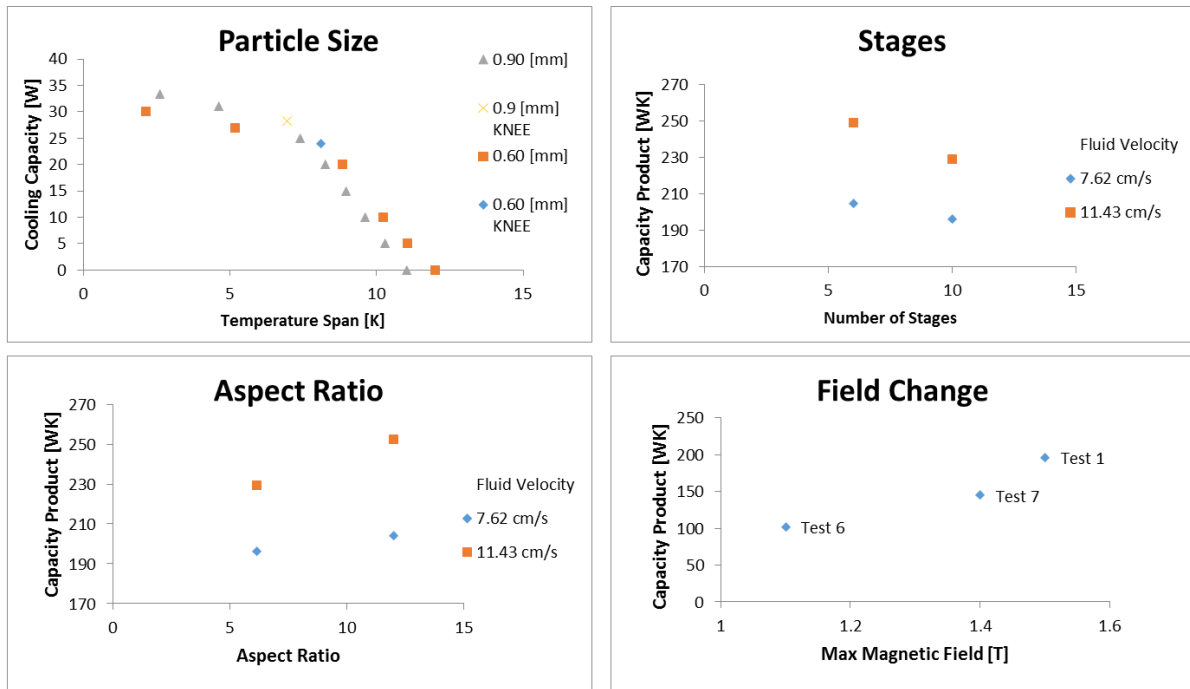


Figure 7-13. Test results with individual parameters isolated and related to the maximum cooling capacity span product.

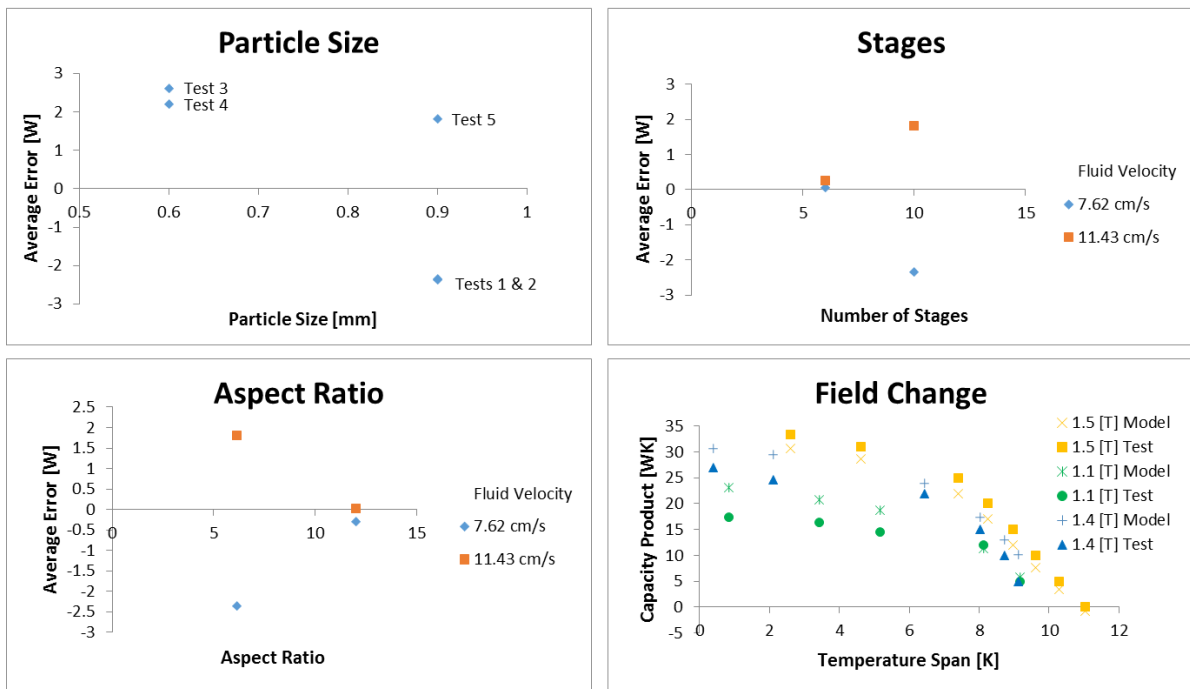


Figure 7-14. Error between the MMM and test data.

CHAPTER 8

MAGNETOCALORIC PARAMETER SPACE

This chapter reviews the details of a series of AMR modeling and analytical investigations used to narrow the parameter space which encompasses the performance of magnetocaloric refrigerators. The MCHP and materials parameters are considered separately and a series of assumptions are made. The original work involved in this chapter is under review for publication in the International Journal of Refrigeration.

There are many parameters involved in the design and operation of a magnetocaloric refrigerator. Scarpa et al. (2012) was used to help define the magnetic system of HA1 in the introduction, and goes on to further define 7 parameters with as many as 10 levels for each parameter. Clearly there many hundreds or thousands of unique MCHP designs. In addition to the distinct design parameters from Scarpa et al. (2012) there are continuous levels for certain parameters such as magnetic field. All of the possible MCHP combinations also have continuous operational parameters in common such as fluid displacement and fluid velocity. The new ability to include materials as a set of parameters further multiplies the possible combinations. To help illustrate the difficulty Table 8-1 contains all of the parameters that have been mentioned here or in Scarpa et al. (2102) organized into separate categories. Though this list is extensive it is by no means exhaustive. Many parameters have already been simplified by assumptions. An example is the assumption that the stages have a uniform volume. Complicated parameters such as this have many combinations that would be outside the capability of this study. Even with such simplifications the current list includes 43 parameters which, with only a simple full factorial study at two levels per

parameter, amounts to 9×10^{12} combinations each representing a full numerical simulation. Though it is impossible currently to simulate this complex set of parameters they have been listed in order help clarify the assumptions made for the following studies and the scope of this research.

Heat Pump Parameter Selection

The first set of assumptions is related to the MCHP parameters. These parameters describe both the physical design and cyclical operation of a MCHP.

Assumption 1: Ideal MCHP

The first assumption made is that the MCHP being modeled is ideal. This has several implications that impact many of the parameter categories. An ideal MCHP is one that experiences no MCHP design related losses. Any physical MCHP will always have losses in the form of heat leaks, or non-uniformities. Ignoring these losses enables the numerical study to become independent of a specific MCHP and better represents the isolated interactions of other parameters which are common to all MCHPs. This assumption directly eliminates the section of parameters titled “LOSSES” from Table 8-1. Losses being eliminated means that parameters that only contribute to the thermodynamic cycle through losses also become unimportant. Heat leak through regenerators is a function of the surface area of the regenerators. The surface area of the regenerators is directly calculated from the regenerator shape, the number of regenerators, the frontal area of the regenerators, and the hydraulic diameter of the regenerator. Ideal also means uniform flow which is impacted by these same parameters. When a regenerator has no heat leak and uniform flow the thermodynamic equations are completely independent of shape and number of regenerators. The

frontal area and length still play a role in the calculation of pressure drop and thermal transport through the regenerator and so must be retained.

Assumption 2: Simplified Cycle

The second major assumption is that the regenerator experiences an ideal AMR cycle. The ideal cycle as described in Chapter 3 is defined by the four steps of magnetize, flow towards hot heat exchanger, demagnetize, flow towards cold heat exchanger. There is no dwell in this cycle. To further de-couple the numerical studies from specific MCHPs the flow profile and magnetization profiles are assumed to be non-overlapping square functions. The magnetization is assumed to take place instantaneously between zero field and high field which is normally the ideal design of a magnetic system since having a non-zero low field means that magnetic field is wasted in the low field section. This assumption may differ greatly from real MCHPs where the implementation of both field and flow can never be instantaneous. The differences between an ideal cycle and a real MCHP are exemplified in Figure 8-1 which shows the field and flow profiles for the HA1 prototype when the magnets are continuously operated along with ideal operation at the same maximum flow velocity, flow time, magnetization, and frequency. The difference in two cycles similar to Figure 8-1 is reported for HA1 (Benedict et al., 2016c).

The simplified cycle can be defined in numerical simulations by a flow rate, and displaced volume. The magnetization profile and frequency are derived directly from these two values and the dwell time and flow profiles are eliminated as parameters. The zero field assumption also eliminates the need for low field as a parameter leaving maximum field to define the change in field for the system.

Assumption 3: Defined Regenerator Structure and Design Condition

There are a many different structures that have been proposed for the shape of magnetocaloric materials. The majority of journal articles and prototypes focus on packed particles, or parallel plates (Yu et al., 2010), but other shapes such as microchannels and more three dimensional structures have also been investigated (Engelbrecht et al., 2011b; Pryds et al., 2011). From the review in Chapter 2 packed particle beds have shown the largest cooling capacities, and are the regenerator structure for the majority of test results. The literature has also shown that plates would need to be thinner than what is currently possible for first order materials to be competitive with packed beds (Tura et al., 2012b). There are no results in the literature for appreciable amounts of more complicated structures of FOMT materials being successfully tested. For this reason packed particle beds are chosen as the regenerator structure. The particles are further specified to be spherical in a random close pack. Spheres show a reduced pressure drop for the same mean diameter and with a similar surface area (Ergun and Orning, 1949). Using spherical particles also eliminates any secondary shape dimensions such as regularity or channel shape. Lastly random close packing has a predictable void fraction of 36% (Scott et al., 1969). The only remaining variable for the structure of the MCM is particle diameter.

The regenerator design conditions are set for this study. The overall span of the regenerator, defined as the difference between the highest temperature MCM stage ΔT_{T_C} and the lowest temperature MCM stage ΔT_{T_C} , is selected as 40°C to 5°C. This is a span similar to a typical domestic refrigerator. A span of 35°C and ensures that multiple FOMT MCMs are needed. The mass of the MCM material is specified as 0.5 kg. Coupled with a set void fraction, material structure, and density a constant mass is

equivalent to a constant regenerator volume. Based on the testing completed with HA1 this is enough material to provide cooling capacity on the order of at least 100 Watts which is also typical of a domestic refrigerator. It is noted that thermal conductivity linearly through the regenerator itself will be a function of the regenerator size and shape as well as the material span. A set volume and regenerator shape means that frontal area of the regenerator is defined by the length. For the purposes of these two calculations the overall regenerator shape is assumed to be a cylinder. The low temperature of the regenerator span means that it is possible to consider water as the heat transfer fluid.

Assumption 4: Average non-MCE Properties

The material properties of density and thermal conductivity are not directly related to the MCE, but are part of the AMR model equations from Chapter 4 which means that they impact MCHP performance. Studies have further supported this fact (Bjørk et al., 2010; Smith et al., 2012). Though it is not possible to predict the exact density of a FOMT MCM it is probable that any new materials would share some common characteristics with current materials. First the magnetocaloric effect in FOMT is brought about by a magnetically induced phase change meaning that a large portion of the MCMs constitute elements are very likely to be magnetic. Indeed of the four most commonly reported FOMT material families; LaFe, MnFe, GdSiGe, NiMn one or both of the first two elements is highly magnetic. The density and thermal conductivity of all these materials are in a similar range. Four examples of specific formulations of the FOMT MCMs mentioned above ($\text{La}(\text{Fe}_{11.4}\text{Si}_{1.6})$, $\text{MnFeP}_{0.45}\text{As}_{0.55}$, $\text{Gd}_5(\text{Si}_2\text{Sn}_2)$, and $\text{Ni}_{54.8}\text{Mn}_{20.2}\text{Ga}_{25.0}$) have densities of 7.22, 7.26, 8.85, and 7.8 g cm^{-3} (Gschneidner Jr., K. A.; Pecharsky, V. K.; Tsokol, 2005). Measurements on the LaFeSi, GdSiGe, and

MnAs show thermal conductivities between 2 and 8 W m⁻¹K⁻¹ (Fujieda et al., 2004). A good indicator of the similarity of the non-MCE specific heat is the B parameter for the Split Lorentzian MMM fits. The B parameter becomes the value for specific heat at temperatures far from the T_C where the magnetocaloric effect is not active. As shown in the experimental studies from Chapter 7 the MnFe based MCMs averaged around 500 J kg⁻¹K⁻¹ while the LaFe based MCMs used a constant B of 500 J kg⁻¹K⁻¹. Based on the currently available materials, average values are selected for the non-MCE properties of all MCMs to be used in the following studies. The Thermal conductivity is set at 5 W m⁻¹K⁻¹, the density is set at 7.5 g cm⁻³, and the baseline value for the specific heat is set to 500 J kg⁻¹K⁻¹. Finally the base value for ΔT is set to zero for all studies. The underlying assumption for a zero base ΔT is that these are FOMT MCMs and therefore the MCE is only active within a small temperature span related to W parameter of ΔT. For a purely FOMT material the W parameter is fully defined by the relationship between specific heat and magnetic field as can be seen in Figure 3-4 and Figure 3-5 in Chapter 3. This assumption was used in the two experimental confirmations from Chapter 7 where the MMM showed better correlation to experimental results than directly measured MCE which does not necessarily trend toward zero as temperatures move away from T_C.

Magnetocaloric Material Selection

The four sets of assumptions make the AMR model studies more universally applicable to all MCHPs. They also help to focus the studies on the materials themselves and their interactions with the fundamental MCHP parameters. Lower numbers of parameters greatly reduce the number of AMR model runs which is necessary given the immensity of the initial parameter space. Table 8-2 shows the original parameter space along with the eliminations that were made based on the

simplifying assumptions. The assumptions leave fifteen parameters remaining in total. Eight of the remaining parameters pertain to MCHP design and operation and the other seven relating to the description of MCM by the MMM. Even with a reduced parameter set of fifteen a full factorial set of simulations at three levels would still result in greater than 14 million runs. In order to make the simulation effort more manageable the parameter space has been split into multiple modeling studies.

AMR Model Configuration

The first modeling studies was carried out on eight non-MMM parameters. The materials for this study are based on the average values from the exiting FOMT MCMs from Chapter 7. To obtain these values a mean value is calculated for each of the MMM constants. Using mean values ensures that the study was not material specific, but was representative of the general capabilities of current materials. The average MMM parameters are shown in Table 8-3.

To reduce the total number of runs the first study (Study 1) will target the elimination of the two remaining specification parameters: Span at target cooling capacity, and hot side rejection temperature. Selecting a single hot side rejection temperature should not have a large impact on the performance of a MCHP for a set MCM span as long as that rejection temperature is not outside the rejection range of a regenerator. The effect of a hot side rejection temperature that is set at too high a temperature can be seen in experimental results as exemplified by Figure 7-4. The range of temperatures covered by the T_{CS} in all of the regenerators has been set as constant as a result of assumption 3. Similarly the span at which the cooling capacity of MCHP is evaluated is an important consideration, but is also largely controlled by the span of regenerator T_{CS} . Ideally the maximum cooling capacity and span product at the

knee point gives the best indication of MCHP performance for design reasons explained in Chapter 7, however finding the exact span for the knee point is difficult. A simplifying assumption can be made by analyzing the cooling capacity at a single temperature which, with regards to the AMR model, is the cold side acceptance temperature. The temperature can be chosen sufficiently high enough such that there is a low probability that most simulations will have passed the knee point, but not so high that the slope of the plateau has a large impact on the resulting cooling capacity. In order to select the cold side and hot side temperatures the first simulation set will vary all of the MCHP parameters in a full factorial manner at three levels. The hot side rejection temperature and cold side acceptance temperature will be varied at five levels. The first level will be selected as the highest T_C for the rejection temperature and the lowest T_C on the cold side. Beyond these temperatures the cooling capacity of the regenerator is obviously diminished because span of the materials has been exceeded. The other four temperatures are selected at 1.5 K intervals above (for the cold side) and below (for the hot side). The results will be analyzed for a relationship between the predicted cooling capacity and the cold and hot side temperatures for the simulations with positive cooling capacities.

In order to test this method it can be applied to the cold side temperatures of the experimental results from Chapter 7. Since all of the runs for this study were successful the entire set of results will be analyzed. The span for these experiments was allowed to vary freely so there is a continuous range of span values rather than a systematically selected set of values. A normal distribution is calculated from the standard deviation and average of the rejection temperatures at the maximum cooling capacity span

product for these runs. The lowest 10th percentile rejection temperature is selected based on this distribution.

The cumulative distribution of knee spans calculated based on Equations (7-5) and (7.6) and assuming a normal distribution is shown in Figure 8-2. Since these experiments had a fixed hot side temperature the span is analogous to the cold side temperature. Selecting the span that includes 90% of the knee spans based on this distribution results in a temperature span of 7.1 K. The information from Table 7-5 is then used to predict the cooling capacity at this span for all of the test cases. The relative rank based on 1 being the highest cooling capacity for the cooling capacities predicted at the 7.1 K span and the relative rank of the actual maximum cooling capacity span products are shown in Table 8-4. Only two tests are out of order in the single span point prediction. Tests 10 and 12 changed places meaning that only one single spot was missed by making the assumption that a single span point can represent the performance of a regenerator. An inspection of the original data shows that the cooling capacity span product for Tests 10 and 12 were 205 and 204 respectively or less than 1% different; by far the closest test results of the study. This method should work better for selecting the hot side rejection temperature since the cold side accepting temperature is directly involved in the resulting cooling capacity by the slope of the plateau region.

The parameters for the simulation cases of Study 1 are shown in

Table 8-5. For set parameters the value was selected in one of the four assumptions listed previously. For active parameters the range of values are shown. All of the parameters are evaluated at three levels evenly spaced in the study range except for rejection temperature and acceptance temperature which are each evaluated at five evenly spaced intervals. The levels for the parameters were chosen based on representative values from the literature. The maximum field is limited between the remnant flux of commonly used permanent magnets: Neodymium Iron Boron and Alnico around 1.5 Tesla and Samarium Cobalt (SmCo_5) around 0.9 Tesla. The number of layers is chosen so that the maximum number of layers corresponds to a spacing of one stage per Kelvin and the minimum corresponds to roughly double that. Since the number of stages is discrete these levels are not perfectly evenly spaced. The regenerator length is chosen so that the corresponding aspect ratio of the regenerator covers over an order of magnitude. Particle size is also chosen in order to cover an order of magnitude. Maximum fluid velocity and displaced volume are both chosen based on the successful values from Chapter 7 and the ranges again cover nearly an order of magnitude.

Results

Study 1 had a total of 18,225 simulations which completed running in just under 72 hours. The simulation routine has several criteria to end a simulation. Convergence

is defined as a change of less than 0.001% in both the heat accepted and heat rejected for the cycle. Cyclical maximum is defined as a simulation that has completed 300 cycles without converging. Time out occurs if the simulation takes more than 10 minutes to reach either of the other two criteria. The results of Study 1 are 55% converged, 41% timed out, and 4% cyclical maximum. The convergent cases have an average simulation time of 276 seconds and an average number of cycles to convergence of 71 showing that the time out and max cycles criteria represent cases that are far from the normal range of convergence. Convergent cases contain a mix of negative and positive cooling capacities. In the conventions of the AMR model positive cooling capacity represents heat being accepted on the cold side and are therefore referred to as successful cases. Negative cooling capacities represent heat being rejected to the cold side meaning that the regenerator is not function as a heat pump for refrigeration. Study 1 was 42% positive cooling capacities. Accounting for cases that either resulted in negative cooling capacities or failed to converge Study 1 resulted in only about one quarter successful simulations.

Thermodynamic Analysis of Study 1

The large number of negative cooling capacities did not represent a failure of the AMR model, but rather was rooted in physical phenomenon. Simulations with negative cooling capacities represent cases in which the regenerator fails to function. These cases are not unrealistic. Two examples of failure mechanisms are used to cross check the results of the AMR model to ensure that future simulations are not carried out under the false assumption of a functioning AMR model. These failure modes come directly from the thermodynamic equations that dictate the performance of the active magnetic regenerator and which are the foundation of the AMR model. Equation (4-1) is the

change in temperature for the fluid nodes. The second term in Equation (4-1) is the heat transfer between the fluid and MCM. The fourth term is the viscous dissipation in the fluid due to flow. When the heat transferred from the fluid to the MCM is equal to the heat generated by the fluid flow the ability of the regenerator to accept heat is cancelled out. As the heat generated by fluid flow increases further the regenerator actually starts to generate heat which will be rejected on both the cold and hot side. This is a case in which the cooling capacity would be negative.

Viscous dissipation can be calculated from the pressure drop in the regenerator bed. The pressure drop is calculated by Equation (8-1) based on correlations developed for packed particle beds (Ergun and Orning, 1949)

$$\frac{\Delta P}{L} = \rho_f v_{sf}^2 \frac{(1-\varepsilon)}{Dp\varepsilon^3} \left[\frac{180}{ReS_{ph}^2} (1 - \varepsilon) + \frac{1.8}{S_{ph}} \right] \quad (8-1)$$

where Re is the Reynolds number and S_{ph} is the sphericity of the MCM particles (1 being perfectly spherical and $0 < S_{ph} < 1$ more irregular). The fluid energy for a single flow period (Q_p) in this case is calculated by Equation (8-2)

$$Q_p = \Delta P v_{sf} A_R t_{flow} \quad (8-2)$$

where t_{flow} is the time of a single flow period. The energy available for cooling per cycle ($Q_{c_{cyc}}$) is an output of the AMR model. A dimensionless ratio of cyclical cooling capacity to pumping power per stroke is defined in Equation (8-3)

$$\theta_1 = \frac{Q_{c_{cyc}}}{Q_p} \quad (8-3)$$

Evaluating θ_1 for only the successful simulations of Study 1 finds that over 46% of the results have a θ_1 values less than 10 meaning that the available cooling energy per cycle is of the same order of magnitude as the pumping energy in the cold stroke.

Almost 5% of the successful runs have a θ_1 less than or equal to 1 which signifies that the pumping energy is at least equal to or perhaps greater than the cooling load. These are significant numbers considering that all of the negative runs have not been included. The conclusion can be drawn that for a vast majority of the simulations pumping energy per stroke is of a comparable value to the cooling capacity per stroke and that pumping power likely plays a large role in many of the negative cooling capacity simulations.

The other major source of heat that can possibly cause regenerator failure is the hot side of the regenerator. The AMR model assumes that the hot and cold sides are fixed in temperature. This means that there is a natural tendency for heat to transfer from the hot to the cold side through the regenerator. The first and third terms of Equation (4-1) represent mass transfer and axial dispersion (which contains conduction through the fluid). The first term of Equation (4-2) is the axial conduction through the MCM. These three terms enable heat to be transferred from the hot to the cold side. In the most extreme case with a magnetic field change of zero or no flow the cooling load would be negative and equal to the conduction through the fluid and MCM of the bed. The conduction is assumed to take place directly through the fluid and material separately and thus a total conduction through the bed is calculated by Equation (8-4)

$$\mathbf{Q}_{\text{cond}} = \Delta T_{\text{H-C}} \frac{A_{\text{reg}}}{L_{\text{reg}}} [k_s(1 - \epsilon) + k_f(\epsilon)] \quad (8-4)$$

The energy that can be attributed to the conduction through the material is much lower than that of the fluid power. On average the conduction heat flow is just 5% of the successful run cooling capacities.

The heat delivered by mass transport from the hot side during the hot to cold stroke can also be detrimental in some cases. In cases where the heat transferred to the MCM on

the hot to cold stroke is too great and at too high a temperature MCMs may be brought to a temperature that is too far from T_C for the material to be active. This scenario can be called “washout” and depends on many factors, but the amount of heat transferred to the regenerator from the hot side is directly related to the percentage of the fluid in the bed that is exchanged each stroke. Figure 8-3 shows the effect of displacement on cooling capacity when negative results are included. As the displacement increases the overall average cooling capacity of the numerical simulations trends downward pointing to washout as a contributor to regenerator failure.

All of the factors explained are present in each of the runs, and along with other factors can contribute to failed runs. The fact that the negative contributions to cooling capacity are largely on the same order of magnitude as the cooling capacity, and that increasing displacements are correlated with increasingly negative modeling results indicate that the AMR model is functioning properly. Since none of the negative factors described above change for the MMM parameters their influence can be assumed to be equally as influential regardless of the MCM that is being used in a regenerator. This fact will be used in future studies to help reduce simulation time while retaining a maximum amount of useful information.

Study 1 Findings for Hot and Cold Side

To evaluate the hot side and cold side temperature which should be used moving forward a subsection of the Study 1 data was considered. Only around a quarter of the simulations from Study 1 were considered successful; having both positive cooling capacity, and finishing at convergence. The hot and cold side temperatures were varied each at five levels meaning that each combination of MCHP design and operational parameters had twenty five simulations where only the hot and cold side were varied.

Many times within these twenty five runs a large proportion of the results were positive with only a few hot and cold side temperatures leading to negative or un-converged results. Figure 8-4 shows an example set of MCHP design and operational parameters with each of the twenty five temperature points plotted with respect to simulated cooling capacity. The cold side temperature's impact on performance can be seen as each set of points trends toward higher cooling capacity at higher cold side temperatures. The diminishing influence of the cold side temperature on the cooling capacity should lead to an optimum cold side temperature when the maximum cooling capacity span product is considered. The hot side influence is evident in the fact that the sets of points are at differing levels. In this example a lower temperature hot side leads to higher cooling capacities. The negative cooling capacities have already been shown in the preceding paragraphs to represent physically realistic performance. In this case they can provide useful information when considering the overall or average effect of the hot and cold side temperatures. If simulations with negative cooling capacities were ignored completely then the average effect for some temperatures would be artificially high. Simulation sets where all results are negative or un-converged are ignored since this data has no theoretical limit on its magnitude which can unfairly weight the overall results and these combinations of MCHP parameters will not be carried forward. To evaluate the hot and cold side temperatures the results from Study 1 are filtered to only include MCHP design and operational parameter combinations where the overall average of the cooling capacity over the twenty five temperature combinations is positive.

The hot side tends to have a lower effect on the cooling capacity. This fact can be seen from Figure 8-4 where for a single cold side temperature the largest difference between cooling capacities for different hot side temperatures is about 15 Watts. The largest difference for single hot side temperature across the cold side temperatures is, by comparison, more than 40 W. Figure 8-5 shows that the average cooling capacity decreases as hot side temperature is increased similarly to Figure 8-4. This result confirms the assumption from the previous section. The trend of decreasing cooling capacity with increasing hot side temperature is non-linear and increases quickly as the hot side temperature approaches the hottest stage T_C . The method for selecting a hot side temperature involves comparing the cooling capacity span product across the variables. Figure 8-6 shows average cooling capacity span product as a function of the hot side temperature. Cooling capacity span product shows the opposite trend with its magnitude increasing for increasing hot side temperature. This trend reverses after a hot side temperature of 312 K. The hot side values for this study were selected at regular intervals which means that a normal distribution will not be applicable as it was for the experimental results. To select a temperature for the hot side the cooling capacity and cooling capacity span product are both normalized to their respective maximum values. Figure 8-7 compares the two trends. The crossing point is almost exactly at 310 K which will be the hot side temperature moving forward. This temperature on average is close to 98% of the maximum for both cooling capacity span product and cooling capacity. Hot side temperatures higher or lower than this will diminish either the cooling capacity span product or cooling capacity rapidly.

Cold side temperature is evaluated only for a hot side temperature of 310 K. A similar comparison is made for the cold side temperature as was made for the hot side temperature. Figure 8-8 shows both the cooling capacity and cooling capacity span product as a function of the cold side temperature. The trends are reversed from the hot side temperature: As the cold side temperature decreases towards the coldest T_C the cooling capacity decreases. The cooling capacity span shows a much more pronounced optimum than the hot side which is concurrent with the experimental results where the slope of the drop off section is much steeper than that of the plateau. Figure 8-9 shows both the cooling capacity span product and the cooling capacity normalized to their respective maximums. The crossing point for the two trends coincides with a cold side temperature of 282.5. This temperature is far from the steep drop offs in both cooling capacity span product and cooling capacity that occurs for temperatures lower than 279.5. The cooling capacity span product and cooling capacities are also above 95% of their maximum value at 282.5. The hot and cold side temperature for the remaining studies will remain constant at 310 and 282.5 based on the results of Study 1.

The remaining parameters for Study 1 were selected based upon ranges of values found in literature and from experimental results with the goal of encompassing a large parameter space. The average effect of these parameters on cooling capacity falls into two classes; those with a local optimum or very little impact on performance and those for which the cooling capacity is affected and shows no optimum. Figure 8-10 shows the average cooling capacity for the displacement and number of stages. Displacement has a maximum average cooling capacity at a value of 22.5 cm³ per stroke. This is a likely indication that the higher values of displacement are experiencing

some degree of wash out. The number of regenerator stages has a slight positive correlation with cooling capacity, but has the lowest range of average values of all the parameters in the study indicating that it has the lowest effect on the regenerator performance. Both of these parameters have acceptable ranges based on the results of Study 1.

Figure 8-11 shows the remaining parameters. High magnetic field predictably has a positive influence on the cooling capacity. As explained before the MCE scales to the two thirds power of the magnetic field. The magnetic field range was set between values which represent physical limitations and is therefore still applicable. Particle diameter and regenerator length seem to be far from optimal values for Study 1. Higher superficial velocity values seem to be beneficial and will be studied. Particle size and regenerator length have the highest impact on cooling capacity from Study 1. The results indicate that smaller particle sizes and shorter regenerators can provide greater cooling capacities. In the case of particle size a new lower limit will be set at 0.050 mm; Below this value particles become much harder to work with for many reasons, the most important of which is safety. Though this study is not material specific most FOMT materials include reactive elements such as rare earths. Even Iron which is present in many of the MCM formulations can be a safety hazard becoming pyrophoric especially when dispersed in a dust cloud at particle sizes at or under 0.050 mm (Wu et al., 2009). The regenerator is limited by the physical requirement that there be at least one particle size per layer of material. The largest particles size is 1 mm and the largest number of stages is 35 resulting in a minimum regenerator length of 3.5 cm.

Study 2 was run with additional levels for particle diameter, superficial velocity, and regenerator length detailed in Table 8-6. The remaining variables which were not changed from Study 1 with the exception of hot and cold side temperature are still varied at the same levels as Figure 8-5 to create a full factorial set of 1485 additional simulations. Hot and cold side temperatures are set to the single temperatures determined from the results of Study 1. The results of Study 2 contain a similar number of failed runs to the results of Study 1. The smaller particle size and increased fluid velocities are both factors that increase the viscous dissipation power. Figure 8-12 shows the average pumping powers and cooling capacities for the particle diameter and superficial fluid velocities from the successful cases of Study 2. For both the particle diameter and superficial fluid velocity the average pumping power increases for the new parameter levels and actually exceeds the cooling capacity. This means that the average pumping power utilizes more than half of the cooling capacity available from the material. The cooling capacity also reaches a maximum and starts to decrease for both of the new variables indicating that the range of values selected for Study 2 now includes the optimums that were missing in Study 1.

The results of Study 2 and Study 1 are combined and compared to the original results from Study 1 in Figure 8-13. Smaller regenerator length continues to increase the overall cooling capacity of the simulations for the added parameter value. This parameter will remain limited by the physical requirement based on particles per stage for future studies. The three parameters which were added for Study 2 have little influence on the results of the simulations for the original parameter levels from Study 1. The number of regenerator stages and magnetic field strength seem to have little

interaction with the new levels added from Study 2, although the higher average cooling capacity from Study 2 can be seen in the upward shift of the cooling capacity.

Displacement alone seems to have an interaction with the new levels added in Study 2.

The crossing of the average cooling capacities between the Study 2 results and combined results means that one or more of the levels had an influence on the relationship between displacement and cooling capacity. There is still, however, a maxima in the parameter range from the combined studies.

From the total parameter space of MCHPs a subset of idealized assumptions has been made and detailed. These assumptions serve to make numerical studies possible while widening the applicability of the study results. A first set of simulations has further narrowed the parameter space by employing an assumption based on, and successfully tested against the physical characteristics of experimental results with multistage FOMT MCM regenerators. The application of thermodynamic analysis has further narrowed the results of this modeling study to only those results which provide useful information. The elimination of failed studies has been justified in the physics which dictate the performance of regenerators and has been shown to be in accordance with the results of the modeling study. A set of physical limitations have been set which create a parameter space with the remaining variables. Where there is no natural physical limitation for the variables a second study has found maxima which help to define an interesting range. Utilizing the successful results from these two studies has reduced the overall number of simulations necessary for future studies by 25%. Although the number of simulations is reduced the replacement of failed simulations with successful

simulations over a wider parameter space provides an increase in the amount of useful information.

Table 8-1. List of parameters that both define a MCHP and its operation.

Class	Parameter Name	Cont or Discreet	Description
MCHP Type			
	Effect	Discreet	Whether two or more regenerators have connected flow and out of phase cycles
	Field Source	Discreet	The use of permanent or electromagnets
	Magnet Type	Discreet	The magnetic circuit that applies the field
	Field Application	Discreet	How the field is changed
	Fluid	Discreet	Selection of heat transfer fluid including gasses
	Fluid Motion	Discreet	How the heat transfer fluid is moved relative to the MCM
	Magnet - Regenerator Motion	Discreet	How the MCM is moved relative to the field
System Specification			
	Regenerator Span	Continuous	Difference between the hottest stage Tc and coldest stage Tc
	Volume of MCM	Continuous	Volume magnetocaloric materials
	Hottest Tc Temperature	Continuous	Highest Tc for the regenerator
	Rejection Temperature	Continuous	Temperature which the hot side heat exchanger rejects heat to
	Acceptance Temperature	Continuous	Temperature which the cold side heat exchanger accepts heat from
Magnetic Regen System			
	Maximum Field	Continuous	Maximum strength of the magnetic field
	Minimum Field	Continuous	Minimum strength of the magnetic field
	MCM Structure	Discreet	Physical shape of the MCM
	Layers of MCM	Discreet	Number of different distinct MCM alloys in a regenerator
	Number of Regenerators	Discreet	Number of MCM containers with distinct cycles
	Regenerator Shape	Discreet	Frontal shape of individual regenerators
	Regenerator Length	Continuous	Length of individual regenerators
	Regenerator Frontal Area	Continuous	Frontal area of individual regenerators
	Regenerator Hydraulic Diameter	Continuous	Hydraulic diameter for individual regenerators
	Void Fraction	Continues	Fraction of regenerator volume that contains heat transfer fluid
	Particle Diameter	Continuous	Diameter of the MCM particles or characteristic length for other structures

Table 8-1. Continued

Class	Parameter Name	Cont Or Discreet	Description
Operational			
	Fluid Maximum Velocity	Continuous	Maximum superficial velocity of fluid inside regenerators
	Displaced Volume	Continuous	Volume of fluid moved during a single flow period
	Fluid Dwell Time	Continuous	Time between fluid flows when fluid is stationary
	Fluid Flow Profile	Continuous	Description of ramp rates for fluid velocity
	Magnetization Profile	Continuous	Description of ramp rates for magnetic field strength including timing of magnetization start and stop
	Frequency	Continuous	Cycle frequency for individual regenerator
Losses			
	Perimeter Heat Leak	Continuous	Heat leak into the perimeter of a regenerator
	Heat Exchanger Heat Leak	Continuous	Heat leak into the cold heat exchanger
	Field Non-Uniformity	Continuous	Field strength as a function of location in the regenerator
MCE			
	ΔT Amplitude	Continuous	See Chapter 6
	ΔT Width	Continuous	See Chapter 6
	ΔT Skew	Continuous	See Chapter 6
	ΔT Base	Continuous	See Chapter 6
	Cp Amplitude	Continuous	See Chapter 6
	Cp width	Continuous	See Chapter 6
	Cp Skew	Continuous	See Chapter 6
	Cp Base	Continuous	See Chapter 6
	Cp Tc Offset	Continuous	The difference between ΔT Tc and Cp Tc
MCM Properties			
	Thermal Conductivity	Continuous	Thermal conductivity of the MCM
	Density	Continuous	Density of the MCM

Table 8-2. Full parameter field with parameter eliminations by assumption.

Classification	Parameter Name	Continuous Or Discreet	Elimination Assumption
MCHP Type			
	Effect	Discreet	1
	Field Source	Discreet	1
	Magnet Type	Discreet	1
	Field Application	Discreet	1
	Fluid	Discreet	1
	Fluid Motion	Discreet	1
	Magnet - Regenerator Motion	Discreet	1
System Specification			
	Regenerator Span	Continuous	3
	Volume of MCM	Continuous	3
	Hottest T_C Temperature	Continuous	3
	Rejection Temperature	Continuous	
	Acceptance Temperature	Continuous	
Magnetic Regen System			
	Maximum Field	Continuous	
	Minimum Field	Continuous	2
	MCM Structure	Discreet	3
	Layers of MCM	Discreet	
	Number of Regenerators	Discreet	1
	Regenerator Shape	Discreet	1
	Regenerator Length	Continuous	
	Regenerator Frontal Area	Continuous	1
	Regenerator Hydraulic Diameter	Continuous	1
	Void Fraction	Continues	3
	Particle Diameter	Continuous	
Operational			
	Fluid Maximum Velocity	Continuous	
	Displaced Volume	Continuous	
	Fluid Dwell Time	Continuous	2
	Fluid Flow Profile	Continuous	2
	Magnetization Profile	Continuous	2
	Frequency	Continuous	2
Losses			
	Perimeter Heat Leak	Continuous	1
	Heat Exchanger Heat Leak	Continuous	1
	Field Non-Uniformity	Continuous	1

Table 8-2. Continued

Classification	Parameter Name	Continuous Or Discreet	Elimination Assumption
MCE			
	ΔT Amplitude	Continuous	
	ΔT Width	Continuous	
	ΔT Skew	Continuous	
	ΔT Base	Continuous	4
	C_p Amplitude	Continuous	
	C_p Width	Continuous	
	C_p Skew	Continuous	
	C_p Base	Continuous	4
	$C_p T_C$ Offset	Continuous	
MCM Properties			
	Thermal Conductivity	Continuous	4
	Density	Continuous	4

Table 8-3. Average parameters used to represent generic currently available FOMT material.

Parameters	ΔT	C_P
A	3.15	1542
T_C (Offset)	293	(-0.54)
S	1.72	0.68
W	3.64	2.78
B	0.00	500

Table 8-4. Prediction using a single span point compared to actual measurement.

Test	Bed	Actual Relative Rank	Predicted Relative Rank
1	Baseline	7	7
2	Baseline	10	10
5	Baseline	3	3
6	Baseline	11	11
7	Baseline	8	8
3	Small particles	4	4
4	Small particles	9	9
10	Half stages	5	6
11	Half stages	2	2
12	High aspect ratio	6	5
13	High aspect ratio	1	1

Table 8-5. List of Parameters Study 1.

Classification	Parameter Name	Set or Active	Value/Range	
System Specification				
	Regenerator Span	Set	35	K
	Mass of MCM	Set	0.5	kg
	Hot side rejection temperature	Active	34-40	C
	Cold side acceptance temperature	Active	5-11	C
Magnetic Regen System				
	Maximum Field	Active	0.9-1.5	
	Minimum Field	Set	0	
	MCM Structure	Set	Particle	
	Layers of MCM	Active	35,23,17	
	Regenerator Length	Active	12-38	cm
	Void Fraction	Set	36%	
	Particle Size	Active	.2-1	mm
Operational				
	Fluid Maximum Velocity	Active	.5-10	cm s ⁻¹
	Displaced Volume	Active	7.5-37.5	cm ³

Table 8-6. Study 2 additional parameters

Particle Diameter [mm]	Superficial Velocity [cm/s]	Regenerator Length [cm]
0.05	14	3.5
0.1	18	

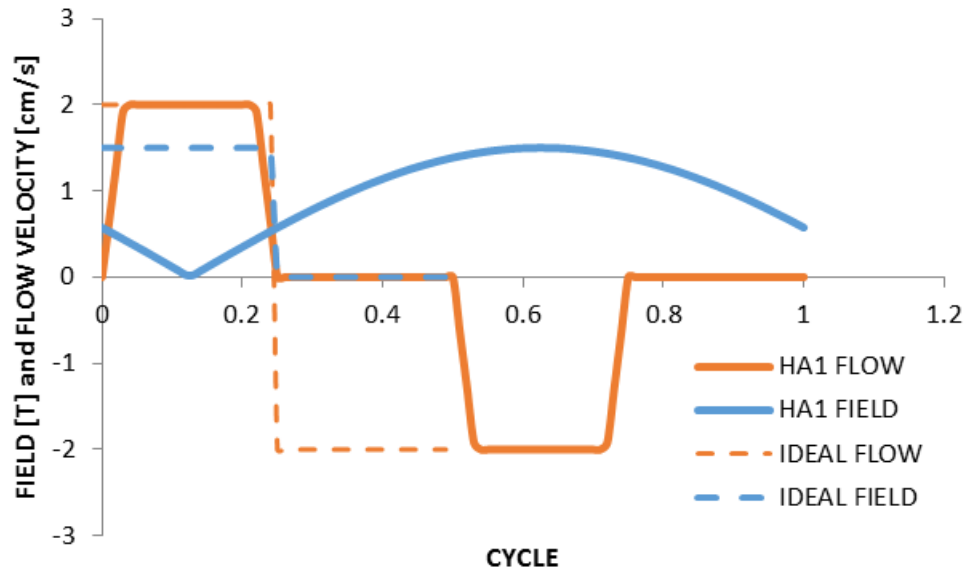


Figure 8-1. An example of HA1 operating with continuous magnet rotation and the same cycle under ideal operating conditions.

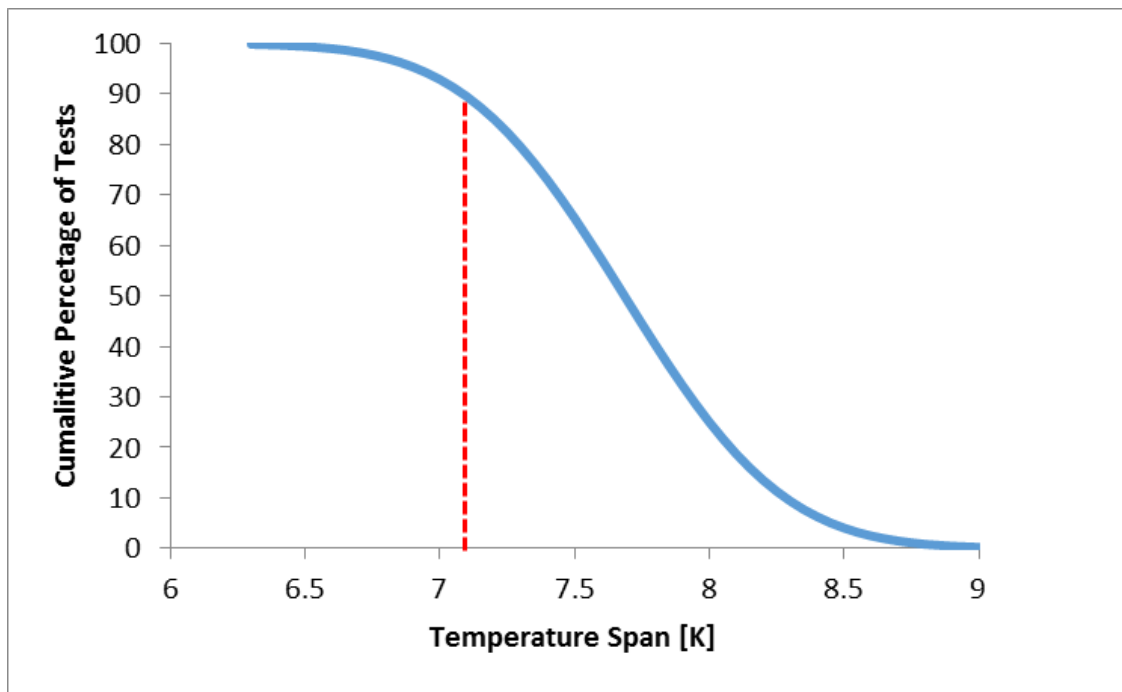


Figure 8-2. Cumulative distribution of spans at the knee point for experimental results.

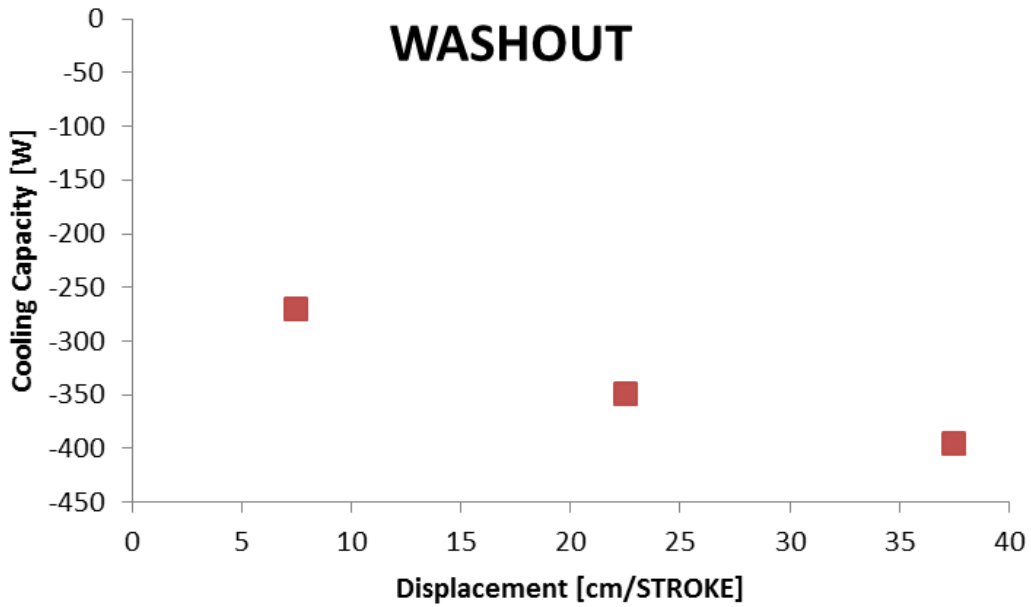


Figure 8-3. Average cooling capacity for all cases compared to displacement. Too much displacement may washout the MCE.

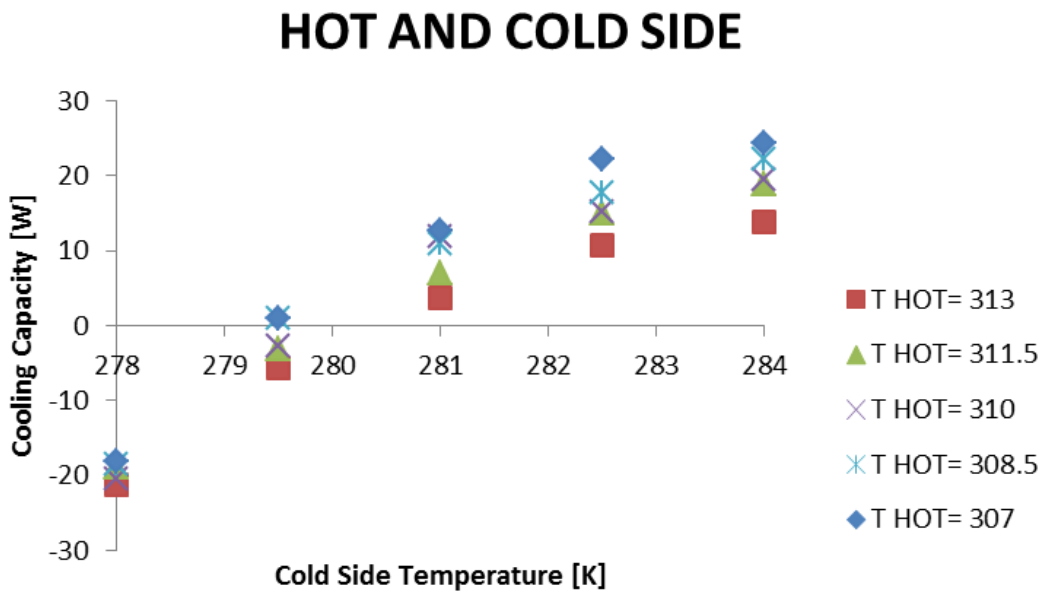


Figure 8-4. Full temperature data for a single set of MCHP design and operational parameters.

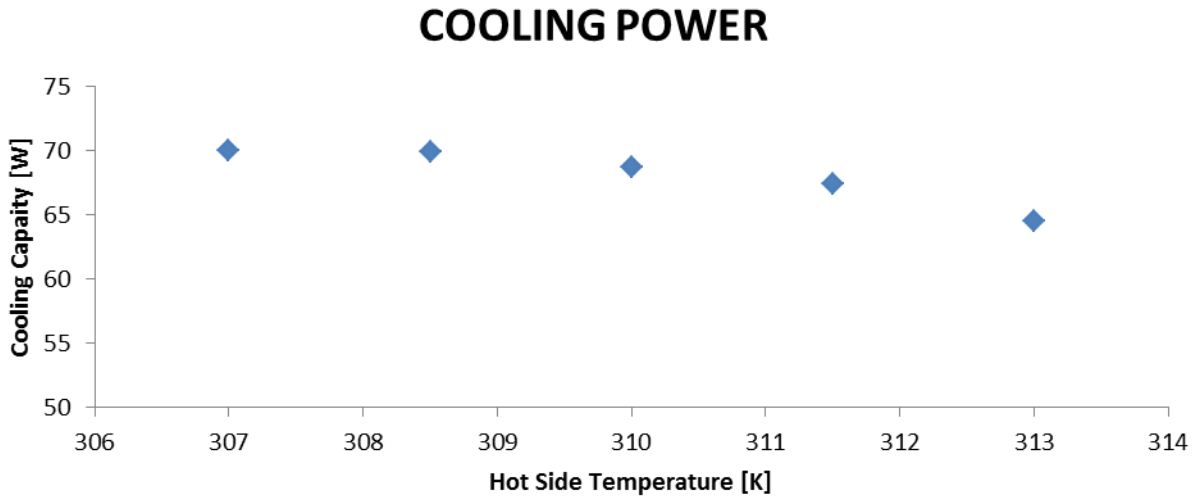


Figure 8-5. Cooling capacity averaged across the selected cases as a function of the hot side temperature.

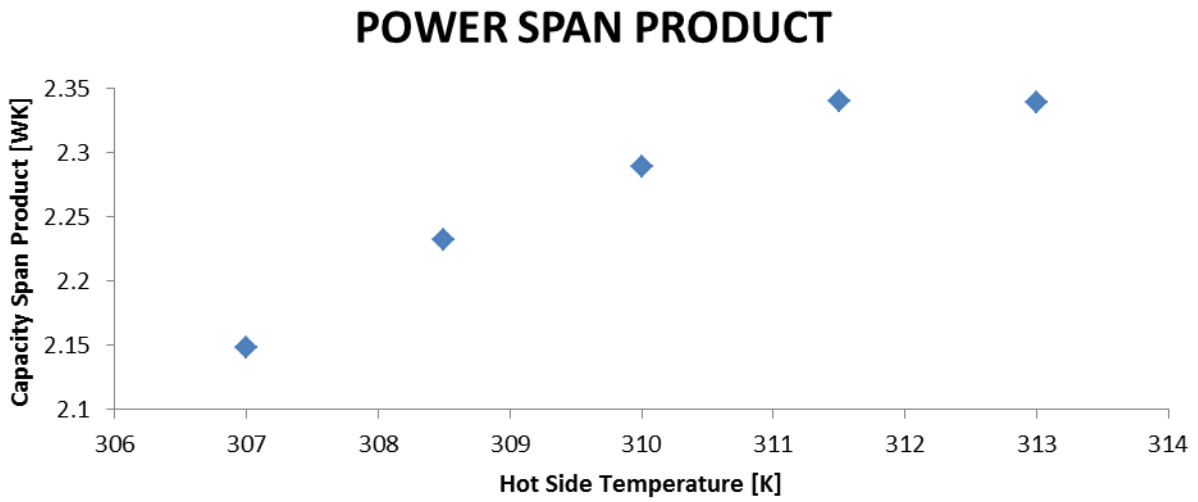


Figure 8-6. Cooling capacity span product averaged across the selected cases as a function of the hot side temperature.

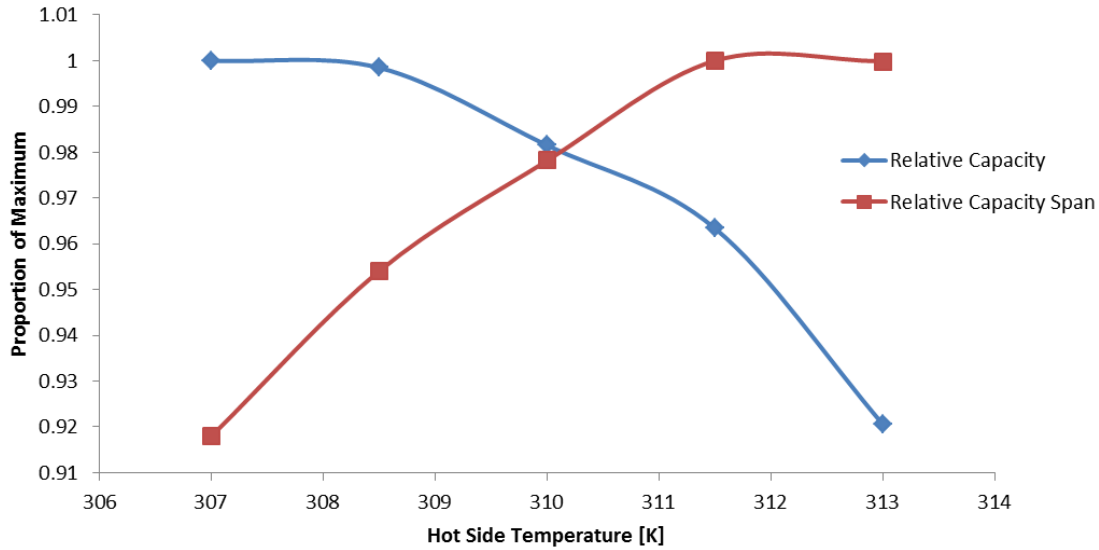


Figure 8-7. Relative cooling capacity and cooling capacity span product as a function of the hot side temperature.

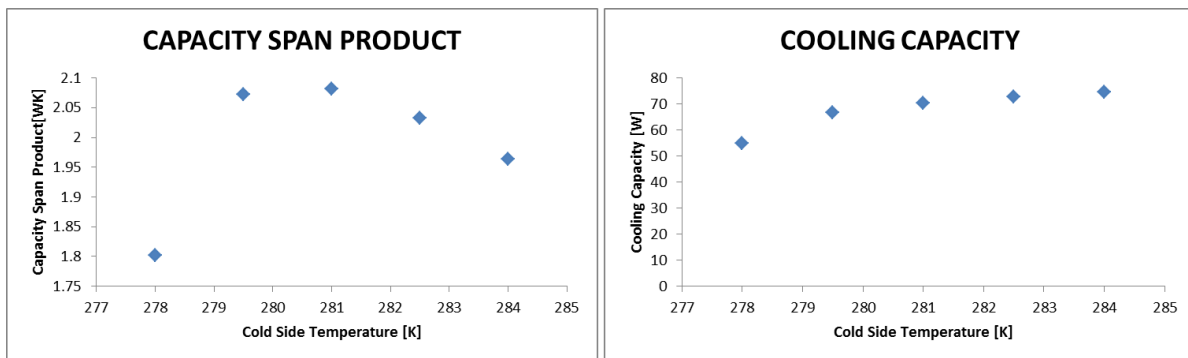


Figure 8-8. Average cooling capacity span product and cooling capacity as a function of the cold side temperature.

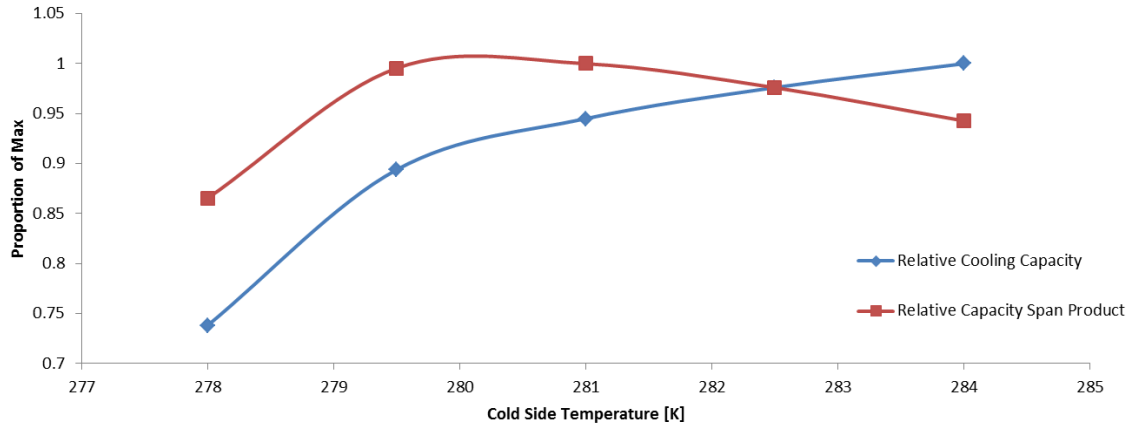


Figure 8-9. Average cooling capacity span product and cooling capacity normalized to maximums as a function of the cold side temperature.

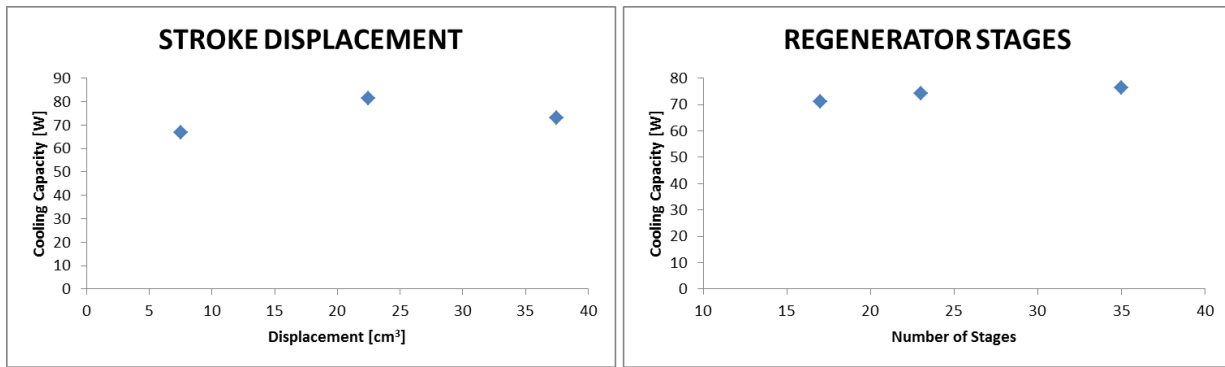


Figure 8-10. Parameters that have a local maximum or low impact on cooling capacity

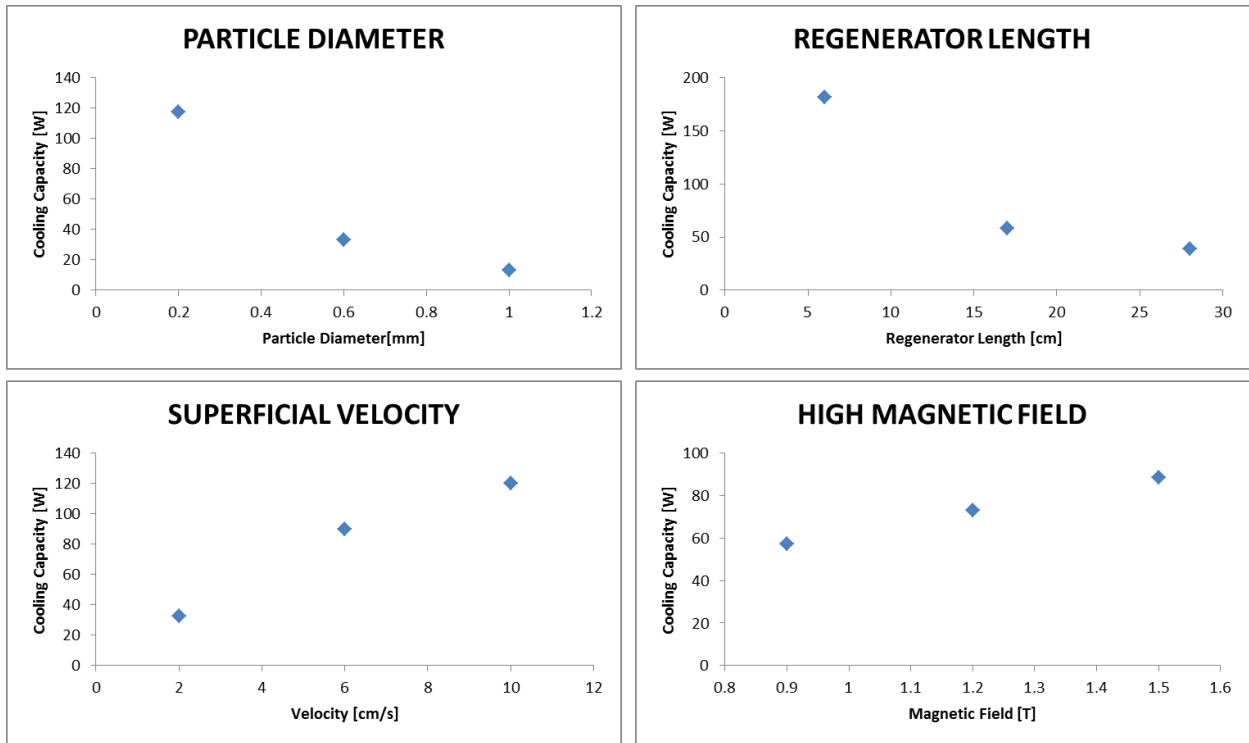


Figure 8-11. Parameters with a large average impact on cooling capacity.

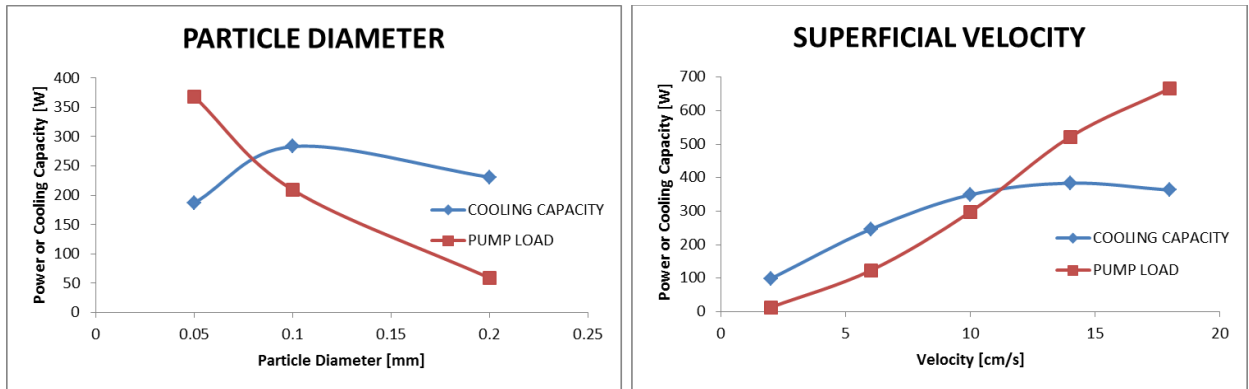


Figure 8-12. Cooling capacity and pumping power averaged as a function of particle diameter and fluid velocity from Study 2.

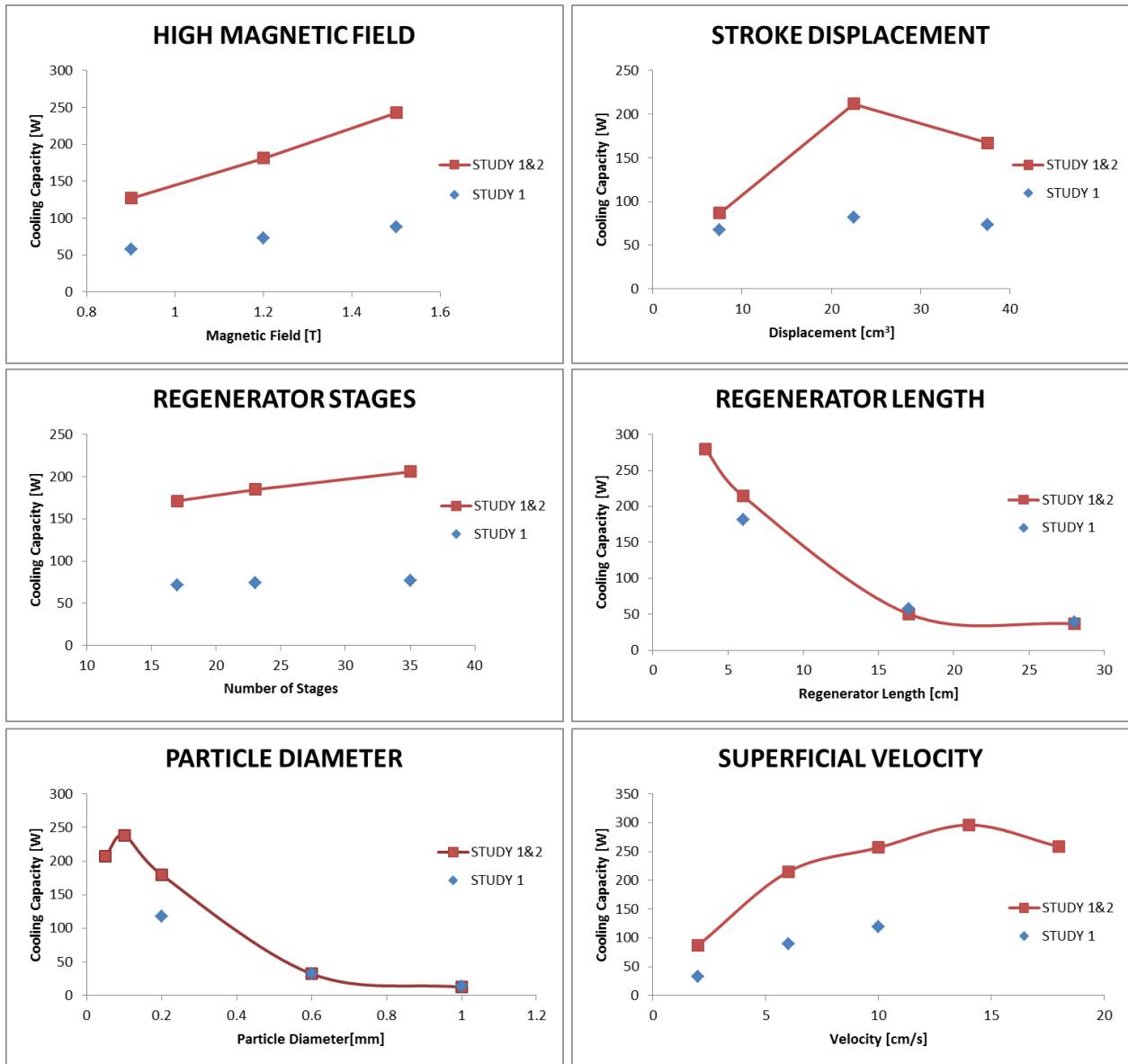


Figure 8-13. Combined results of Study 1 and 2 compared to the results of Study 1.

CHAPTER 9

MMM STUDY OF CURRENT MATERIALS PARAMETER SPACE

This chapter reviews details of a large AMR model study which combines both MCHP and material parameters. Work to expand the capability of the AMR model through code changes is reported. The results of the modeling study are reviewed with reference to the impact of magnetocaloric materials on MCHP performance. The original work involved in this chapter is under review for publication in the International Journal of Refrigeration.

The experiments of Chapter 7 confirmed the ability of the MMM to represent FOMT MCMs. Studies 1 and 2 of Chapter 8 identified a subset of the parameters that define the design and operation of a magnetocaloric heat pump. Chapter 8 also reduced the number of simulations necessary to analyze these parameters while maintaining the amount of useful information that comes from these simulations. This chapter will investigate the values of the constants that make up the MMM to better understand how magnetocaloric materials interact with magnetocaloric heat pumps.

AMR Model Simulation Time Reduction

Before beginning any studies involving the MMM parameters the AMR model speed had to be further increased. Chapter 8 reduced the number of simulations to describe the MCHP parameter space to just over 1000. There are seven MMM parameters from Table 8-2. The average run time from studies 1 and 2 was 640 seconds. If all of the MMM parameters were considered at three levels for all of the MCHP parameters this would result in 125 days of run time which is not feasible. For this reason the AMR model will be modified by changing the existing convergence criteria and adding new sections of code.

The first method for decreasing simulation time is to optimize the existing portions of the AMR model that control the convergence criteria. The AMR model terminates simulations when the change in cooling capacity for a cycle is less than a certain amount. Relaxing the convergence criteria will allow the AMR model to converge in fewer cycles. This increase in speed will come at the cost of accuracy.

Other speed increases involved changes to the operational structure of the code. The results from Studies 1 and 2 had a significant percentage of simulations that could be considered failed either do to non-convergent results, or negative cooling capacities. While these simulations may represent physically realistic situations they are far less useful when trying to understand the impact of the MCM properties on the performance of MCHPs. A large increase in speed can come from identifying these failed cases earlier in simulations and stopping them from proceeding.

The first new section of code is a limitation on the time for a simulation. This section of the code will check after every iteration in the code is completed to ensure that a maximum amount of time has not been exceeded. If the time has been exceeded the numerical simulation is assumed to be non-convergent and is terminated. The maximum amount of time for the simulations is set to twice the average amount of time from studies 1 and 2.

The second new section of code identifies simulations which are very likely to end with negative cooling capacities and terminates them as early as possible. To identify probable negative cooling capacities the cooling capacity of the simulation is checked based on two values shown in Equations (9-1) and (9-2)

$$\mathbf{dCL} = CL_c - CL_{c-1} \quad (9-1)$$

$$\mathbf{ACL} = dCL_c - dCL_{c-1} \quad (9-2)$$

where dCL is the change in cooling load, ACL is the acceleration of cooling load change, and the subscript c represents the cycle (i.e. c = current cycle, c-1 = previous cycle). The flowchart of the new section of code is shown in Figure 9-1. In Figure 9-1 t_{crit} is the maximum allowable simulation time, c is cycles, c_{min} is the minimum number of cycles dCL_{crit} is the change in cooling capacity between cycles that is set as the convergence criteria for the simulation.

At the end of each cycle the code now goes through a series of checks in order to determine if any of the criteria for ending the simulation have been met. The first criteria for termination of the simulation is a maximum time defined by t_{crit}. After this there is a check for c_{min} which if met enables the two checks which indicate if the simulation is likely to end in a negative cooling capacity. The first ends the simulation if ACL and dCL are negative for the current cycle. This would be the case if the current cycle simulation cooling capacity is less than the previous cycle cooling capacity and the current value of dCL is more negative than the value of dCL for the previous cycle. A simulation fitting these criteria is headed towards negative cooling capacity and is actually increasing the rate at which it is moving toward negative cooling capacities. The second check will terminate the simulation if the current cooling capacity is already negative and if the current cycle cooling capacity is more negative than the previous cycle cooling capacity. This would be the case only when a negative simulation is becoming more negative. In either of these cases the simulation would need to stop becoming more negative, change directions and then increase cooling capacity which is unlikely. Finally if none of the other termination criteria are reached than the simulation

is checked for convergence and either terminated if convergence is reached, or another cycle is run.

The selection of both dCL_{crit} and c_{min} can increase the speed of the AMR model at the cost of some amount of accuracy. The tradeoff between speed and accuracy is determined by Study 3. Study 3 utilizes the same parameters from Studies 1 and 2 while additionally varying dCL_{crit} and c_{min} . The levels of dCL_{crit} and c_{min} for Study 3 along with t_{crit} are shown in Table 9-1. dCL_{crit} and c_{min} are both kept at the level which leads to the most accurate answer while the other variable is being changed to help ensure that interaction is avoided. The case where dCL_{crit} is 0.001 and c_{min} is at the highest level is chosen as the basis of comparison because this was the dCL_{crit} that was used by default in Studies 1 and 2. The baseline additionally has higher t_{crit} than the rest of the simulations. Figure 9-2 shows the influence of dCL_{crit} on both the error and simulation time. The error is calculated as the absolute value of the difference between the baseline case and the current case. The average percent is taken relative to the baseline cooling capacity. For the calculation of the average error only simulations in which the baseline case had converged are considered. The percent reduction of simulation time is taken relative to the average simulation time for converged baseline cases. The percent reduction in simulation time includes only cases in which both the baseline and current case converged in order to avoid including reductions in time due to reducing the maximum cycle time. The percentage error in all cases is below 3% of the average baseline cooling load. It seems that as the convergence criteria is relaxed there may be a nonlinear increase in error at higher levels. The reduction in simulation time is very nonlinear at the lower levels of convergence criteria. The lowest level of

convergence criteria is actually lower than the baseline and has a negative value for reduction in simulation time indicating, as would be expected, that the simulation time increased on average. The benefits in time reduction decrease as the convergence criteria is relaxed with the greatest value approximately 30% faster than the baseline. With a non-linear increase in error and a non-linear decrease in benefit a value midway between the most relaxed case and the next closest case of 0.03 is selected going forward. If trends stay similar this value would represent only a 2% increase in error for a 25% increase in speed. Additionally this value is not close to a strongly non-linear portion of the error curve allowing some buffer in case of additional interactions between error and other variables to be studied.

Time reduction in C_{\min} is shown in Figure 9-3. As the minimum number of cycles is increased the amount of time reduction is decreased. In order to check the negative impact of ending simulations early based on the indication that they will become negative false positives were looked for. These are cases where the baseline eventually converged to a positive value, but the non-baseline cases ended early. No false positives were found indicating that the routines developed to terminate negative simulations early are effective. Since there seems to be no immediate drawback of this new piece of code the smallest c_{\min} is selected for studies moving forward.

Magnetocaloric Material Selection

In Chapter 8 a FOMT MCM was created from the average measurements of current MCMs. A new set of materials will now be created with the material from Chapter 8 as the baseline. In order to keep the results comparable while the constants of the MMM are varied a measure of the materials refrigeration capacity, the Total Refrigeration Capacity (TR_{cap}) has been created. Past attempts at comparing materials

normally involved defining a figure of merit which related to the refrigeration capacity of an MCM. These figures of merit have involved peak entropy changes, peak temperature changes, and integrations of entropy changes. While giving some comparative measure for the materials, they are inadequate to describe the ability of an MCM to perform in multistage MCHP (Engelbrecht and Bahl, 2010). The MMM utilizes the ΔT and zero field C_P to define the rest of the MCE properties, therefore these two characteristics are used to create a unique figure of merit which will be held constant for the MCMs of Study 4.

The heat absorption available from the MCM is related to the product of $M_{MCM}C_P\Delta T$ where M_{MCM} is the mass of the MCM. With the density assumed to be constant the mass term can be dropped for this constant volume study. The MCM is utilized in a cyclical manner with heat being transferred from the fluid to the MCM after the adiabatic de-magnetization step. The highest amount of heat that can be transferred takes place when there is zero-span which can be ascertained from Figure 7-11. In this limiting case the MCM is magnetized and demagnetized at the same temperature. Regenerators in steady state have a gradient of temperature from the hot to the cold end and across each stage: In cyclical operation a single stage of MCM will be at different temperatures at the start of demagnetization depending on its physical location in the bed. TR_{cap} takes into account all temperatures at which it is possible to absorb heat due to the magnetocaloric effect. The FOMT MCM specific heat is characteristically a strong function of temperature which must be taken into account. For heat absorption the ΔT will be taken on demagnetization and C_P at zero field. TR_{cap} can be described as the total heat across all temperatures that an MCM can absorb on

demagnetization. Equation (9-3) is the calculation for TR_{cap} independent of material mass

$$\mathbf{TRcap} = \int_{T=0}^{T=\infty} \int_T^{T-\Delta T} C_p T \, dT \, dT \quad (9-3)$$

Though the outermost integral is given for all temperatures, for the MMM TR_{cap} trends towards zero for temperatures far from the T_C of ΔT . TR_{cap} represents all possible heat that can be absorbed by a MCM. This does not mean that all materials with the same TR_{cap} will result in the same cooling capacity which will be apparent from the results of Study 4. It is not possible to directly calculate the double integral of TR_{cap} on the current MMM. A second piece of computer code was written to compute this value numerically. The values for the MMM are input in the same manner as the numerical simulation. Since, unlike the numerical simulation, the TR_{cap} is not calculated at every cycle the number of increments within the temperature space is increased to 2000 to help minimize error due to numerical integration.

The materials for Study 4 are produced to examine the effects of the MMM parameters on MCHP operation. The three and four parameters for ΔT and C_p are each varied from the baseline material of Studies 1-3 at three different levels in a full factorial manner. The goal of maintaining a constant TR_{cap} is to represent MCMs that do not require additional volumetric cooling capacity when compared to today's materials, and therefore might be more realistic in the short term. As such the TR_{cap} is maintained at the same level as that of the baseline material.

To create a constant level ΔT and C_p were separately evaluated. When either the ΔT or C_p parameter sets were altered based on factorial levels the other parameter set was scaled up or down without changing its shape to offset the change in TR_{cap} . The

necessity of calculating TR_{cap} numerically means that there is no closed solution to decide the scaling factor for offsetting TR_{cap} . An independent program was written to carry out this task by iteratively altering the scaling factor given a set of altered input parameters with the goal of converging on a TR_{cap} that was equal to the baseline material.

The program flow chart is shown in Figure 9-4. First either ΔT or C_p is altered based on the full factorial levels. The factorial levels for this MMM parameter are held constant and the other MMM parameter is scaled. The convergence criteria is set to $\pm 0.01\%$ of the baseline material TR_{cap} . An example of a material which has been altered compared to the baseline material is shown in Figure 9-5 to illustrate how scaling is applied. In Figure 9-5 the MMM properties of the ΔT have been changed factorially creating a new ΔT with a unique shape. The code from Figure 9-4 has scaled the C_p for this new material such the TR_{cap} is the same as the baseline. The shape of the new C_p , however, remains the same as the baseline case though the width and amplitude are smaller.

The materials created for Study 4 were also checked to ensure that there are no physical properties that violate the laws of thermodynamics. As described in Chapter 6 the use of two properties to determine the other properties of a material ensures that the thermodynamic properties close which carries over to Study 4 where ΔT and C_p are used. There are other ways to violate the laws of thermodynamics which becomes the basis for the selection of factorial levels for Study 4.

The first concern is a C_p which has a value less than the base value for C_p or even below zero. This can happen as the Amplitude of C_p is scaled down to offset

larger values for ΔT . The second concern is a ΔT which has a slope less than negative 1 described in Equation (3-21). Nielsen et al. (2010) gives a detailed description of how this violates thermodynamics. The first violation can be directly detected when A_{Cp} is less than 1. The second violation is detected by calculating the derivative of the MMM ΔT at the positive root of the second derivative of ΔT by Equations (9-4) and (9-5) respectively

$$\frac{dMMM}{dT} = \frac{2A(T-T_C)}{(SW)^2 \left(\frac{(T-T_C)^2}{(SW)^2} + 1 \right)^2} \quad (9-4)$$

$$\text{Second Root } \frac{d^2MMM}{dT^2} = \frac{3\sqrt{SW}-3T_C}{3} \quad (9-5)$$

Equation (9-4) is given only for the $T > T_C$ half of the MMM for ΔT . This is the half which has a negative slope. Equation (9-5) is only one root of second the derivative of the MMM. This root represents the maximum slope on the $T > T_C$ side of ΔT . Equation (9-4) must be greater than negative one in order for the MMM parameters to be valid.

To pass these two checks the values for $A_{\Delta T}$ and $W_{\Delta T}$ are limited to 15% above and below the baseline. The same variation is applied to A_{Cp} , W_{Cp} , and offset in $C_P T_C$ (O_{Cp}). S for both ΔT and C_P is such that 1 is the midpoint of the three values considered. This effectively changes which side of T_C has a greater width with a value of 1 having symmetric widths.

Table 9-2 shows the values which were used. All of the values represent the properties of the MCM at 1.5 Tesla which is the maximum used in the studies. Equation (7-4) can be used to show that lower magnetic fields only have the effect of lowering $A_{\Delta T}$ which being on the numerator of Equation (9-4) can only result in a more positive

maximum negative slope; meaning that there is no danger of violating the laws of thermodynamics by studying the materials of Study 4 at different magnetic fields.

Much of the reporting on MCMs and other figures of merit focus on ΔS . The following equations can help to relate this work to ΔS and ΔS based figures of merit. ΔS is not directly studied here, but is indirectly varied. A loose relationship for realistic FOMT MCMs can be made between the ΔT and C_p parameters and the peak and width for ΔS by considering the simplified MMM of Chapter 3. For these purely first order materials the peak value of ΔS will be given by Equation (9-6)

$$A_{\Delta S} = \frac{A_{Cp}}{T_{c_{Cp}}} \quad (9-6)$$

Real FOMT MCMs are not instantaneous. Equation (9-7) gives an approximate relationship between the MMM parameters for a non-ideal first order C_p and $A_{\Delta S}$

$$A_{\Delta S} \approx \frac{A_{Cp} W_{Cp}}{T_{c_{Cp}}} \quad (9-7)$$

Magnetocaloric entropy change and temperature change must always be present over the same range of temperatures. For this reason a good approximation for $W_{\Delta S}$ is simply $W_{\Delta T}$.

Results

Each of the new materials that were created for Study 4 were simulated for all of the cases from Study 1 and Study 2. Study 4 consisted of 125,000 runs with an average run time of 400 seconds. The runs had a completion percentage of 65%, of which 96% were positive. The incomplete runs consisted of four different cases which caused the simulation to end. Two of the cases account for the majority of the cancelled runs. Divergent cases have temperatures which are far outside the realm of normal operation

and are normally due to an extremely poor choice of variables. Runs that have timed out have exceeded the maximum simulation time. The maximum simulation time was set as described above and is necessary for the simulation to operate reliably.

Simulations can also be terminated by reaching a maximum number of cycles, or by the case described earlier in which a simulation is heading toward a negative cooling capacity. Figure 9-6 shows a breakdown of how the Study 4 runs were completed.

To further break down the modeling results each of the parameters has been analyzed in terms of how the run was ended. This comparison can provide insight into the sensitivity of the AMR model and may be useful for other AMR models which operate based on the same fundamental equations. Runs that timed out or reached the maximum number of cycles are combined into a “failed-to-converge” category. Runs stopped for heading in a negative direction are not considered because the impact of individual parameters on performance is evaluated in detail separately. Figure 9-7 shows the percent of the runs in each category by the level for each physical parameter. The number of simulations that were run at each level of the parameters is not evenly distributed because of the work done in Studies 1 and 2. The percentages are, therefore, best compared to the convergent case. Magnetic field and fluid velocity both show similar values across each of the parameter levels for the different termination conditions. This means that a similar percentage of runs terminated due to convergence at all levels of these parameters and that the AMR model is not very sensitive to these parameters in terms of its ability to converge. The number of stages and regenerator length show a generally positive correlation for both non-convergent cases. The percentage of divergent and failed-to-converge cases for these two parameters starts

below that of the convergent cases. As the value of these parameters increases the percentage of divergent and failed-to-converge cases increases to and surpasses the percentage of convergent cases. Displacement shows the opposite trend with both failed-to-converge and divergent cases starting at higher percentages at lower levels of displacement relative to convergent cases and ending at lower percentages than convergent cases for higher displacements. Convergent cases are relatively high for simulations of 0.2 mm, with no other discernable trend present.

The same evaluation cannot be carried out for the material parameters because, as a result of scaling for constant TR_{cap} , the levels of the parameters are nearly continuous. An observation can be made based on whether the ΔT or C_p was altered based on the full factorial design. The input for Study 4 was 25% runs where ΔT was altered at factorial levels and 75% where C_p was altered at factorial levels. The percentage of converged results is very similar to this starting percentage. The percentage of divergent and failed-to-converge cases differed greatly from the input. Failed to converge were made up of 67% runs where ΔT was altered based on factorial levels, while the divergent cases were only 1% runs where ΔT was altered based on factorial levels. Whether to ΔT or C_p was changed to the factorial levels did not greatly influence the likelihood of a run converging, but runs that were not convergent were much more likely to be divergent when C_p was altered to the factorial levels.

Average Impact MMM of Parameters

Having established that the MMM parameters did not cause an uneven mix on the converged outputs the individual parameters were analyzed. The main effects or average influence on MCHP performance is first considered. In order to assess the relative impact of each of the variables at their different levels the average cooling

capacity was normalized to the maximum average cooling capacity within each MMM parameter and is referred to as β as in Equation (9-8)

$$\beta = 100 \times \frac{Q_C}{Q_{\max}} \quad (9-8)$$

where Q_C is the cooling capacity and Q_{\max} is the maximum cooling capacity. Efficiency is reported in terms of second law efficiency (ϕ) and is referred to simply as “efficiency”.

The Carnot coefficient of performance is calculated for the heat exchanger defined at the beginning of the study. The simulated COP is calculated from cooling capacity and rejected heat rate Q_H , both of which are calculated as energy balances for the fluid leaving and returning to the cold and hot ends of the regenerator as in Equation (9-9)

$$\phi = 100 \times \frac{\left(\frac{Q_C}{Q_H - Q_C}\right)}{\left(\frac{T_{\text{Cold}}}{T_{\text{Hot}} - T_{\text{Cold}}}\right)} \quad (9-9)$$

The levels of the parameters were also normalized to the baseline material case which was the middle level for every MMM parameter except S. S was not normalized as the middle value is one. Figure 9-8 shows an example for the MMM parameter ΔT amplitude. In Figure 9-8 the cooling capacity is normalized to 275 Watts which is the maximum average cooling capacity. The amplitude is normalized to 3.64 which is the amplitude for the baseline material. The absolute values for the rest of the values can be found in Table 9-2.

Normalizing all of the cooling capacities and parameter levels allows for the MMM parameters to be compared directly to each other in terms of relative impact on average performance as shown in Figure 9-9. Skew was selected differently than amplitude and width so it covers a slightly extended range. Width shows the least impact on average cooling capacity of the three ΔT parameters. All of the results for width were within 5% of each other. This indicates that on average the width has the

lowest impact on performance. Skew has a larger impact on average performance. The relationship between average cooling capacity and skew is nearly linear. Larger skew numbers results in lower average cooling capacity. The larger skew will have a greater width on the $T > T_C$ side of ΔT . Amplitude had the greatest impact on the average performance. Larger amplitudes greatly increased average cooling capacity. The response is nearly linear in the range that was tested with a slope of 1.25. This slope means that the average performance increases 1.25% for every 1% increase over the baseline amplitude. With such a large slope this result is an indication that the performance of a magnetocaloric heat pump is greatly improved by materials which have a higher amplitude ΔT even when the overall cooling capacity available for these materials is maintained.

Specific heat was normalized in the same manner. Figure 9-10 shows the normalized results from Study 4 for the runs which varied C_p at the factorial levels. Similar to the adiabatic temperature change the width of specific heat did not have a large impact on performance. Total average variation over the levels of width was just over five percent. Unlike the relationship between width and performance for ΔT increasing widths corresponded to universally decreasing cooling capacity.

Offset and amplitude were similar in their impact on average cooling capacity. Both showed peak cooling capacity near the baseline value. In both case values above the baseline have higher performance than the value below the baseline. The minimum value of performance for both the amplitude and offset is around 82% of the maximum.

The amplitude of C_p had a non-linear relationship to the average cooling capacity. The greatest cooling capacity was found at the middle value of A_{C_p} . The

relationship between amplitude and performance for C_p showed much less impact than the same relationship for ΔT .

Skew of C_p had a similar impact on performance as skew for ΔT . In both cases the lowest average performance was roughly 80% of the peak performance. In both cases the relationship between increasing skew and performance was universally negative. For C_p , skew showed a non-linear relationship with performance. The response for lower values of skew seemed to be more sensitive than that of higher values.

An Analysis of the Usefulness of Averaging

The material and MCHP parameters studied were analyzed in terms of their impact on MCHP cooling capacity and efficiency. The large parameter space lead to a large number of runs having poor performance, or not having useful cooling capacity as shown in Chapter 8. One result of this trend is that both cooling capacity and efficiency were heavily weighted toward low performance in terms of the number of successful runs. This fact is exemplified in Figure 9-11 where the percentage of successful runs is compared to ϕ and the β . In Figure 9-11 the percentage of runs (Y axis) completing at least the performance indicated on the X axis is compared. There is an exponential decay toward zero with the majority of runs achieving less than 50% of the maximum performance for either β or ϕ . As a result of this general trend the average performance of any parameter gives much more information about the low performance runs. This is not desirable if the goal is to understand how parameters can lead to high performance.

To better illustrate the ability of parameters to create high cooling capacities and efficient running conditions the percentage of total runs attributed to a parameter is analyzed with respect to the relative performance. An example of this form of analysis is

shown in Figure 9-12. The vertical axis of Figure 9-12 is the percent of simulations at the given level of β . For example, the point marked with a star on the 1.15 line can be interpreted as 65% of the simulations achieving 85% of the maximum cooling capacity having a ΔT with a relative amplitude of 1.15. As β increases towards 100% an increasing portion of the successful simulations came from the largest amplitude ΔT . The low amplitude ΔT accounts for no simulations above 80% of maximum cooling capacity.

Figure 9-13 is a similar comparison but with the amplitude of C_p being the parameter. Above 80% of maximum cooling capacity, none of the simulations come from the materials for which the C_p parameters were varied. This also reinforces the findings of Engelbrecht and Bahl (2010) since the amplitude of C_p is most directly related to the amplitude of entropy change on magnetization as described in Equation (9-6) and (9-7). This result is especially interesting because the number of starting simulations for the C_p parameter set was three times the size of that for the ΔT parameter set due to the additional MMM parameter of O_{Cp} .

This method of analysis offers an increased amount of information in comparison to simply considering average performance. For comparison Figure 9-9 and Figure 9-12 both show the effects of $A_{\Delta T}$ on cooling capacity. From both the conclusion can be drawn that the highest $A_{\Delta T}$ was correlated to higher cooling capacities. Additionally Figure 9-12 shows that the lowest levels of $A_{\Delta T}$ lead to virtually none of the high cooling capacity simulations, while the highest level of $A_{\Delta T}$ is responsible for nearly two thirds of all high cooling capacity simulations. This overwhelming majority is not obvious in Figure 9-9.

The parameters of $W_{\Delta T}$ and $S_{\Delta T}$ are shown in Figure 9-14. The smallest widths correlated with the highest cooling capacities. This suggests that more narrow stages with higher amplitudes can lead to the greatest volumetric cooling capacity. ΔT with a neutral or positive skew was also correlated to high cooling capacities.

The remaining C_p parameters are shown in Figure 9-15. Materials having the median W_{C_p} resulted in the largest number of high cooling capacity cases. High cooling capacity was also correlated to materials with either type of skew, symmetric C_p resulted in the lowest number of high cooling capacity cases. The offset of C_p does not seem to be a particularly influential parameter with the number of high cooling capacity cases staying relatively close to the 1/3rd starting distribution.

MMM Parameter Impact on Efficiency

The impact of the MMM parameters on efficiency was analyzed. It is noted that the assumptions made in Chapter 8 mean that the COPs of this study are high compared to what would be achievable in a real MCHP where MCHP design dependent losses reduce efficiency. As previously explained ϕ from Equation (9-9) is calculated at the outlet of the regenerator for the hot and cold side. This ϕ can then be thought of as the regenerator efficiency. By definition this efficiency does not include any losses that might occur due to additional system effects such as pressure drop in heat exchangers, pump efficiency, or motor efficiency. Therefore, it is best to consider the following results in relative terms to the other results of this study as opposed to absolute efficiencies that can be expected in MCHPs.

The material parameters are first compared to the average ϕ values from the study. Figure 9-16 shows the average impact of the ΔT parameters on ϕ . Amplitude has the largest impact on the efficiency of operation. Higher levels of $A_{\Delta T}$ lead to higher

efficiencies on average. The highest level of $A_{\Delta T}$ had an efficiency 39% higher than the lowest level of $A_{\Delta T}$. Width of ΔT had a nonlinear effect on the efficiency with the highest efficiencies predicted for the middle value of $W_{\Delta T}$ and the lowest efficiencies predicted for the lowest values of $W_{\Delta T}$. Higher levels of skew lead to decreased efficiencies. The lowest level of $S_{\Delta T}$ had a 13% higher efficiency than the highest level of $S_{\Delta T}$ meaning that efficiency is not as sensitive to $S_{\Delta T}$ as $A_{\Delta T}$. The average trends for efficiency with respect to ΔT MMM parameters look similar to the trends for cooling capacity. This stems at least partially from the fact that Q_C is a part of the calculation of ϕ . The average effect of the ΔT parameters on ϕ is, however, relative greater than on Q_C . The shape of the $W_{\Delta T}$ curve is also slightly different with the impact on efficiency leveling off for higher widths.

The average ϕ relative to the C_P parameters are shown in Figure 9-17. A_{Cp} has the greatest effect on efficiency of all the C_P parameters. The median value of A_{Cp} lead to 13% higher efficiencies on average than the low or high value. A similarly strong trend existed for O_{Cp} . The higher and lower values of O_{Cp} resulted in 7% and 10% lower efficiency predictions than the median value. Efficiencies universally decreased for increased W_{Cp} . The decrease in average efficiency was nearly linear with relative W_{Cp} , though the total decrease in efficiency was only 3% over the full range. Efficiency first decreased between the lowest and middle level of S_{Cp} and then leveled off for the highest level. The initial decrease in efficiency was on average 7%.

The impact of the material parameters on ϕ was also assessed in terms of the number of runs reaching high efficiencies. The most influential material parameters on efficiency were the amplitude of C_P and ΔT . Figure 9-18 shows the results from these

two parameters. Unlike β a continually increasing amplitude did not lead to an increasingly higher proportion of the highest ϕ values. For $A_{\Delta T}$ the highest fraction of the highest efficiency runs comes from the median level. For C_p the median and high level of A lead to a similar portion of high efficiency runs. Interestingly in both cases the lowest value of A contributes almost one quarter of the high efficiency runs. These results suggest that efficiency is less sensitive to the material parameters.

The remaining material parameters had even less impact on the proportion of high efficiency runs. The results from these parameters are shown in Figure 9-19. Of the remaining materials parameters only $S_{\Delta T}$ seems to have an impact on proportion of high efficiency simulations. The lowest values of $S_{\Delta T}$ resulted in a higher percentage of the most efficient runs.

MMM Parameters and Physical Parameters Interaction

Interactions between materials parameters and MCHP parameters are of interest because they can illuminate how the choice of materials in an AMR impacts the design of a MCHP. This is an area of research that as of yet has not been reported on in the literature. To simplify the data from this large set of input and output parameters three subsets of results are considered. The simulations which resulted 20% highest efficiencies, the simulations which resulted the top 20% of cooling capacities, and the simulations which had results that were in both the top 20% cooling capacity and top 20% efficiency.

For the following figures the material parameter is on the horizontal axis and is again presented in relative levels. The MCHP parameters are represented as different data series and are given in the absolute levels chosen for the study. The vertical axis is the percentage of simulations for the given subset of runs. As an example the number

of stages is compared to A_{Cp} for the top 20% most efficient runs in Figure 9-20. The point marked with a star is interpreted as simulations having the median level of A_{Cp} and 35 stages, accounted for 15% of the high-efficiency simulations. The result is three sets of 36 graphs. Only the results which showed significant interesting interaction are explicitly analyzed while the full sets of original figures are presented in the appendices. Interaction is recognized by a changing relationship between the material parameter and the measure of performance for different levels of the secondary MCHP parameter.

Highest 20% of Efficiency

Much of the research on AMR is based around the prediction that this technology can be more efficient than existing technologies. Figure 9-21 highlights the most interesting interactions from the highest efficiency subset of the results. Each of the first three graphs of Figure 9-21 is related to the magnetic field. The magnetic field represents a key driver to both cost and MCHP volume in AMR design (Rowe, 2011). Though a higher magnetic field universally lead to a higher percentage of efficient runs there were some beneficial interactions with material parameters. In particular higher $A_{\Delta T}$, higher $W_{\Delta T}$, and symmetric $S_{\Delta T}$, each lead to a relatively high percentage of the efficient runs, and a comparable percentage of efficient runs between the highest and second highest levels of magnetic fields. This indicates the possibility that materials with these characteristics might enable more MCHP designs with lower magnetic fields that still reach competitive efficiencies.

The last three figures of Figure 9-21 include graphs from both particle diameter and superficial fluid velocity. These two MCHP parameters are directly related to the maximum pressure in a MCHP. Pressure affects many non-cyclical aspects of MCHP design including limiting structural materials and seals choices. Lower pressure drops

can lead to cheaper components and more materials selection. Therefore lower fluid velocities and larger particle sizes can be advantageous to a MCHP designer. Though the second smallest particle size in the bottom left graph makes up the largest percentage of efficient runs, median and high levels of $S_{\Delta T}$ bring a particle size twice as large up to nearly the same percentage of efficient runs. In a similar manner low values of $W_{\Delta T}$ and $S_{\Delta T}$ enable a greater number of efficient runs for the lowest flow rate.

Highest 20% of Cooling Capacity

Cooling capacity is a key performance metric for AMR. This study was designed with a constant material mass so the cooling capacity reported is analogous to a volumetric cooling capacity when considered relatively. For the highest cooling capacities, a few MCHP parameters dominated the successful simulations. Figure 9-22 shows some examples of these MCHP factors as well as beneficial interactions with the materials parameters. The top row of Figure 9-22 shows the dominant parameters of the high cooling capacity runs. More than three quarters of all the runs came from the second smallest particle size and the shortest regenerator length. The smallest particle size greatly increases the rate of heat transfer from the MCM to the fluid which is a large factor in the cooling capacity of an AMR system. In order for that system to maintain a low pressured drop shorter regenerators with a wider frontal area are needed. The narrowest $W_{\Delta T}$ are most highly correlated with the small particles and short regenerator lengths. Interestingly fluid velocity, shown in the bottom right graph, seems to have relatively little influence on the number of successful runs. Outside of the highest and lowest fluid velocities most of the points are a few percentage different from each-other. There is also very little interaction with materials parameters. Most of the graphs look similar to the S_{Cp} graph shown. Similar to the high efficiency subset high values of $A_{\Delta T}$

help to offset the need for a high magnetic field which can lead to smaller and cheaper MCHP designs.

Highest 20% of Efficiency and cooling capacity

The high efficiency and high cooling capacity subsets isolated cooling capacity and efficiency from each other to allow for easier individual evaluation. In reality it is desirable for a prototype to combine high cooling capacity with high efficiency. Figure 9-23 shows some of the interesting trends from the subsection of simulations that had both efficiencies in the highest 20% and cooling capacities in the highest 20%. The first three graphs in Figure 9-23 shows that the small particle diameter and short regenerator length trends carried over from the high cooling capacity simulations. Since these runs are a subset of the high cooling capacity simulations this is not a surprise. It is however interesting to note that a High A_{Cp} is very strongly correlated to the 0.1 mm particles for high performance. Nearly all of the high cooling capacity and high efficiency runs have the highest two values of A_{Cp} with the 0.1 mm particles. Fluid velocity and displacement are much more important in this simulation subset. There is an interaction between lower fluid velocities and higher skew in ΔT .

For a full set of original results graph sets are shown for high efficiency, high cooling capacity, and high cooling capacity with high efficiency Appendices A, B and C respectively.

Table 9-1. Values for the speed up parameters from Study 3.

dCL_{crit}	C_{min}	t_{crit}
0.0500	500	1200
0.0100	500	1200
0.0050	500	1200
0.0010	500	2400
0.0005	500	1200
0.0010	100	1200
0.0010	200	1200
0.0010	300	1200
0.0010	400	1200

Table 9-2. Values for the MMM parameters to be used in Study 4.

Level	$A_{\Delta T}$	$W_{\Delta T}$	$S_{\Delta T}$	A_{Cp}	O_{Cp}	W_{Cp}	S_{Cp}
1	3.62	4.19	1.30	1774	-0.46	3.20	1.47
2	3.15	3.64	1.00	1542	-0.54	2.78	1.00
3	2.68	3.09	0.77	1311	-0.62	2.36	0.68

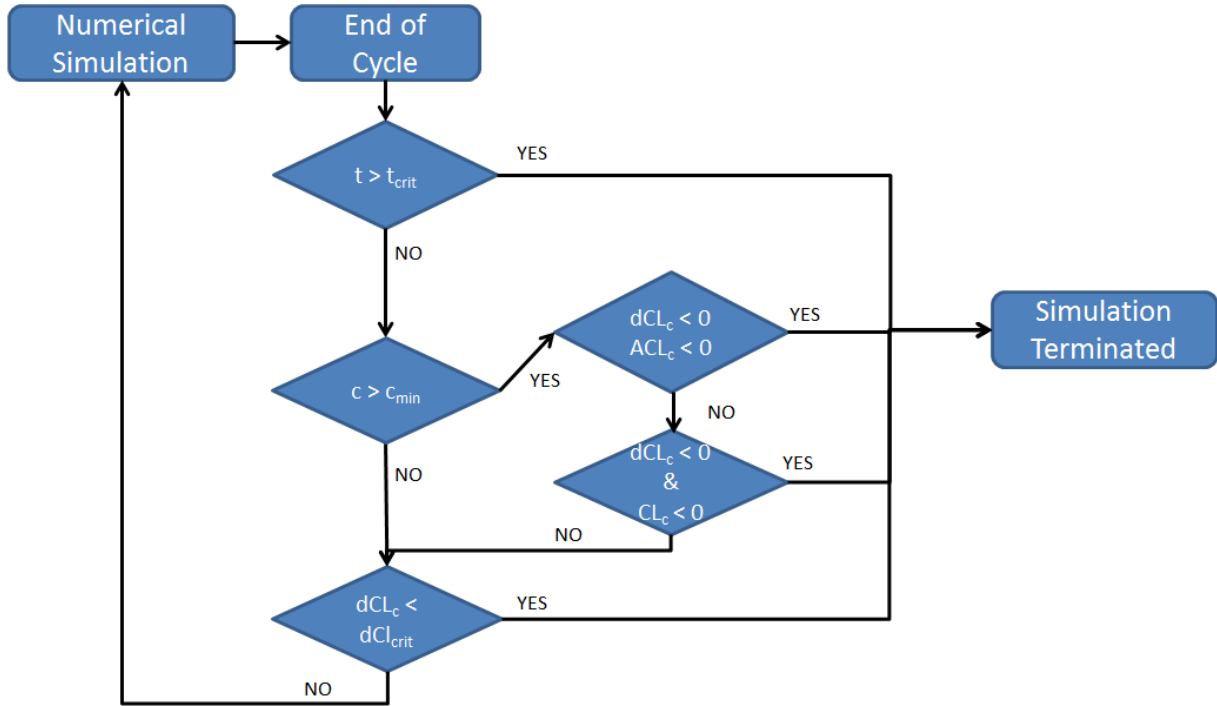


Figure 9-1. Flow diagram of additional code implemented to increase simulations speed.

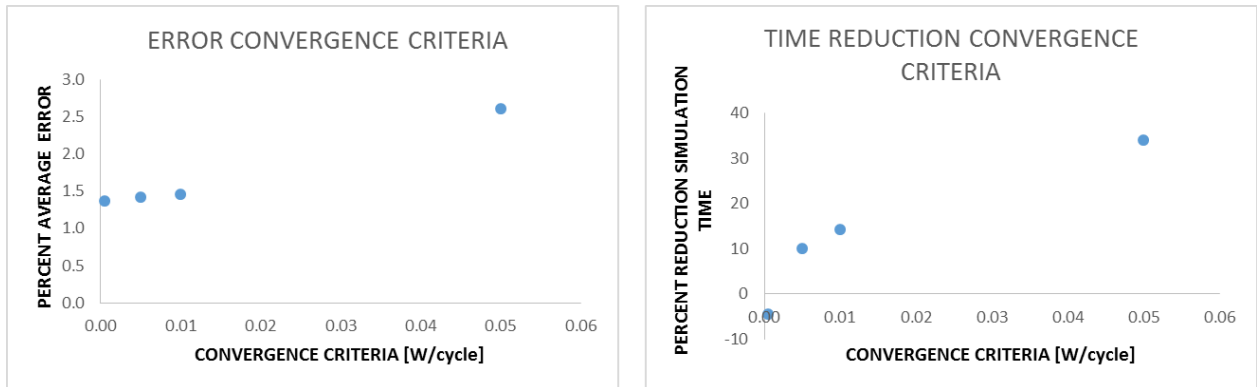


Figure 9-2. Results from convergence criteria study

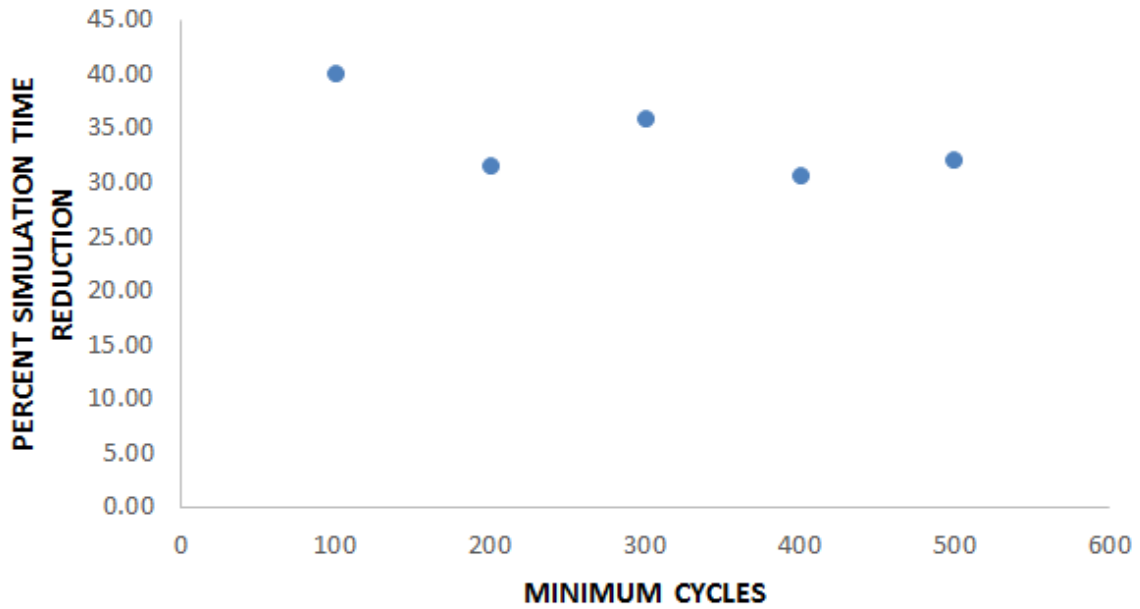


Figure 9-3. Effect on simulation time of c_{min} .

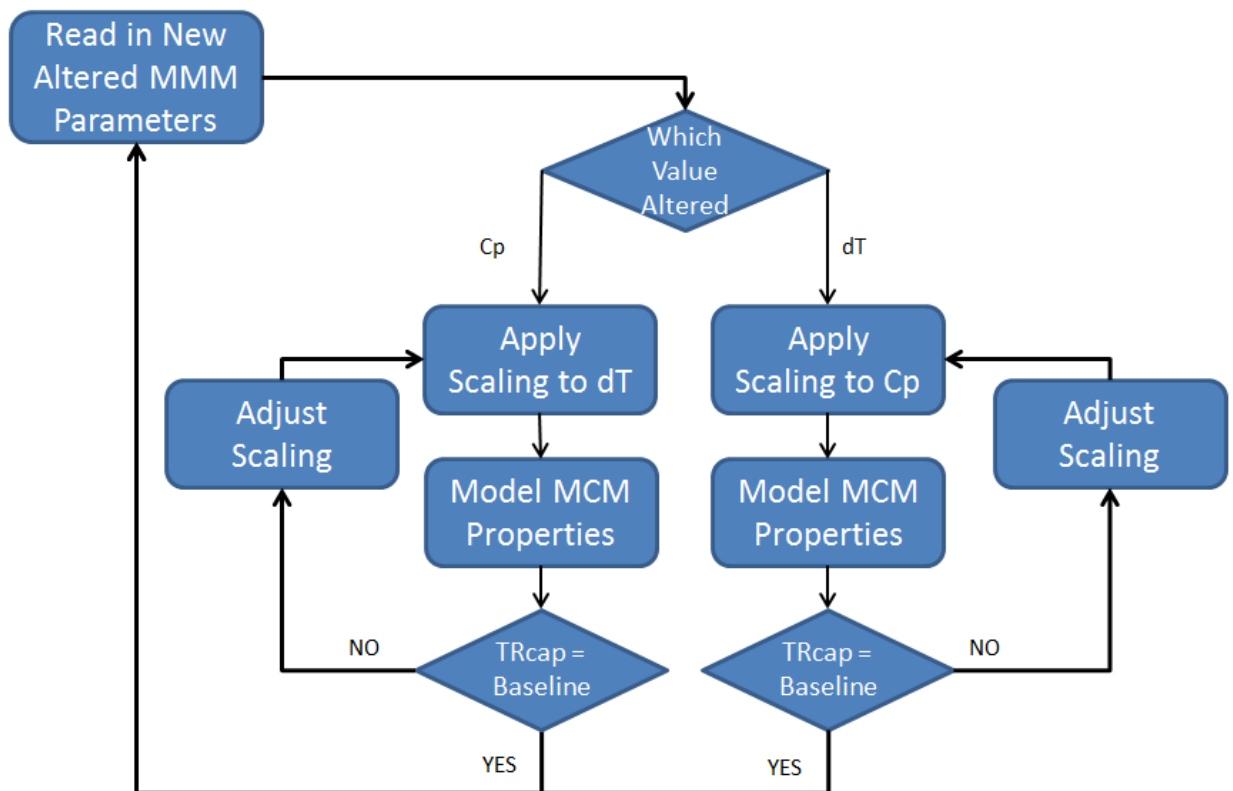


Figure 9-4. Code diagram for program which maintains a constant TR_{cap} for Study 4

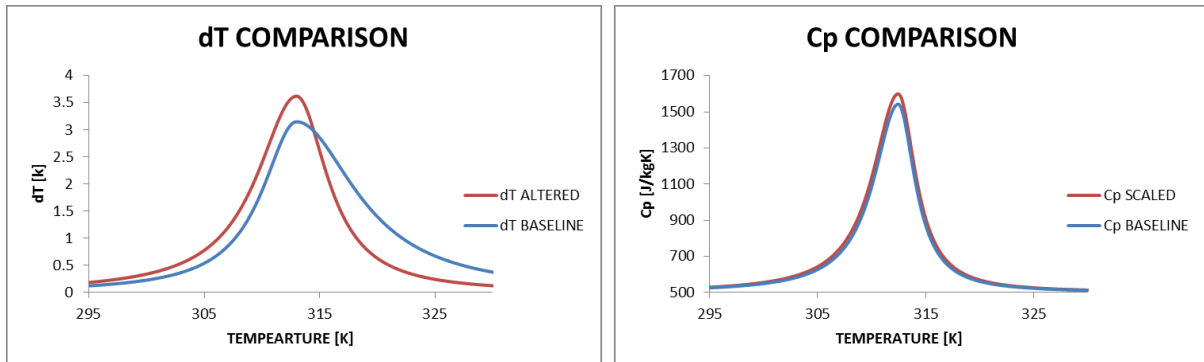


Figure 9-5. Example of a material from Study 4.

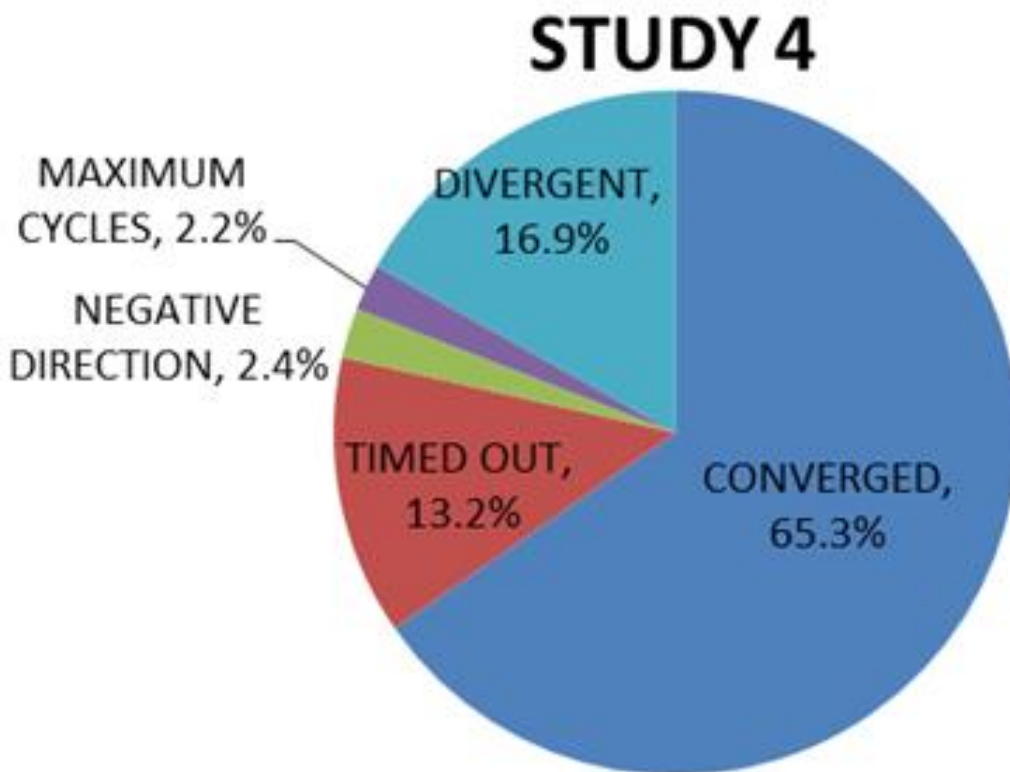


Figure 9-6. Results of the Study 4 runs.

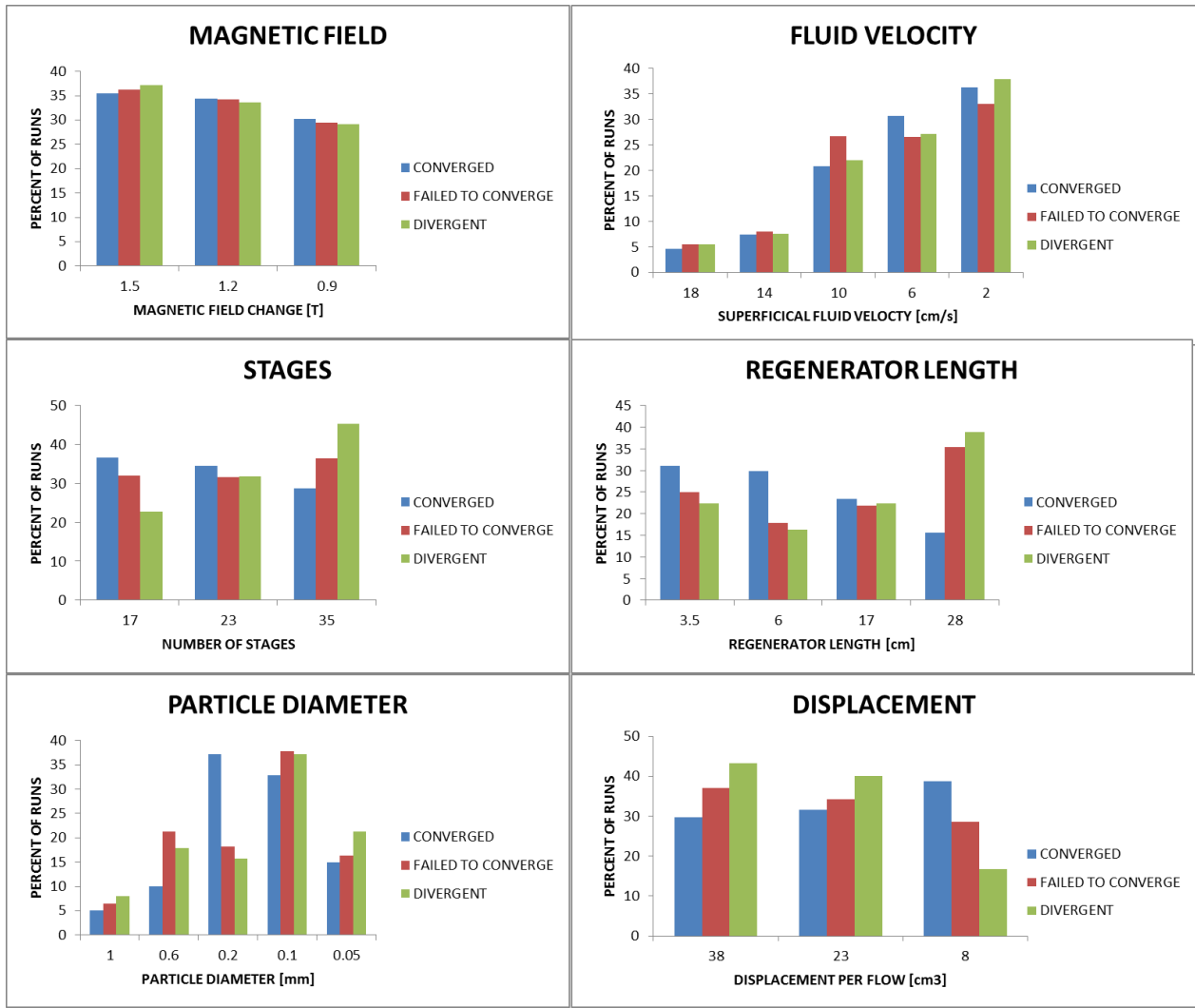


Figure 9-7. Physical parameters shown by the percentage of runs at each of the levels of the parameter based on the termination condition of the simulations.

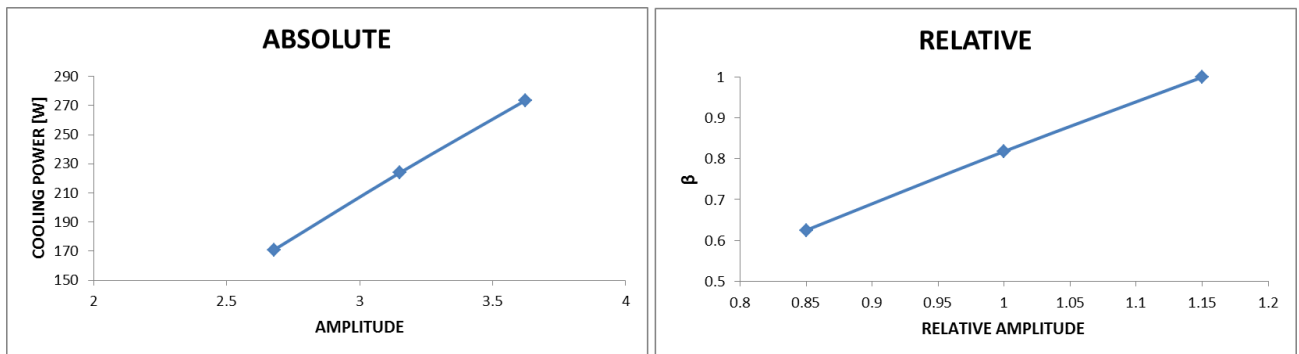


Figure 9-8. Example of how each of the MMM parameters is normalized.

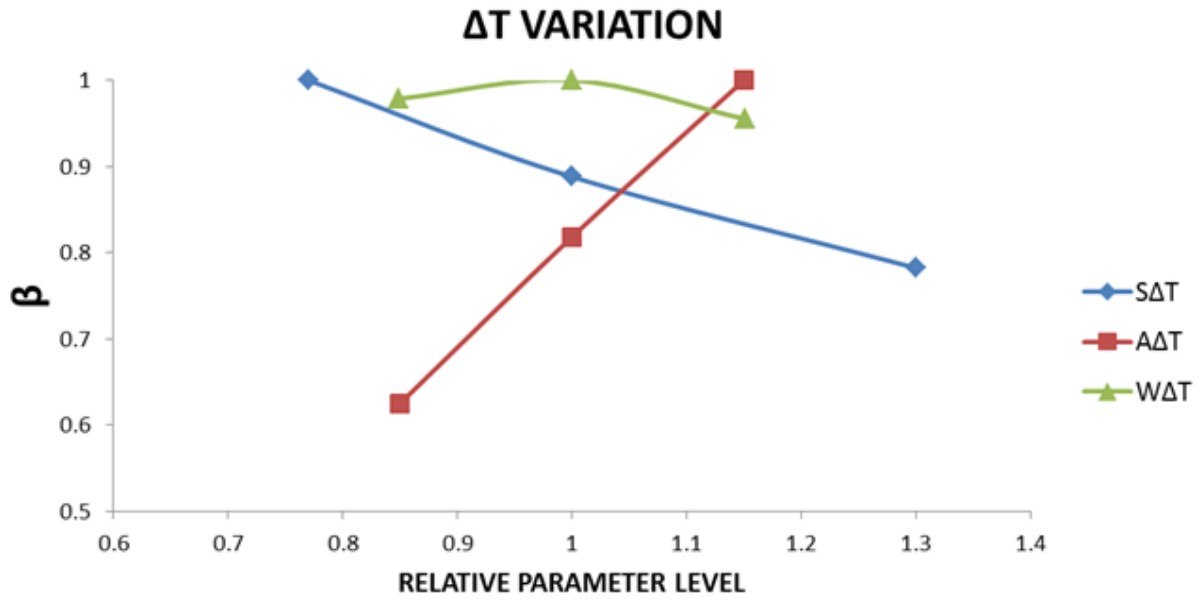


Figure 9-9. Comparison of the ΔT MMM parameters on average predicted performance.

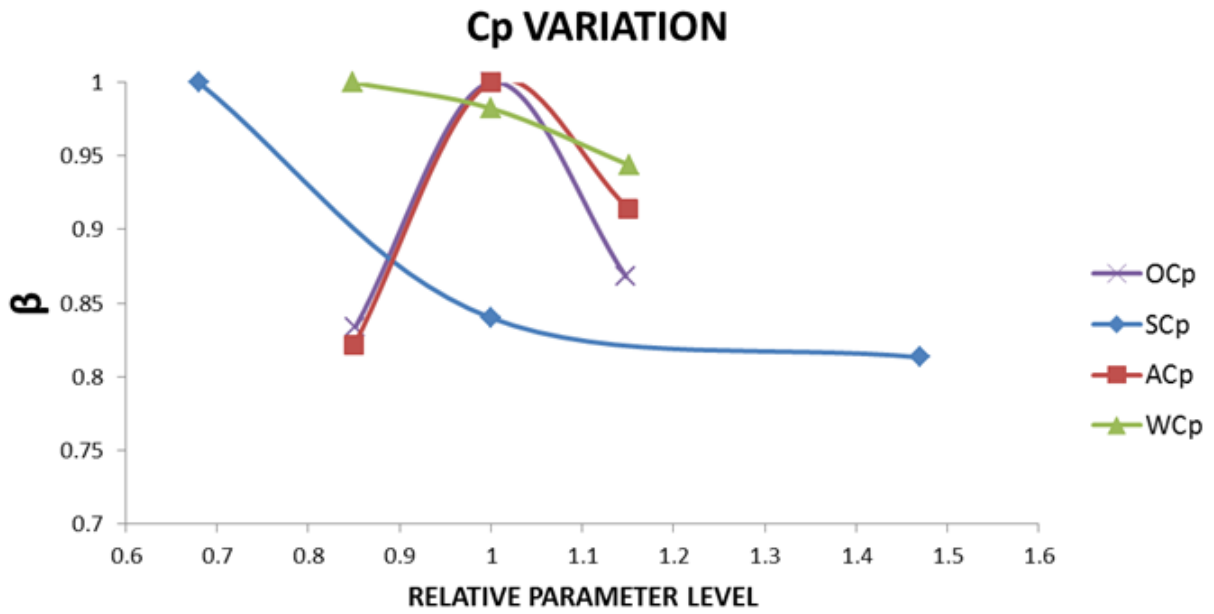


Figure 9-10. Results from Study 4.

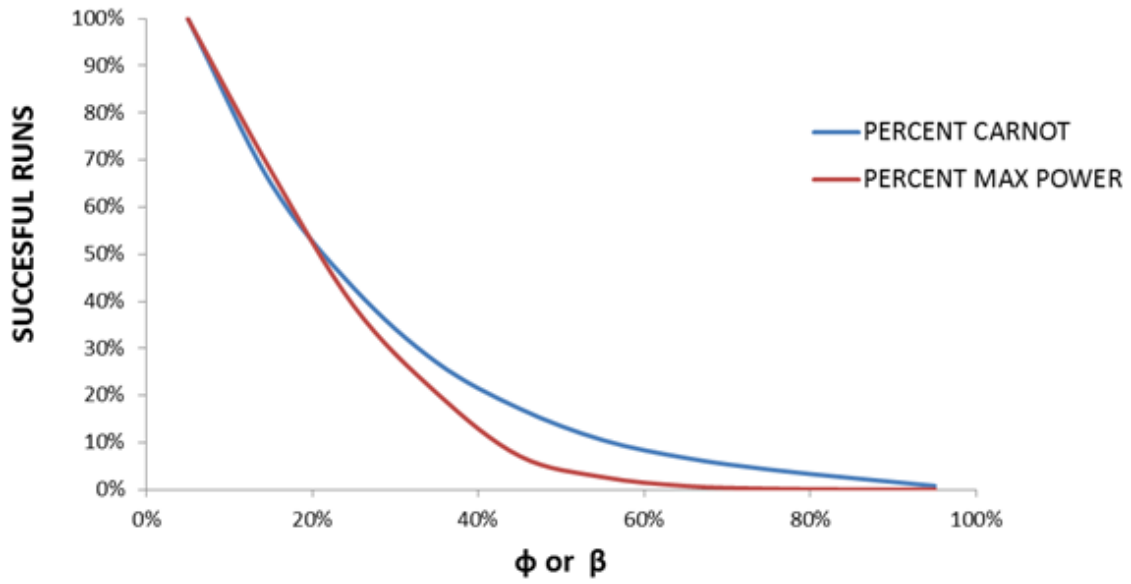


Figure 9-11. The distribution of completed runs compared to MCHP performance.

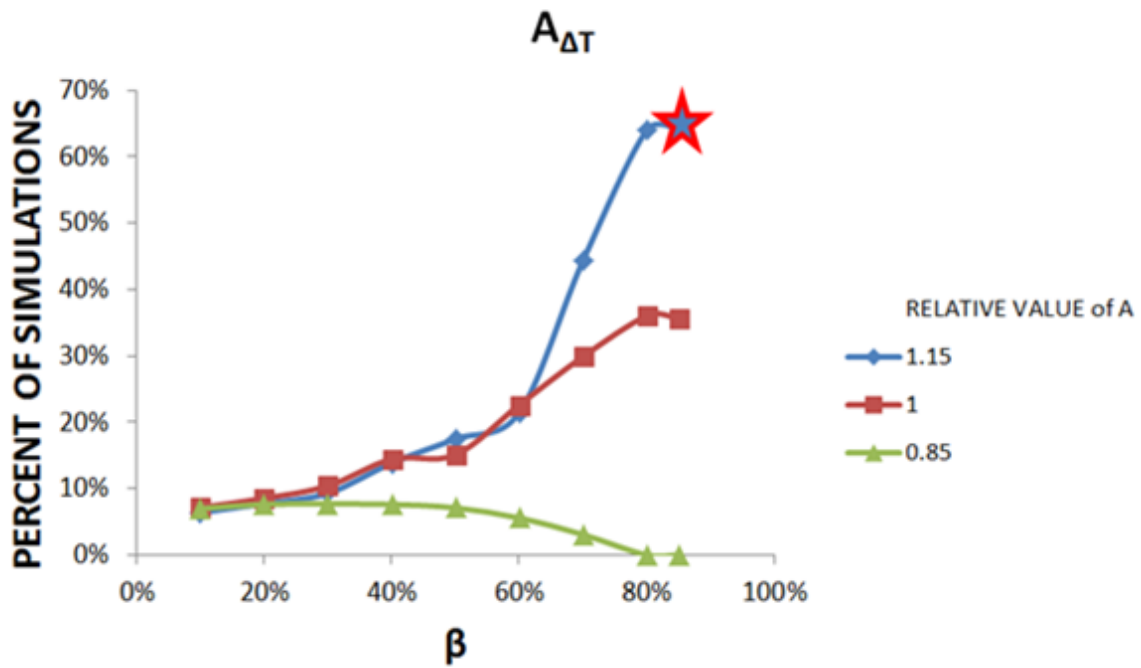


Figure 9-12. Effect of the amplitude of ΔT on cooling capacity.

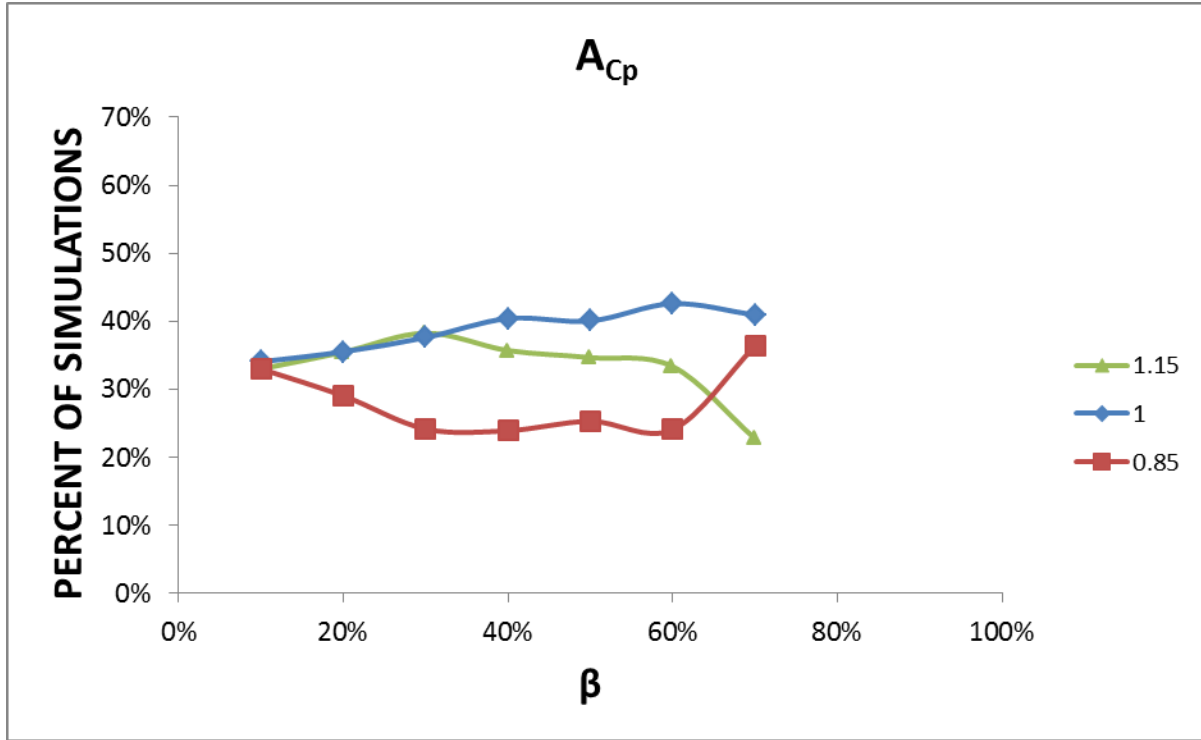


Figure 9-13. Effect of the amplitude of C_p on cooling capacity.

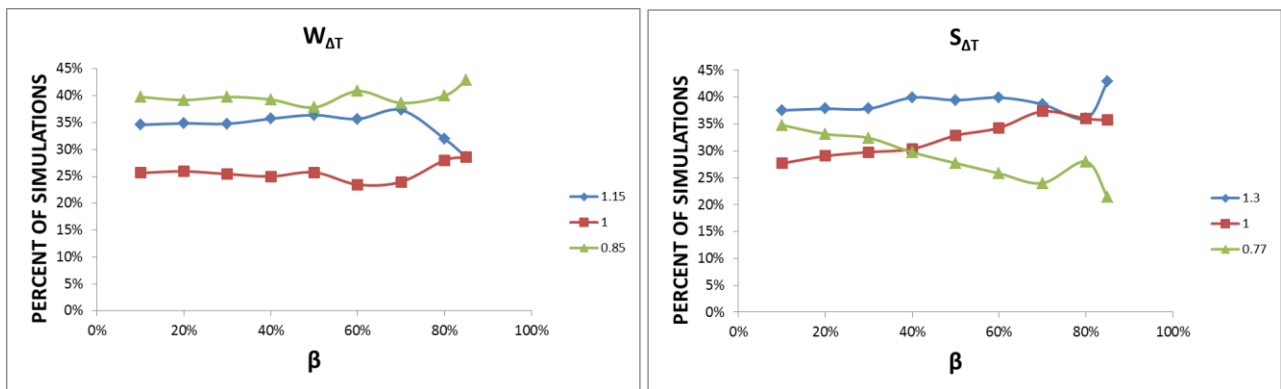


Figure 9-14. ΔT parameters' influence on cooling capacity.

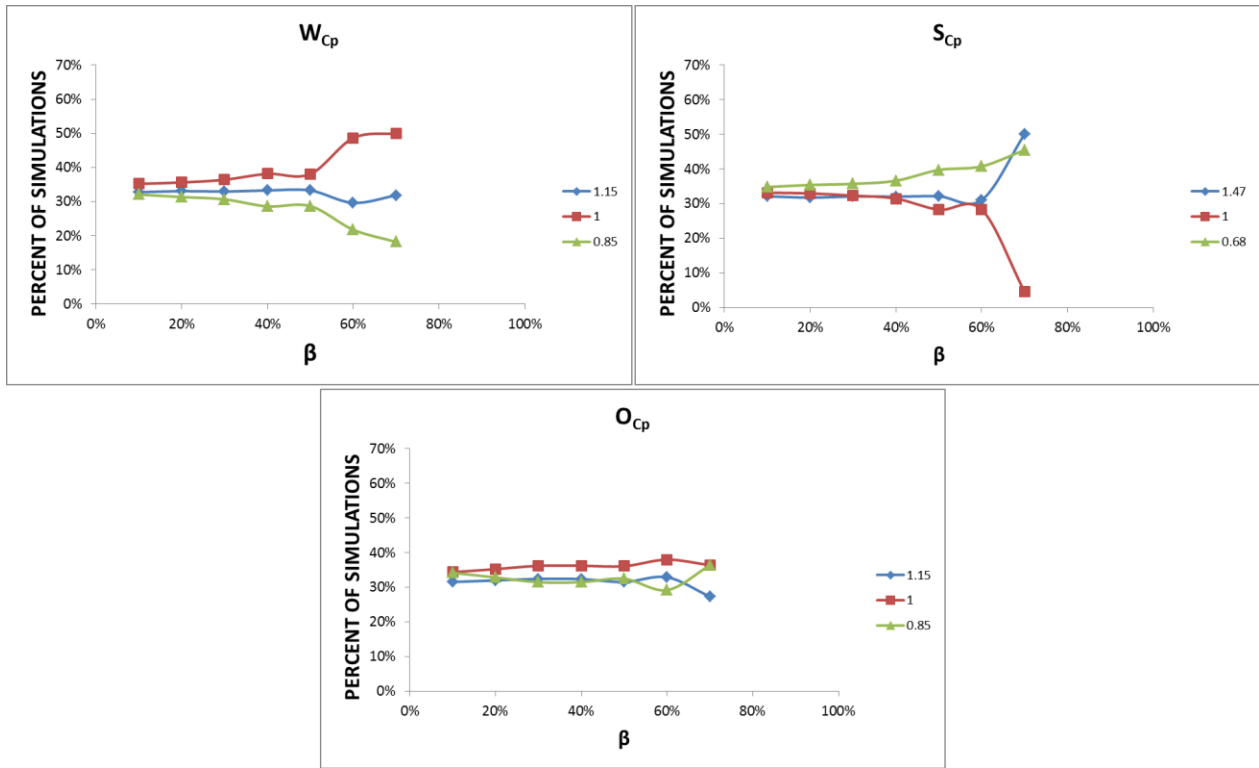


Figure 9-15. C_p parameters' influence on cooling capacity.

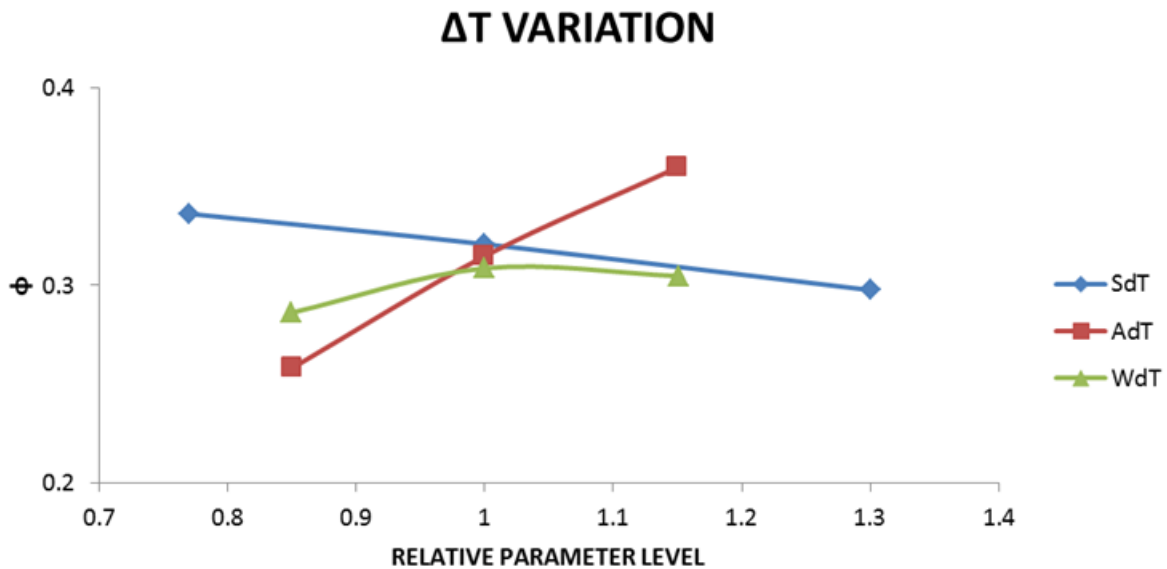


Figure 9-16. Average ϕ as a function of the relative ΔT parameter levels.

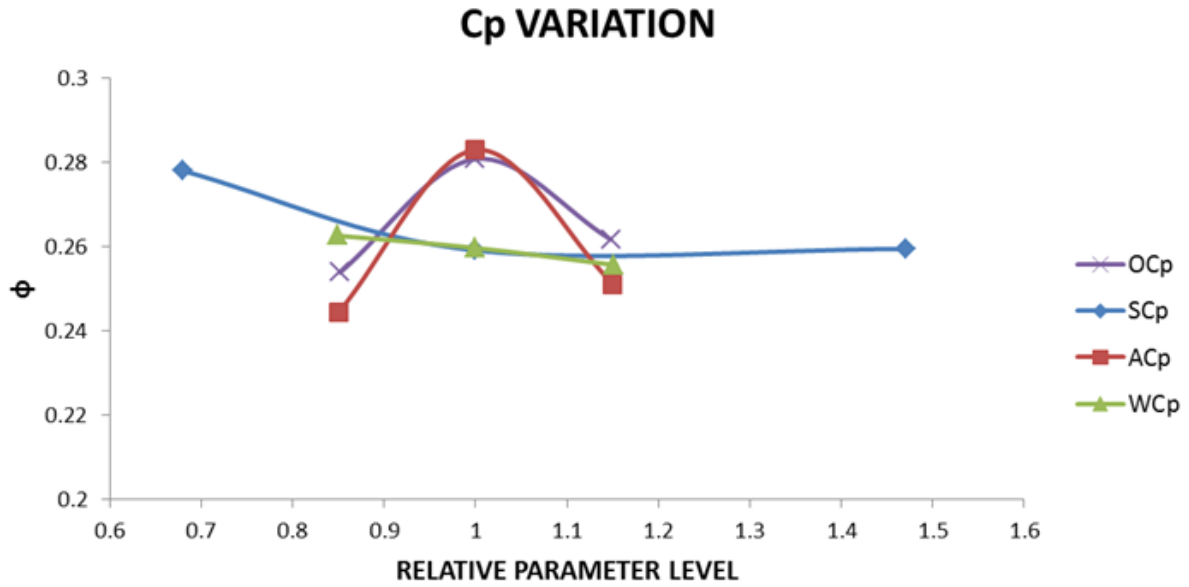


Figure 9-17. Average ϕ as a function of the relative C_p MMM parameter levels.

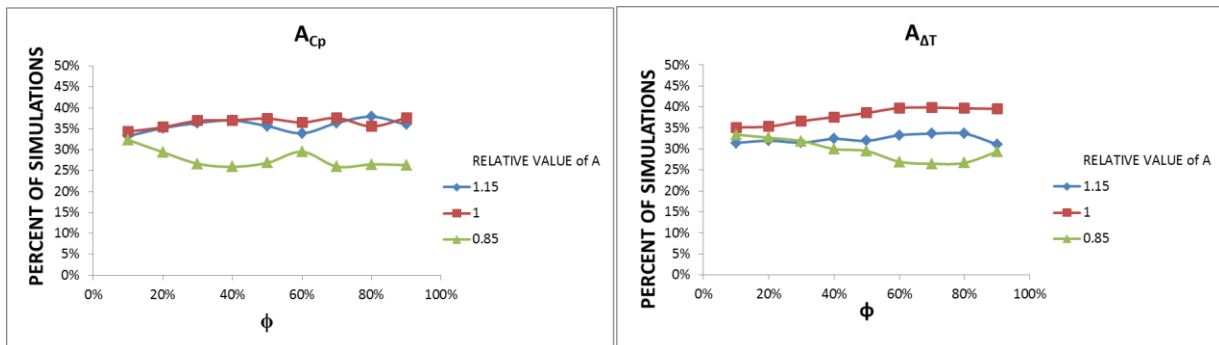


Figure 9-18. Material parameters with the largest influence on ϕ .

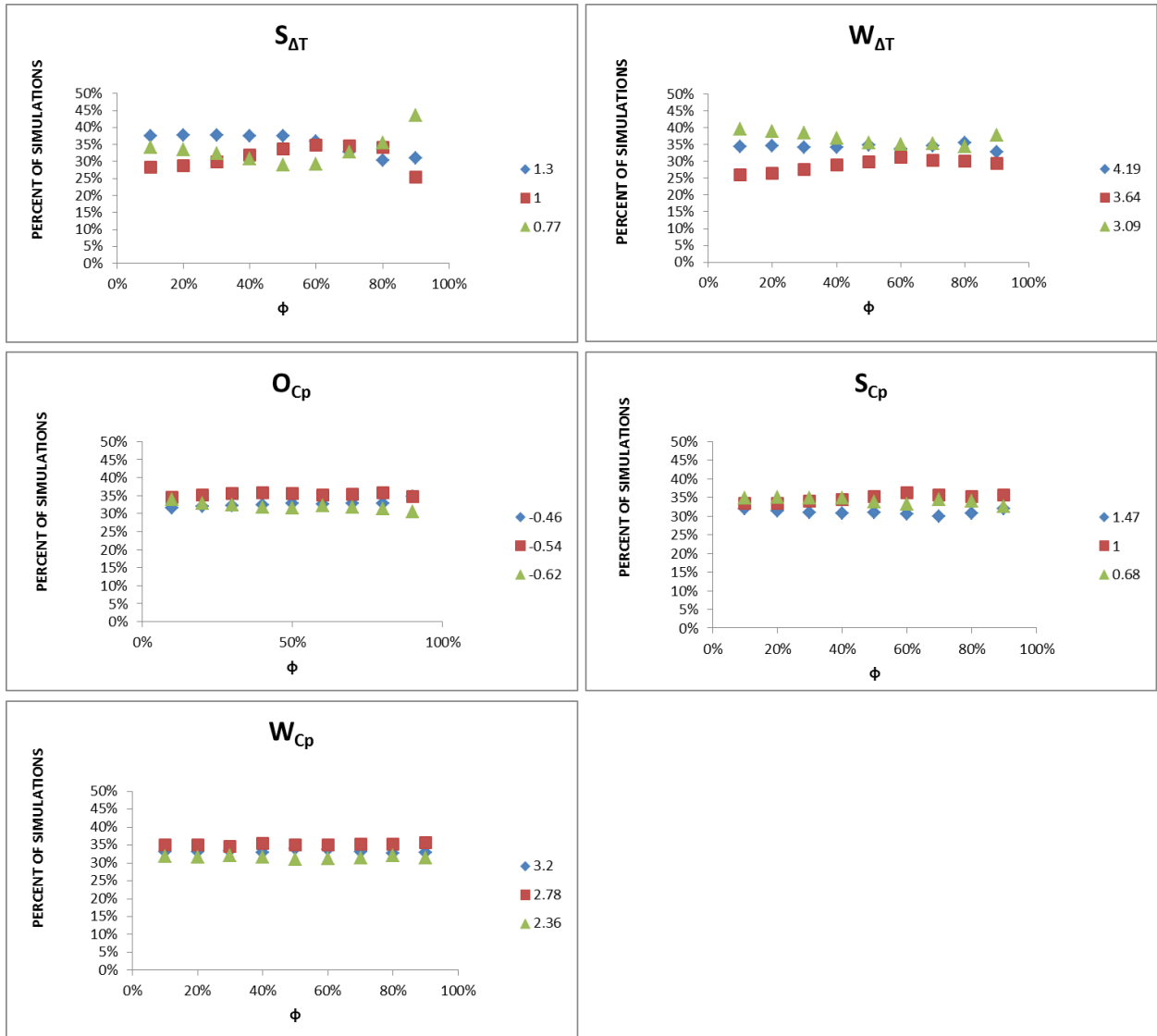


Figure 9-19. Results from the remaining material parameters.

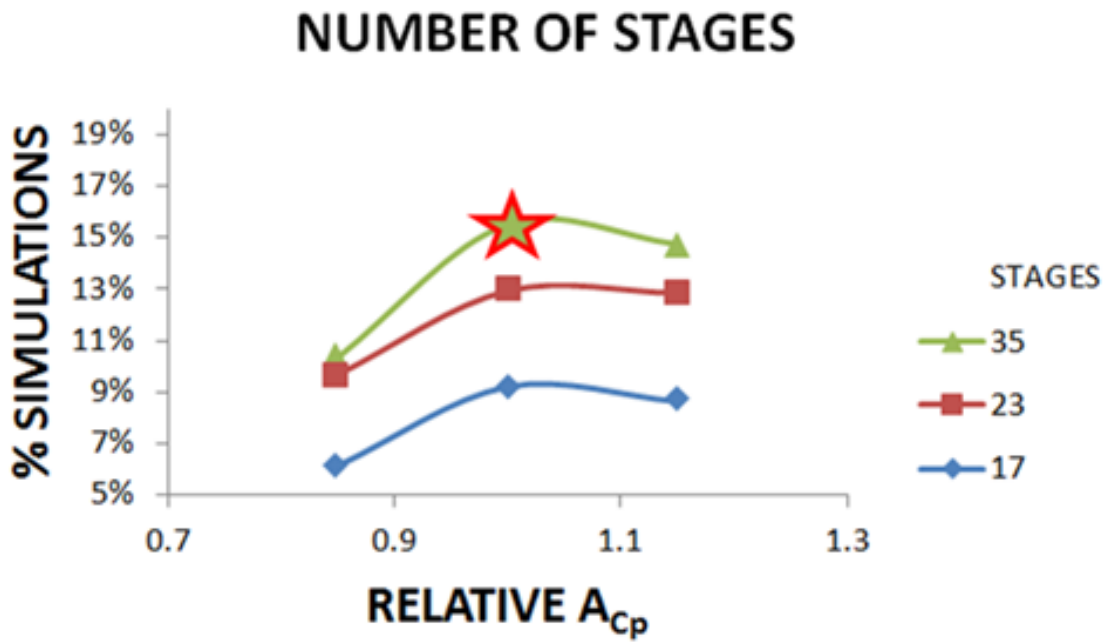


Figure 9-20. Comparison of A_{Cp} and the number of stages to high efficiency.

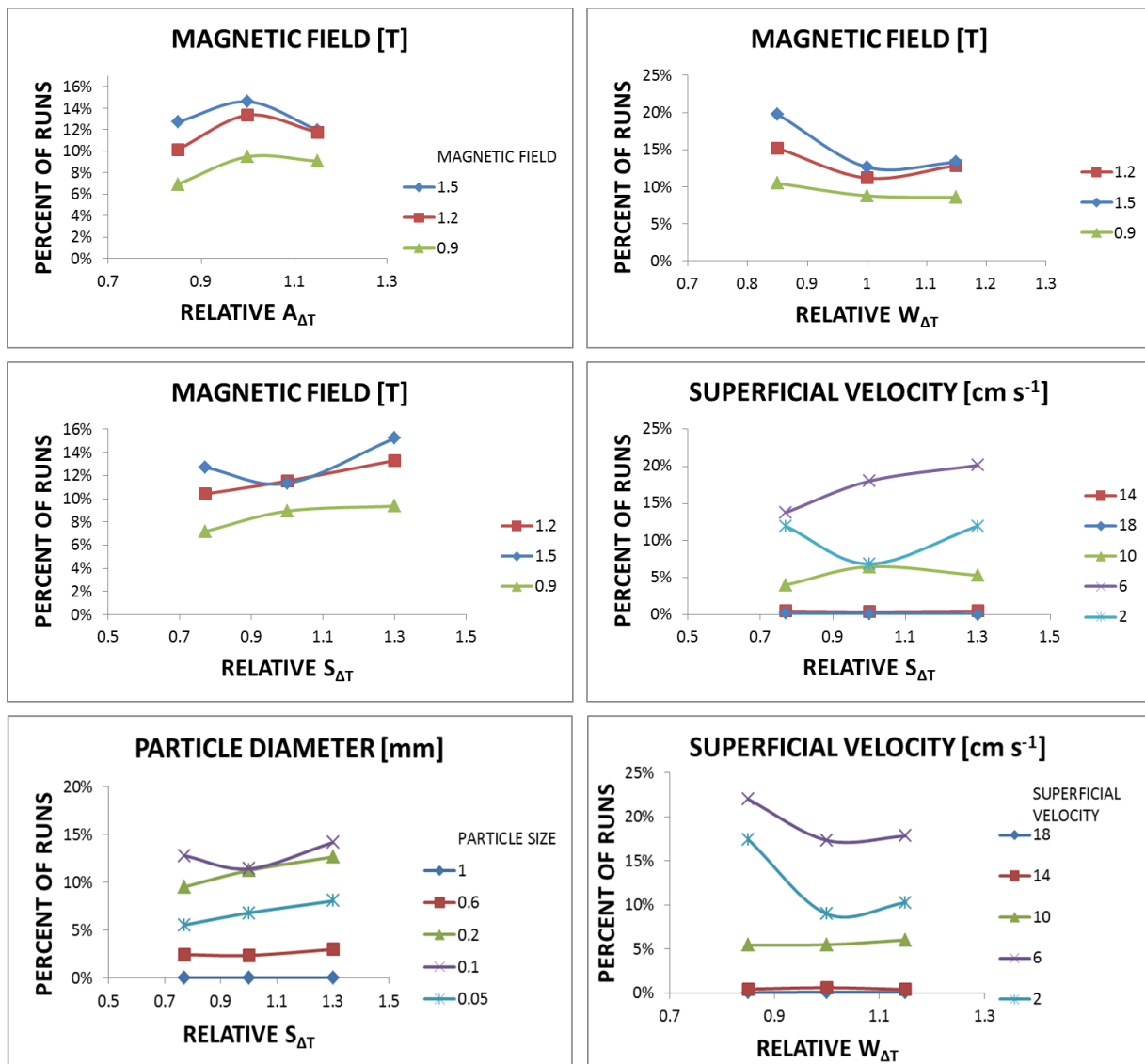


Figure 9-21. Interactions from most efficient runs subset.

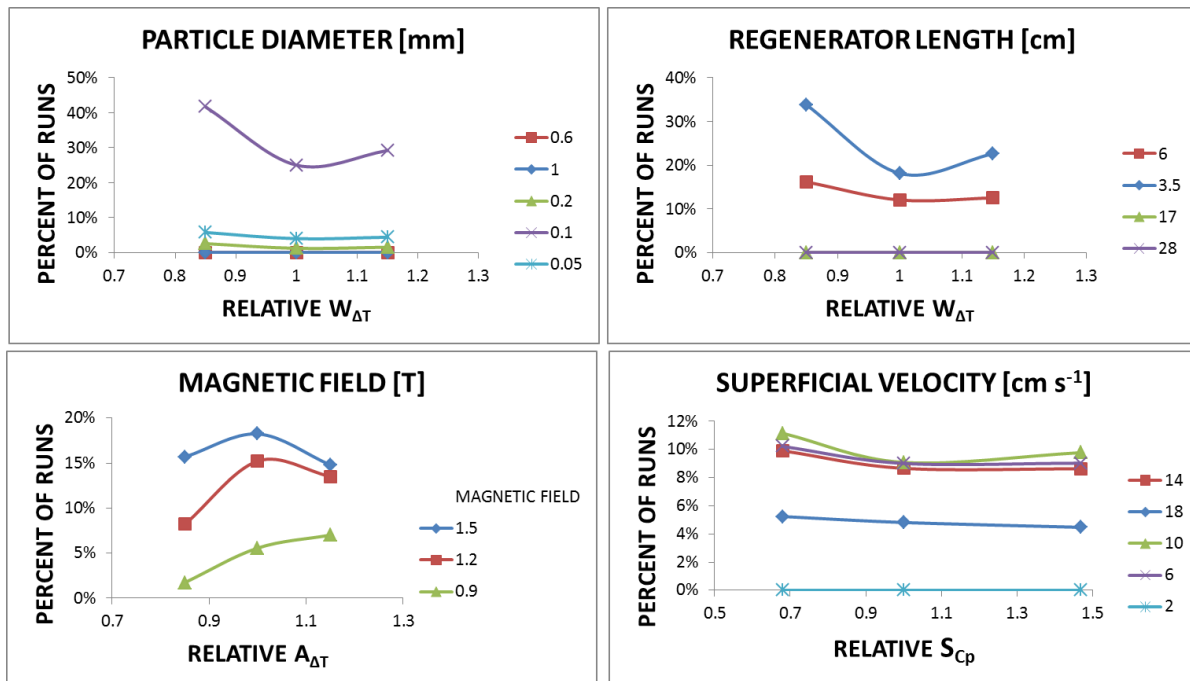


Figure 9-22. Highest 20% of cooling capacity results.

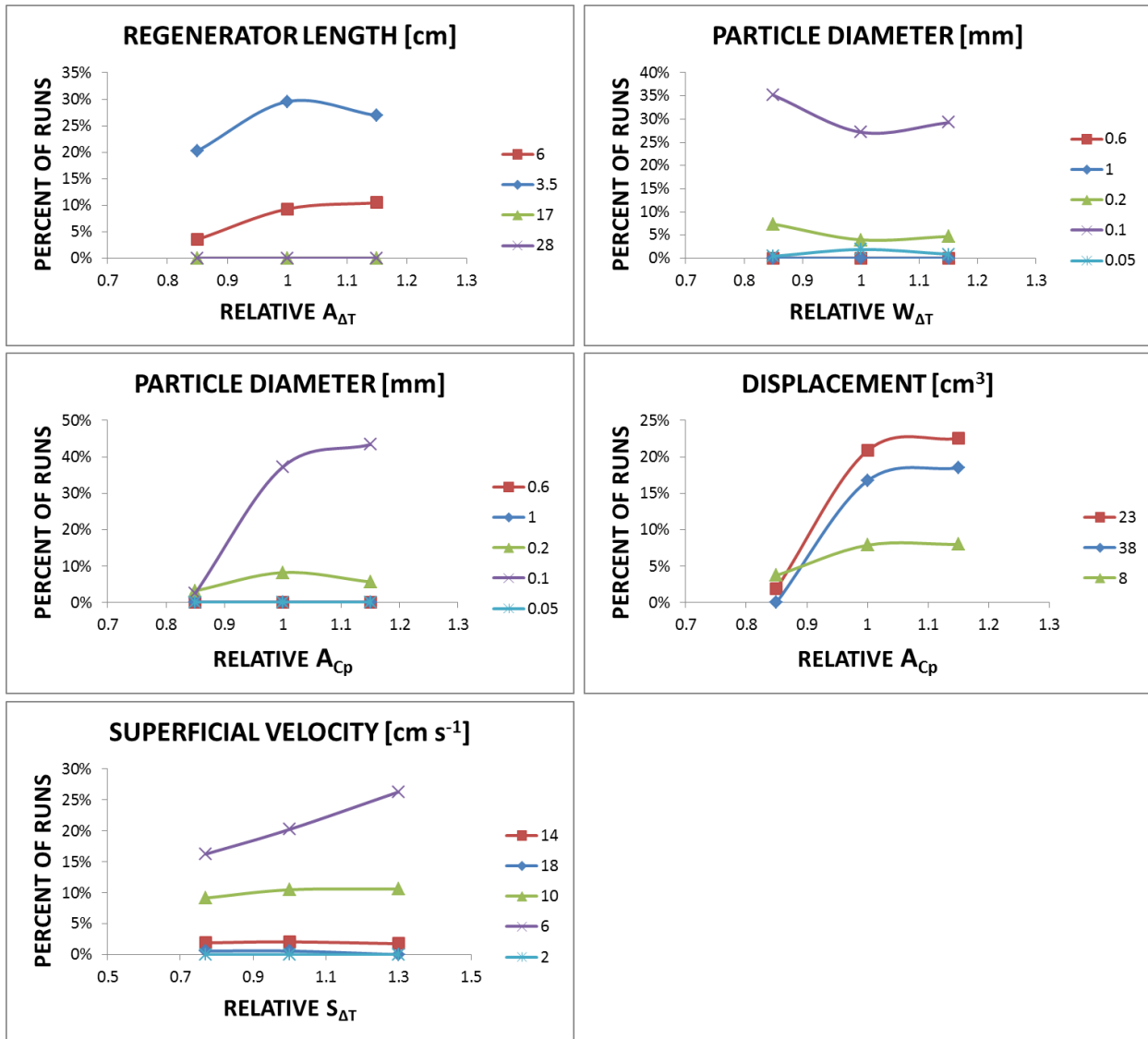


Figure 9-23. High cooling capacity and efficiency results.

CHAPTER 10 DISCUSSION AND CONCLUSIONS

This chapter is a summary of the contributions, conclusions, and recommendations gained from the preceding work. A flexible magnetocaloric prototype has been built and characterized. The prototype has been used in order to validate both a AMR model of regenerator performance and an MMM. The MMM was developed as a part of this work to enable further study of magnetocaloric properties and their effects on MCHP design and operation. The MMM has been shown to accurately represent the two commonly used first order magnetocaloric materials both statistically and in the prediction of experimental results. Some key insights have been gained.

MCHP Insights

In order to build a MCHP which is able to validate modeling attention must be paid to every aspect of the MCHP design. The incorporation of measurability and controllability should be key objectives. As with all physical systems losses cannot be avoided so they must be characterized and understood. The ease of measurement and characterization of these losses should also be a priority in MCHP design. The AMR model used as part of this work has been developed such that there is an analytical baseline for every effect incorporated in the AMR model and no arbitrary fitting coefficients are used. As such each of these effects must also be measured and understood in the HA1 design. Several learnings can be carried forward from the HA1 design to future MCHP designs to enable greater accuracy in measurement and correlation.

- Simple regenerator geometries can have several beneficial impacts for MCHP performance. The use of a cylindrical regenerator minimizes surface the surface area to volume ratio. This in turn minimizes many losses such as radial heat leak,

regenerator housing thermal mass, and heat transfer fluid bypass. The use of standard size tubing increases repeatability in bed construction and minimizes cost. De-magnetization is also minimized for elliptical shapes when packed powder beds are utilized. Lastly by only having a single flow path fluid flow rate is guaranteed to be correct.

- One dimensional frontal area constructions better enable one dimensional AMR models. Multi-dimensional factors such as flow maldistribution and radial temperature gradients are naturally minimized.
- Decoupling of the fluid and hydraulic systems is a key advantage. The need to change physical parts, which can lead to reduced repeatability, is eliminated. It is also possible to create a wide range of operational conditions easily. Having separate systems greatly increased the ability to work on a particular subsystem or subcomponent of the system.
- Direct physical measurement of inputs helps to minimize the error of experimental results. The magnetic system of HA1 has direct feedback on rotation angle. The hydraulic system is based on positive displacement which allows for the physical measurement of piston position and therefore flow rate. These direct measurements are more reliable than output measurements such as internal field, or fluid flow rate which are especially hard to measure.
- Direct loss measurement is essential. Even with a minimized surface area and a minimal distance to temperature measurement there are still detectable heat leaks in the HA1 prototype. An analytical model can give a good understanding of the nature of these heat leaks, but the absolute measurement is necessary and helped to achieve sub 10% error between experiment and AMR model.

Magnetocaloric Material Model Insights

Several MMMs were developed as part of this work. Evaluation of these MMMs based on a set of design goals lead to the selection of a single MMM. This MMM was incorporated successfully into the AMR model for use in simulations. The MMM was shown to be effective in conjunction with the AMR model in predicting experimental results. Key insights into the modeling of magnetocaloric materials were developed as result of this work.

- In order to accurately model the adiabatic temperature change due to magnetic field change or the specific heat at a single external field only 5 basic parameters are needed. Additional parameters were also shown to be successful in modeling

of FOMT materials, but the additional complexity did not come with additional accuracy.

- It is possible to represent the specific heat of magnetocaloric materials with a fully integratable mathematic function. This enables the direct calculation of entropy at a constant field, and therefore all of the relevant thermodynamic properties of the magnetocaloric material while eliminating the need for numeric integration. The method of property calculation inherently has lower error.
- A thermodynamic understanding of the magnetocaloric effect in conjunction with an MMM may be able to reduce error in measured MCM data. Noise from data is reduced due to an averaging effect when the MMM is fit to raw data. Additionally it was shown that by forcing the adiabatic temperature change to a base value of zero AMR model predictions were consistently closer to experimental results. It was also shown based on first principles that a truly first order materials would have no temperature change far from the Curie temperature which is in line with the zero base ΔT assumption.
- Using an MMM can reduce the size and modeling time of an AMR simulation. Typical raw data sets have several hundred data points per stage of magnetocaloric material. The implementation scheme outlined in this work requires just 10 points of data for a stage. Additionally when modeling cascades of identical materials only a single additional data point is needed for each stage. It was also shown that several reductions in the time for convergence of the AMR model were possible with data being generated by the MMM.

Model Validation Insights

To validate the AMR model and MMM the HA1 prototype was used to carry out a series of tests on FOMT materials. These tests are important because, as shown in the literature review, relatively little experimental data exists for multistage FOMT materials. Of the data that does exist many data sets are limited in the scope of the parameters tested. Additionally no MCHP testing a substantial number of parameters has reported data from both of the currently available FOMT materials. Through this series of tests several insights were gained.

- The MMM can represent multiple FOMT materials. The statistical accuracy as gauged by the R^2 coefficient is similar for both of the currently available first order materials, in both cases the full range was above 90% with averages above 95%. The error between predictions with the MMM and experimental results was shown to average under 5%.

- The results of first order multistage cascades in terms of cooling capacity with respect to span follow a repeatable pattern regardless of the MCHP parameters varied for successful tests. The pattern can be summarized by only three values (two slopes and a single point). Utilizing these three values only minimal data is lost. This method of results reporting can significantly cut down on test time. This is an important consideration when testing resources are limited as a typical test point on HA1 may take up to an hour to stabilize thermally. Minimizing test time is also an important consideration when materials or systems may be unstable of long test durations.
- Regenerators may be very sensitive to operational parameters. In some tests changing a single parameters such as flow rate by 30% could lead to a reduction in performance of up to 25%. This reiterates the need for careful flow measurements on prototypes.
- Implementing a cycle as near as possible to the AMR cycle is beneficial to MCHP performance. Implementing an AMR cycle is also essential if the AMR model being validated does not take concurrent magnetization and flow into account. Many existing MCHPs do not consider this effect which directly impacts the performance of MCHPs and accuracy of AMR models.
- Making assumptions about the dependence of magnetocaloric materials on magnetic field can lead to increased errors. The largest errors between the AMR model and MCHP were when the full magnetocaloric effect data was not available for different field levels. In these cases assumptions were made to scale the magnetocaloric effect. The error in the scaled versions of this test was nearly double that of the unscaled version.

Modeling Study Design Insights

The final portion of this work included a large modeling study. The modeling study was meant to investigate all MCHP parameters that are universally applicable while for the first time also incorporating the first order magnetocaloric materials as parameters through use of the MMM. Simplifications were made to the parameter space for both materials and MCHPs. Due to the size of the remaining parameter space updates were made to the AMR model code to increase the AMR model speed. Through the design and implementation of the modeling study several insights were gained.

- Considering an idealized MCHP also helps to make a parameter space more non-MCHP specific, and accordingly makes the results more universally applicable. A full parameter space for an idealized and non-specific MCHP includes nine parameters. To further include idealized materials represented with the MMM seven more parameters are needed. Though this is a much reduced subset of all the possible parameters, it still represents a very challenging space for time stepping AMR models.
- A single hot side and cold side temperature can be chosen to compare MCHP designs. The selection of these temperatures needs to be made carefully as there is an interaction with the MCHP parameters and material parameters. A method by which these temperatures can be selected was presented and its impact assessed on both experimental and AMR model results.
- The use of an MMM enabled the changing of the AMR model fidelity which greatly increased AMR model speed. These speed increases are likely due to the fact that the MMM is by definition thermodynamically consistent, and the data follows a smooth trend free of the noise inherent to measured data.
- It is possible to have negative cooling capacity predictions, which represent the movement of heat from the hot side of a heat pump to the cold side of a heat pump, which are physically realistic. Several mechanisms were presented by which these results can arise including heat generation due to viscous dissipation, and mass transport in a passive regenerator. Though these results represent physically possible scenarios they may not be interesting when considering data sets since the parameters which effect heat movement in these passive cases do not impact active cases in the same manner.
- Though many coefficients of performance have been suggested in the literature to analyze MCMs none sufficiently describes the available energy of a magnetocaloric material. TR_{cap} a new coefficient of performance was utilized to ensure that materials generated by the MMM had an equivalent available energy.

Modeling Study Results Insights

The results of the modeling study included information on both the cooling capacity and efficiency of parameter sets. The MCHP and material parameters were compared to the resulting cooling capacity and efficiency. Several subsets of data were used to further investigate the interactions between MCHP parameters and material parameters.

- It was shown that utilizing only the average outcomes for cooling capacity or efficiency in a large modeling study is not sufficient to fully understand the

results. An alternative method which reports the tendency of a parameter to lead to high cooling capacities or efficiencies can provide additional information which is useful in assessing the impact of that parameter.

- In agreement with past materials studies the amplitude of the adiabatic temperature change on magnetization was found to be particularly important. The average cooling capacity was most positively correlated with this single parameter. It was also shown that the simulations having the highest cooling capacities disproportionately resulted from the highest amplitude ΔT .
- Materials for which C_P had a small amplitude were associated with the poorest cooling capacity. This association was not as strong as the impact of high $A_{\Delta T}$.
- Very narrow widths for C_P lead to the fewest high cooling capacity runs. Materials for which the skew value of C_P was 1 which leads to a symmetric curve also lead to few high cooling capacity runs.
- For high volumetric cooling capacity MCHPs the best recommendation for materials manufacturers would be to focus on first improving the amplitude of ΔT while maintaining a moderately high amplitude and width of C_P . The curve of C_P should also be skewed to either side if possible.
- The average efficiency was highest for stages that had a high amplitude of ΔT and a median value for the O and A parameter for C_P .
- The highest proportion of high efficiency runs comes from stages that had a high amplitude of C_P . The median value of A for ΔT had the highest proportion of high efficiency runs with the high amplitude A also having an increased proportion of the high efficiency runs.
- Interactions were identified in the subset of the highest efficiency runs that could be beneficial for MCHP design. It may be possible to reduce the magnetic field necessary in some cases by combining materials and MCHP design. It also may be possible to reduce pressure drop by considering materials properties along with MCHP design.
- For the highest cooling capacity runs the MCHP parameters of particle diameter and regenerator length were dominant in their impacts. There were still interactions which could offer a benefit to magnetic field when materials parameters are considered.
- For the intersection of high cooling capacity and high efficiency the dominant impact of particle size and regenerator length carry over. There is, however, a larger relationship between the fluid flow parameters and performance. Several interactions were present which could be considered in a joint materials and MCHP design.

Recommendations

Magnetocaloric refrigeration shows the potential to greatly effect energy consumption worldwide. In spite of this potential and years of research in the area there are currently no published results showing competitive efficiencies. Current efforts are largely segregated between materials and MCHP design. The results of this work show that combining the study of materials and MCHP design can lead to improved results and a better whole system understanding. Importantly the results also show that there is no one ideal material for magnetocaloric refrigeration. The choice of a material depends heavily upon the application goals. For instance Study 4 showed that a MCHP with the highest volumetric cooling capacity has a clear preference for materials with large adiabatic temperature changes. This same material, however, may not be the best choice for a MCHP that needs to perform at the highest levels of efficiency. Specific recommendations for the field of research are as follows.

- Material data should be reported both as raw data and as MMM coefficients. Several advantages are inherent in this method.
 - Material data can be condensed to the point that it can be easily reported in journal articles.
 - The use of the MMM inherently leads to thermodynamically consistent data.
 - The lack of ambiguity in the few parameters needed for the MMM can enhance reproducibility.
 - The MMM can be used to easily describe existing as well as theoretical materials.
- Cooling capacity and span curves can be reported in the three variable format proposed in this work with several advantages.
 - The condensed data format makes transmission of results in journal articles possible.
 - Test time can be greatly reduced as fewer test points are needed.

- Time based variation will be reduced in tests.
- Materials producers can enhance existing materials by directly focusing on a few tradeoffs.
- Greater amplitude in the adiabatic temperature change greatly increases cooling capacity.
- Sharper and larger amplitudes in C_P are beneficial to cooling capacity and efficiency
- Materials and MCHP researchers should start to consider a system level approach to research. The materials and MCHP designs are coupled on many different levels.
- Materials manufacturers who wish to commercialize should consider if certain aspects of their process can be used to control materials properties. It may be the case the system of one customer can benefit from different material properties than another customer.

Summary of Contributions

- Comprehensive and combined literature review of MCHPs, materials, and modeling.
- A new flexible prototype capable of investigating MCHP parameters.
- Experimental results from both currently available first order magnetocaloric materials in a single MCHP across multiple parameters for the first time.
- First material model compared statistically and experimentally to first order magnetocaloric materials.
- A new method of reporting multi-stage first order regenerator results.
- AMR Model speed improvements which may be universally applicable to other AMR models.
- A large modeling study for the first time combining a correlated MMM with MCHP parameters
- Recommendations and observations on the impact of materials parameters.
- Identification of interactions between materials parameters and MCHP parameters.

Three articles published in scientific journals.

APPENDIX A HIGH EFFICIENCY GRAPHS

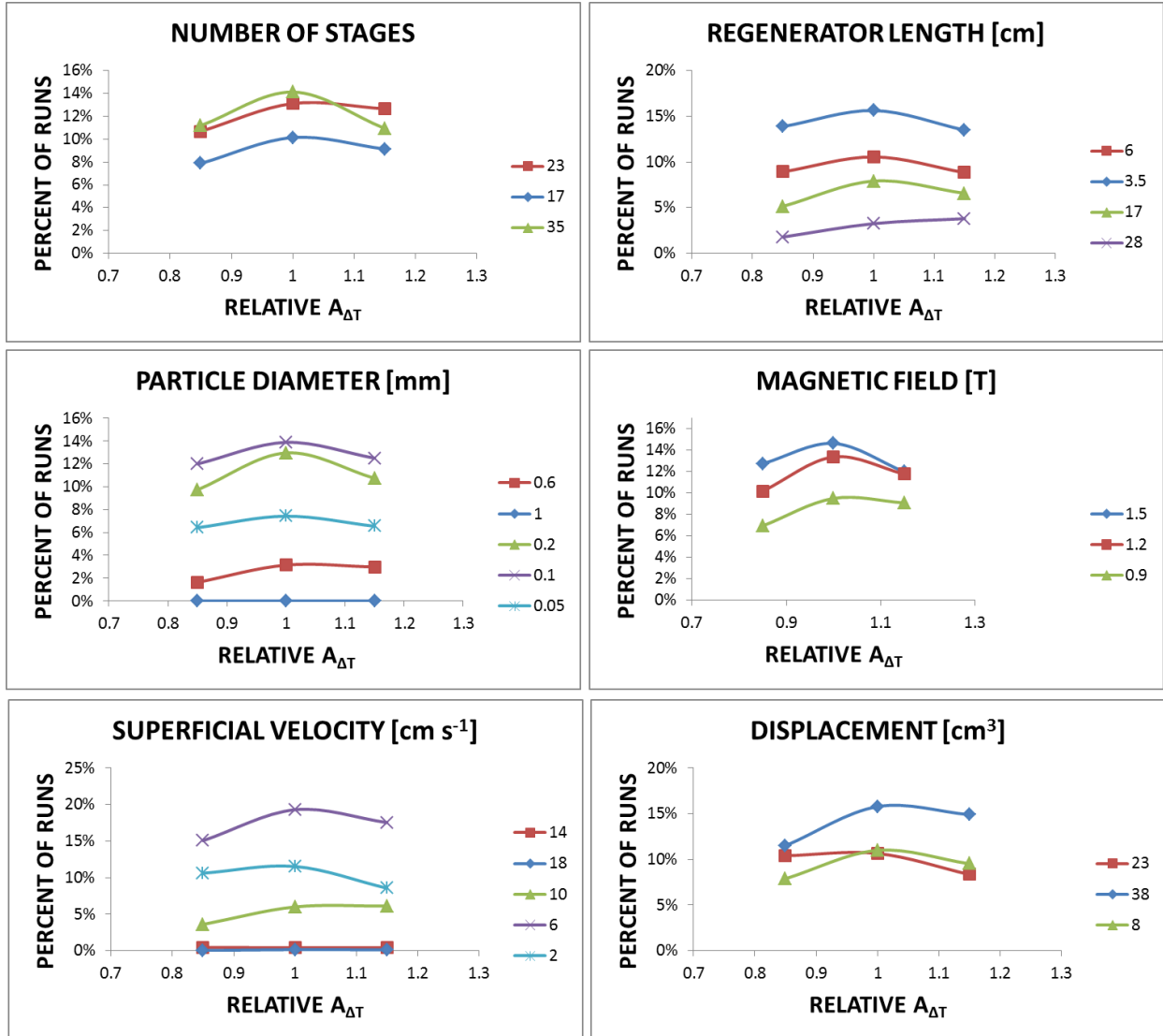


Figure A-1. $A_{\Delta T}$ with each MCHP parameter.

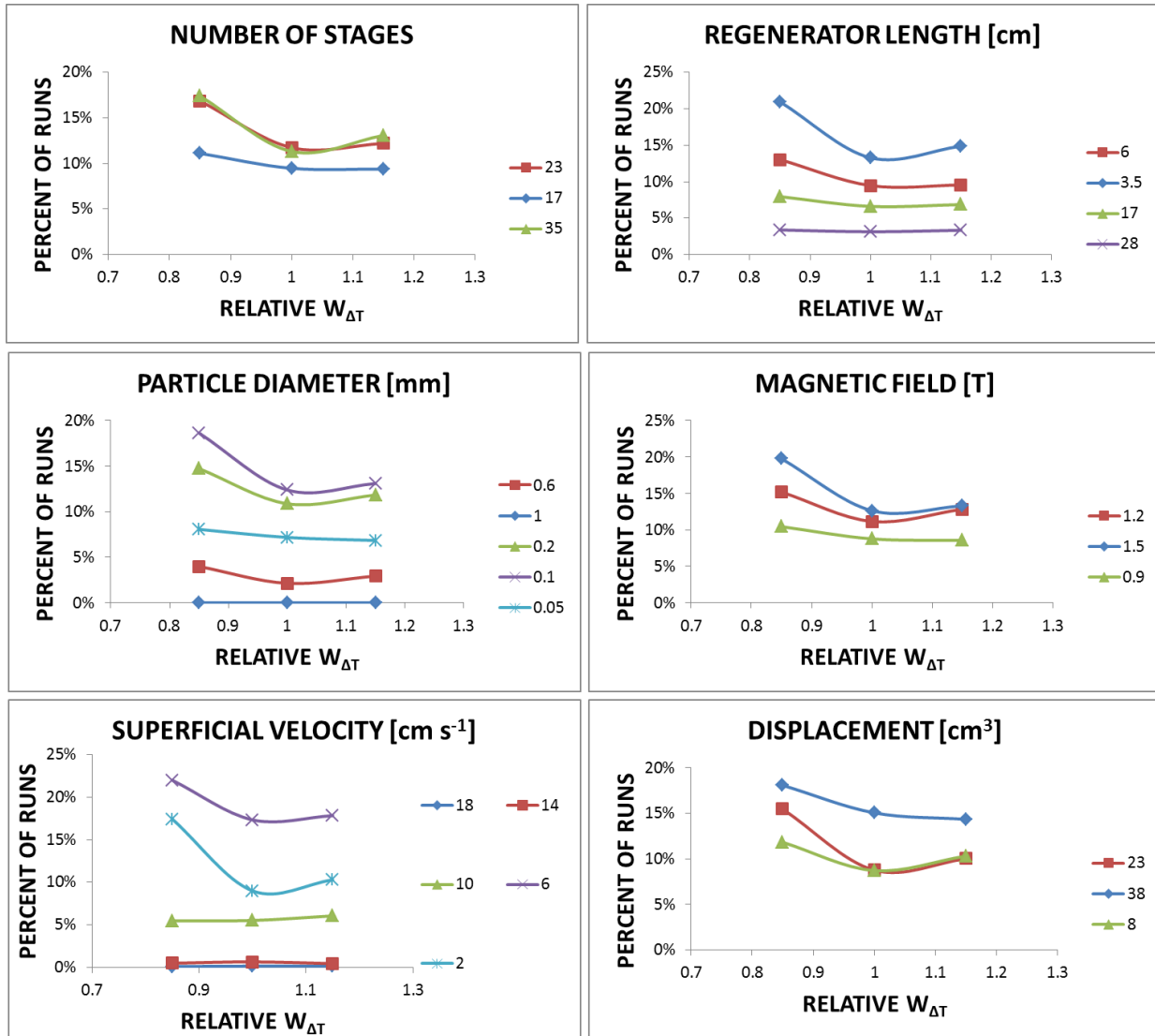


Figure A-2. $W_{\Delta T}$ with each MCHP parameter.

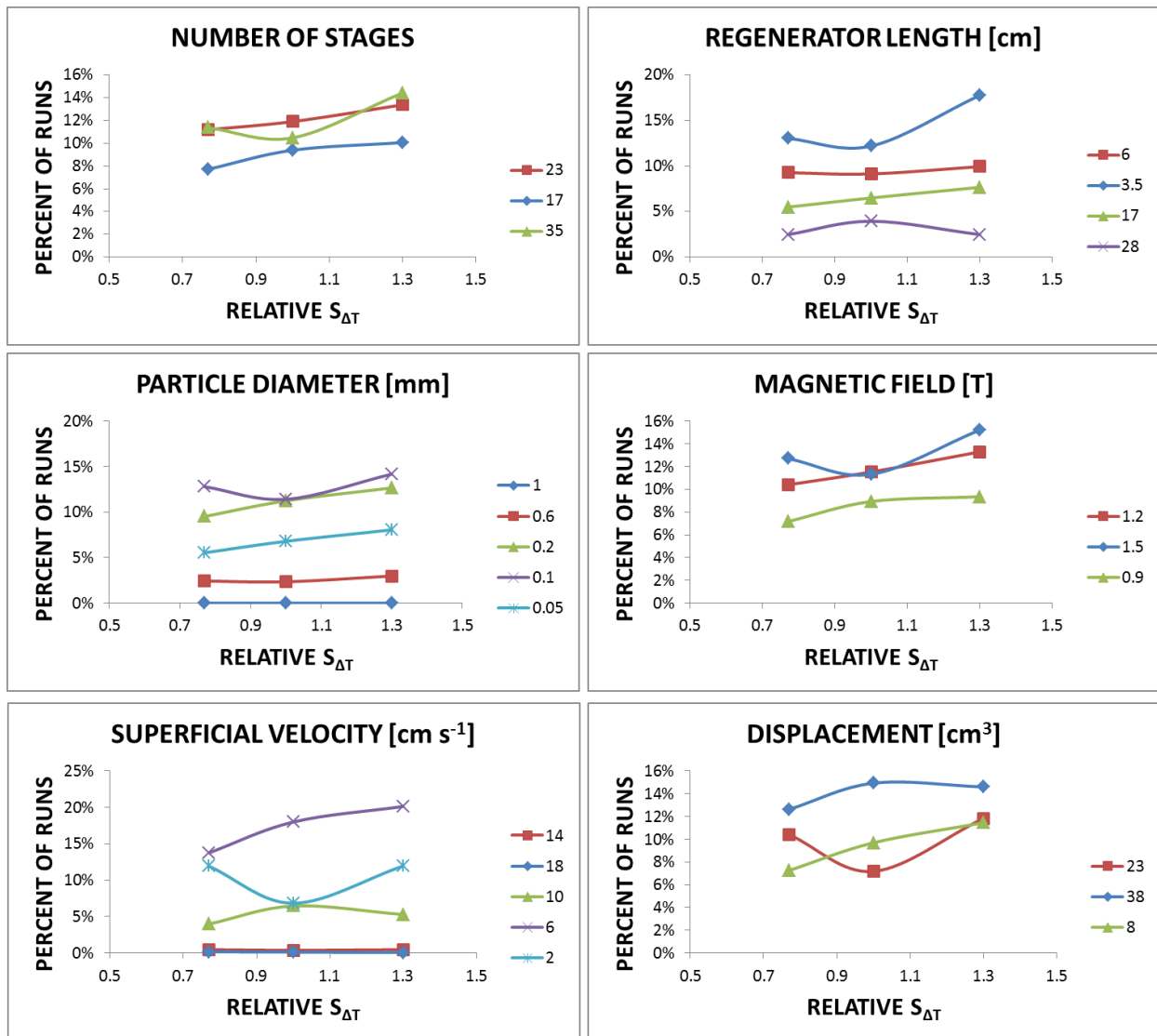


Figure A-3. $S_{\Delta T}$ with each MCHP parameter.

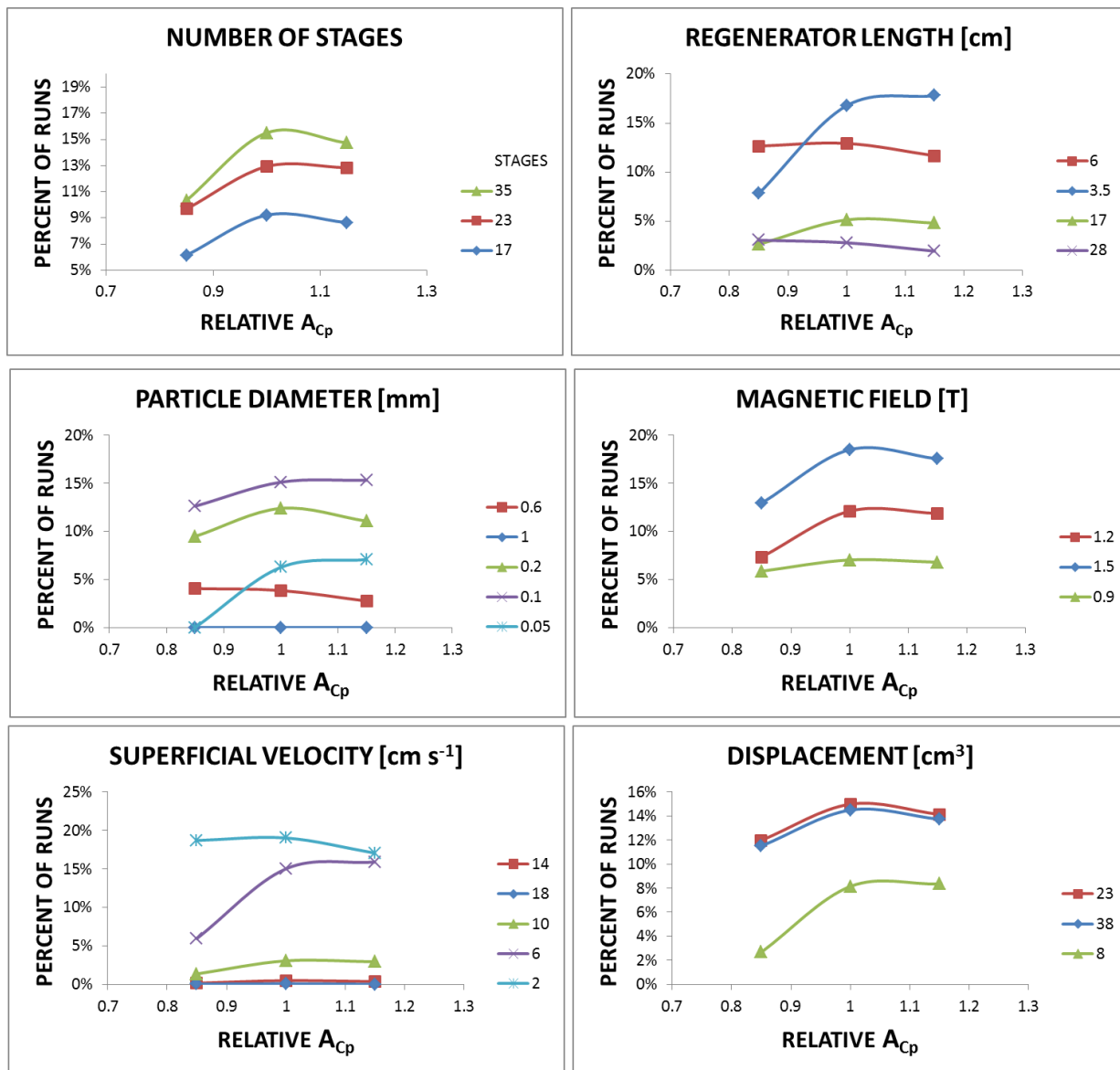


Figure A-4. A_{Cp} with each MCHP parameter.

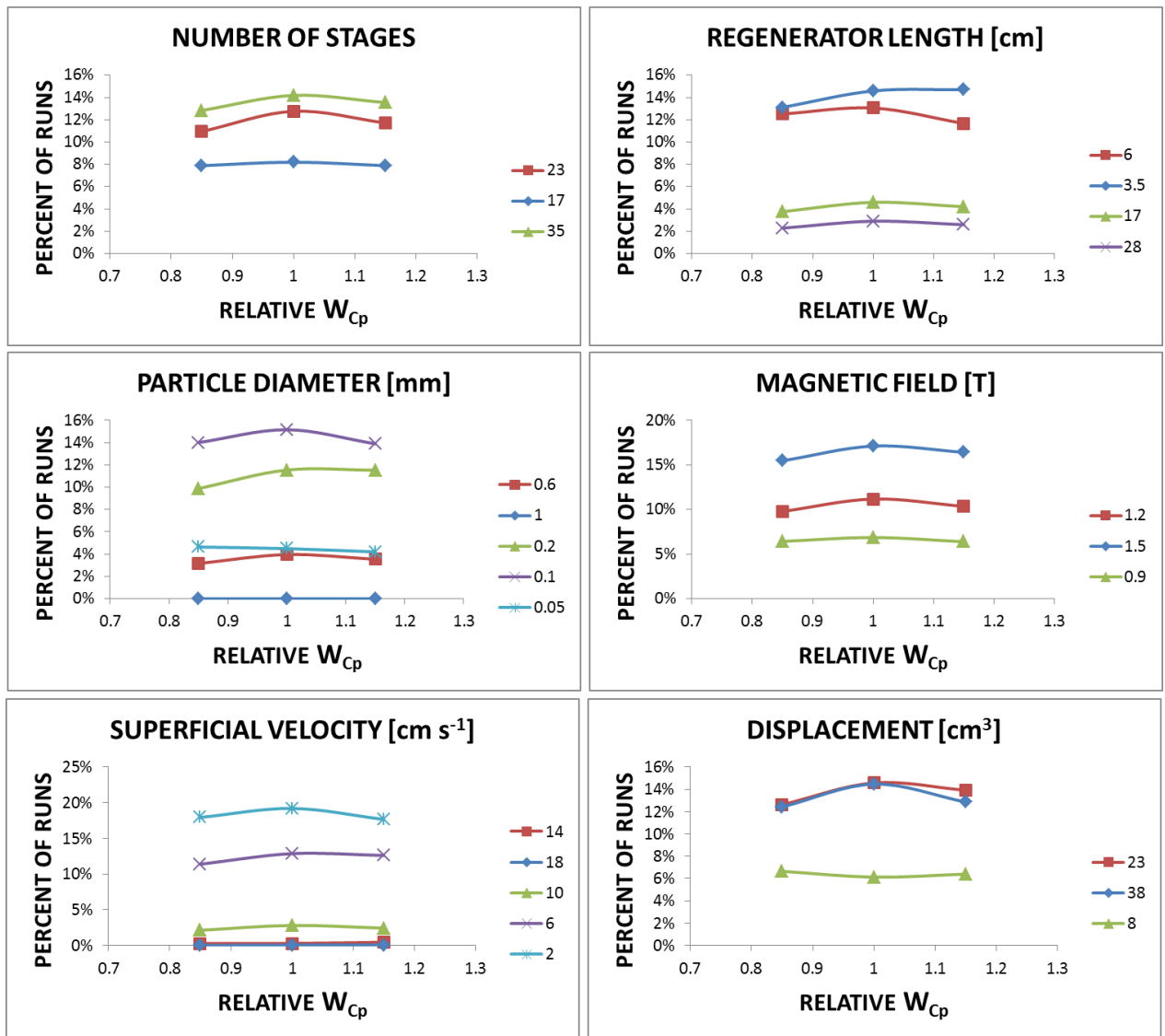


Figure A-5. W_{Cp} with each MCHP parameter.

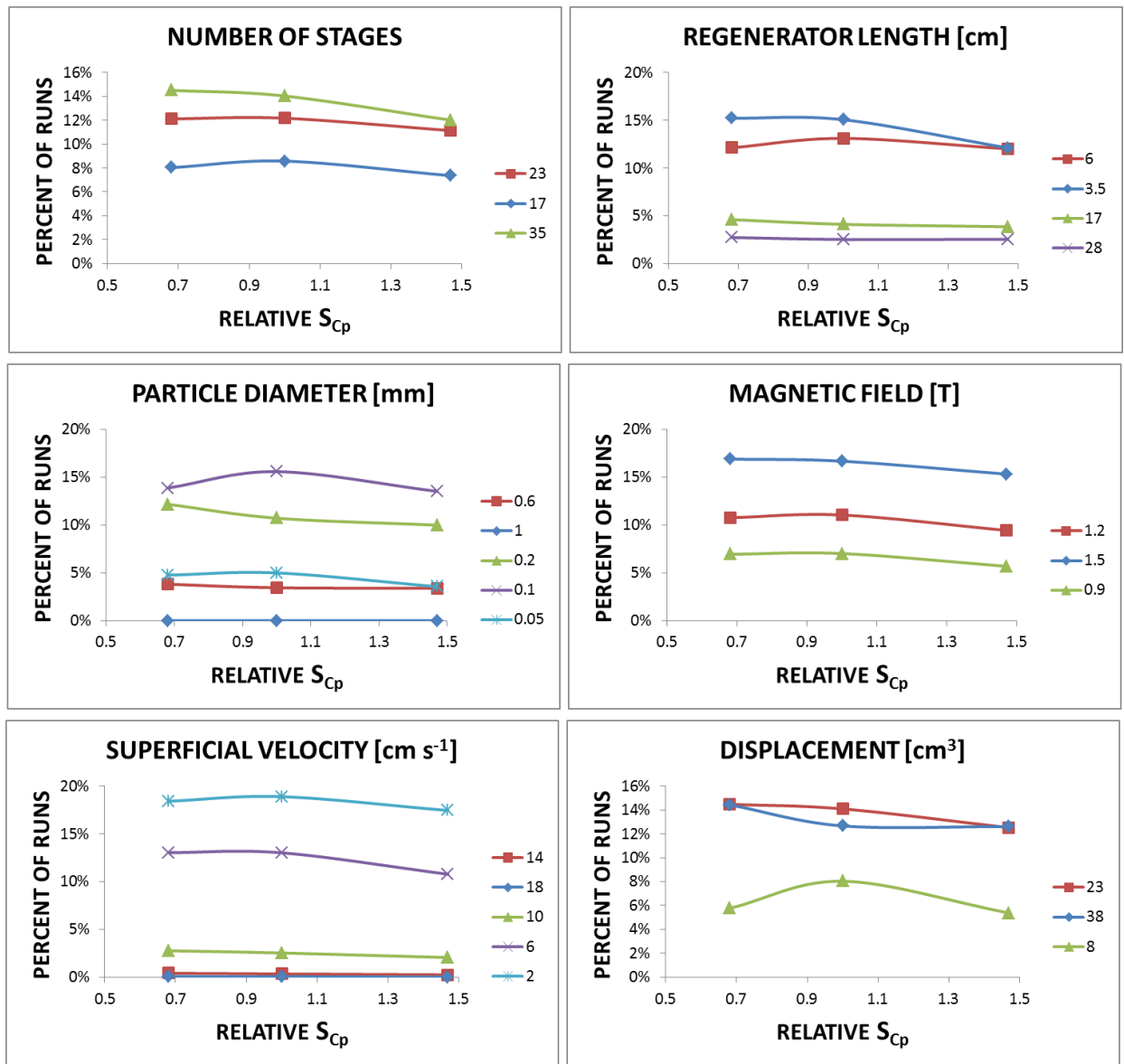


Figure A-6. S_{Cp} with each MCHP parameter.

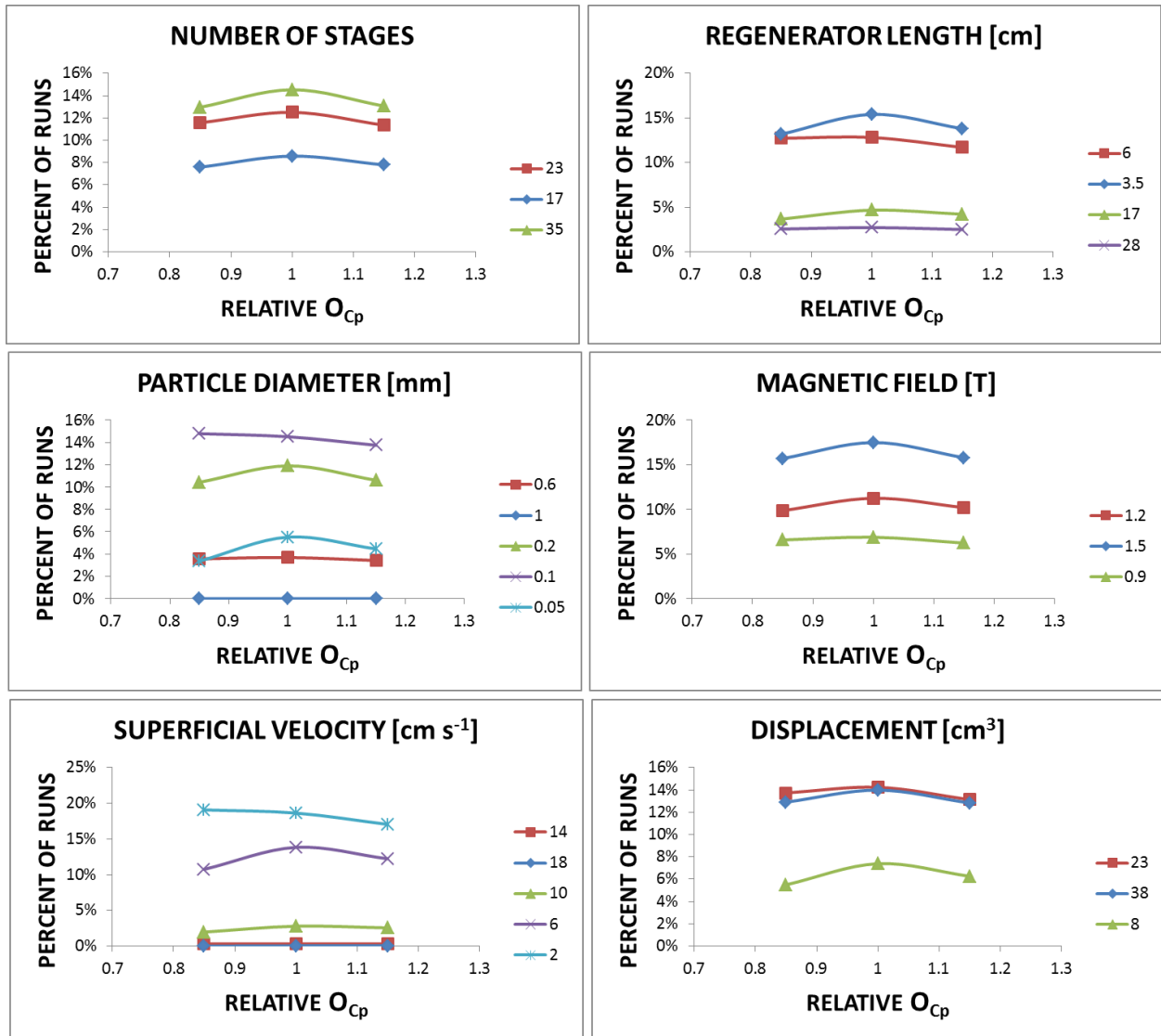


Figure A-7. O_{Cp} with each MCHP parameter.

APPENDIX B HIGH COOLING CAPACITY GRAPHS

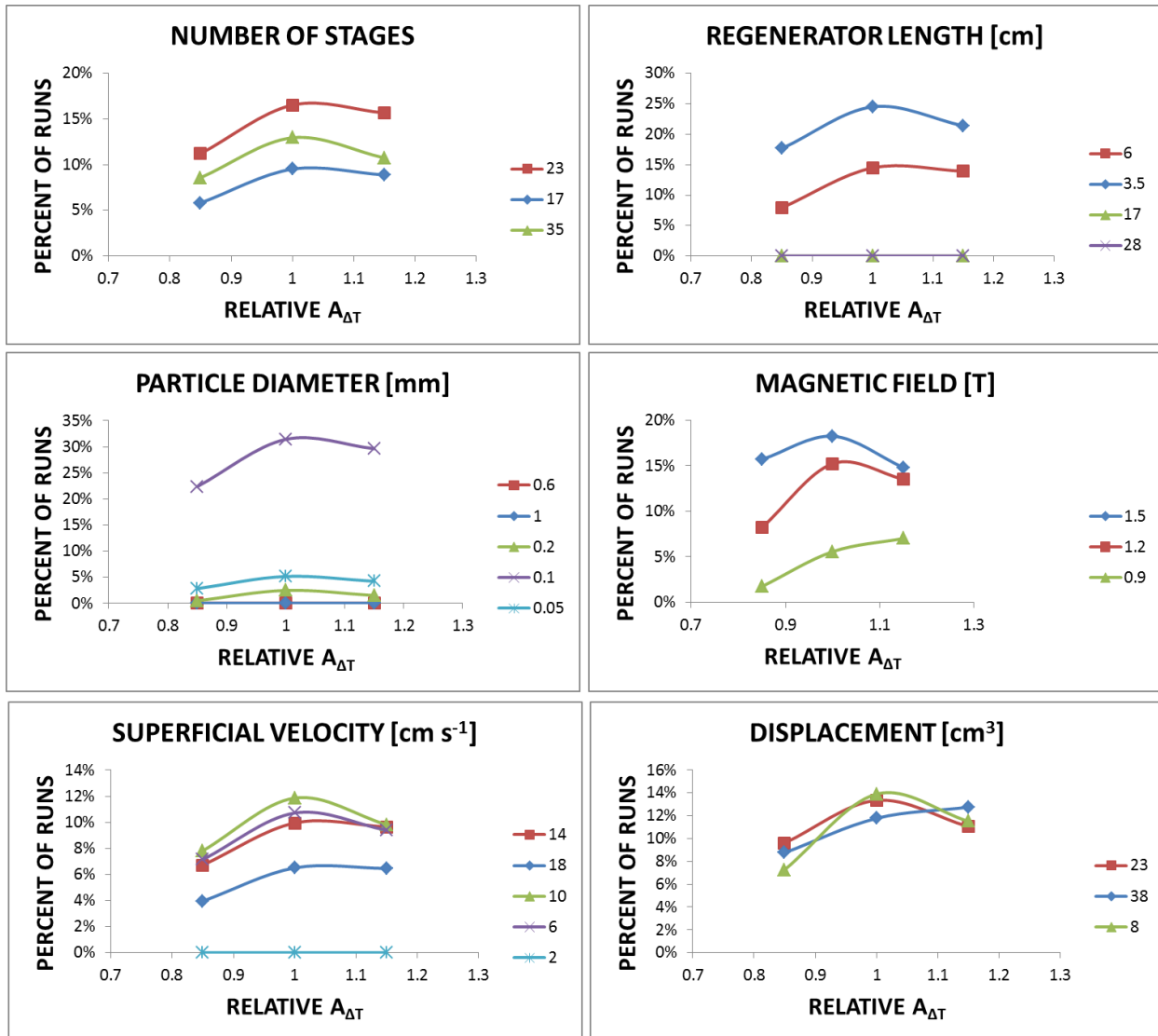


Figure B-1. $A_{\Delta T}$ with each MCHP parameter.

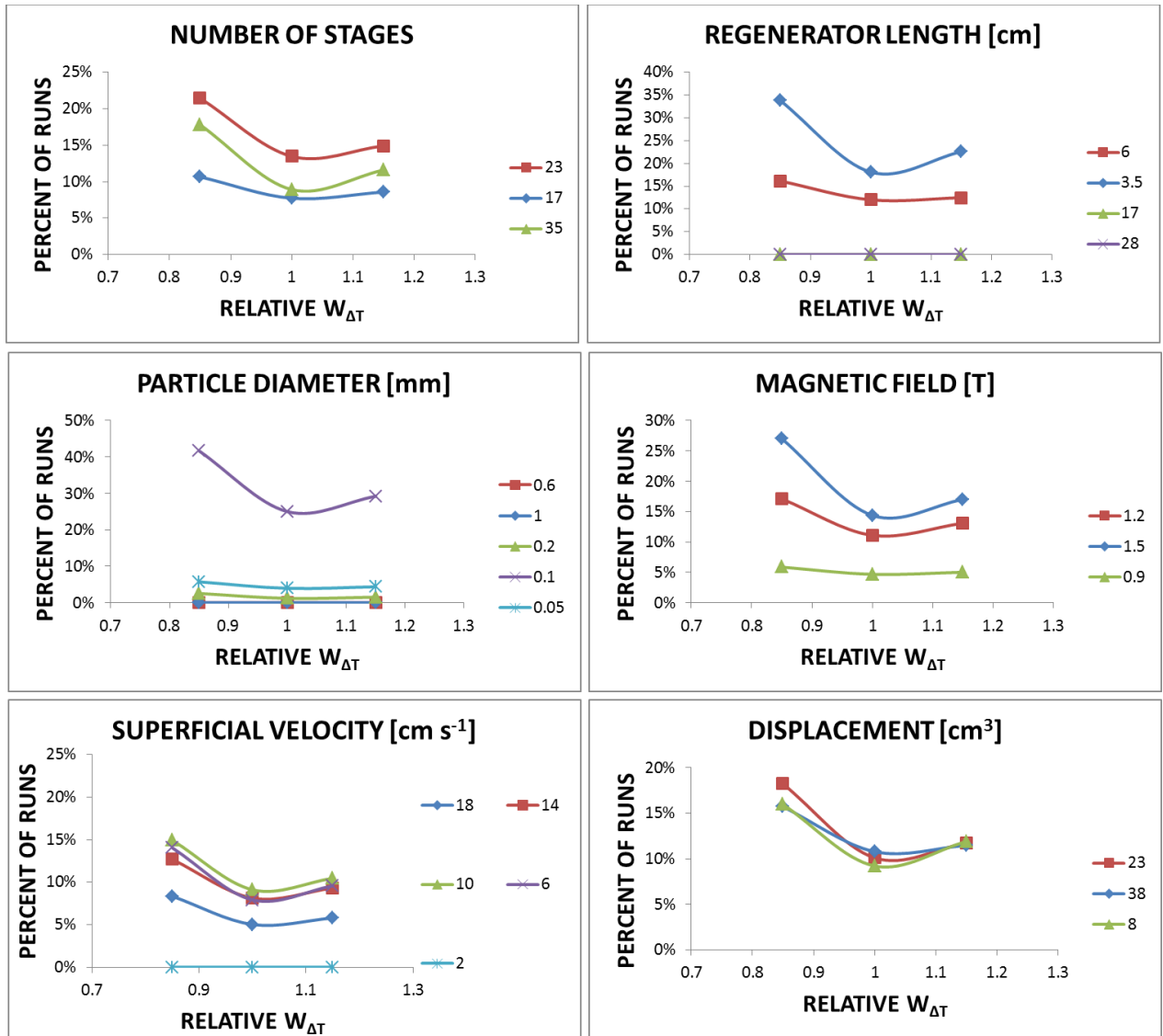


Figure B-2. $W_{\Delta T}$ with each MCHP parameter.

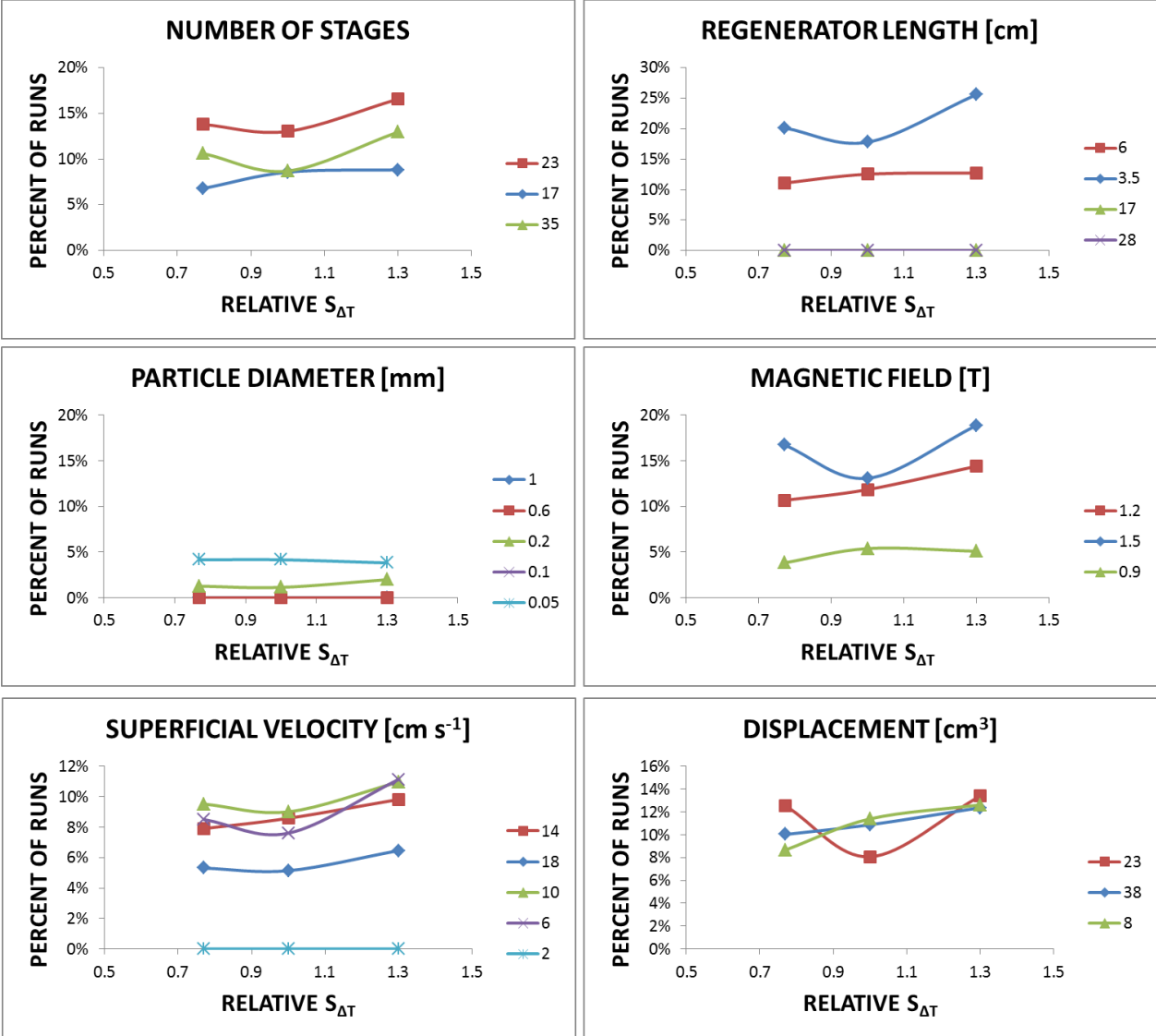


Figure B-3. $S_{\Delta T}$ with each MCHP parameter.

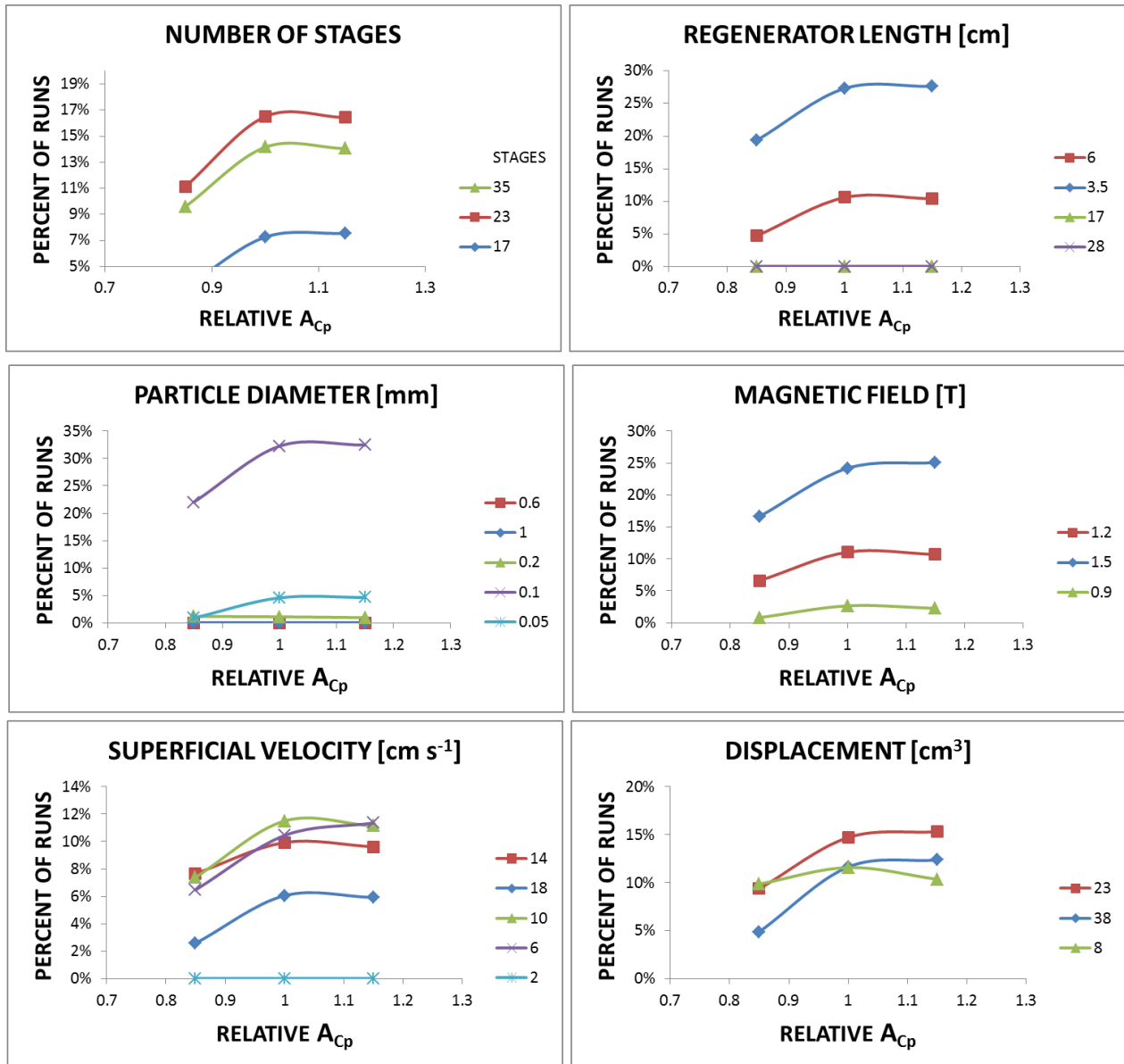


Figure B-4. A_{Cp} with each MCHP parameter.

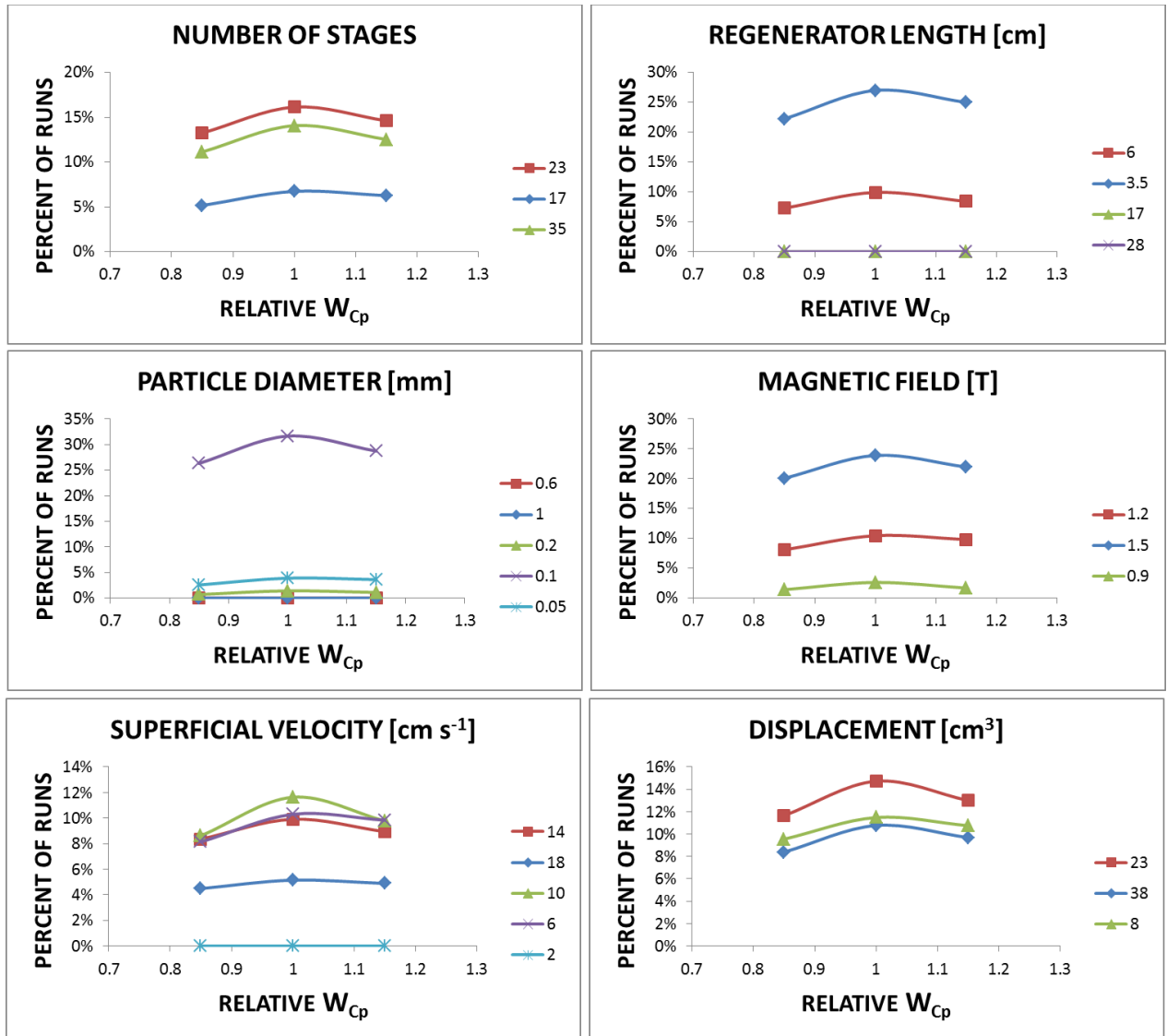


Figure B-5. W_{Cp} with each MCHP parameter.

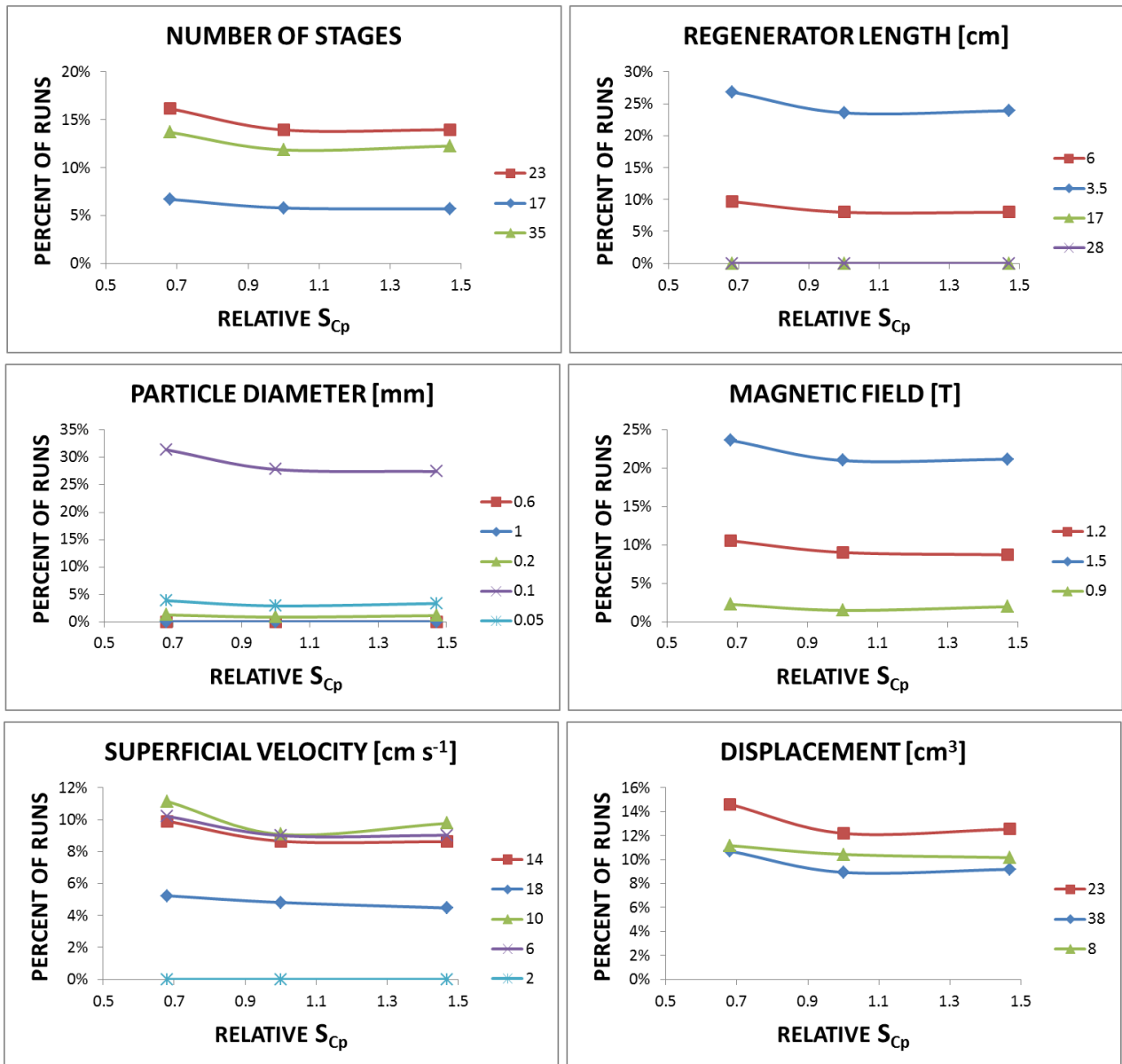


Figure B-6. S_{Cp} with each MCHP parameter.

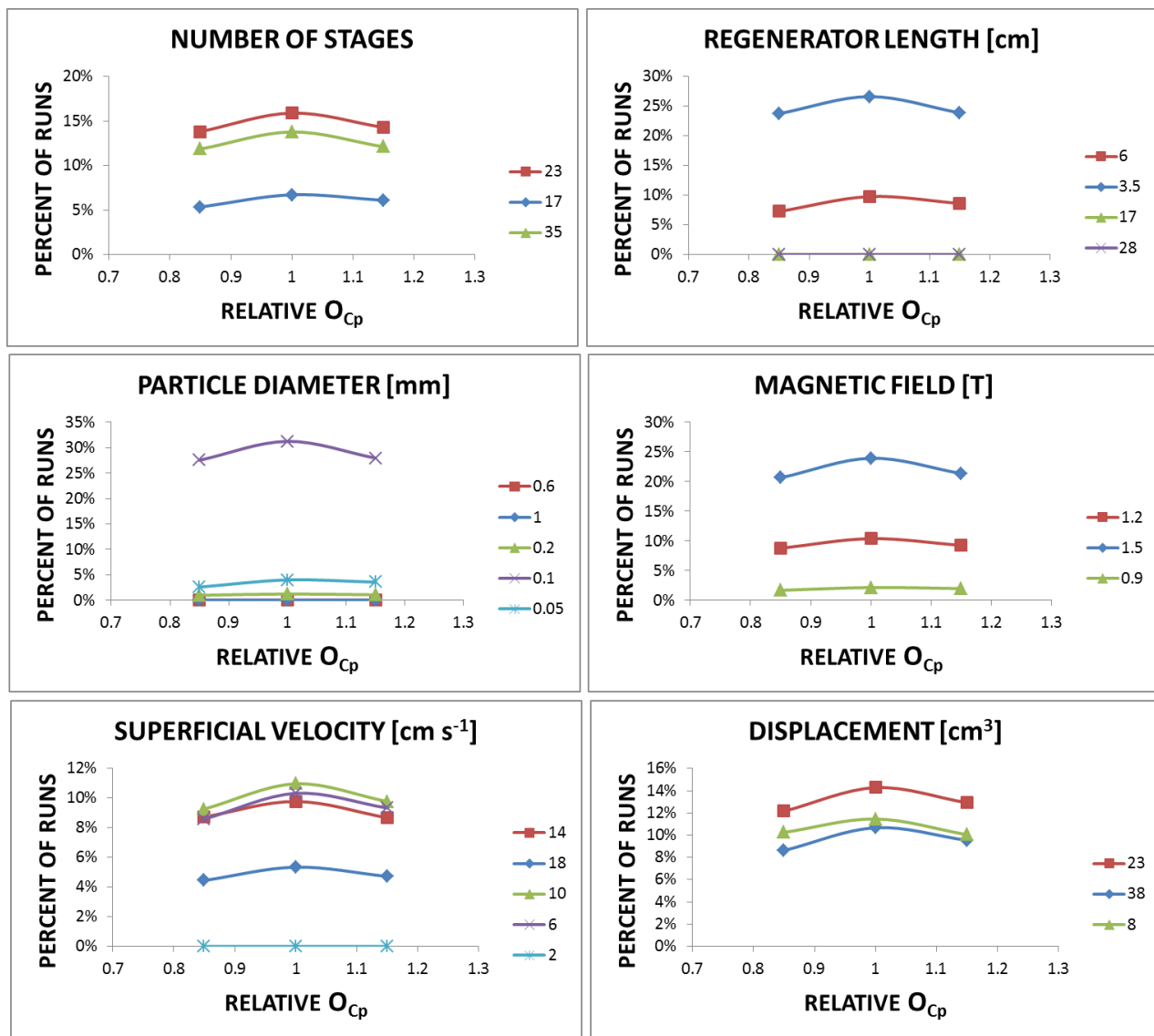


Figure B-7. O_{Cp} with each MCHP parameter.

APPENDIX C HIGH COOLING CAPACITY AND EFFICIENCY GRAPHS

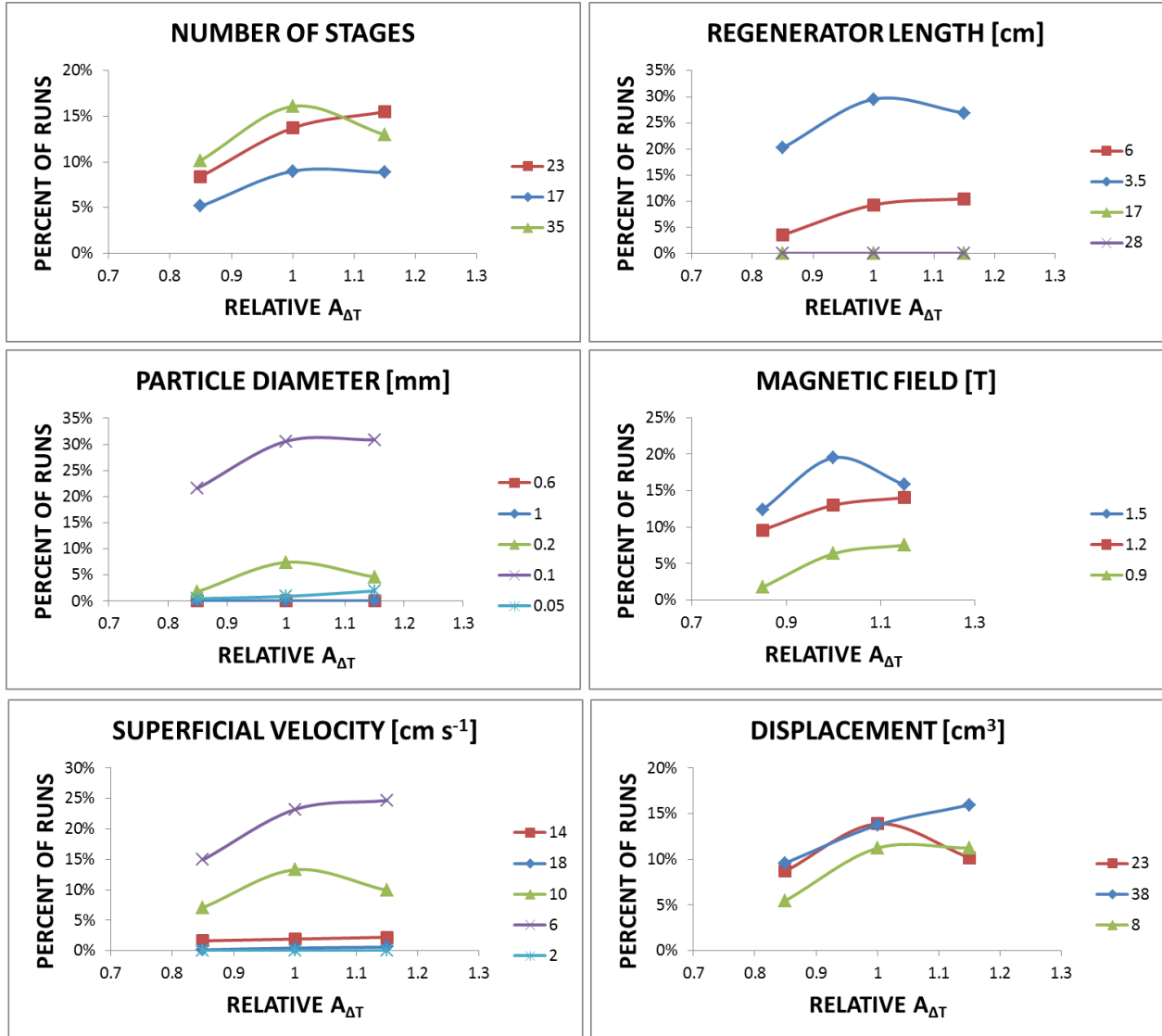


Figure C-1. $A_{\Delta T}$ with each MCHP parameter.

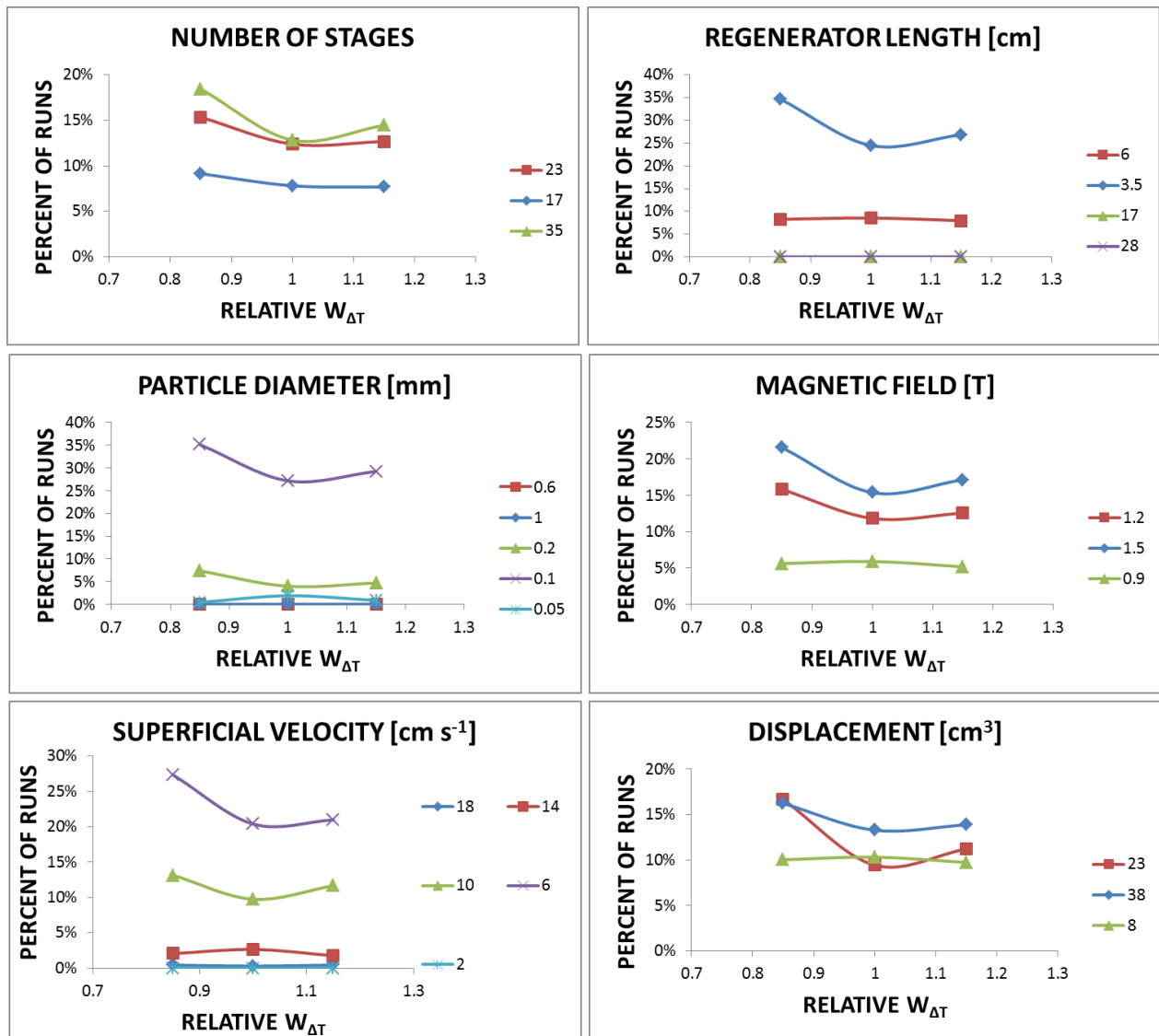


Figure C-2. $W_{\Delta T}$ with each MCHP parameter.

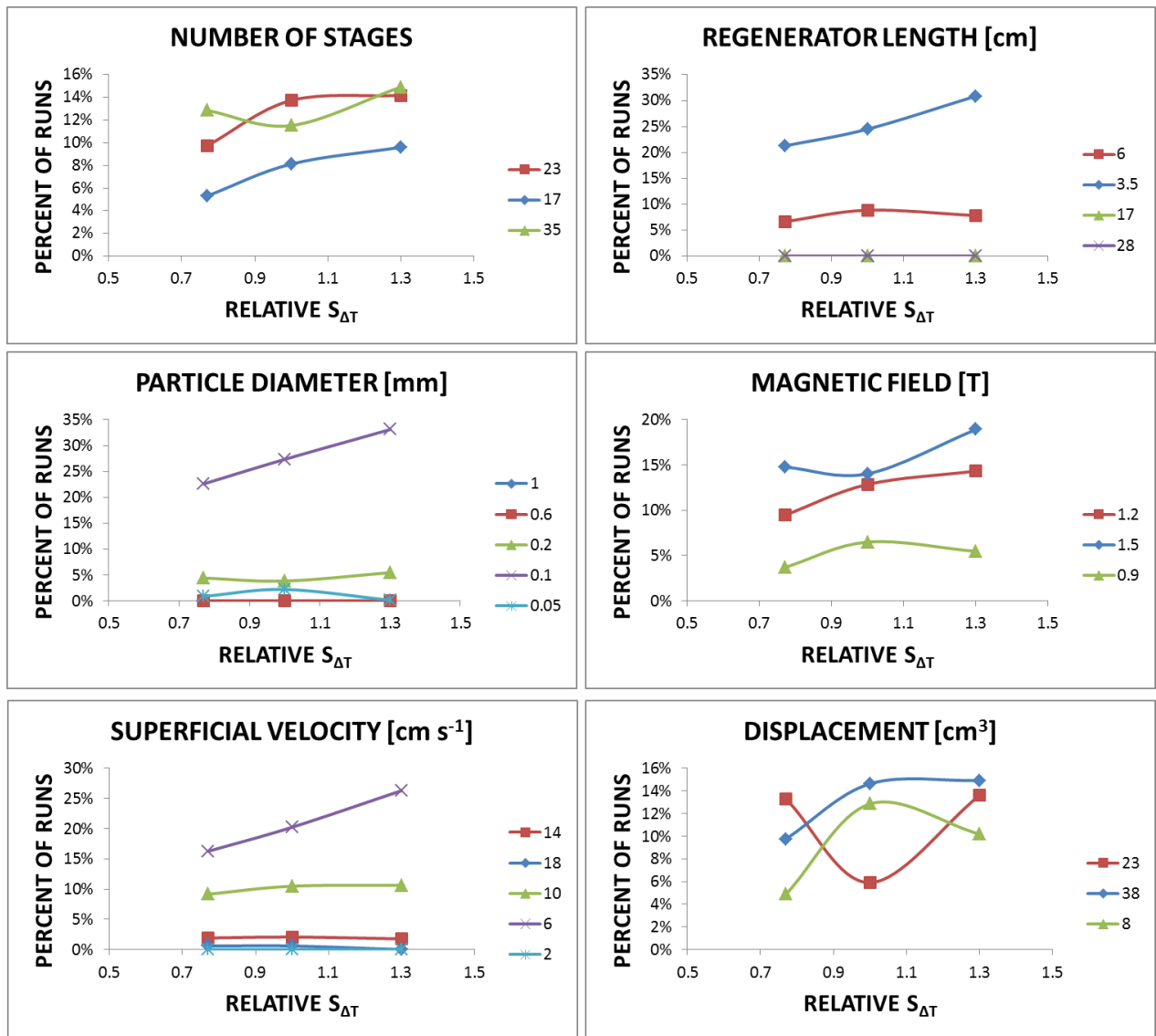


Figure C-3. $S_{\Delta T}$ with each MCHP parameter.

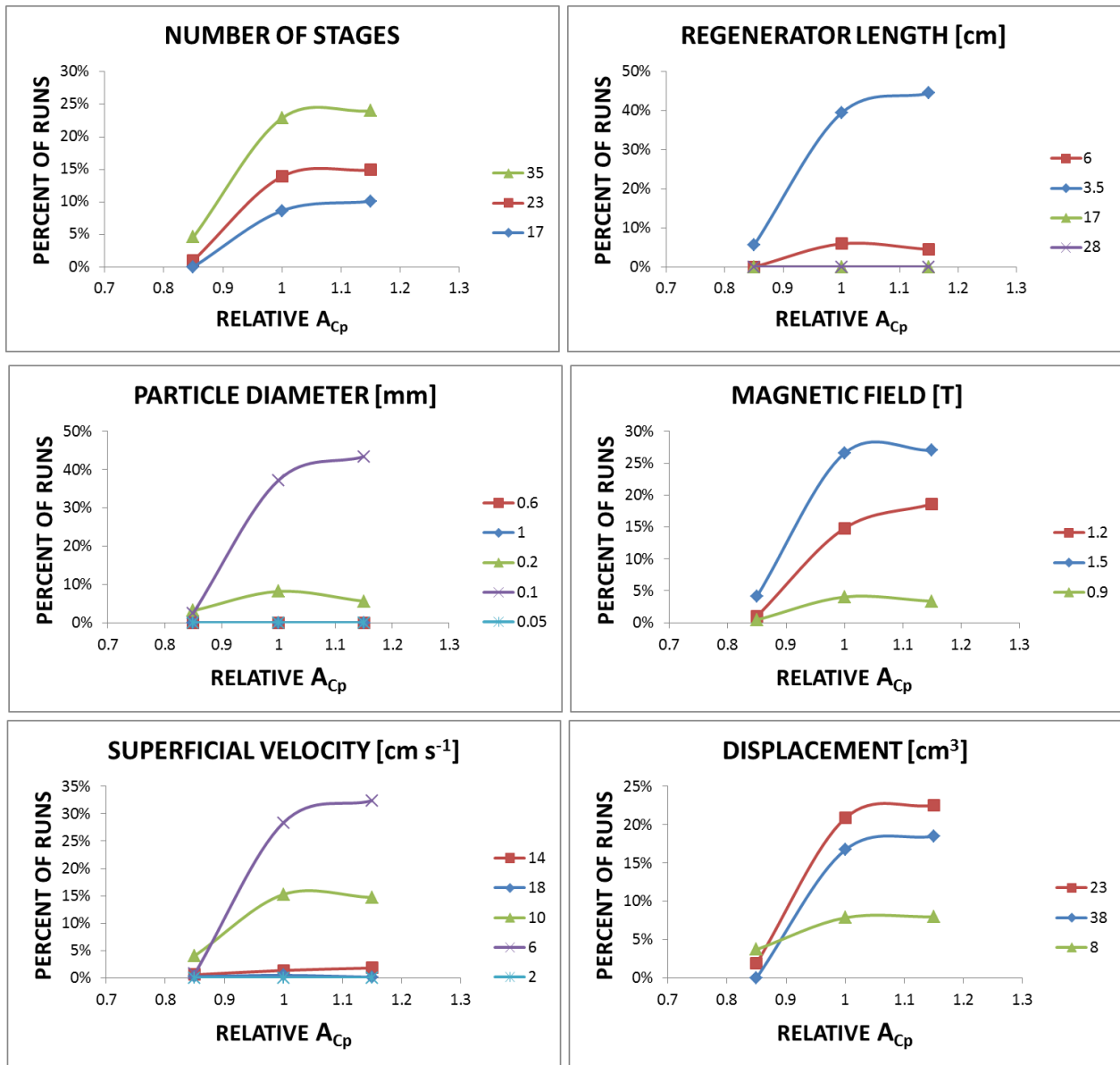


Figure C-4. A_{Cp} with each MCHP parameter.

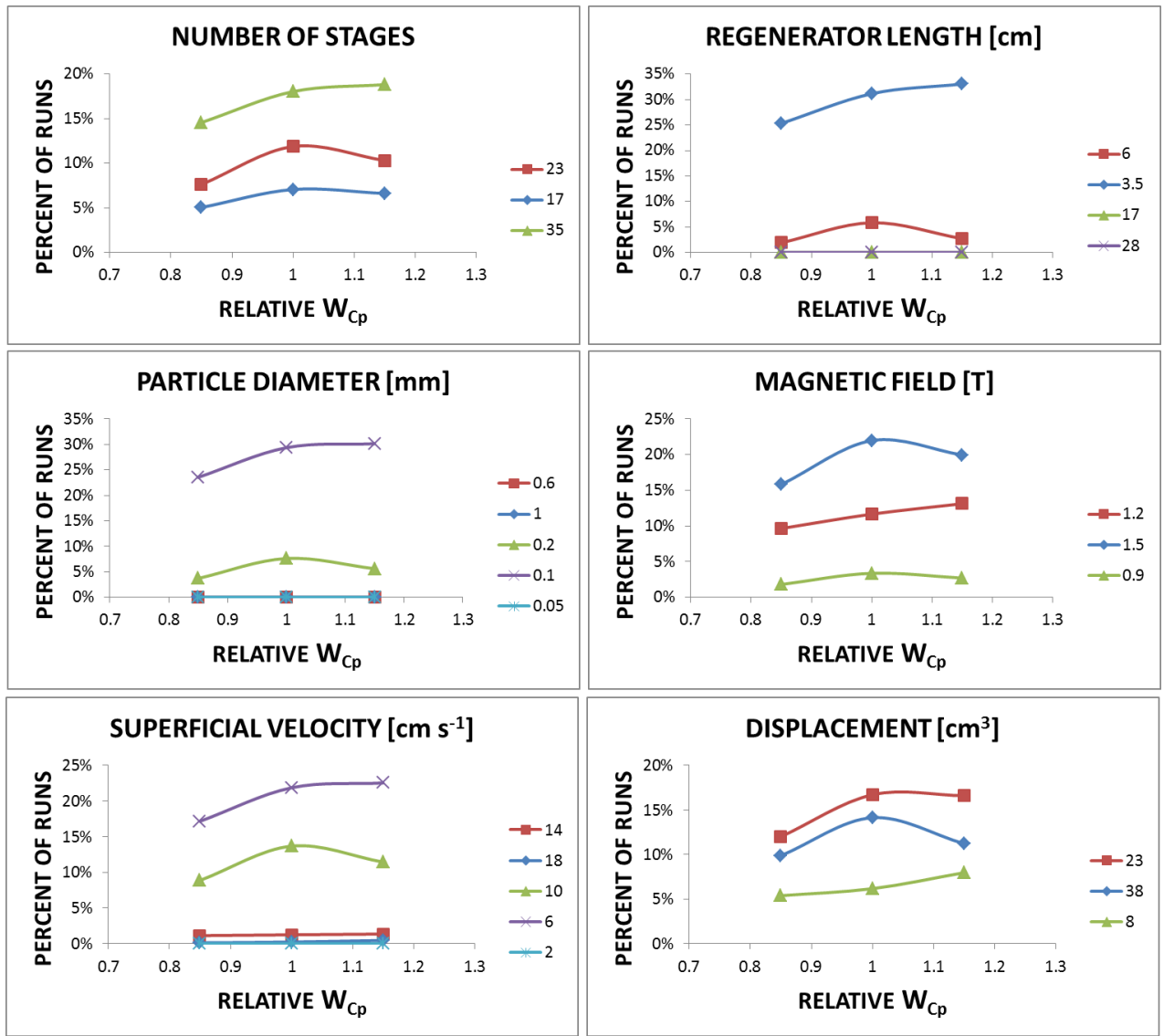


Figure C-5. W_{Cp} with each MCHP parameter.

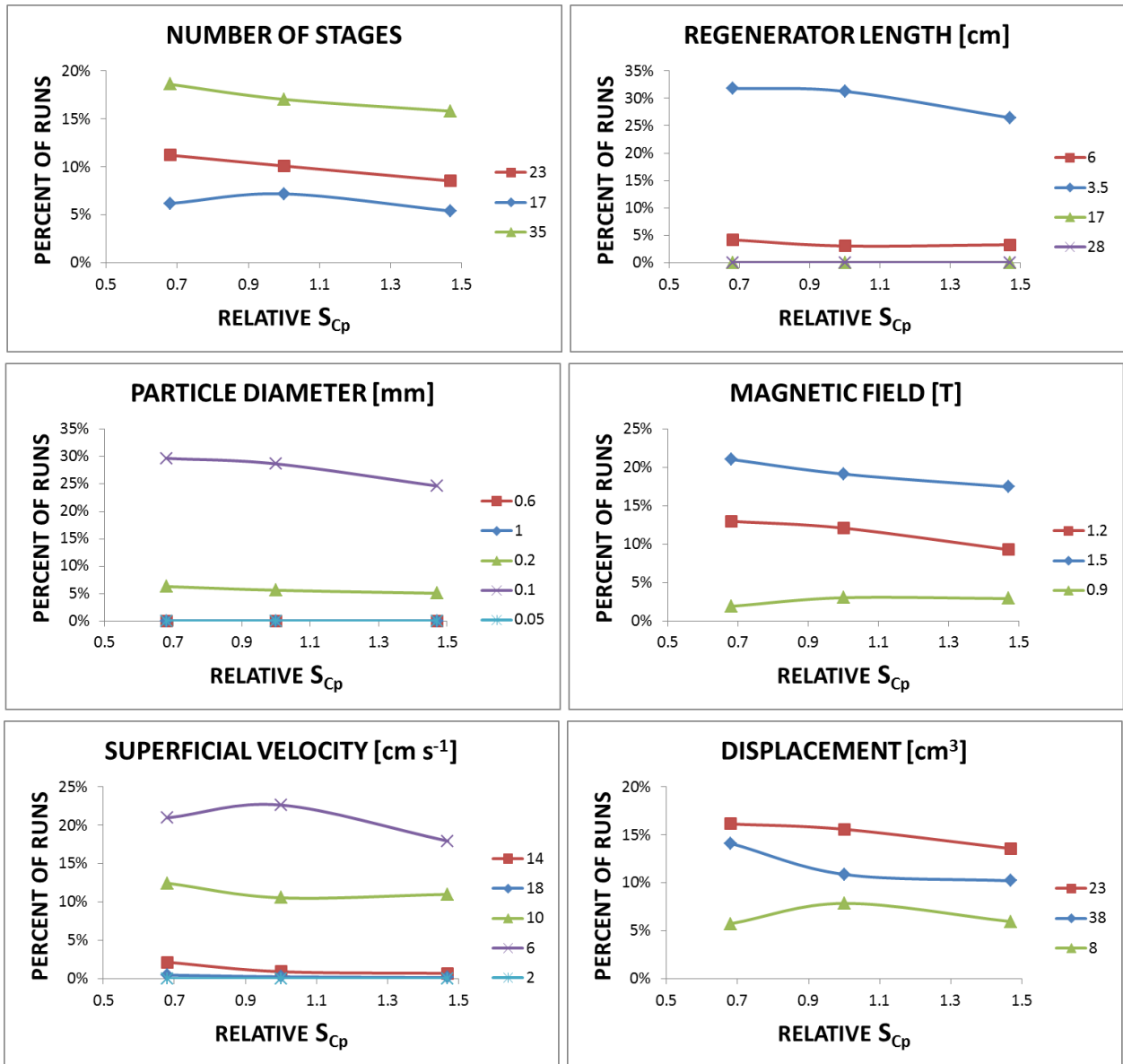


Figure C-6. S_{Cp} with each MCHP parameter.

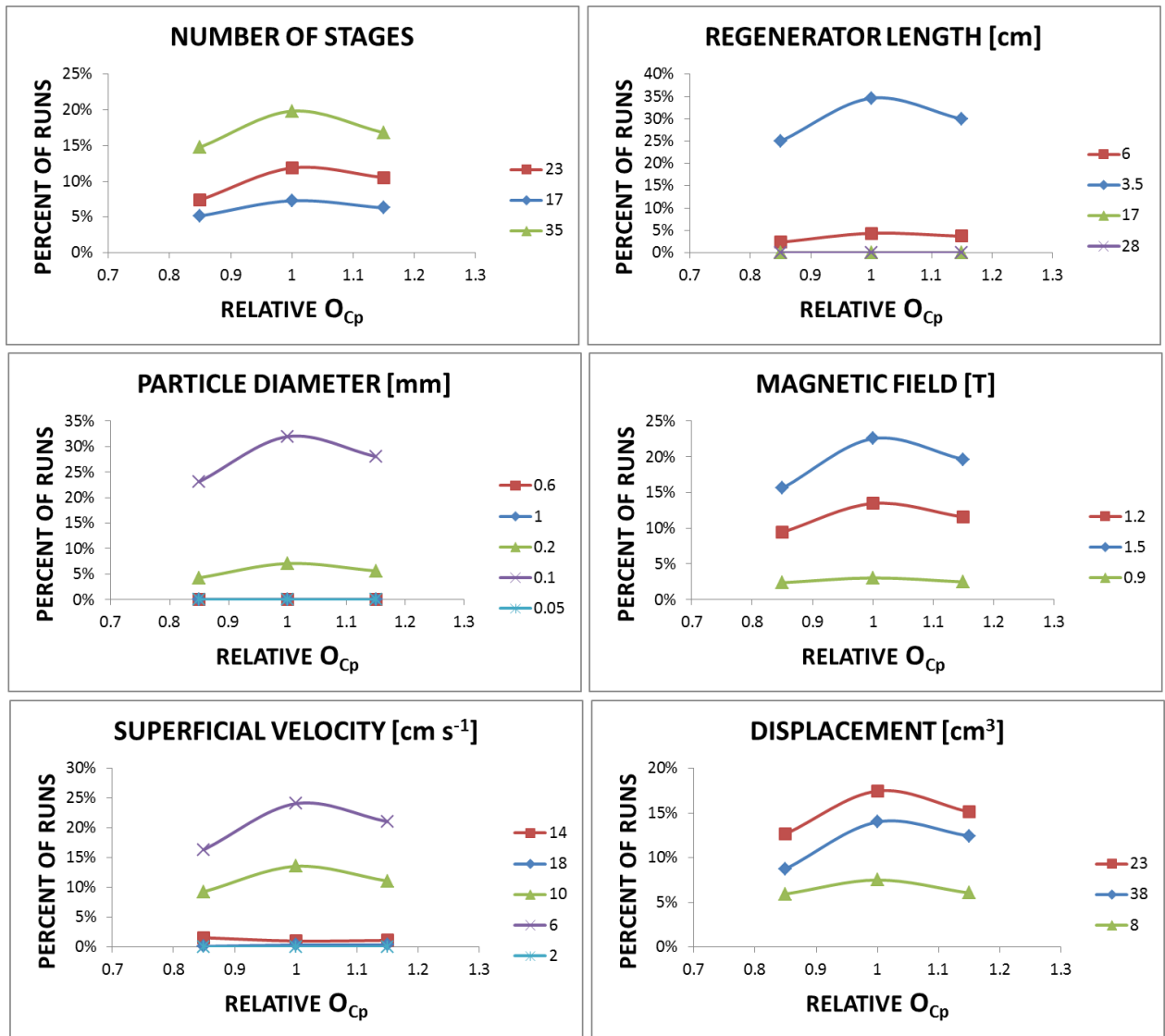


Figure C-7. O_{Cp} with each MCHP parameter.

LIST OF REFERENCES

- Allab, F., Kedous-Lebouc, A., Fournier, J.-M., Yonnet, J.-P., 2005. Numerical modeling for active magnetic regenerative refrigeration. *Magn. IEEE Trans.* 41, 3757–3759. doi:10.1109/TMAG.2005.854757
- Aprea, C., Greco, A., Maiorino, A., 2013. The use of the first and of the second order phase magnetic transition alloys for an AMR refrigerator at room temperature: A numerical analysis of the energy performances. *Energy Convers. Manag.* 70, 40–55. doi:10.1016/j.enconman.2013.02.006
- Aprea, C., Greco, A., Maiorino, A., 2012. Modelling an active magnetic refrigeration system: A comparison with different models of incompressible flow through a packed bed. *Appl. Therm. Eng.* 36, 296–306. doi:10.1016/j.applthermaleng.2011.10.034
- Aprea, C., Greco, A., Maiorino, A., 2011. A numerical analysis of an active magnetic regenerative refrigerant system with a multi-layer regenerator. *Energy Convers. Manag.* 52, 97–107. doi:10.1016/j.enconman.2010.06.048
- Aprea, C., Greco, A., Maiorino, A., Masselli, C., 2015. A comparison between rare earth and transition metals working as magnetic materials in an AMR refrigerator in the room temperature range. *Appl. Therm. Eng.* 91, 767–777. doi:10.1016/j.applthermaleng.2015.08.083
- Aprea, C., Maiorino, A., 2010. A flexible numerical model to study an active magnetic refrigerator for near room temperature applications. *Appl. Energy* 87, 2690–2698. doi:10.1016/j.apenergy.2010.01.009
- Arnold, D.S., Tura, A., Rowe, A., 2011. Experimental analysis of a two-material active magnetic regenerator. *Int. J. Refrig.* 34, 178–191. doi:10.1016/j.ijrefrig.2010.08.015
- Arnold, D.S., Tura, A., Ruebsaat-Trott, A., Rowe, A., 2014. Design improvements of a permanent magnet active magnetic refrigerator. *Int. J. Refrig.* 37, 99–105. doi:10.1016/j.ijrefrig.2013.09.024
- Bahl, C.R.H., Engelbrecht, K., Bjork, R., Eriksen, D., Smith, A., Nielsen, K.K., Pryds, N., 2011. Design concepts for a continuously rotating active magnetic regenerator. *Int. J. Refrig.* 34, 1792–1796. doi:10.1016/j.ijrefrig.2011.07.013
- Bahl, C.R.H., Engelbrecht, K., Eriksen, D., Lozano, J.A., Bjørk, R., Geyti, J., Nielsen, K.K., Smith, A., Pryds, N., 2014. Development and experimental results from a 1 kW prototype AMR. *Int. J. Refrig.* 37, 78–83. doi:10.1016/j.ijrefrig.2013.09.001
- Bahl, C.R.H., Petersen, T.F., Pryds, N., Smith, A., 2008. A versatile magnetic refrigeration test device. *Rev. Sci. Instrum.* 79. doi:10.1063/1.2981692

- Balli, M., Fruchart, D., Gignoux, D., Miraglia, S., Hlil, E.K., Wolfers, P., 2007. Modelling of the magnetocaloric effect in Gd_{1-x}Tbx and MnAs compounds. *J. Magn. Magn. Mater.* 316, 558–561. doi:10.1016/j.jmmm.2007.03.019
- Balli, M., Sari, O., Mahmed, C., Besson, C., Bonhote, P., Duc, D., Forchelet, J., 2012a. A pre-industrial magnetic cooling system for room temperature application. *Appl. Energy* 98, 556–561. doi:10.1016/j.apenergy.2012.04.034
- Balli, M., Sari, O., Zamni, L., Mahmed, C., Forchelet, J., 2012b. Implementation of La(Fe, Co)_{13-x}Si_x materials in magnetic refrigerators: Practical aspects. *Mater. Sci. Eng. B Solid-State Mater. Adv. Technol.* 177, 629–634. doi:10.1016/j.mseb.2012.03.016
- Barclay, J. ~A., 1983. Theory of an active magnetic regenerative refrigerator. NASA Conf. Publ.
- Barcza, A., Katter, M., Zellmann, V., Russek, S., Jacobs, S., Zimm, C., 2011. Stability and magnetocaloric properties of sintered La(Fe, Mn, Si)₁₃H alloys. *IEEE Trans. Magn.* 47, 3391–3394. doi:10.1109/TMAG.2011.2147774
- Basso, V., K pferling, M., Curcio, C., Bennati, C., Barzca, A., Katter, M., Bratko, M., Lovell, E., Turcaud, J., Cohen, L.F., 2015. Specific heat and entropy change at the first order phase transition of La(Fe-Mn-Si)₁₃-H compounds. *J. Appl. Phys.* 118, 53907. doi:10.1063/1.4928086
- Benedict, M.A., Sherif, S.A., Beers, D.G., Schroeder, M., 2016a. A new model of first-order magnetocaloric materials with experimental validation. *Int. J. Refrig.* doi:10.1016/j.ijrefrig.2016.07.001
- Benedict, M.A., Sherif, S.A., Beers, D.G., Schroeder, M.G., 2016b. Design and performance of a novel magnetocaloric heat pump. *Sci. Technol. Built Environ.*
- Benedict, M.A., Sherif, S.A., Schroeder, M.G., Beers, D.G., 2016c. Experimental Impact of Magnet and Regenerator Design on the Refrigeration Performance of First-Order Magnetocaloric Materials. *Int. J. Refrig.*
- Bj rk, R., 2010. Designing a magnet for magnetic refrigeration.
- Bjork, R., Bahl, C.R.H., 2013. Demagnetization factor for a powder of randomly packed spherical particles. *Appl. Phys. Lett.* 103, 2–5. doi:10.1063/1.4820141
- Bj rk, R., Bahl, C.R.H., Katter, M., 2010. Magnetocaloric properties of LaFe_{13-x-y}CoxSi_y and commercial grade Gd. *J. Magn. Magn. Mater.* 322, 3882–3888. doi:10.1016/j.jmmm.2010.08.013
- Borgnakke, C. (Claus), Sonntag, R.E., 2013. Fundamentals of thermodynamics, 8th ed.
- Bouchard, J., Nesreddine, H., Galanis, N., 2009. Model of a porous regenerator used

- for magnetic refrigeration at room temperature. *Int. J. Heat Mass Transf.* 52, 1223–1229. doi:10.1016/j.ijheatmasstransfer.2008.08.031
- Brey, W., Nellis, G., Klein, S., 2014. Thermodynamic modeling of magnetic hysteresis in AMRR cycles. *Int. J. Refrig.* 47, 85–97. doi:10.1016/j.ijrefrig.2014.07.013
- Brown, G. V., 1976. Magnetic heat pumping near room temperature. *J. Appl. Phys.* 47, 3673–3680. doi:10.1063/1.323176
- Chen, F.C., Murphy, R.W., Mei, V.C., Chen, G.L., 1992. Thermodynamic Analysis of Four Magnetic Heat-Pump Cycles. *J. Eng. Gas Turbines Power* 114, 715. doi:10.1115/1.2906647
- Chiba, Y., Smaili, A., Mahmed, C., Balli, M., Sari, O., 2014. Thermal investigations of an experimental active magnetic regenerative refrigerator operating near room temperature. *Int. J. Refrig.* 37, 36–42. doi:10.1016/j.ijrefrig.2013.09.038
- Christensen, D. V, Nielsen, K.K., Bahl, C.R.H., Smith, a, 2011. Demagnetizing effects in stacked rectangular prisms. *J. Phys. D. Appl. Phys.* 44, 215004. doi:10.1088/0022-3727/44/21/215004
- Clot, P., Viallet, D., Allab, F., Kedous-Lebouc, A., Fournier, J.M., Yonnet, J.P., 2003. A Magnet-Based Device for Active Magnetic Regenerative Refrigeration. *IEEE Trans. Magn.* 39, 3349–3351. doi:10.1109/TMAG.2003.816253
- Conti, J.J., Holtberg, P.D., Diefenderfer, J.R., Napolitano, S.A., Schaal, M., Turnure, J.T., Westfall, L.D., 2014. Annual Energy Outlook 2014, Annual Energy Outlook. Washington, DC. doi:10.1007/s13398-014-0173-7.2
- Dan'kov, S., Tishin, a., Pecharsky, V., Gschneidner, K., 1998. Magnetic phase transitions and the magnetothermal properties of gadolinium. *Phys. Rev. B* 57, 3478–3490. doi:10.1103/PhysRevB.57.3478
- Dan'kov, S.Y., Tishin, a. M., Pecharsky, V.K., Gschneidner, K. a., 1997. Experimental device for studying the magnetocaloric effect in pulse magnetic fields. *Rev. Sci. Instrum.* 68, 2432. doi:10.1063/1.1148057
- Degregoria, A.J., Barclay, J.A., Claybaker, P.J., Jaeger, S.R., Kral, S.F., Pax, R.A., Rowe, J.R., Zimm, C.B., 1990. Preliminary design of a 100 W 1.8 K to 4.7 K regenerative magnetic refrigerator. *Adv. Cryog. Eng.* 35, 1125–1131.
- Differential Scanning Calorimetry (DSC) Instruments | PerkinElmer [WWW Document], n.d. . 1998. URL <http://www.perkinelmer.com/category/differential-scanning-calorimetry-dsc-instruments> (accessed 9.17.16).
- Dikeos, J., Rowe, A., Tura, A., 2006. Numerical Analysis of an Active Magnetic Regenerator (AMR) Refrigeration Cycle, in: *Advances in Cryogenic Engineering: Transactions of the Cryogenic Engineering Conference*. AIP, Keystone , pp. 993–

1000. doi:10.1063/1.2202512

- Engelbrecht, K., 2008. A Numerical Model of an Active Magnetic Regenerator Refrigerator with Experimental Validation by. University of Wisconsin-Madison.
- Engelbrecht, K., 2004. A numerical model of an active magnetic regenerator refrigeration system. University of Wisconsin-Madison.
- Engelbrecht, K., Bahl, C.R.H., 2010. Evaluating the effect of magnetocaloric properties on magnetic refrigeration performance. *J. Appl. Phys.* 108. doi:10.1063/1.3525647
- Engelbrecht, K., Bahl, C.R.H., Nielsen, K.K., 2011a. Experimental results for a magnetic refrigerator using three different types of magnetocaloric material regenerators. *Int. J. Refrig.* 34, 1132–1140. doi:10.1016/j.ijrefrig.2010.11.014
- Engelbrecht, K., Eriksen, D., Bahl, C.R.H., Bjørk, R., Geyti, J., Lozano, J.A., Nielsen, K.K., Saxild, F., Smith, A., Pryds, N., 2012. Experimental results for a novel rotary active magnetic regenerator. *Int. J. Refrig.* 35, 1498–1505. doi:10.1016/j.ijrefrig.2012.05.003
- Engelbrecht, K., Nielsen, K.K., Bahl, C.R.H., Carroll, C.P., van Asten, D., 2013. Material properties and modeling characteristics for $\text{MnFeP}_{1-x}\text{As}_x$ materials for application in magnetic refrigeration. *J. Appl. Phys.* 113, 173510. doi:10.1063/1.4803495
- Engelbrecht, K., Nielsen, K.K., Pryds, N., 2011b. An experimental study of passive regenerator geometries. *Int. J. Refrig.* 34, 1817–1822. doi:10.1016/j.ijrefrig.2011.07.015
- Engelbrecht, K., Tušek, J., Nielsen, K.K., Kitanovski, A., Bahl, C.R.H., Poredoš, A., 2013. Improved modelling of a parallel plate active magnetic regenerator. *J. Phys. D. Appl. Phys.* 46, 255002. doi:10.1088/0022-3727/46/25/255002
- Ergun, S., Orning, A.A., 1949. Fluid Flow through Randomly Packed Columns and Fluidized Beds. *Ind. Eng. Chem.* 41, 1179–1184. doi:10.1021/ie50474a011
- Franco, V., Blázquez, J.S., Ingale, B., Conde, a., 2012. The Magnetocaloric Effect and Magnetic Refrigeration Near Room Temperature: Materials and Models. *Annu. Rev. Mater. Res.* 42, 305–342. doi:10.1146/annurev-matsci-062910-100356
- Fujieda, S., Hasegawa, Y., Fujita, A., Fukamichi, K., 2004. Thermal transport properties of magnetic refrigerants $\text{La}(\text{Fe}_x\text{Si}_{1-x})_{13}$ and their hydrides, and $\text{Gd}_5\text{Si}_2\text{Ge}_2$ and MnAs . *J. Appl. Phys.* 95, 2429–2431. doi:10.1063/1.1643774
- Fujita, A., Fujieda, S., Hasegawa, Y., Fukamichi, K., 2003. Itinerant-electron metamagnetic transition and large magnetocaloric effects in $\text{La}(\text{Fe}_x\text{Si}_{1-x})_{13}$ compounds and their hydrides. *Phys. Rev. B* 67, 104416. doi:10.1103/PhysRevB.67.104416

- Giauque, W.F., 1927. A THERMODYNAMIC TREATMENT OF CERTAIN MAGNETIC EFFECTS. A PROPOSED METHOD OF PRODUCING TEMPERATURES CONSIDERABLY BELOW 1° ABSOLUTE. *J. Am. Chem. Soc.* 49, 1864–1870. doi:10.1021/ja01407a003
- Gschneidner Jr., K. A.; Pecharsky, V. K.; Tsokol, A.O., 2005. Recent developments in magnetocaloric materials. *Reports Prog. Phys.* 68, 1479–1539. doi:10.1088/0034-4885/68/6/R04
- Halbach, K., 1980. Design of permanent multipole magnets with oriented rare earth cobalt material. *Nucl. Instruments Methods* 169, 1–10. doi:10.1016/0029-554X(80)90094-4
- Hsieh, C.M., Su, Y.C., Lee, C.H., Cheng, P.H., Leou, K.C., 2014. Modeling of graded active magnetic regenerator for room-temperature, energy-efficient refrigeration. *IEEE Trans. Magn.* 50. doi:10.1109/TMAG.2013.2274097
- Hu, F., Shen, B., Sun, J., 2000. Magnetic entropy change in Ni_{51.5}Mn_{22.7}Ga_{25.8} alloy. *Appl. Phys. Lett.* 76, 3460. doi:10.1063/1.126677
- Hu, F.X., Shen, B.G., Sun, J.R., 2002. Very large magnetic entropy change near room temperature in {LaFe_{11.2}Co_{0.7}Si_{1.1}}. *Appl. Phys. Lett.* 80, 826. doi:10.1063/1.1447592
- Ingale, B., Gopalan, R., Raja, M.M., Chandrasekaran, V., Ram, S., 2007. Magnetostructural transformation, microstructure, and magnetocaloric effect in Ni-Mn-Ga Heusler alloys. *J. Appl. Phys.* 102, 13906. doi:10.1063/1.2751489
- Jacobs, S., Auringer, J., Boeder, A., Chell, J., Komorowski, L., Leonard, J., Russek, S., Zimm, C., 2014. The performance of a large-scale rotary magnetic refrigerator. *Int. J. Refrig.* 37, 84–91. doi:10.1016/j.ijrefrig.2013.09.025
- Johnson, J.W., Zimm, C.B., 1996. Performance modeling of a 4 K active magnetic regenerative refrigerator. *J. Appl. Phys.* 79, 2171. doi:10.1063/1.361422
- Kawanami, T., Chiba, K., Sakurai, K., Ikegawa, M., 2006. Optimization of a magnetic refrigerator at room temperature for air cooling systems. *Int. J. Refrig.* 29, 1294–1301. doi:10.1016/j.ijrefrig.2006.07.018
- Kim, Y., Jeong, S., 2011. Numerical simulation and its verification for an active magnetic regenerator. *Int. J. Refrig.* 34, 204–215. doi:10.1016/j.ijrefrig.2010.07.003
- Kitanovski, A., Plaznik, U., Tušek, J., Poredoš, A., 2014. New thermodynamic cycles for magnetic refrigeration. *Int. J. Refrig.* 37, 28–35. doi:10.1016/j.ijrefrig.2013.05.014
- Koch, D.L., Brady, J.F., 1985. Dispersion in fixed beds. *J. Fluid Mech.* 154, 399. doi:10.1017/S0022112085001598

- Li, J., Numazawa, T., Nakagome, H., Matsumoto, K., 2011. Numerical modeling on a reciprocating active magnetic regenerator refrigeration in room temperature. *Cryogenics (Guildf)*. 51, 347–352. doi:10.1016/j.cryogenics.2010.12.008
- Li, P., Gong, M., Yao, G., Wu, J., 2006. A practical model for analysis of active magnetic regenerative refrigerators for room temperature applications. *Int. J. Refrig.* 29, 1259–1266. doi:10.1016/j.ijrefrig.2006.07.021
- Lionte, S., Vasile, C., Siroux, M., 2015. Numerical analysis of a reciprocating active magnetic regenerator. *Appl. Therm. Eng.* 75, 871–879. doi:10.1016/j.applthermaleng.2014.10.076
- Liu, M., Yu, B., 2011. Numerical investigations on internal temperature distribution and refrigeration performance of reciprocating active magnetic regenerator of room temperature magnetic refrigeration. *Int. J. Refrig.* 34, 617–627. doi:10.1016/j.ijrefrig.2010.12.003
- Lozano, J.A., Engelbrecht, K., Bahl, C.R.H., Nielsen, K.K., Barbosa, J.R., Prata, A.T., Pryds, N., 2014. Experimental and numerical results of a high frequency rotating active magnetic refrigerator. *Int. J. Refrig.* 37, 92–98. doi:10.1016/j.ijrefrig.2013.09.002
- Lozano, J.A., Engelbrecht, K., Bahl, C.R.H., Nielsen, K.K., Eriksen, D., Olsen, U.L., Barbosa, J.R., Smith, A., Prata, A.T., Pryds, N., 2013. Performance analysis of a rotary active magnetic refrigerator. *Appl. Energy* 111, 669–680. doi:10.1016/j.apenergy.2013.05.039
- Marcos, J., Casanova, F., Batlle, X., Labarta, A., Planes, A., Mañosa, L., 2003. A high-sensitivity differential scanning calorimeter with magnetic field for magnetostructural transitions. *Rev. Sci. Instrum.* 74, 4768–4771. doi:10.1063/1.1614857
- Matsumoto, K., Hashimoto, T., 1990. Thermodynamic analysis of a magnetically active regenerator from 30 to 70 K with a Brayton-like cycle. *Cryogenics (Guildf)*. 30, 840–845.
- Morrish, A.H., 2001. *The physical principles of magnetism*. IEEE Press.
- Nielsen, K.K., Bahl, C.R.H., Smith, A., 2010a. Constraints on the adiabatic temperature change in magnetocaloric materials. *Phys. Rev. B - Condens. Matter Mater. Phys.* 81, 1–5. doi:10.1103/PhysRevB.81.054423
- Nielsen, K.K., Bahl, C.R.H., Smith, A., Bjork, R., Pryds, N., Hattel, J., 2009. Detailed numerical modeling of a linear parallel-plate Active Magnetic Regenerator. *Int. J. Refrig.* 32, 1478–1486. doi:10.1016/j.ijrefrig.2009.03.003
- Nielsen, K.K., Bahl, C.R.H., Smith, A., Pryds, N., Hattel, J., 2010b. A comprehensive parameter study of an active magnetic regenerator using a 2D numerical model. *Int. J. Refrig.* 33, 753–764. doi:10.1016/j.ijrefrig.2009.12.024

- Nielsen, K.K., Engelbrecht, K., Bahl, C.R.H., 2013. The influence of flow maldistribution on the performance of inhomogeneous parallel plate heat exchangers. *Int. J. Heat Mass Transf.* 60, 432–439. doi:10.1016/j.ijheatmasstransfer.2013.01.018
- Nielsen, K.K., Tusek, J., Engelbrecht, K., Schopfer, S., Kitanovski, A., Bahl, C.R.H., Smith, A., Pryds, N., Poredos, A., 2011. Review on numerical modeling of active magnetic regenerators for room temperature applications. *Int. J. Refrig.* 34, 603–616. doi:10.1016/j.ijrefrig.2010.12.026
- Ott, R.L., Longnecker, M.T., 2004. *A First Course in Statistical Methods*, 1st ed. Thomson, Belmont.
- Pearson, K., 1894. Contributions to the mathematical theory of evolution. *Philos. Trans. R. Soc. London. A* 185, 71–110.
- Pecharsky, V., Gschneidner, K., Pecharsky, A., Tishin, A., 2001. Thermodynamics of the magnetocaloric effect. *Phys. Rev. B* 64, 144406. doi:10.1103/PhysRevB.64.144406
- Pecharsky, V.K., Gschneidner, K.A., 2005. Magnetocaloric Effect Associated with Magnetostructural Transitions, in: Planes, A., Mañosa, L., Saxena, A. (Eds.), *Magnetism and Structure in Functional Materials*. Springer Berlin Heidelberg, Berlin, Heidelberg, pp. 199–222. doi:10.1007/3-540-31631-0_11
- Pecharsky, V.K., Gschneidner, K.A., 1997a. Giant Magnetocaloric Effect in Gd₅(Si₂Ge₂). *Phys. Rev. Lett.* 78, 4494–4497. doi:10.1103/PhysRevLett.78.4494
- Pecharsky, V.K., Gschneidner, K.A., 1997b. Tunable magnetic regenerator alloys with a giant magnetocaloric effect for magnetic refrigeration from ~20 to ~290 K. *Appl. Phys. Lett.* 70, 3299. doi:10.1063/1.119206
- Peksoy, O., Rowe, A., 2005. Demagnetizing effects in active magnetic regenerators. *J. Magn. Magn. Mater.* 288, 424–432. doi:10.1016/j.jmmm.2004.09.131
- Petersen, T.F., Engelbrecht, K., Bahl, C.R.H., Elmegaard, B., Pryds, N., Smith, A., 2008a. Comparison between a 1D and a 2D numerical model of an active magnetic regenerative refrigerator. *J. Phys. D. Appl. Phys.* 41, 105002. doi:10.1088/0022-3727/41/10/105002
- Petersen, T.F., Pryds, N., Smith, A., Hattel, J., Schmidt, H., Hogaard Knudsen, H.J., 2008b. Two-dimensional mathematical model of a reciprocating room-temperature Active Magnetic Regenerator. *Int. J. Refrig.* 31, 432–443. doi:10.1016/j.ijrefrig.2007.07.009
- Pryds, N., Clemens, F., Menon, M., Nielsen, P.H., Brodersen, K., Bjork, R., Bahl, C.R.H., Engelbrecht, K., Nielsen, K.K., Smith, A., 2011. A monolithic perovskite structure for use as a magnetic regenerator. *J. Am. Ceram. Soc.* 94, 2549–2555. doi:10.1111/j.1551-2916.2011.04398.x

- Python.com [WWW Document], 2015. . Python Softw. Found. URL [http](http://python.com)
- Risser, M., Vasile, C., Engel, T., Keith, B., Muller, C., 2010. Numerical simulation of magnetocaloric system behaviour for an industrial application. *Int. J. Refrig.* 33, 973–981. doi:10.1016/j.ijrefrig.2010.02.004
- Risser, M., Vasile, C., Keith, B., Engel, T., Muller, C., 2012. Construction of consistent magnetocaloric materials data for modelling magnetic refrigerators. *Int. J. Refrig.* 35, 459–467. doi:10.1016/j.ijrefrig.2011.11.001
- Romero-Muñiz, C., Ipus, J.J., Blázquez, J.S., Franco, V., Conde, a., 2014. Influence of the demagnetizing factor on the magnetocaloric effect: Critical scaling and numerical simulations. *Appl. Phys. Lett.* 104, 252405. doi:10.1063/1.4885110
- Roudaut, J., Kedous-Lebouc, A., Yonnet, J.P., Muller, C., 2011. Numerical analysis of an active magnetic regenerator. *Int. J. Refrig.* 34, 1797–1804. doi:10.1016/j.ijrefrig.2011.07.012
- Rowe, A., 2012. Thermodynamics of active magnetic regenerators: Part i. *Cryogenics (Guildf)*. 52, 111–118. doi:10.1016/j.cryogenics.2011.09.005
- Rowe, A., Barclay, J. a, 2002. Design of an active magnetic regenerator test apparatus. *Adv. Cryog. Eng.* 47 a, 1073. doi:<http://dx.doi.org/10.1063/1.1472122>
- Rowe, A., Tura, A., 2006. Experimental investigation of a three-material layered active magnetic regenerator. *Int. J. Refrig.* 29, 1286–1293. doi:10.1016/j.ijrefrig.2006.07.012
- Sarlah, A., Poredos, A., 2010. Dimensionless numerical model for simulation of active magnetic regenerator refrigerator. *Int. J. Refrig.* 33, 1061–1067. doi:10.1016/j.ijrefrig.2010.04.003
- Scarpa, F., Tagliafico, G., Tagliafico, L.A., 2012. Classification proposal for room temperature magnetic refrigerators. *Int. J. Refrig.* 35, 453–458. doi:10.1016/j.ijrefrig.2011.09.010
- Schroeder, M., Brehob, E., 2016. A flexible numerical model of a multistage active magnetocaloric regenerator. *Int. J. Refrig.* 65, 250–257.
- Scott, G.D., Kilgour, D.M., D, B.J., L, B.J.D. and F.J., L, M.P.C. and W.E., K, R.O., R, R., D, S.G., D, S.G., D, S.G., R, W.A.E.R. and H.H., Yerazunis S, C.S.W. and W.B., 1969. The density of random close packing of spheres. *J. Phys. D. Appl. Phys.* 2, 311. doi:10.1088/0022-3727/2/6/311
- Shir, F., Della Torre, E., Bennett, L.H., Mavriplis, C., Shull, R.D., 2004. Modeling of magnetization and demagnetization in magnetic regenerative refrigeration. *IEEE Trans. Magn.* 40, 2098–2100. doi:10.1109/TMAG.2004.832475

- Siddikov, B., Wade, B., Schultz, D., 2005. Numerical simulation of the active magnetic regenerator. *Comput. Math. with* doi:10.1015/j.camwa.2004.07.026
- Skomski, R., Hadjipanayis, G.C., Sellmyer, D.J., 2007. Effective Demagnetizing Factors of Complicated Particle Mixtures. *IEEE Trans. Magn.* 43, 2956–2958. doi:10.1109/TMAG.2007.893798
- Smaïli, A., Chahine, R., 1998. Thermodynamic investigations of optimum active magnetic regenerators. *Cryogenics (Guildf)*. 38, 247–252. doi:10.1016/S0011-2275(97)00140-9
- Smith, A., Bahl, C.R.H., Bjork, R., Engelbrecht, K., Nielsen, K.K., Pryds, N., 2012. Materials challenges for high performance magnetocaloric refrigeration devices. *Adv. Energy Mater.* 2, 1288–1318. doi:10.1002/aenm.201200167
- Smith, A., Nielsen, K.K., Bahl, C.R.H., 2014. Scaling and universality in magnetocaloric materials. *Phys. Rev. B - Condens. Matter Mater. Phys.* 90, 1–17. doi:10.1103/PhysRevB.90.104422
- Srivistava, V., Johnson, F., 2014. Interrelation of magnetic phase diagram and magnetic refrigerator performance, in: 6th International Conference on Magnetic Refrigeration at Room Temperature (Thermag VI). Proceedings. IIR, Victoria, Canada.
- Steyert, W.A., 1978. Stirling-cycle rotating magnetic refrigerators and heat engines for use near room temperature. *J. Appl. Phys.* 49, 1216. doi:10.1063/1.325009
- Tagliafico, G., Scarpa, F., Canepa, F., 2010. A dynamic 1-D model for a reciprocating active magnetic regenerator; influence of the main working parameters. *Int. J. Refrig.* 33, 286–293. doi:10.1016/j.ijrefrig.2009.10.001
- Tegus, O., Brück, E., Buschow, K.H.J., de Boer, F.R., 2002. Transition-metal-based magnetic refrigerants for room-temperature applications. *Nature* 415, 150–152. doi:10.1038/415150a
- Tishin, A.M., Gschneidner Jr., K.A., Pecharsky, V.K., 1999. Magnetocaloric effect and heat capacity in the phase-transition region. *Phys. Rev. B* 59, 503–511.
- Tishin, A.M., Spichkin, Y.I., 2003. The magnetocaloric effect and its applications. Institute of Physics Pub.
- Tura, A., Nielsen, K.K., Rowe, A., 2012a. Experimental and modeling results of a parallel plate-based active magnetic regenerator, in: *International Journal of Refrigeration*. pp. 1518–1527. doi:10.1016/j.ijrefrig.2012.04.016
- Tura, A., Nielsen, K.K., Rowe, A., 2012b. Experimental and modeling results of a parallel plate-based active magnetic regenerator. *Int. J. Refrig.* 35, 1518–1527. doi:10.1016/j.ijrefrig.2012.04.016

- Tura, A., Roszmann, J., Dikeos, J., Rowe, A., 2006. Cryogenic Active Magnetic Regenerator Test Apparatus, in: AIP Conference Proceedings. AIP, pp. 985–992. doi:10.1063/1.2202511
- Tura, A., Rowe, A., 2011. Permanent magnet magnetic refrigerator design and experimental characterization. *Int. J. Refrig.* 34, 628–639. doi:10.1016/j.ijrefrig.2010.12.009
- Tusek, J., Kitanovski, A., Prebil, I., Poredos, A., 2011. Dynamic operation of an active magnetic regenerator (AMR): Numerical optimization of a packed-bed AMR. *Int. J. Refrig.* 34, 1507–1517. doi:10.1016/j.ijrefrig.2011.04.007
- Tušek, J., Kitanovski, A., Tomc, U., Favero, C., Poredoš, A., 2014. Experimental comparison of multi-layered La-Fe-Co-Si and single-layered Gd active magnetic regenerators for use in a room-temperature magnetic refrigerator. *Int. J. Refrig.* 37, 117–126. doi:10.1016/j.ijrefrig.2013.09.003
- Tušek, J., Kitanovski, A., Zupan, S., Prebil, I., Poredoš, A., 2013. A comprehensive experimental analysis of gadolinium active magnetic regenerators. *Appl. Therm. Eng.* 53, 57–66. doi:10.1016/j.applthermaleng.2013.01.015
- Vibrating Sample Magnetometers | Lake Shore Cryotronics, Inc. [WWW Document], 2016. URL <http://www.lakeshore.com/products/Vibrating-Sample-Magnetometer/Pages/Model-Landing.aspx>
- Von Moos, L., Bahl, C.R.H., Nielsen, K.K., Engelbrecht, K., Kupferling, M., Basso, V., 2014. A Preisach approach to modeling partial phase transitions in the first order magnetocaloric material MnFe(P,As). *Phys. B Condens. Matter* 435, 144–147. doi:10.1016/j.physb.2013.09.054
- von Ranke, P.J., de Oliveira, N.A., Alho, B.P., Plaza, E.J.R., de Sousa, V.S.R., Caron, L., Reis, M.S., 2009. Understanding the inverse magnetocaloric effect in antiferro- and ferrimagnetic arrangements. *J. Phys. Condens. Matter* 21, 56004. doi:10.1088/0953-8984/21/5/056004
- Vuarnoz, D., Kawanami, T., 2012. Numerical analysis of a reciprocating active magnetic regenerator made of gadolinium wires. *Appl. Therm. Eng.* 37, 388–395. doi:10.1016/j.applthermaleng.2011.11.053
- Wada, H., Tanabe, Y., 2001. Giant magnetocaloric effect of MnAs[1-x]Sb[x]. *Appl. Phys. Lett.* 79, 3302. doi:10.1063/1.1419048
- Wakao, N., Kaguei, S., Funazkri, T., 1979. Effect of fluid dispersion coefficients on particle-to-fluid heat transfer coefficients in packed beds. *Chem. Eng. Sci.* 34, 325–336. doi:10.1016/0009-2509(79)85064-2
- Warburg, E., 1881. E . WARBURG . - Magnetische Untersuchungen etiques); Ann . der Physik und u " ber einige Wirkungen der magnetischen Coercitivkraft (Remarques

sur un Memoire de M . Warburg relatif ` a quelques actions de la force coercitive magn ´ etique); Ann . der Ph. Ann. der Phys. und Chemie 8, 495–500.

Wu, H.C., Chang, R.C., Hsiao, H.C., 2009. Research of minimum ignition energy for nano Titanium powder and nano Iron powder. *J. Loss Prev. Process Ind.* 22, 21–24. doi:10.1016/j.jlp.2008.10.002

Yu, B., Liu, M., Egolf, P.W., Kitanovski, A., 2010. A review of magnetic refrigerator and heat pump prototypes built before the year 2010. *Int. J. Refrig.* 33, 1029–1060. doi:10.1016/j.ijrefrig.2010.04.002

Zhang, L., Sherif, S.A., DeGregoria, A.J., Zimm, C.B., Veziroglu, T.N., 2000. Design optimization of a 0.1-ton/day active magnetic regenerative hydrogen liquefier. *Cryogenics (Guildf)*. 40, 269–278. doi:10.1016/S0011-2275(00)00039-4

Zimm, C., Boeder, A., Chell, J., Sternberg, A., Fujita, A., Fujieda, S., Fukamichi, K., 2006. Design and performance of a permanent-magnet rotary refrigerator. *Int. J. Refrig.* 29, 1302–1306. doi:10.1016/j.ijrefrig.2006.07.014

Zimm, C., Jastrab, A., Sternberg, A., Pecharsky, V.K., Gschneidner Jr, K.A., Osborne, M., Anderson, I., 1998. Description and performance of a near-room temperature magnetic refrigerator. *Adv. Cryog. Eng.* 43, 1759–1766. doi:10.1007/978-1-4757-9047-4_222

BIOGRAPHICAL SKETCH

Michael A. Benedict was born in 1984 to Donna and Michael Benedict in Clearwater, Florida. Michael was interested in science, math, and engineering from an early age. These interests stayed with him through high school and into college. His undergraduate degree was in mechanical engineering at the University of South Florida.

After the University of South Florida Michael decided to continue his education in engineering at the University of Florida. He graduated with a Master of Science in mechanical engineering in 2009, and entered the workforce at General Electric in Louisville, KY. In Louisville Michael worked in GE's Edison Engineering Leadership Development Program. Upon finishing the two year rotational program he was hired full time into the research department heading up an effort on magnetocaloric refrigeration. Here he was given the option to pursue his Ph.D. which he chose to do at the University of Florida. It was also at GE that Michael met his future wife Jessica Alvarado through their mutual interests in engineering, rock climbing, and travel.